Numerical studies of non-equilibrium dynamics in $\mathbb{Z}_3$ chiral clock model

A thesis submitted in partial fulfilment of the requirements for the
degree of
Doctor of Philosophy
by

Naveen Nishad
Reg. ID - 20152039

IISER PUNE

INDIAN INSTITUTE OF SCIENCE EDUCATION AND RESEARCH,
PUNE

April 2022

Dedicated to Yogesh

CERTIFICATE

Certified that the work incorporated in the thesis entitled "Numerical studies of non-equilibrium dynamics in $\mathbb{Z}_3$ chiral clock model" submitted by Naveen Nishad was carried out by the candidate under my supervision. The work presented here or any part of it has not been included in any other thesis submitted previously for the award of any degree or diploma from any other university or institution.

Supervisor

Sreejith G J

Date: 22.02.2022

DECLARATION

I, **Naveen Nishad**, declare that the written submission entitiled "**Numerical studies of non-equilibrium dynamics in $\mathbb{Z}_3$ chiral clock model**" represents my ideas in my own words and where others ideas have been included, I have adequately cited and referred original sources. I also declare that I have adhered to all principles of academic honesty and integrity and have not misrepresented or fabricated or falsified any idea/data/fact/source in my submission. I understand that violation of the above will be cause for disciplinary action by the institute and can also evoke penal action from the sources which have thus not been properly cited or from whom proper permission has not been taken when needed. The work reported in this thesis was done under the guidance of Dr. G J Sreejith.

Naveen Nishad
Reg. ID - 20152039
April 2022

Acknowledgements

I will start by thanking my advisor Dr. G J Sreejith. Having him as my advisor is the best thing that happened to me in my journey through the wonderland of Physics till now. I will always look up to his intense focused work throughout the day, professionalism, and discipline. I will always be grateful to him for providing me ample opportunities to attend several schools and conferences, and resources for my research.

I am grateful to Deepak Dhar for the insightful discussions and his feedback on manuscripts of my every project. I want to thank Bijay Kumar Agarwalla for our discussions on the open quantum system and Green's function. I would like to thank Fabian Alet for his valuable suggestions and help in the work presented in Chapter 6 of this thesis. I also want to thank Shashi Srivastav for his help on level spacing calculations. I thank Arun M. Thalapillil for letting me use his computational resources. I want to thank T S Mahesh and M S Santhanam for being members of my Research Advisory Committee and giving me their valuable feedback on my research.

I am grateful to my parents and Chotu chacha for their love and support. Special thanks to my elder brother Praveen for taking responsibility of our family while I was away for my education and never stopping believing in me.

I have been blessed with great friends at all stages of my life. I want to thank Dinkar for constantly supporting and guiding me with his taunts. My time at IISER would have never been enjoyable without Arindam, Deepak, and Shailendra. I will always miss and cherish our UNO nights and evening walks. I want to thank Bhumika, Angira, Sunny, Shruti, Surya, Rinku, Unmesh, Abhijeet and Sumit for their company and for making this stay at IISER memorable. I would like to thank my labmate Abhishek for interesting discussions on video games, physics, coding, and music from which I learned a lot.

Special thanks to the team of opensouce package iTensor which I have extensively used in my research. I acknowledge the Ministry of Human Resource Development, India, and IISER Pune for providing financial support during the period of research.

Abstract

This thesis addresses the out-of-equilibrium physics of the one-dimensional $\mathbb{Z}_3$ chiral clock model. The model is the $\mathbb{Z}_3$ symmetric generalization of the quantum Ising model. Jordan-Wigner transformation maps the model to parafermions similar to the mapping to fermions of the Ising model, however, this does not make the model exactly solvable. The interplay of chirality, multiple domain wall flavors, and integrability of the chiral clock model reflects in the quantum dynamics; we explore this using the matrix product states technique.

We drive the chiral clock model out of equilibrium through three different protocols - periodic boundary drive, quench, and through coupling to two thermal baths of unequal temperature. For the slow boundary periodic drive of the critical $\mathbb{Z}_3$ clock chain, we argue using Kibble-Zurek mechanism and critical scaling properties that the Loschmidt echo scales with frequency as a power law whose exponent depends on the functional form of the boundary perturbation. We demonstrate this using large scale matrix product states calculations.

For weak quenches from an ordered state, we showed that the system thermalizes in the bulk, but the boundary fails to thermalize in the chiral case but thermalizes in the non-chiral system. We present an understanding in terms of entanglement growth due to domain wall dynamics and scattering properties at the boundaries.

Lastly, we present the energy transport properties of the model and explore its dependence on chirality. Non-equilibrium steady-state energy transport arising in response to a thermal gradient is modeled by using the Lindblad master equation implemented. We show that energy transport is ballistic at the integrable points and superdiffusive otherwise. In addition to the results on $\mathbb{Z}_3$ chiral clock model, we also discuss the temporal order observed in a nearly-$\mathbb{Z}_2$-symmetric realization of interacting spin-half degrees of freedom in an NMR system . The system shows robust period two response when driven out of equilibrium by approximate π-pulse sequences.

Table of contents

List of Publications **xv**

List of figures **xvii**

1 Introduction **1**
- 1.1 Transverse field Ising model . . . 2
- 1.2 Lattice boson model . . . 3
- 1.3 $\mathbb{Z}_3$ Chiral Clock Model . . . 6
  - 1.3.1 Classical Ground states at $f = 0$ . . . 7
  - 1.3.2 Symmetries of Chiral Clock Model . . . 8
  - 1.3.3 Phase Diagram . . . 9
  - 1.3.4 Parafermions and Edge zero modes . . . 11
  - 1.3.5 Domain wall picture . . . 13
- 1.4 Problems addressed . . . 18

2 Matrix Product States and Operators **21**
- 2.1 Physical corner of the Hilbert space . . . 21
- 2.2 Tensor representation . . . 23
- 2.3 Singular Value Decomposition . . . 24
- 2.4 Matrix Product States . . . 25
- 2.5 Matrix Product Operators . . . 28
- 2.6 Computing Expectation values . . . 31
- 2.7 Ground state search . . . 32
- 2.8 Time evolution . . . 33
- 2.9 Density matrices . . . 36
- 2.10 Conclusion . . . 36

3 Boundary Driving a Critical $\mathbb{Z}_3$ Clock Chain **37**
- 3.1 Introduction . . . 37

3.2 Boundary driven critical Ising chain 39
3.3 Model and description of scaling 41
3.4 Numerical methods 45
3.5 Fourth order approximant for time evolution 45
3.6 Numerical results 49
3.7 Conclusions 53

4 Post quench entropy dynamics 55
4.1 Introduction 55
4.2 Quench in TFIM 58
4.3 Model 59
4.4 Numerical simulation of the time evolution 63
4.5 Numerical results: Quench into the non-chiral model 63
  4.5.1 Magnetization 67
  4.5.2 Two point correlations 69
  4.5.3 Entanglement entropy 70
4.6 Numerical results: Quench into the chiral Hamiltonian 73
  4.6.1 Magnetization 76
  4.6.2 Two point correlations 79
  4.6.3 Entanglement entropy 79
4.7 Summary and Conclusion 80

5 Lindblad Master Equation implementation using MPS 85
5.1 Open Quantum System 85
5.2 Lindblad Master Equation 86
5.3 Microscopic derivation of LME 87
5.4 Choi Isomorphism 90
5.5 MPS implementation of time evolution 92
5.6 Lindblad Dissipators 95

6 Energy transport in $\mathbb{Z}_3$ chiral clock model 99
6.1 Introduction 99
6.2 Transport in spin-1/2 Models 100
6.3 Model 102
6.4 NESS currents at θ, $\theta + 2\pi/3$ and $-\theta$ 107
6.5 Numerical Implementation 108
6.6 Results 109

6.6.1 NESS Current and Conductance 110
6.6.2 Operator space entanglement 117
6.7 Level spacing statistics 117
6.7.1 Spectrum through Exact Diagnoalization 118
6.7.2 Unfolding Procedure 119
6.8 Conclusion 119

7 Temporal order in periodically driven spins in star-shaped clusters 121
7.1 Introduction 121
7.2 Model and numerical results 123
7.3 NMR setup: 127
7.4 Results and discussion 128
7.5 Conclusion 130

8 Conclusion 133

References 139

List of Publications

This thesis is based on the following manuscripts which has already been published in the international peer reviewed journals. Author contributed majorly in the following projects and Chapter 3, 4 and 6 of this thesis are based on it.

- Scaling of Loschmidt echo in a boundary-driven critical $\mathbb{Z}_3$ Potts model
  Naveen Nishad and GJ Sreejith
  Phys. Rev. B 101, 144302 (2020)

- Postquench entropy growth in a chiral clock model
  Naveen Nishad, M Santhosh and GJ Sreejith
  Phys. Rev. B 103, 195141 (2021)

- Energy transport in $\mathbb{Z}_3$ chiral clock model
  Naveen Nishad and GJ Sreejith
  New J. Phys. 24, 013035 (2022)

Chapter 7 is based on the follwoing manuscript in which numerical and analytical explanation was done by the author while experiments were performed by Soham Pal and T. S Mahesh.

- Temporal Order in Periodically Driven Spins in Star-Shaped Clusters
  Soham Pal, **Naveen Nishad**, T.S. Mahesh, and G.J. Sreejith
  Phys. Rev. Lett. 120, 180602 (2018)

List of figures

1.1 Phase diagram of the lattice boson model proposed by Fendley *et. al.* Figure reproduced with permission from Ref. [1] 4

1.2 Phase diagram of the Hamiltonian Eq. 1.9 as a function of Hamiltonian paramters Δ/Ω and blockade radius defined in units of trap spacing a by R_b/a. Figure reproduced with permission from Ref. [2] 6

1.3 Schematic representation of the effect of θ on eigenstates of the two spin interaction: Eigenvalues of $e^{\iota\theta}\sigma_i\sigma^\dagger_{i+1}$ are plotted as vectors in the argand plane. These are labelled by the values of $\sigma_i\sigma^\dagger_{i+1}$ for the same states. In the boxed panel, states of the spin on site i and $i+1$ that can result in these eigenvalues $1, \omega$ and $\bar{\omega}$ for $\sigma_i\sigma_{i+1}$ are shown. 7

1.4 Phase diagram of the chiral clock model using $J = 1 - f$ in Eq. 1.10 showing phase boundary between trivial, topological and incommensurate phase as function of parameters f, θ and ϕ. Figure reproduced with permission from Ref. [3]. 10

1.5 Trivial ($J = 0$) and topological phase ($f = 0$) in the parafermionic representation of chiral clock model Hamiltonian. Here the solid black lines represent the coupled parafermionic terms of the Hamiltonian. Parafermionic edge modes χ_1 and ψ_L are encircled for $f = 0$ case. . . . 11

1.6 Figure summarises the features of zero modes on basis of splitting in first excited state for $\theta \in (0, \pi/3)$ 13

1.7 Spectrum features of the Hamiltonian Eq. 1.10 for $f = 0$. Ground states are triply degenerate for both $\theta = 0$ and $\neq 0$. First excited state for non-chiral Hamiltonian is with single domain wall with both positive and negative chirality states having same energy *i.e.* $E^+_{1-\text{domain}} = E^-_{1-\text{domain}}$. For the chiral case, degeneracy of positive and negative chirality one domain wall states is broken. Figure reproduced with permission from Ref. [4]. 14

1.8 Figure shows the simplest possible mechanism of inter-conversion of degenerate states at the level of the ground and excited state in panels a and b, respectively. Y-axis is the perturbation step, and the x-axis is the position in the chain. A solid line drawn is the domain wall location in the chain, which is changing with time because of the hopping process. Figure reproduced with permission from Ref. [4]. 16
1.9 Single domain wall band energies for positive and negative chirality states is shown in blue and orangle color respectively. Two different scenarios are shown $\theta < \theta_{c1}$ and $\theta > \theta_{c1}$ which explains the exponential and power law splitting of the degenerate excited states. 18

2.1 Panel a conveys the idea of area law scaling of entanglement betweent the subsystem A and B. States obeying the area law occupies only a tiny fraction of the Hilbert space $\mathcal{H}$ as shown in panel b. 22
2.2 Pictorial representation of a scalar, vector and rectangular matrix is shown in (a), (b) and (c) respectively. Dual of a vector v is shown as v^* in (b). Typically the leg of the dual tensor is flipped. Matrix-vector and matrix-matrix multiplication operation are shown in panel (d) and (e). 23
2.3 Coeffecient of many-body wavefunction $c_{\sigma_1\sigma_2\ldots\sigma_N}$ shown as a tensor of rank N. 24
2.4 Diagramatic notation for the MPS representation of Eq. 2.3 open and periodic boundary condition. 25
2.5 Diagramatic notation for understanding the gauge degree of freedom in MPS representation arising from the invariance of state $|\psi\rangle$ after insertion of product of tensors $X_{i+1}X_{i+1}^{-1}$ in between the consecutive local tensor T 27
2.6 Property of the left and right canonical form mentioned in Eq. 2.11 and 2.13 is shown in the tensor diagramatic notation in (a) and (b) respectively. 28
2.7 Diagramatic notation for the MPO representation of opertor $\hat{O}$ 29
2.8 Finite state automaton representation of MPO of Hamiltonian Eq. 2.16. 30
2.9 Figure showing simplification of the calculation of the expectation value by using mixed canonical form. 32
2.10 Equation 2.30 can be visualized by the tensor network diagram shown. Darkened circle represents the local tensor $\vec{M}^{\sigma_i}$ and the H_{eff} is the rest of the tensor network after excluding $\vec{M}^{\sigma_i}$ in network shown in left hand side. 33

2.11 Time evolution of an MPS $|\psi(0)\rangle$ using the MPO's estimated by first order Suzuki-Trotter decomposition mentioned in Eq. 2.32. After contracting MPO with MPS we get the time evolved state $|\psi(t)\rangle$. . . . 34

2.12 Often in initially weakly entangled states, subsystem entanglement $S(t)$ grows linearly with time and the bond dimension D_{min} needed to accurately describe the state increases exponentially with time. Figure shows exponential growth of minimum bond dimension D_{min} with time results in entanglement barrier when D_{min} crosses the bond dimension D_0. 35

3.1 Figure showing adibatic and frozen region resulting from divergence of relaxation time near the critical point f_c as Hamiltonian paramter f is varied. Kibble-Zurek time seperates the adiabatic and frozen region. . 41

3.2 (a) Overlap of the time evolved state $|\psi(t)\rangle = e^{-\imath H_B t} |0_A\rangle$ with the initial state $|0_A\rangle$ shown schematically. In complex time, this is the partition function on a strip with the fixed state $|0_A\rangle$ at the top and bottom ends of the strip. (b) Since $|0_A\rangle$ is the ground state of H_A, this can be interpreted as the state evolved after a long time from an arbitrary state under complex time evolution under H_A. (c) Identifying the arbitrary initial and final states maps the overlap to a partition function on a cylinder with Hamiltonians H_B and H_A in two regions. (d) Effect of the two Hamiltonians can be approximated as enforcing two boundary conditions in the corresponding regions. (e) The changing boundary conditions can be interpreted as insertion of suitable boundary condition changing operators. Figure reproduced with permission from Ref. [6]. 42

3.3 (a) Loschmidt echo after a quench of the boundary field from h_b to $-h_b$ plotted as a function of the rescaled time $t/\tau = th_b^3$ for system size L=300. Inset shows the same data as a function of time. (b) Same as panel (a) but after filtering out the oscillatory components of the Loschmidt echo. (c) Exponent $\gamma(t, h_b)$ estimated near specific times t plotted as a function of h_b. $\gamma(t, h_b)$ is estimated from the slope of $\log \mathcal{L}(t)$ vs $\log t$ shown in panel (b). Comparison with data from $L = 120, 180$ indicate saturation to the expected exponent $8/5$ at large Th^3 in large systems. (d) Same as panel (c) but plotted as a function of rescaled time. Figure reproduced with permission from Ref. [6]. 46

3.4 (a) Loschmidt echo $\mathcal{L}(T)$ at the end of a time period plotted as a function of rescaled time period $T/\tau = Th_b^3$ for a triangular-wave boundary field for system size L=300 in the low frequency regime. (b) $\mathcal{L}(T)$ plotted as a function of the time period. (c) Scaling exponent $\gamma(T)$ estimated using data at fixed T by calculating the slope of $\ln \mathcal{L}$ vs $\ln Th_b^3$. Large T limit of γ is obtained by fitting the data to $\gamma(T) = \gamma(\infty) + \frac{axT^{-x}}{1+aT^{-x}}$. Figure reproduced with permission from Ref. [6]. 50

3.5 Loschmidt echo for a sinusoidal wave perturbation for system size L=300 in the low frequency regime. Loschmidt echo at the end of one drive cycle (N=1) as a function of rescaled time period $T/\tau = Th_b^3$ is shown in panel (a). Panel (b) shows the same data as a function of T. Scaling exponent $\gamma(T)$ estimated from data at fixed time period T. Asymptotic value is estimated by fitting to $\gamma(\infty) + \frac{axT^{-x}}{1+aT^{-x}}$. Figure reproduced with permission from Ref. [6]. 52

4.1 Panel a shows the Hamiltonian matrix in the one-domain-wall space after relabeling $1\bar{\omega}$ domain wall at bond number $i < L$ as $x = 2L - i - 1$ and 1ω domain wall at bond number $i < L$ as $x = i$. Effective dispersions of opposite chirality (the two colors represent the bands for the two different chiralities) domain walls are shown schematically for the case of small θ(panel b) and large θ(panel c). Panels d and f schematically show the fate of a domain wall wave-packet that bounces off a boundary in a system with small θ. Panel d shows the incoming packet and panel f shows the fate after collision with the boundary. Incoming domain wall has one chirality (indicated in orange) whereas the reflected domain wall is primarily of opposite (blue) chirality. Panels e and g are similar but for a case where θ is larger. Here the domain wall bounces back without change in the flavor. Figure reproduced with permission from Ref. [7]. 62

4.2 Schematic representation of the state of the system after a weak quench. State after the quench is, to a good approximation, a linear combination of the ordered state and $1\omega 1$ and $1\bar{\omega}1$ type two domain wall states. The vertical direction represents the time evolution of domains in each term. Flipped spin domains are nucleated from all parts of the chain forming different terms of the linear combination in the computational basis. The domains expand as the domain walls propagate. In a system with non-linear dispersion, the domain walls of different momenta propagate at different group velocities. Dashed vertical lines demarcate a subsystem. For each cone, spins flipped to ω and $\bar{\omega}$ inside the subsystem are shown in blue and orange colors. The flipped spins outside the system are colored gray irrespective of direction of the spins inside them. Figure reproduced with permission from Ref. [7]. 64

4.3 Panel a shows the total probability of domain wall pair states that occur with non-zero probabilities after the quench from a fully ordered state to a final Hamiltonian with $f = 0.1$ and $\theta = 0$. System size is $L = 40$. Panel b shows the probabilities but in a system with an additional longitudinal field $h = 0.02$ in the final Hamiltonian. In Panel a and b, domain wall types $1\omega 1$ and $1\bar{\omega}1$ have equal probabilities and the corresponding lines (orange and blue) completely overlay over one another. Similarly, lines corresponding to domain wall configurations $1\omega\bar{\omega}$, $\bar{\omega}\omega 1$, $1\bar{\omega}\omega$ and $\omega\bar{\omega}1$ also overlay over each other. Panels (c,d) show the corresponding results for the three domain wall states of the form $ABCA$. Figure reproduced with permission from Ref. [7]. 65

4.4 Scattering dynamics of a domain wall of flavor $\ldots\omega\omega 11\ldots$ localized at bond $x = 5$ is shown here for quench Hamiltonian parameters $f = 0.1$ and $\theta = 0.0$. From panel (a) to (f) in alphabetical order, probability of single domain wall flavors $1-\omega$, $\omega-1$, $1-\bar{\omega}$, $\bar{\omega}-1$, $\omega-\bar{\omega}$ and $\bar{\omega}-\omega$ localized at bond x at time t is plotted with t and x on y and x axis respectively. In the panel (b) and (d) we can see that domain wall of flavor $\ldots\omega\omega 11\ldots$ changes its flavor to $\ldots\bar{\omega}\bar{\omega}11\ldots$ after scattering from the boundary for the nonchiral quench. 66

4.5 Magnetization as a function of time for quenches to different final Hamiltonians is shown in panel a. Panel b shows the power spectrum of magnetization for a specific example where the final non-chiral Hamiltonian has $f = 0.1, h = 0.1$. The peaks correspond to the masses m_i of the domain wall bound states or the differences between the masses $m_{ij} = |m_i - m_j|$. Variation of first three masses with longitudinal field h is shown in panel c. System size used is $L = 40$. Figure reproduced with permission from Ref. [7]. 68

4.6 Panel a shows the absolute value of the connected correlations as a function of position and time in the case of a quench to the non-chiral clock model. The lines show constant height contours and have a slope of 1.0/0.38 consistent with the expected correlation spread rate of $2v_g = 4f \sim 0.4$. Panel b shows same quantity in the case where the final Hamiltonian has an additional longitudinal field constraining the spread of domains. System size used is $L = 40$. Figure reproduced with permission from Ref. [7]. 70

4.7 Panel a shows entanglement growth in a subsystem in the bulk after a quench to the non-chiral Hamiltonian from a fully ordered initial state. The results for a subsystem at the boundary of the system is shown in panel d. Panels b and e show the corresponding results for the case of a quench to a Hamiltonian with an additional longitudinal field, demonstrating the suppression of entanglement growth. Panels c and f show the entropy growth in the bulk and near the boundary in a scenario where the initial state is the parity eigenstate $|11...1\rangle + |\omega\omega...\omega\rangle + |\bar{\omega}\bar{\omega}...\bar{\omega}\rangle$. System size simulated is $L = 40$. Figure reproduced with permission from Ref. [7]. 71

4.8 Illustration of an $\ell = 4$ site subsystem located at the boundary (a) and one located in the bulk of the system (b). The entanglement entropy of these subsystems with the rest of the system are labeled as S_ℓ^{boundary} and S_ℓ^{bulk}. Figure reproduced with permission from Ref. [7]. 73

4.9 Panel a shows the total probability (over all positions) of two domain wall states corresponding to the ones in Fig 4.3a after a quench to a Hamiltonian with $\theta = \pi/8$ and $f = 0.1$. Unlike the non-chiral case, the domain walls do not scatter into other forms at the boundary resulting in a steady probability. Panel b shows the same but with a final Hamiltonian that has an additional longitudinal field h. Panels c and d shows the probability weight of three domain wall states of type $ABCA$. Unlike the non-chiral case, the probabilities of $1\omega\bar{\omega}1$ and $1\bar{\omega}\omega1$ states occur with different probabilities. Note that in Panels a and b lines corresponding to $1\bar{\omega}\omega$,$1\omega\bar{\omega}$, $\bar{\omega}\omega1$ and $\omega\bar{\omega}1$ overlap on each other. Same is true of $1\omega1$ and $1\bar{\omega}1$ lines. In panels c and d lines corresponding to $\omega\bar{\omega}1\omega$, $\bar{\omega}\omega1\omega$, $\omega1\bar{\omega}\omega$ and $\omega1\omega\bar{\omega}$ overlap with each other. System size is $L = 50$. Figure reproduced with permission from Ref. [7]. 74

4.10 Scattering dynamics of a domain wall of flavor $\ldots\omega\omega11\ldots$ localized at bond $x = 5$ is shown here for quench Hamiltonian parameters $f = 0.1$ and $\theta = 0.26$. From panel (a) to (f) in alphabetical order, probability of single domain wall flavors $1-\omega$, $\omega-1$, $1-\bar{\omega}$, $\bar{\omega}-1$, $\omega-\bar{\omega}$ and $\bar{\omega}-\omega$ localized at bond x at time t is plotted with t and x on y and x axis respectively. In the panel (b) we can see that domain wall of flavor $\ldots\omega\omega11\ldots$ retains its flavor after scattering from the boundary for the chiral quench. 75

4.11 Energy of bound domain wall pairs extracted from the power spectrum of magnetization in the same manner as in Fig 4.5. Panel a shows the masses as a function of the longitudinal field for a fixed θ. Panel b shows the dependence of the masses on θ for fixed h. Spectra are calculated from magnetization time series upto time $t = 90$ in a system of size $L = 40$. The scatter in the data is primarily caused by the finite frequency resolution in a Fourier transformation of data over a finite range of time. Figure reproduced with permission from Ref. [7]. 76

4.12 Panels a and b show the real and imaginary parts of the correlator $C(i,t)$ after the fully ordered state is quenched to a final Hamiltonian with $f = 0.1, \theta = \pi/8$. Straight lines overlayed in the figure showing the rate of spread of correlations are obtained by fitting to constant C contours. The slope of the line is consistent with the expected rate of spread of correlations $2v_g = 4f$. Panel c shows the rate of spread as a function of f for different θ values. The dotted line shows the expected dependence $4f$. In Panel d, $\mathrm{Im}\langle\sigma_0\sigma_i^\dagger\rangle_c(t)$ as a function of position is shown for different θ values and a fixed time slice t (corresponding to the time slice indicated by the horizontal line in panel b). System size used for the calculation is $L = 40$. Figure reproduced with permission from Ref. [7]. 77

4.13 Panels a and d show the entanglement entropy as a function of time for subsystems located in the bulk and at the edge of the system. Panels b and e show the same for the cases where the final Hamiltonian has an additional longitudinal field. Panels c and f show the results for the case where the initial state is a parity eigenstate of the form $|..1111...\rangle + |...\omega\omega\omega...\rangle + |...\bar{\omega}\bar{\omega}\bar{\omega}...\rangle$. Above results are obtained in a system of size $L = 40$ and for a final Hamiltonian with $f = 0.1$ and $\theta = \pi/8$. Figure reproduced with permission from Ref. [7]. 78

4.14 Rate of change of entropy in a subsystem located at the edge at an instant ($Jt = 60$) after the saturation time ℓ/v_g is shown as a function of θ for different f in the final Hamiltonian. The arrows are crossover θ_c estimated for each f based on Eqn 4.10. Entropy saturates for $\theta > \theta_c$. Figure reproduced with permission from Ref. [7]. 80

4.15 Magnetization profile in the chain with open boundary conditions at the left and right ends. The magnetization at the boundary of the chain decays with time in the non-chiral model (panel a), whereas it saturates to constant in the chiral model (panels b,c). The saturation values vary linearly with distance from the boundary. Panel d shows the magnetization at a fixed position near the edge as a function of time for three different values of θ. Figure reproduced with permission from Ref. [7]. 83

5.1 Pictorial representation for a composite closed quantum system comprised of system and bath. Interaction between system and bath makes the system an open quantum system. 86

5.2 Figure showing vectorization process of the density matrix ρ into vector $|\rho\rangle$ in the tensor network representation. The primed indices corresponds to the bra indices is transformed to ket indices and then both primed and non primed ket indices are fused into a single index μ_i. 91

5.3 Left and Right action of operator O on the ρ contracting with non primed and primed index is shown in Panel (a) and (b) respectively. Two different versions of the O are needed for its action on the $|\rho\rangle$ as shown in Panel (c) and (d). Version of O for the left and right action over the $|\rho\rangle$ are shown in green and yellow color in (e) and (f). 93

6.1 Pictorial representation of the bath system setup is shown in panel (a). Action of the jump operators $L_{|11\rangle\to|1\omega\rangle}$ and $L_{|1\omega\rangle\to|11\rangle}$ are shown for the ferromagnetic regime for dissipators $\mathcal{D}^0$ and $\mathcal{D}^\theta$ is shown in (b) and (c). Figure reproduced with permission from Ref. [8]. 104

6.2 Plot of the NESS current I^θ as a function of θ for its full range of values from 0 to 2π showing the equivalence of transport properties at θ, $-\theta$ and $\theta + 2\pi/3$. Data is shown for the system size $N = 14$, with the dissipator $\mathcal{D}^\theta$ at model parameters $f/J = 0.4$. Vertical lines show multiples of $\pi/3$. Inverse temperatures used for left and right baths are $\beta_L = 0.133$ and $\beta_R = 0.266$ respectively. Figure reproduced with permission from Ref. [8]. 108

6.3 NESS current $\langle I^\theta \rangle$ as a function of θ in the ferromagnetic regime. Panel (a) shows the current when the Liouvillian is defined using the dissipator $\mathcal{D}^\theta$ and $f/J = 0.4$. Panel (b) and (c) show the current for the case of the dissipator $\mathcal{D}^0$ with $f/J = 0.4$ and $f/J = 0.2$ respectively. Different lines indicate different system sizes. The peak current appears at the integrable point $\theta = \cos^{-1}(f/J)/3$ shown by vertical dashed lines in all cases. Inverse temperatures used for left and right bath are $\beta_L = 0.133$ and $\beta_R = 0.266$ respectively. Figure reproduced with permission from Ref. [8]. 110

6.4 Panel (a) presents $I^\theta(N)$ (rescaled by the current in the smallest system size) vs $N-4$ in log-scale for fixed values of θ for $f/J = 0.4$ and using the dissipator $\mathcal{D}^\theta$. Panels (b) and (c) show the scaling exponent γ estimated from the system size dependence of the NESS current $I^\theta(N)$. Estimated γ is plotted as function of θ in panels (b) and (c). In panel (b), we compare the exponent γ obtained from the two different choice of dissipators $\mathcal{D}^0$ and $\mathcal{D}^\theta$. In panel (c) we compare the estimated γ obtained using the same dissipator $\mathcal{D}^0$ but for $f/J = 0.2$ and $f/J = 0.4$. Inverse temperatures used for left and right bath are $\beta_L = 0.133$ and $\beta_R = 0.266$ respectively. Figure reproduced with permission from Ref. [8]. 111

6.5 Spatial profile of energy density and current for system sizes N=14, 20, 24, and 28 with position shown on the x-axis rescaled by a factor of $1/(N-2)$. Profiles for Hamiltonian parameters $\theta = 0.2$ in panel (a) and (d), $\theta = 0.38$ in panel (b) and (e), and $\theta = 0.2$ in panel (c) and (f). $\theta \sim 0.38$ is close to the integrable point. Inverse temperatures used for left and right bath are $\beta_L = 0.133$ and $\beta_R = 0.266$ respectively. Figure reproduced with permission from Ref. [8]. 112

6.6 Energy density as a function of the position in the NESS obtained after attaching only one bath to a chain. The two different lines indicate the energy densities realized upon attaching baths with parameters β_R and β_L. Different overlapping lines of different thicknesses show the data for different system sizes. Figure reproduced with permission from Ref. [8]. 113

6.7 Each panel shows the energy densities as a function of the position for different system sizes. Position on the x-axis has been rescaled and shifted that center of the chain is at 0 and the 4th spin from the ends are at ±0.5. The two dotted lines show the expected energy densities had the each one of the baths fully equilibrated with the chain (See Fig 6.6). The four panels show the data for four different cases. Panels (a) and (c) show results for θ less than that of the integrable point. Panel (b) shows the data at a θ very close to the integrable point. Panel (d) shows the same at θ larger than that of the integrable point. Inverse temperatures used for left and right bath are $\beta_L = 0.133$ and $\beta_R = 0.266$ respectively. Figure reproduced with permission from Ref. [8]. 114

6.8 In panel (a) and (b), $\log(I^{\theta}(N)/\Delta E)$ vs $\log(N-7)$ is shown for both dissipators $\mathcal{D}^0$ and $\mathcal{D}^{\theta}$. Scaling exponent γ is obtained by linearly fitting $\log(I^{\theta}(N)/\Delta E)$ vs $\log(N-7)$ data and is plotted as function of θ in panels (c) and (d). θ in the vicinity of integrable points (vertical dashed line) are not shown as the numerically obtained conductance κ show wild oscillations due to vanishing energy gradient. Figure reproduced with permission from Ref. [8]. 115

6.9 (a) Rescaled current I_{rescaled} of NESS as a function of θ and f/J is plotted. Comparison of numerically estimated $\theta_{\text{ballistic}}$ and the integrable line $\theta = \cos^{-1}(f/J)/3$ is shown in (b). Figure reproduced with permission from Ref. [8]. 116

6.10 Operator space entanglement entropy S_i plotted as a function of the bond location i. All data are for system size $N = 32$ and at $f/J = 0.4$. The two panels show the entropy for the NESS obtained under the dissipators $\mathcal{D}^0$ and $\mathcal{D}^{\theta}$. Figure reproduced with permission from Ref. [8]. 117

6.11 Level spacing distributions for $\theta = 0.1$ and $\theta = 0.456$ (close to the ballistic point) are shown in panels (a) and (b) respectively. In (c), variation of mean level spacing ratio $\langle r \rangle$ is plotted versus θ showing change in level spacing statistics from GOE to Poissonian at the integrable point $\cos^{-1}(f/J)/3$. Figure reproduced with permission from Ref. [8]. 120

7.1 Molecules used in the experiments - acetonitrile (a), trimethyl phosphite (TMP) (b) and tetrakis(trimethylsilyl)silane (c) with the 4, 10 and 37 NMR active nuclei encircled. (d) Experimentally measured magnetization $\langle S_i^z \rangle$ of satellite spins of TMP for the pulse sequence in Eq. 7.1 with $JT/\hbar = 6.5$ and $\theta = \pi - 0.1$. Red/green dots show the magnetization at odd/even time steps. For visibility in the plot, the y axis has been rescaled at every 100^{th} time step. (e) Blue line shows experimentally measured magnetization oscillations of free/non-interacting spins of protons in acetonitrile which contain a spinless $\mathrm{C}-12$ central spin, at a pulse angle $\theta = \pi - 0.27$. Gray lines indicate the expected response in the absence of a bath. Figure reproduced with permission from Ref. [9]. 122

7.2 Numerical simulations of spins in the rotating basis. (a-b) Time dependence of the expectation values of the three spin components of a satellite (a) and central (b) spin for a system with $N = 8$ spins, $\frac{JT}{\hbar} = 4$ and pulse angle $\theta = e = 0.4$. Initial state is the fully z-polarized state. (c) Entanglement entropy of the central spin. (d) Bloch sphere representing the spin components of a central spin (of a 6 spin cluster) at times $t = 0$, T^+, $2T^-$ and $2T^+$; $+/-$ labels the time just after/before the pulse. Sequence of intermediate dots track the evolution between time $t = T$ and $2T$. (e) Same as (d) but for a satellite spin. (f) Bloch vectors for a single isolated spin at successive time steps. Figure reproduced with permission from Ref. [9]. 124

7.3 (a,b) Time dependence of cross correlation (multiplied by $(-1)^t$) between the central spin S_0^z and a satellite spin S_i^z from simulations of systems of different sizes ($JT/\hbar = 4, e = 0.05$, $\psi = R_x(\pi/8)\left|\uparrow\uparrow\ldots\right\rangle$, $R_x(\pi/8)$ being the rotation of all spins by $\pi/8$ about x). Disorder strengths are 0 (a,c) and 0.5 (b,d). (c,d): Entanglement entropy of the central spin. Disorder averaging has been performed in (b,d). Figure reproduced with permission from Ref. [9]. 126

7.4 Experimentally measured satellite spin magnetization $\sum_{i=1}^{N-1}\langle S_i^z\rangle$. (a,d): Magnitude of the subharmonic peak upon varying e in TMP and Acetonitrile. Solid continuous lines show results from simulations. Different markers indicate Fourier transforms of experimental measurements in different time windows. (b): Waterfall plot of the Fourier spectrum (time-window $0 < t < 80T$) of the experimentally observerd magnetization of TMP at different deviations e. Dashed blue lines indicate the location of peaks expected for a free spin. (c): Variation of the decay time of the experimentally observerd magnetization amplitude with e for TMP. (e,f): Same as (b) but for acetonitrile with a spinfull C-13 (e) and spinless C-12 (f) atom at the center. Figure reproduced with permission from Ref. [9]. 129

7.5 Experimental values of central spin magnetization $\langle S_0^z \rangle$ in TTSS. (a): Subharmonic peak strength as a function of the deviation e. Different markers indicate Fourier transforms in different time windows. (b): Waterfall plot of the Fourier spectrum of the experimentally observed central spin magnetization at different e. Blue dashed line shows the location of the Fourier peaks expected for free spins. (c): Decay time scale as a function of e. Inset shows a semi log plot of the amplitude of magnetization as a function of time. Figure reproduced with permission from Ref. [9]. 130

8.1 Panels a and d show the heatmap for the relative OTOC $\mathcal{F}_{ij}^r$ versus operator separation distance $i - j$ for parameter $\phi = 0.0$ and 0.1 respectively. we have $\theta = 0.3$ for the all the plots presented here. Asymmtery inside the light cone between $+(i - j)$ and $-(i - j)$ is clearly visible when we use the lineplots with $\mathcal{F}_{ij}^r$ and t plotted in y and x axis respectively. Asymmtery inside the light cone can be seen for $(\theta, \phi) = (0.3, 0.1)$ which is plotted in panel (e) while inside of light cone is symmetric for $(\theta, \phi) = (0.3, 0.0)$ which is plotted in panel (b). Velocity dependent Lyapunov exponent λ_v [10] is ploted as a function of velocity v for cases $(\theta, \phi) = (0.3, 0.0)$ and $(\theta, \phi) = (0.3, 0.1)$ in panels (c) and (f). Data presented here is obtained using Krylov subspace technique. 136

Chapter 1

Introduction

Closed quantum many-body systems driven out-of-equilibrium generally relax under their own dynamics at long times. The long time averages of local observables in typical interacting many-body systems approach the values expected from the thermal density matrix [11]. Unitary evolution governs the dynamics of a closed quantum system. Unitary evolution and thermalization are contradictory concepts as the former preserves the information about the initial state while it is lost in the latter. The eigenstate thermalization hypothesis (ETH)[12–14] is the most widely accepted mechanism to reconcile the apparent inconsistency between observed thermalization and the unitary dynamics. The validity of the ETH has been verified numerically [15, 16] for many generic quantum systems. However, there are a few exceptions where a quantum system can escape the eventual fate of thermalization. An integrable system which has an extensive number of conserved quantities relaxes to a generalized Gibbs ensemble [17, 18]. Many-body localized phase for a system with quenched disorder [19–22] can also violate ETH by retaining initial state information at long times. General principles that govern the relaxation process and time scale [23–26] for general quantum systems are still active areas of research.

The field of quantum systems out-of-equilibrium is driven by the quest to understand the route and mechanism for relaxation from a microscopic level. Advances made in experimental and numerical techniques in the past two decades have drastically changed the research landscape in the field. On the experimental front, ultracold atoms and trapped ion systems provide an unprecedented level of control needed to explore out-of-equilibrium dynamics. Several out-of-equilibrium phenomena like quantum Newton's cradle [27, 28], quantum scars [2, 29], time crystals [30, 31] have been realized in such cold atom systems. Emergence of realistic quantum computing systems are also motivating radically new questions, ideas and means of probing quantum many body dynamics [32–35]. With the increase in classical computational power and development of techniques like Density Matrix Renormalization Group (DMRG) [36], tensor network-based methods (Matrix product states [37], Projected entangled pair states [38], time-dependent variational principle [39]) have enabled us to study the non-equilibrium dynamics for a longer time as well as for larger system sizes. Aided by these techniques, numerical experiments in specific quantum many-body systems such as Hubbard models, XXZ model reveal rich quantum dynamical phenomena.

This thesis explores the out-of-equilibrium dynamics of a model beyond these - namely a quantum three-state model that belongs to a larger class of models called $\mathbb{Z}_n$ clock models. A large number of studies have focused on the non-equilibrium dynamics of $n = 2$ case of $\mathbb{Z}_n$ clock model called the Transverse Field Ising Model (TFIM) [40]. TFIM is the paradigmatic model to study quantum phase transitions, dynamics *etc.* owing to its exact solvability. Several studies also explore two-state models other than TFIM. However, there are few studies on higher spin systems. This thesis ventures away from these and analyze some of the out-of-equilibrium properties of the three-state model called $\mathbb{Z}_3$ chiral clock model, which is the simplest non-trivial $\mathbb{Z}_n$ clock model beyond the exactly solvable TFIM.

This chapter is structured in the following manner. We start with a summary of the TFIM in Sec. 1.1. Then we review the lattice boson model in Sec. 1.2. The lattice boson model has a ground state phase diagram with the phase transitions belong to the chiral clock model universality class. Then we introduce the model that is the central theme in this thesis *i.e* Chiral clock model in Sec. 1.3. Problems studied in this thesis are summarised in Sec. 1.4

1.1 Transverse field Ising model

The transverse field Ising model [40], also called as quantum Ising model, has the Hamiltonian

$$H = -J\sum_i \sigma_i^z \sigma_{i+1}^z - f\sum_i \sigma_i^x \tag{1.1}$$

Here σ^x and σ^z are Pauli spin-half operators. The model has an Ising interaction between the z-components of adjacent spins, and a transverse field in the x-direction whose strength is quantified by f. The model has global $\mathbb{Z}_2$ symmetry associated with the parity $\mathcal{P} = \prod_i \sigma_i^x$ which rotates all the spins by π around the x-axis. The ground-state phase diagram has two phases - ferromagnetic $(J > f)$ and paramagnetic $(J < f)$. A local order parameter $\langle \sigma_i^z \rangle$ distinguishes the two phases. The ferromagnetic phase has a dominant ZZ coupling term resulting in nonzero $\langle \sigma_i^z \rangle$ while the local order parameter is zero in the paramagnetic phase. Ferromagnetic and paramagnetic phases are also called symmetry broken, and symmetric phases as the symmetry $\mathcal{P}$ is broken and preserved in these phases, respectively. There is a second-order quantum phase transition at point $f = J$ belonging to the Ising universality class with central charge $c = 1/2$.

This model is solvable using the Jordan-Wigner transformation,

$$\sigma_i^x = 1 - 2c_i^\dagger c_i, \quad \sigma_i^z = \prod_{j<i}(1 - 2c_j^\dagger c_j)(c_i + c_i^\dagger) \tag{1.2}$$

which non-locally maps the spin degrees of freedom to fermionic degrees of freedom followed by a Bogoliubov transformation. Fermionic operators c's satisfy the following anticommutation relations.

$$\{c_i, c_j^\dagger\} = \delta_{i,j}, \quad \{c_i, c_j\} = \{c_i^\dagger, c_j^\dagger\} = 0 \tag{1.3}$$

In the fermionic language, Eq. 1.1 has the following form

$$H = -J\sum_i (c_i^\dagger c_{i+1} + c_i^\dagger c_{i+1}^\dagger + \text{H.c}) + 2f\sum_i c_i^\dagger c_i \tag{1.4}$$

The commutation relation of the operators c and $c^\dagger$ with the Hamiltonian gives

$$\begin{aligned} [H, c_i] &= J(c_{i-1}^\dagger + c_{i-1} + c_{i+1}^\dagger + c_{i+1}) - 2fc_i \\ [H, c_i^\dagger] &= J(c_{i-1}^\dagger + c_{i-1} + c_{i+1}^\dagger + c_{i+1}) + 2fc_i^\dagger \end{aligned} \tag{1.5}$$

The commutation action of H are linear in the fermionic operators $\{c, c^\dagger\}$. This makes the system solvable in terms of fermionic ladder operators obtained by diagonalizing this linear action.

1.2 Lattice boson model

Superfluid-Mott transition of Bose-Hubbard model was experimentally realized in an ultracold atom setup in [41]. This landmark experiment lead to the study of Hamiltonians which can be realized in such controlled artificial environments. With the motivation of designing a Hamiltonian with multiple competing ground states which can be studied experimentally, Fendley *et al.* proposed the lattice boson model in Ref. [1]. One dimensional lattice boson model is a kinetically constrained model

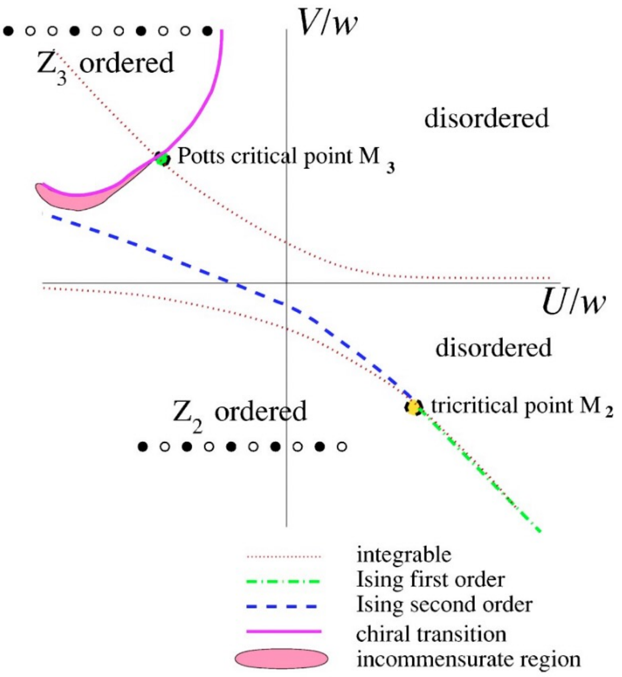
V/w
U/w
Z3 ordered
disordered
Potts critical point M 3
disordered
Z2 ordered
tricritical point M 2
integrable
Ising first order
Ising second order
chiral transition
incommensurate region

Fig. 1.1 Phase diagram of the lattice boson model proposed by Fendley *et. al.* Figure reproduced with permission from Ref. [1]

for hardcore bosons. This model has constraint that simultaneous occupation of two consecutive sites is prohibited

$$\langle n_j n_{j+1} \rangle = 0 \tag{1.6}$$

Here $n_j = b_j^\dagger b_j$ is the bosonic occupation number operator for bosons created and annihilated by $b_j^\dagger$ and b_j. The above constraint is also known as a one-site blockade. Hamiltonian of the lattice boson model is given by

$$H = \sum_j -w(b_j + b_k^\dagger) + U n_j + V n_j n_{j+2} \tag{1.7}$$

This model has an interesting ground state phase diagram. The system has four phases, namely $\mathbb{Z}_2$ ordered, $\mathbb{Z}_3$ ordered, disordered and incommensurate phase as shown in Fig. 1.1. We have a disordered phase for large U/w which is translationally invariant and has a finite density of bosons. For negative U/w with large and negative V/w, each second site is filled with a boson in the ground state, giving a $\mathbb{Z}_2$ ordered state. For negative U/w with large and positive V/w, we have a $\mathbb{Z}_3$ ordered state with each third site occupied. Ground-state properties of an equivalent 2D classical model, which is of interacting hard squares on a square lattice, is studied in [42]. Equation 1.7 can be obtained by taking the limit of the transfer matrix of this model. The hard square model is integrable along the line

$$w^2 = UV + V^2 \tag{1.8}$$

Along this integrable line, there are single points where the phase transition belongs to Ising tricritical and three-state Potts universality class. A particular case of the Hamiltonian (Eq. 1.7) also describes the ground state physics of the Bose-Hubbard model with tilted external potential [43]. PXP model [44] which is a very well-known model in the context of quantum scars, is also a particular case of Eq. 1.7.

The Hamiltonian shown in Eq. 1.7 was realized [2] in a cold atom system of neutral Rydberg atoms. Each atom in the chain of atoms can be in two possible states represented by $|g\rangle$ and $|r\rangle$. Here $|g\rangle$ is the ground state and $|r\rangle$ is the excited state. The Hamiltonian describing the dynamics of the trapped cold atom system is

$$\mathcal{H} = \sum_i \frac{\Omega_i}{2}\sigma_i^x - \sum_i \Delta_i n_i + \sum_{i<j} V_{ij} n_i n_j \tag{1.9}$$

The parameters Δ and Ω are detuning parameters and Rabi frequency decided by the driving laser pulse. Here $n_i = |r_i\rangle\langle r_i|$ is the occupation in the excited state and $\sigma_i^x = |g_i\rangle\langle r_i| + |r_i\rangle\langle g_i|$. Two atoms at sites i and j separated by R_{ij} repel each other with Van der Waals interaction $V_{ij} = C/R_{ij}^6$ if both atoms are in their excited states. Here $C > 0$ is the Van der Waals coeffecient. The Rydberg blockade implements kinetic constraints of the Hamiltonian Eq. 1.7 in this experimental setup. In this cold atom setup, varying the separation between atoms tunes the range of the Rydberg blockade. The range of blockade is called blockade radius denoted by R_b. The phase diagram of the Hamiltonian Eq. 1.9 is shown in Fig. 1.2 as a function of parameters Δ/Ω and interaction range characterized by ratio of blockade radius R_b and trap spacing a. Realization of $\mathbb{Z}_3$ ordered phase in the chain of 51-atoms motivated theoretical and numerical works to study the properties of transitions in $\mathbb{Z}_3$ chiral clock model. From earlier studies, the exact phase boundaries critical exponents were not known exactly, and these were addressed in the [45, 46, 3] numerically.

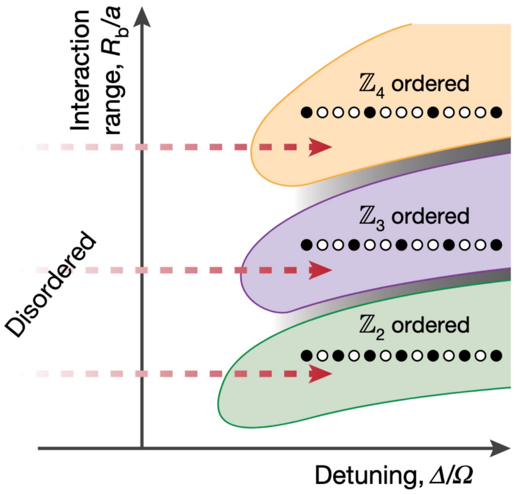

Fig. 1.2 Phase diagram of the Hamiltonian Eq. 1.9 as a function of Hamiltonian paramters Δ/Ω and blockade radius defined in units of trap spacing a by R_b/a. Figure reproduced with permission from Ref. [2]

.

1.3 $\mathbb{Z}_3$ Chiral Clock Model

The $\mathbb{Z}_3$ analog of the TFIM for the chain of N spins with open boundary condition has Hamiltonian

$$H = -Je^{\iota\theta}\sum_{i=1}^{N-1}\sigma_i\sigma_{i+1}^{\dagger} - fe^{\iota\phi}\sum_{i=1}^{N}\tau_i + \text{H.c.} \tag{1.10}$$

The chain has 3 dimensional Hilbert space at each site. Operators σ and τ are the generalizations of the Pauli matrices σ^z and σ^x in the three dimensional Hilbert space with a representation

$$\sigma = \begin{pmatrix} 1 & 0 & 0 \\ 0 & \omega & 0 \\ 0 & 0 & \bar{\omega} \end{pmatrix} \quad \tau = \begin{pmatrix} 0 & 1 & 0 \\ 0 & 0 & 1 \\ 1 & 0 & 0 \end{pmatrix} \tag{1.11}$$

where $\omega = e^{\iota 2\pi/3}$. Operator σ measures the spin, and τ rotates the spin in a clockwise direction in the argand plane. τ_i introduces the local quantum fluctuation in the system, and the relative value of parameters J and f decide the strength of the fluctuation ($J, f \geq 0$ without loss of generality). Note that the name “spin” is used in a general sense and the three dimensional Hilbert space has no direct relation to a spin-1 representation of SU(2).

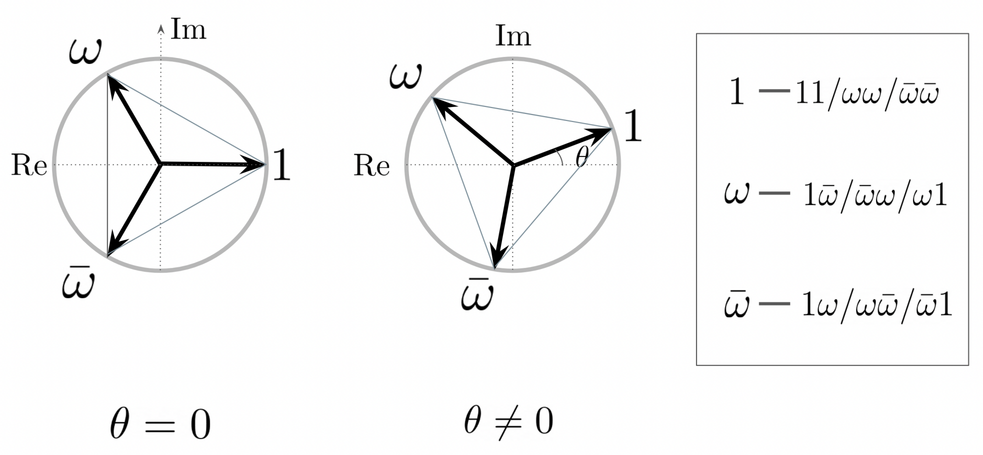
Im
ω
Re
1
$\bar{\omega}$
$\theta = 0$
Im
ω
Re
1
θ
$\bar{\omega}$
$\theta \neq 0$
$1 - 11/\omega\omega/\bar{\omega}\bar{\omega}$
$\omega - 1\bar{\omega}/\bar{\omega}\omega/\omega 1$
$\bar{\omega} - 1\omega/\omega\bar{\omega}/\bar{\omega}1$

Fig. 1.3 Schematic representation of the effect of θ on eigenstates of the two spin interaction: Eigenvalues of $e^{\iota\theta}\sigma_i\sigma_{i+1}^\dagger$ are plotted as vectors in the argand plane. These are labelled by the values of $\sigma_i\sigma_{i+1}^\dagger$ for the same states. In the boxed panel, states of the spin on site i and $i+1$ that can result in these eigenvalues $1, \omega$ and $\bar{\omega}$ for $\sigma_i\sigma_{i+1}$ are shown.

The operator algebra is

$$\begin{aligned} &\sigma^3 = \tau^3 = 1, \quad \sigma^\dagger = \sigma^2 \\ &\tau^\dagger = \tau^2, \quad \sigma\tau = \bar{\omega}\tau\sigma \end{aligned} \tag{1.12}$$

1.3.1 Classical Ground states at $f = 0$

Setting $f = 0$ in Eq. 1.10 removes all the quantum fluctuation resulting in the eigenstates which are direct products of the eigenstates of the local operator σ_i. In this section, we will discuss the role of the parameter θ in the nature of the ground states in the $f = 0$ limit. Content of this subsection closely follows the discussion of the classical states of chiral clock model in Ref. [47]. We have the following Hamiltonian

$$H_{\text{classical}} = -\sum_i (Je^{\iota\theta}\sigma_i\sigma_{i+1}^\dagger + Je^{-\iota\theta}\sigma_i^\dagger\sigma_{i+1}) \tag{1.13}$$

To understand the role of parameter θ on the ground state we will focus on the individual term $e^{\iota\theta}\sigma_i\sigma_{i+1}^\dagger$ for the site i and $i+1$ of $H_{\text{classical}}$. Possible eigenvalues of $\sigma_i\sigma_{i+1}^\dagger$ are 1, ω and $\bar{\omega}$. These are rotated anti-clockwise by an angle θ when considering the eigenvalaues of $e^{\iota\theta}\sigma_i\sigma_{i+1}^\dagger$ (visualized as vectors in Fig. 1.3). For each possible value of $\sigma_i\sigma_{i+1}^\dagger$, there are three possible spin configurations at site i and $i+1$ which is shown in Fig. 1.3. Energy eigenvalues of these states are $-2J$ times the real part of the vectors. Ground states are the configurations with the largest real part. For $\theta = 0$, the rightmost vertex labeled by 1 in Fig. 1.3 minimizes the energy. A nonzero θ results in broken spatial parity as the configurations $|1\omega\rangle$ and $|\omega 1\rangle$ have different energies.

$\sigma_i \sigma_{i+1}^\dagger = 1$ has minimum energy for $-\pi/3 < \theta < \pi/3$. For $\pi/3 < \theta < \pi$, vertices with $\sigma_i \sigma_{i+1}^\dagger = \bar{\omega}$ are the configurations with minimum energy. Similarly for $-\pi < \theta < -\pi/3$, states with $\sigma_i \sigma_{i+1}^\dagger = \omega$ have the minimum energy. $\theta = \pi/3$ corresponds to an antiferromagnetic ground state as we have two values of $\sigma_i \sigma_{i+1}^\dagger$ that minimize the energy. $\theta = \pm\pi/6$ and $\pm\pi/2$ correspond to symmetric cases in which for every state with energy E we have a state with energy $-E$.

1.3.2 Symmetries of Chiral Clock Model

Understanding the symmetries present in the system simplifies the analytical and numerical treatment of the problem. A transformation $\mathcal{U}$ is a symmetry of a system if it leaves the Hamiltonian invariant under its action. According to Wigner's theorem the transformation $\mathcal{U}$ can be both unitary or anti-unitary. Chiral clock Hamiltonian Eq. 1.10 has following symmetries namely $\mathbb{Z}_3$ parity $\mathcal{P}$, charge conjugation $\mathcal{C}$, time-reversal $\mathcal{T}$ and spatial inversion $\mathcal{S}$. Among these symmteries, time reversal is anti-unitary while the remaing are unitary operations. The parity $\mathcal{P}$ is a symmetry in all parameter regimes; presence of the remaining symmetries depend on the values of θ and ϕ.

$\mathbb{Z}_3$ parity symmetry is implemented by

$$\mathcal{P} = \prod_i \tau_i \tag{1.14}$$

It is similar to the $\mathbb{Z}_2$ parity symmetry in TFIM with σ^x replaced by the τ operator. It has three possible eigenvalues $1, \omega$ and $\bar{\omega}$. $\mathcal{P}$ rotates all spins by $2\pi/3$ in the clockwise direction. Under the parity $\mathcal{P}$ operators σ_i and τ_i transform as

$$\mathcal{P}\sigma_i\mathcal{P}^\dagger = \omega\sigma_i, \;\; \mathcal{P}\tau_i\mathcal{P}^\dagger = \tau_i \tag{1.15}$$

Charge conjugation $\mathcal{C}$ swaps the states $|\omega\rangle$ and $|\bar{\omega}\rangle$ on all sites. $\mathcal{C}$ can be written as product of local operations $\mathcal{C}_i$ *i.e* $\mathcal{C} = \Pi_i \mathcal{C}_i$ and matrix representation of $\mathcal{C}_i$ is

$$\mathcal{C}_i = \begin{pmatrix} 1 & 0 & 0 \\ 0 & 0 & 1 \\ 0 & 1 & 0 \end{pmatrix} \tag{1.16}$$

Under the charge conjugation operation, operators transform as

$$\mathcal{C}\sigma_i\mathcal{C}^\dagger = \sigma_i^\dagger, \;\; \mathcal{C}\tau_i\mathcal{C}^\dagger = \tau_i^\dagger \tag{1.17}$$

and satisfies the relation $\mathcal{C}^2 = 1$. Under the time reversal symmetry $\mathcal{T}$, operators σ and τ operators transform as

$$\mathcal{T}\sigma\mathcal{T}^\dagger = \sigma^\dagger, \;\; \mathcal{T}\tau\mathcal{T}^\dagger = \tau \tag{1.18}$$

Spatial inversion interchanges the states at sites i and $N-i+1$. All three symmetries are present at $\theta = \phi = 0$ while the model has only spatial inversion symmetry when $\theta = 0$ and $\phi \neq 0$. None of the three symmetries $\mathcal{T}$, $\mathcal{C}$ and $\mathcal{S}$ are present when both θ and ϕ are non-zero. For $\phi = 0$ and $\theta \neq 0$, the individual symmetries $\mathcal{C}$ and $\mathcal{S}$ are broken but their product is preserved. Hamiltonian is also time-reversal symmetric for $\theta \neq 0$ and $\phi = 0$.

At $\theta = \phi = 0$, the Hamiltonian Eq. 1.10 is invariant under uniform permutation S_3 of the states on each site. This S_3 symmteric Hamiltonian is equivalent to three-state quantum Potts model [48].

1.3.3 Phase Diagram

Similar to the $\mathbb{Z}_2$ case, $\mathbb{Z}_3$ chiral clock model also has two gapped phases called trivial and ordered phases. The trivial phase corresponds to $J \ll f$. The ground states are non-degenerate and are $\mathbb{Z}_3$ parity eigenstates *i.e* $\mathcal{P}|\mathrm{GS}\rangle = |\mathrm{GS}\rangle$. Since the ground states are parity eigenstates, the trivial state is also called the symmetric phase. The other extreme case of the Hamiltonian parameter $f/J \ll 1$ is an ordered phase with the triply degenerate ground states (with three different parity eigenvalues). The ground state in this phase does not preserve the $\mathbb{Z}_3$ parity symmetry and hence is a symmetry broken phase. Note that the three fold degeneracy is not always present at finite energy eigenstates. The ordered phase has been shown to be a related to a topological phase of a parafermion chain [49] based on quantum numers of the reduced density matrices. Parafermions are the higher dimensional generalization of the Majorana fermions, and this is briefly discussed separately in a separate subsection 1.3.4.

Other than the two phases mentioned above, chiral clock model also has a critical incommensurate phase separating the topological and trivial phases. This incommensurate phase is not present in the TFIM, or the TFIM with the chiral interactions [50].

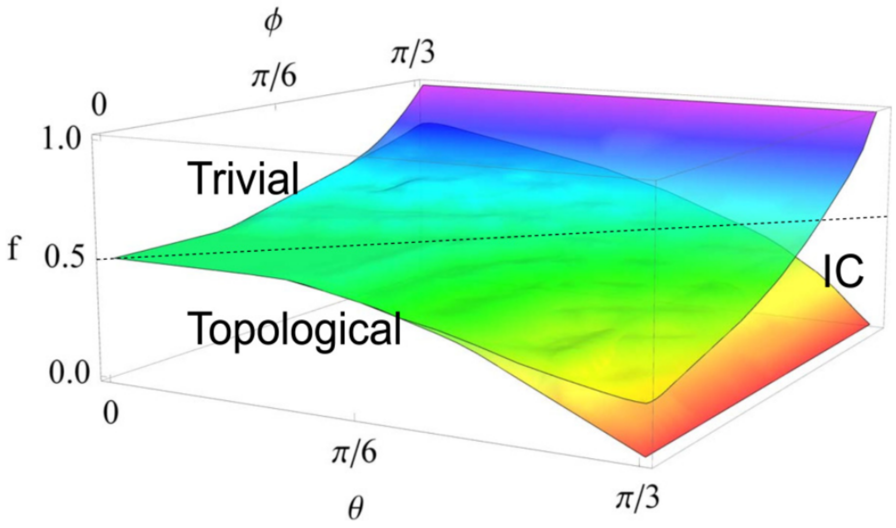

Fig. 1.4 Phase diagram of the chiral clock model using $J = 1 - f$ in Eq. 1.10 showing phase boundary between trivial, topological and incommensurate phase as function of parameters f, θ and ϕ. Figure reproduced with permission from Ref. [3].

In the phase diagram of the $\mathbb{Z}_3$ chiral clock model, puzzle of whether the transition between the topological and trivial phase is direct or not has been resolved recently. Using the entanglement entropy as diagnostic, Zhuang *et.al* [3] mapped out the whole phase diagram of $\mathbb{Z}_3$ chiral clock model as a function of parameters $J = 1 - f$, θ and ϕ; the summary of this is shown in Fig. 1.4. The transition between the topological and trivial phase can be direct or indirect depending the the parameters θ, ϕ and f.

We have three different phase transitions in the whole phase diagram, and all belong to different universality classes. Quantum phase transition between the gapped topological and trivial phase belongs to the $\mathbb{Z}_3$ universality class. At the same time, the disorder-incommensurate and the ordered-incommensurate transition are of Kosterlitz-Thouless and Pokrovski-Talapov type [51], respectively. The nature of phase transition is discussed in detail in Ref. [46]. The phase diagram also has a tricritical Lifshitz point expected to be at $f = J$ and $\theta = \phi = \pi/6$.

For $\theta = \phi = 0$, chiral clock model exhibits a continuous quantum phase transition at $f = J$ with the dynamical critical exponent $z = 1$. This transition is in the same universality class as the classical three-state Potts model. For the nonzero θ and ϕ, the direct transition between the ordered-disordered phase has $z \neq 1$. The aforementioned is the only known transition between gapped phases known for the strongly coupled system with $z \neq 1$ [46, 52].

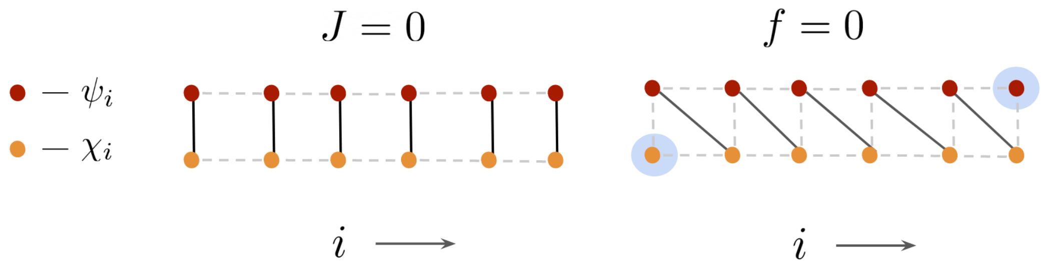

Fig. 1.5 Trivial ($J = 0$) and topological phase ($f = 0$) in the parafermionic representation of chiral clock model Hamiltonian. Here the solid black lines represent the coupled parafermionic terms of the Hamiltonian. Parafermionic edge modes χ_1 and ψ_L are encircled for $f = 0$ case.

1.3.4 Parafermions and Edge zero modes

Analogous to the Jordan-Wigner transformation[53] from spin-half system to a system of fermions, the three state model can be mapped to a system with parafermion degrees of freedom. We have two parafermionic operators χ_i and ψ_i for each site i defined as

$$\chi_j = \Big(\prod_{i=1}^{j-1} \tau_i\Big)\sigma_j, \quad \psi_j = \omega\Big(\prod_{i=1}^{j-1} \tau_i\Big)\sigma_j\tau_j \tag{1.19}$$

Parafermionic operators for a particular site j satisfy the algebra

$$\begin{gathered} \psi_j^\dagger = \psi_j^2, \quad \chi_j^\dagger = \chi_j^2 \\ \chi_j^3 = \psi_j^3 = 1, \quad \chi_j\psi_j = \omega\psi_j\chi_j \end{gathered} \tag{1.20}$$

and the following relations are satisfied by operators acting on two different sites i and j where $i < j$

$$\begin{aligned} \chi_i\chi_j &= \omega\chi_j\chi_i \\ \psi_i\psi_j &= \omega\psi_j\psi_i \\ \chi_i\psi_j &= \omega\psi_j\chi_i \end{aligned} \tag{1.21}$$

Note that parafermions acting on different sites neither commute nor anti-commute. The chiral clock model Hamiltonian in the parafermionic language is

$$H = -Je^{\iota\theta}\sum_i \bar{\omega}\psi_i\chi_{i+1}^\dagger - fe^{\iota\phi}\sum_i \bar{\omega}\chi_i^\dagger\psi_i + \text{H.c} \tag{1.22}$$

Let us look at the extreme limits of the Hamiltonian for parameters J and f in the parafermionic representation. For J=0, Hamiltonian Eq. 1.22 becomes

$$H_{J=0} = fe^{\iota\phi}\sum_i \bar{\omega}\chi_i^\dagger\psi_i + \text{H.c} \tag{1.23}$$

Here, parafermionic operators associated with different sites get decoupled, schematically shown in Fig. 1.5. In the other extreme limit where we have $f = 0$, the Hamiltonian has form

$$H_{f=0} = -Je^{\iota\theta}\sum_{i=1}^{L-1} \bar{\omega}\psi_i\chi_{i+1}^\dagger + \text{H.c} \tag{1.24}$$

For open boundary conditions, modes χ_1 and ψ_L are absent from the Hamiltonian Eq. 1.24 which means χ_1 and ψ_L commute with the Hamiltonian. This is schematically shown in Fig. 1.5. Modes χ_1 and ψ_L are special and are parafermionic edge zero-modes. These modes do not commute with $\mathcal{P}$. The combined algebra of χ_1, ψ_L, $\mathcal{P}$ and H implies that each eigenvalue should be three-fold degenerate with each state having different parity. This also means that the spectrum of H must be identical in all the $\mathbb{Z}_3$ parity sectors. Because of the degeneracies across the whole spectrum, such edge zero modes are referred to as "Strong edge zero modes". TFIM in the Majorana language is a system hosting strong edge zero modes. χ_1 and ψ_L are strong edge zero modes in the limit $f = 0$ for chiral clock model.

For the topological phase in 1D, we only require degeneracy in the ground state, so it is useful to introduce the idea of "weak edge zero-mode" to deal with the topological phase. A weak zero mode differs from strong modes in the sense that degeneracy is present only in the low energy subspace but at higher energies there is no degeneracy.

Interestingly topological phase in chiral clock model has strong and weak edge zero modes in distinct parameter regimes [54]. For nonzero f, it is shown in [47] chirality is needed for existence of strong zero modes and the nonchiral Hamiltonian ($\theta = 0$) only has weak zero modes. Presence and absence of the strong edge modes can be understood using iterative construction of zero-mode [47] and from analyzing the domain wall dynamics [4]. Discussion of the domain wall dynamics for the zero modes is in the subsection 1.3.5.

We summarise the iterative construction of the edge zero-mode here. For $f \neq 0$, edge modes χ_1 and ψ_L get modified to form $\chi_1 + \ldots$ and $\psi_L + \ldots$, iterative construction intends to find those additional term $(\ldots)$. To get the additional term, we start with splitting the Hamiltonian Eq. 1.22 in the form $H = JV + fF$. We will focus on χ_1, but the same line of arguments is followed for ψ_L. Parafermions χ_1 commutes with

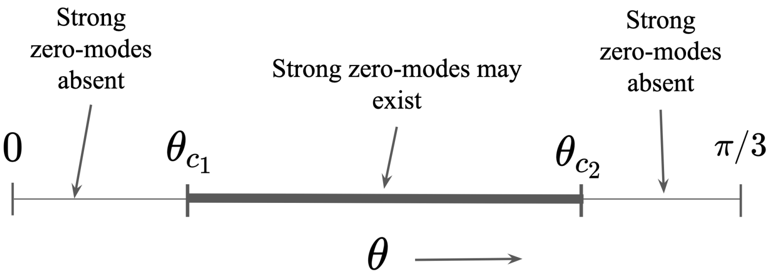

Fig. 1.6 Figure summarises the features of zero modes on basis of splitting in first excited state for $\theta \in (0, \pi/3)$

the V but not with the F part of Hamiltonian. So we have $[H, \chi_1] = f[F, \chi_1]$ which is nonzero. Next we find X such that $[F, \chi_1] = [V, X]$ giving us the first term in the correction to χ_1 which is $\chi_1 - (f/J)X$. Now we have $[H, \chi_1 - (f/J)X]$ which is of order $(f/J)^2$. This repeated process gives edge zero-mode Ψ as a power series in terms of dimensionless parameter $f/J \sin 3\theta$ having the form

$$\Psi = \chi_1 - \frac{f}{J \sin 3\theta} X + \left(\frac{f}{J \sin 3\theta} \right)^2 Y + \dots \tag{1.25}$$

The radius of convergence of the expansion is dependent on θ. For $\sin 3\theta = 0$ the Eq. 1.25 blows up which proves that strong modes do not exist for the $\theta = 0$ and $\pi/3$.

The parafermionic description presented here is not essential for understanding the results of our work. However, we note that some of the results in Chapter 4 can also be understood in terms of strong zero-edge modes appearing in the parafermionic dual to the chiral clock model.

1.3.5 Domain wall picture

Using the iterative construction of edge modes, we saw that strong modes do not exist for $\theta = 0$ and $\theta = \pi/3$ for nonzero f. For the $\theta \neq 0$ edge modes features are complex, and careful analysis of domain wall dynamics shows that there exist critical values θ_{c1} and θ_{c2}, below and above this values, edge modes of the chiral clock model are weak. This statement is summarized in diagrammatic form in Fig. 1.6. The domain wall analysis presented here follows the discussion in [4]

In the chiral clock model we will treat the spin spin coupling term $-Je^{\iota\theta}\sigma_i\sigma_{i+1}^\dagger + h.c$ as our unperturbed Hamiltonian and $f\tau + h.c$ is treated as the perturbing term. We will restrict in the range $\theta \in [0, \pi/3]$. Ground state of unperturbed Hamiltonian is triply degenerate in the symmetry broken phase which are as follows - $|A\rangle = |111\dots11\rangle$,

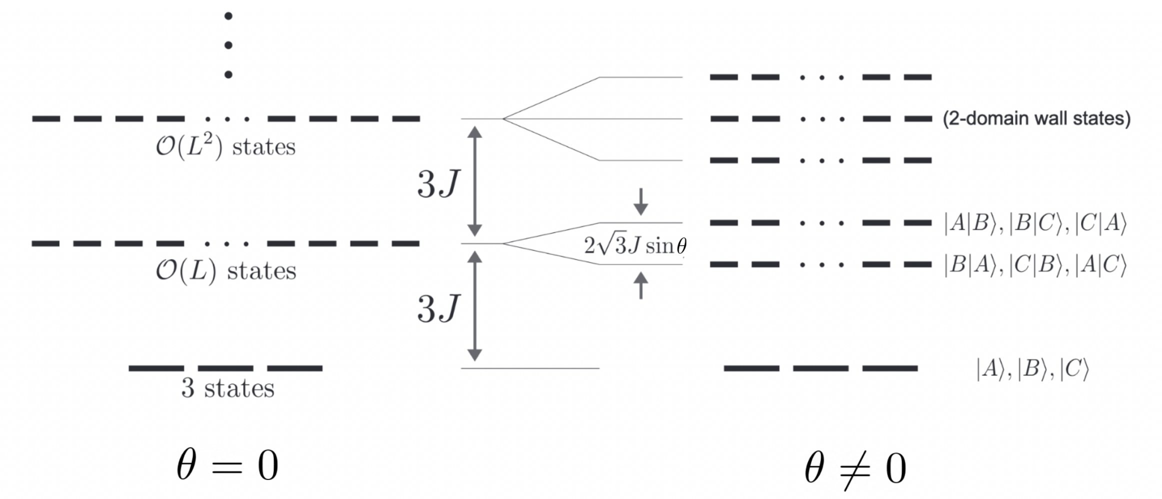
$\mathcal{O}(L^2)$ states
$3J$
$\mathcal{O}(L)$ states
$3J$
3 states
$2\sqrt{3}J\sin\theta$
(2-domain wall states)
$|A|B\rangle, |B|C\rangle, |C|A\rangle$
$|B|A\rangle, |C|B\rangle, |A|C\rangle$
$|A\rangle, |B\rangle, |C\rangle$
$\theta = 0$
$\theta \neq 0$

Fig. 1.7 Spectrum features of the Hamiltonian Eq. 1.10 for $f = 0$. Ground states are triply degenerate for both $\theta = 0$ and $\neq 0$. First excited state for non-chiral Hamiltonian is with single domain wall with both positive and negative chirality states having same energy *i.e.* $E^{+}_{1-\text{domain}} = E^{-}_{1-\text{domain}}$. For the chiral case, degeneracy of positive and negative chirality one domain wall states is broken. Figure reproduced with permission from Ref. [4].

$|B\rangle = |\omega\omega\omega\ldots\omega\omega\rangle$ and $|C\rangle = |\bar{\omega}\bar{\omega}\bar{\omega}\ldots\bar{\omega}\rangle$. We have six flavors for the excited state with single domain walls which are $|A|B\rangle$, $|B|A\rangle$, $|B|C\rangle$, $|C|B\rangle$, $|C|A\rangle$ and $|A|C\rangle$. In this domain wall state notation for example for state $|A|B\rangle$, on the left of domain wall we have $|A\rangle$ and on its right we have $|B\rangle$. We divide the single domain wall states into two separate classes on the basis of their chirality. The positive chirality class are $|A|B\rangle$, $|B|C\rangle$ and $|C|A\rangle$ whereas the negative chirality states are $|B|A\rangle$, $|A|C\rangle$ and $|C|B\rangle$. We represent their energies by $E^{+}_{1-\text{domain}}$ and $E^{-}_{1-\text{domain}}$

$$E^{\pm}_{1-\text{domain}} = 2J[\cos\theta - \cos(2\pi/3 \pm \theta)] \tag{1.26}$$

For a spin chain with an open boundary condition of length L, each flavor has $L-1$ possible positions. For the $\theta = 0$ case, all six flavors have equal energy and are separated by a gap of $3J$ from the ground state. For the $\theta \neq 0$ degeneracy among the states with flavors of opposite chirality *e.g* $|A|B\rangle$ and $|B|A\rangle$ is lifted and is separated by energy gap of $2\sqrt{3}J\sin\theta$. The spectrum features are shown in Fig. 1.7

Perturbing field f causes mixing of unperturbed eigenstates by domain wall creation, annihilation, and hopping processes as the local τ_i operators cause rotation of spin at site i. We will study the splitting of energy levels in ground and excited states separately after turning on the field f. For this energy splitting calculation using the perturbative analysis, we will focus on the processes arising because of field f through which an unperturbed state can convert into another unperturbed eigenstate with the same energy. We are interested in these conversion processes because they are responsible for the degenerate perturbation theory's finite-size energy splitting for degenerate energy levels.

Splitting of ground state energy

Let us look at the ground state first. For the nonchiral case, we want the processes we can go from, let us say, $|A\rangle$ to $|B\rangle$. This conversion is not possible without leaving the ground state subspace. The simplest possible mechanism is to create a domain wall of flavor $|A|B\rangle$ at the right end of the chain by flipping the boundary spin at the right end of the chain and then traversing the domain wall from right to left end. At the left end, the domain wall will be annihilated, giving the state $|B\rangle$. The mentioned process is shown in panel a of Fig. 1.8 involving the creation, hopping, and annihilation of domain walls, all achievable by local field f in multiple steps. In the perturbation theory connecting two degenerate states involves a macroscopic number of perturbation steps, as we have seen, giving the energy splitting of

$$\Delta E_{\text{GS}} \sim f\left(\frac{f}{3J}\right)^{(L-1)} \tag{1.27}$$

Energy splitting also has the same exponential form as Eq. 1.27 for the chiral case. with the modified denominator. The denominator in the Eq. 1.27 get modified to Δ, where Δ is the energy difference between the ground state and first excited state. This exponential splitting shows that ground state degeneracy is forwarded to the nonzero f for chiral and nonchiral Hamiltonian.

Splitting of excited state energy

Above mechanism becomes interesting in the case of single domain wall states or first excited states for $f = 0$. Unlike the ground state we can go from a 1-domain wall state to another 1-domain wall state without leaving the degenerate space. For converting a state of flavor $|A|B\rangle$ to $|B|C\rangle$, starting with flavor $|A|B\rangle$ domain wall can be moved to the right end where boundary scatters domain wall $|A|B\rangle$ to flavor $|A|C\rangle$. Then the new domain wall of flavor $|A|C\rangle$ has to be moved to the right end where after reaching the boundary, flavor $|A|C\rangle$ will be converted to $|B|C\rangle$. This mechanism is shown in panel b of Fig. 1.8.

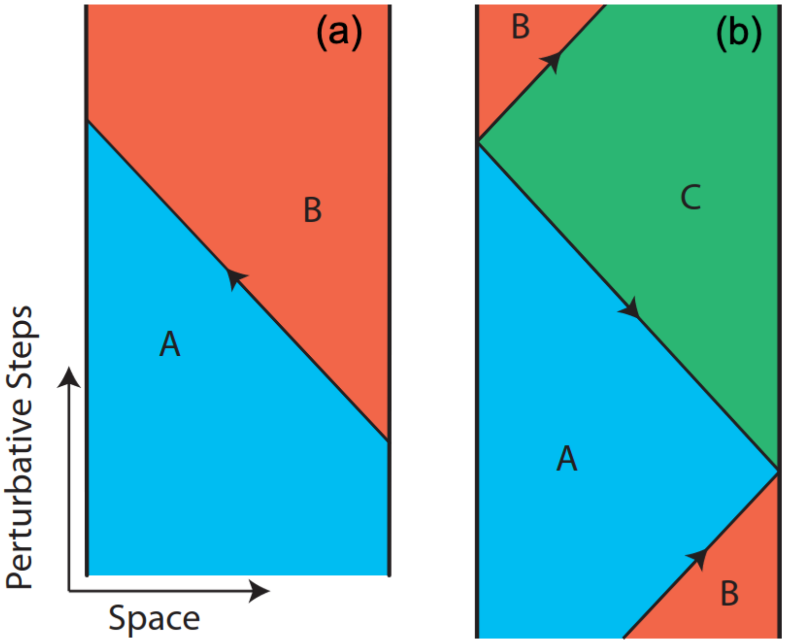

Fig. 1.8 Figure shows the simplest possible mechanism of inter-conversion of degenerate states at the level of the ground and excited state in panels a and b, respectively. Y-axis is the perturbation step, and the x-axis is the position in the chain. A solid line drawn is the domain wall location in the chain, which is changing with time because of the hopping process. Figure reproduced with permission from Ref. [4].

To understand the splitting in the excited state, we project the Hamiltonian Eq. 1.10 in the single domain wall subspace denoted by $H_{1-\text{domain}}$. This projected Hamiltonian is equivalent to six-coupled tight binding chains [4] for six flavors of particles, each length $L-1$ with periodic boundary conditions. Chirality of the domain wall flavor decides the onsite energy of each tight-binding chain which results in two excitation branches whose band energies are given by

$$E_{\pm}(k,\theta) = E^{\pm}_{\text{wall}}(\theta) - 2f\cos k \tag{1.28}$$

Each energy band is threefold degenerate belonging to the single domain wall states of the same chirality. Single domain wall band energies are shown in Fig. 1.9. Comparative values of bandwidth $4f$ and the band separation energy which is $E^{+}_{1-\text{domain}} - E^{-}_{1-\text{domain}} = 2\sqrt{3}J\sin\theta$ gives rise to two different scenario shown in Fig. 1.9 (a) and (b). Domain walls behave as a particle in this effective Hamiltonian description. For our convenience we define the parameter $\lambda = \sqrt{3}J\sin\theta/2f$.

For $\lambda > 1$, the energy bands for positive and negative chirality particles are well separated as shown in Fig. 1.9(b). In particular there is energy gap between opposite chirality states *e.g.* $|A|B\rangle$ to $|A|C\rangle$. Particles in the bottom band can not transition to the upper band, and the particle remains here for a macroscopic number of steps leading to the exponential splitting of the energy in the perturbative analysis of the excited state with system size L.

Exponential splitting changes to power law at critical value $\lambda \approx 1$. The energy bands of opposite chirality starts to overlap for $\lambda \leq 1$ as shown in Fig. 1.9(a) resulting to continuous change of particle flavor as it moves around the closed chain. This continuous change of flavor of particle results in power law splitting of excited states for non-zero f which implies the weak zero modes for $\lambda \leq 1$ or $\theta \leq \theta_{c_1} = \sin^{-1}(2f/\sqrt{3}J)$.

When θ is closer to $\pi/3$, energy of positive chirality domain wall states becomes larger than two domain wall states $|C|B|A\rangle$, $|A|C|B\rangle$ and $|B|A|C\rangle$ for $f = 0$. Here the splitting changes its behavior from power law to an exponential with L at the θ_{c_2} given by

$$\theta_{c_2} = \pi/3 - \sin^{-1}\Big(\frac{2f}{\sqrt{3}J}\Big) \tag{1.29}$$

This analysis does not ensure that edge modes are strong for $\theta_{c1} < \theta < \theta_{c2}$ as the higher excited states can have the power-law splitting for the finite f.

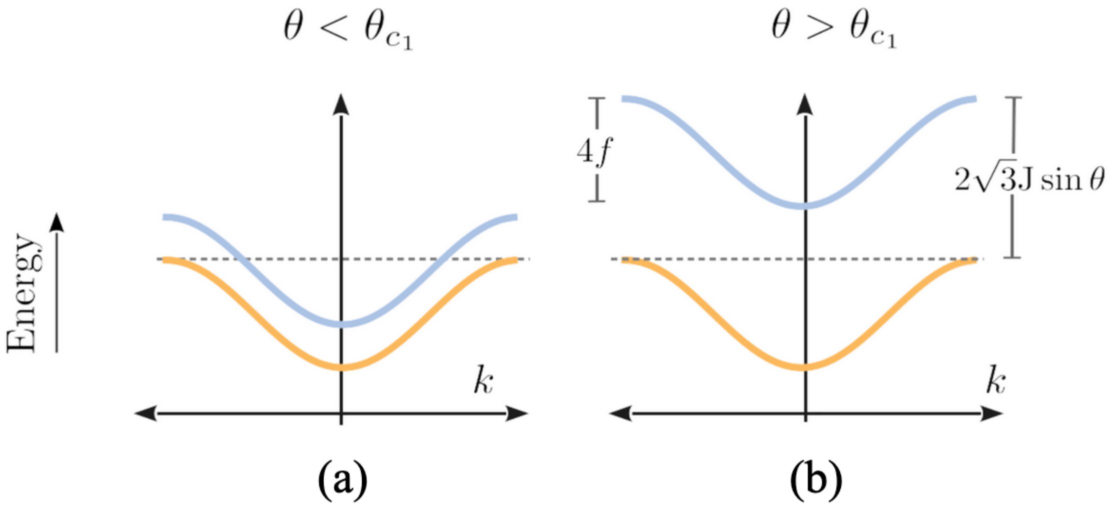

Fig. 1.9 Single domain wall band energies for positive and negative chirality states is shown in blue and orangle color respectively. Two different scenarios are shown $\theta < \theta_{c1}$ and $\theta > \theta_{c1}$ which explains the exponential and power law splitting of the degenerate excited states.

1.4 Problems addressed

In this chapter we have discussed the broad ideas and features of the chiral clock model specifically its ground state phase diagram, symmetries and its connection to different experimentally realizable Hamiltonians. This thesis addresses the features of nonequilibrium quantum dynamics of the model. In this section, we outline the contents of the remaining chapters.

Since chiral clock model is a strongly interacting model and is difficult to tackle using simple numerical methods, we have extensively used the matrix product state based techniques for studying the dynamics. A basic overview of MPS formalism is presented in Chapter 2.

In Chapter 3 we report our findings on the boundary-driven critical clock model for step, sinusoidal and triangular drive. This study is motivated by a previous study [5] which showed that Loschmidt echo has universal scaling for $\mathbb{Z}_2$ case in the slow driving regime which can be explained using combined arguments from from conformal field theory and the Kibble-Zurek mechanism. We have extended the validity of results to the case of $\mathbb{Z}_3$ clock model. This Chapter is based on our work - *Scaling of Loschmidt echo in a boundary-driven critical* $\mathbb{Z}_3$ Potts model, Naveen Nishad and G. J. Sreejith, Phys. Rev. B 101, 144302 (2020).

Chapter 4 is about the entropy dynamics after the quench in ferromagnetic phase. Here we studied the entropy dynamics for the two kinds of subsystems considered at the boundary and bulk of the chain. The subsystem at boundary has different qualitative features in entropy dynamics for chiral and nonchiral quench. Different entropy dynamics also implies different thermalization features in the boundary and bulk. In particular boundary spins has long coherence time for the chiral quench. This chapter is based on our work - *Post quench entropy growth in a chiral clock model*, Naveen Nishad, M. Santhosh, and G. J. Sreejith, Phys. Rev. B 103, 195141 (2021).

Chapter 5 discusses the open quantum system, precisely using the Lindblad master equation. This chapter outlines the matrix product states implementation of Lindblad master equation to study the dynamics of an open quantum system. Then in chapter 6, we study the energy transport in the chiral clock model using the MPS implementation of the Lindblad master equation. Using the finite-size scaling of steady-state current, we show that energy transport is ballistic at the integrable points and otherwise diffusive for non-integrable points. Content of this chapter is taken from *Energy transport in* $\mathbb{Z}_3$ *chiral clock model*, Naveen Nishad and G. J. Sreejith, New Journal of Physics 24, 013035 (2022).

We digress from the chiral clock model in chapter 7 to time crystalline order, a non-equilibrium phase of matter observed in star-shaped clusters of spin-half particles in our study. We show that a star-shaped cluster where satellite spin interacts with central with Ising-like interaction shows temporal order in magnetization when driven with π-pulses. This temporal order is robust against additional perturbation and inaccuracy in the π-pulse. Content of this chapter is based on *Temporal order in periodically driven spins in star-shaped clusters*, Soham Pal, Naveen Nishad, T. S. Mahesh, and G. J. Sreejith, Phys. Rev. Lett. 120, 180602 (2018). Soham Pal and T. S. Mahesh did the experimental work. Naveen Nishad and G. J. Sreejith did numerics and analytical explanation of this work.

Finally, we conclude this thesis with our summary of work and open questions in Chapter 8.

Chapter 2

Matrix Product States and Operators

2.1 Physical corner of the Hilbert space

For most physicsl quantum many-body system of interest, interactions between the constituents are local which means all constituents interact only with their finite number of neighbors.The locally interacting gapped systems have ground states with short-range correlations, and weak entanglement between their subsystems. The statement has been more rigorously argued in one dimension[55]. Matrix product states (MPS) formalism is an effecient way of representing these locally entangled states. MPS was originally formulated for ground state search however the technique can be extended to time evolution, excited states and density matrices [56]. A brief summary of the ideas of the MPS formalism which is central numerical technique of this thesis is provided in this chapter. This chapter also standardizes the notion, convention and ideas used in rest of the thesis.

A local Hamiltonian H can be written as

$$H = \sum_i h_i \tag{2.1}$$

here each term h_i has finite support on a finite number of sites. The distance between the farthest site over which h_i acts is also finite. The effect of the locality of Hamiltonian is reflected in the behavior of correlation functions for the ground state. For the gapped models, correlation functions decay exponentially with distance with a characteristic length ξ for the ground state. Correlation functions can decay algebraically with distance for the gapless models and have a diverging correlation length.

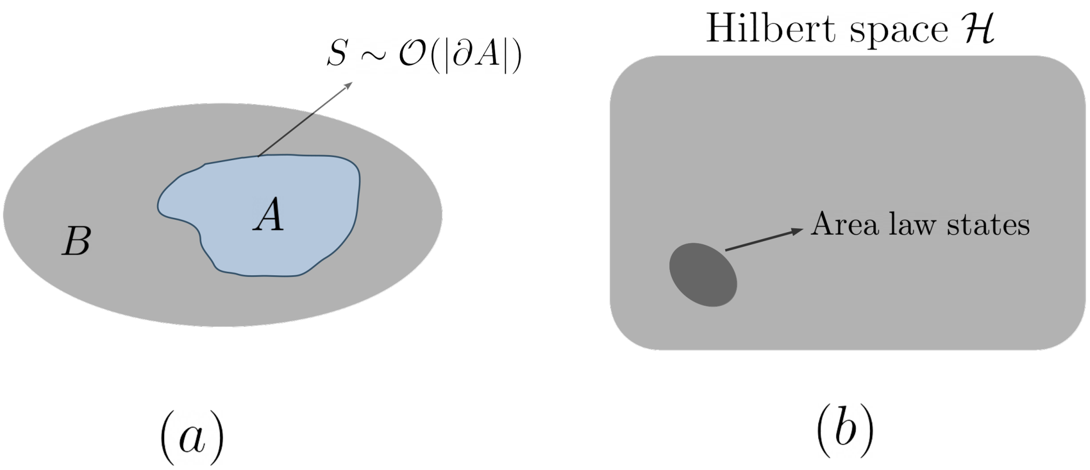
$S \sim \mathcal{O}(|\partial A|)$
A
B
Hilbert space $\mathcal{H}$
Area law states
(a)
(b)

Fig. 2.1 Panel a conveys the idea of area law scaling of entanglement betweent the subsystem A and B. States obeying the area law occupies only a tiny fraction of the Hilbert space $\mathcal{H}$ as shown in panel b.

A similar effect of locality is also seen in the entanglement entropy of the subsystem. For a system bipartitioned into subsystems A and B, von-Neumann entropy is the widely used measure of entanglement defined as

$$S(\rho_A) = -\mathrm{Tr}(\rho_A \log(\rho_A)) \tag{2.2}$$

where ρ_A is the reduced density matrix for the subsystem A. If subsystems A and B are unentangled $S(\rho_A) = 0$ which means state of full system ρ can be written as direct product of state of subsystem A and B $i.e$ $\rho = \rho_A \otimes \rho_B$. Subsystem of entangled systems have positive entropy and is bounded by the maximum value $S(\rho_A) \leq |A| \log_2(d)$ where d is the Hilbert space dimension of local degrees of freedom and $|A|$ is the size of the smaller subsystem. Entanglement entropy of the ground state of a one-dimensional local gapped Hamiltonian is independent of the subsystem size, which is the area law for entanglement entropy in 1D. For a one-dimensional gapped quantum system, this has been proved in Ref. [55]. Area law does not hold for the ground state of the gapless Hamiltonian [57–60]. Conditions for validity of area law in higher dimensional gapped Hamiltonian is an open problem [61].

Majority of the eigenstates of a generic Hamiltonian follows volume law [62, 63] for entanglement. However the ground state follows area law, such states occupies a tiny fraction of the Hilbert space $\mathcal{H}$. This tiny fraction has been called the “physical” corner of the $\mathcal{H}$ (in the sense that when studying low energy physics, the system is likely to be found in a small part of the Hilbert space). The methods based on tensor

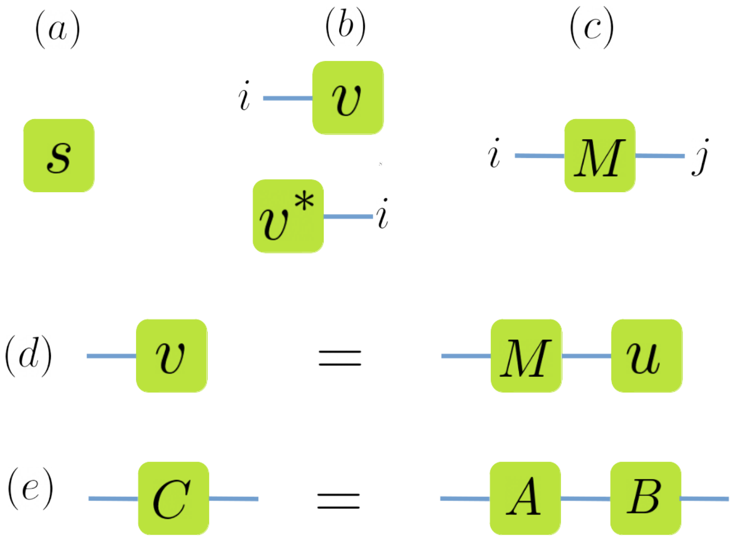

Fig. 2.2 Pictorial representation of a scalar, vector and rectangular matrix is shown in (a), (b) and (c) respectively. Dual of a vector v is shown as v^* in (b). Typically the leg of the dual tensor is flipped. Matrix-vector and matrix-matrix multiplication operation are shown in panel (d) and (e).

network formalism like Matrix product states (MPS) for 1D, Projected entangled pair states (PEPS), and Multiscale entanglement renormalization ansatz (MERA) for higher dimensions, *etc.* effeciently exploits the area law property of the ground state and low lying states.

2.2 Tensor representation

This section discusses the pictorial representation of the tensors and their operations which is used throughout this thesis for visual representation of the MPS.

A *tensor* is a multi-dimensional mathematical object with complex valued entries that generalizes the ideas of arrays. The number of indices of a tensor is called its rank or order. In the pictorial notation, any tensor is denoted by a square or circle with as many indices as its rank or order. We start with the simplest tensor *i.e* a scalar denoted by s. It is tensor of rank 0, and in pictorial notation, it has no legs, as shown in Fig. 2.2(a). Similarly a vector v_i and a matrix M_{ij} are tensors of rank 1 and 2 respectively. Their equivalent pictorial representation is shown in Fig. 2.2(b) and (c) respevtively. Dual of a vector v_i is denoted by v^* with entries of v being complex conjugated is shown in Fig. 2.2(b). For a vector v_i in a n dimensional Hilbert space, value of index i varies from 1 to n.

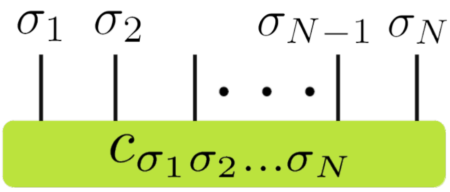

Fig. 2.3 Coeffecient of many-body wavefunction $c_{\sigma_1\sigma_2\ldots\sigma_N}$ shown as a tensor of rank N.

Tensors can be modified to another tensor using different operations. The simplest would be the multiplication of a matrix M with a vector u resulting in a new vector $v = M \cdot u$. Another example of such tensor operation would be the multiplication of two matrices A_{ij} and B_{jk} giving another matrix $C = A \cdot B$. In the Einstein summation convention, the index j got contracted, and $C = A \cdot B$ can be written as $C_{ik} = A_{ij} \cdot B_{jk}$ Pictorial notation of matrix-vector multiplication and matrix-matrix multiplication operations are shown in the Fig. 2.2(d) and (e) respectively.

A many-body wavefunction for a system of N spins with local Hilbert space of dimension d is given by

$$|\psi\rangle = \sum_{\sigma_1\ldots\sigma_N=1}^{d} c_{\sigma_1\sigma_2\ldots\sigma_N} |\sigma_1\sigma_2\ldots\sigma_N\rangle \tag{2.3}$$

In the above equation, the coefficient of the wavefunction is a tensor of rank N with each index of dimension d, and σ_i are the single-particle basis. Its visualization is shown in Fig. 2.3. The vertical legs representing indices σ's are called physical indices as they correspond to physical degrees of freedom of the spin chain.

2.3 Singular Value Decomposition

Matrix product states represent quantum states in the form of the product of matrices, as evident from its name. Singular value decomposition (SVD), a technique from linear algebra, is fundamental to the MPS representation of quantum states. Any complex rectangular matrix M of dimension $N_A \times N_B$ can be decomposed in the form

$$M = USV^\dagger \tag{2.4}$$

where matrices U, S and $V^\dagger$ have the following properties. The above decomposition is called the SVD of matrix M.

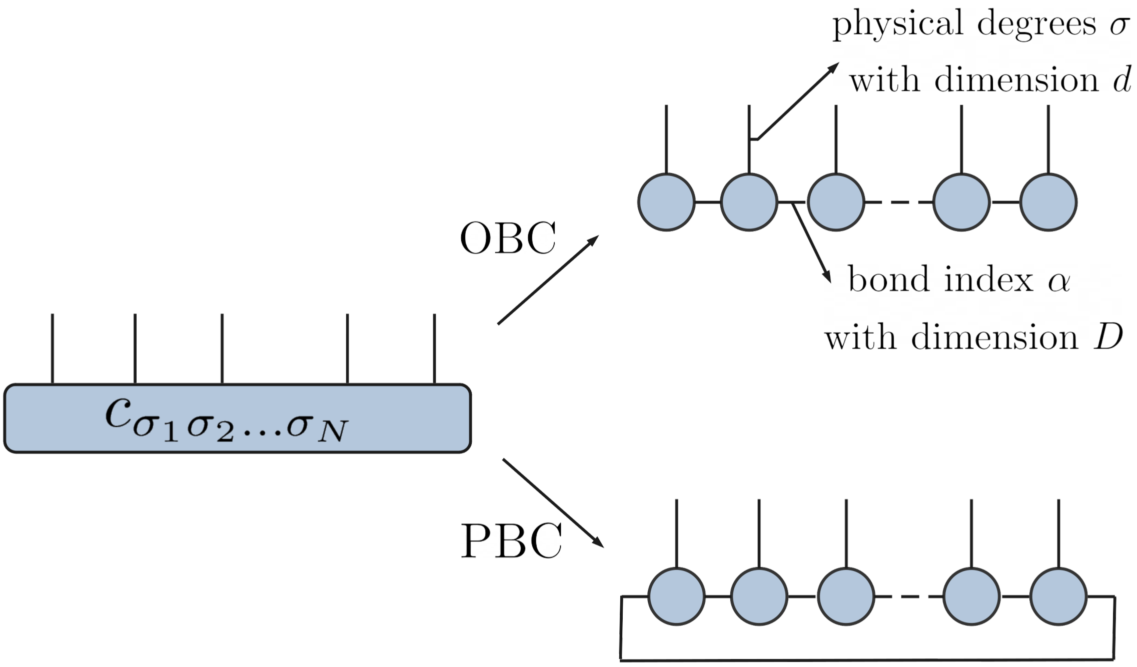
physical degrees σ
with dimension d
OBC
bond index α
with dimension D
$c_{\sigma_1\sigma_2\ldots\sigma_N}$
PBC

Fig. 2.4 Diagramatic notation for the MPS representation of Eq. 2.3 open and periodic boundary condition.

- U and V are of dimension $(N_A \times \lambda)$ and $(N_B \times \lambda)$ resepectively with orthonormal columns. U and V satisfy $U^\dagger U = V^\dagger V = 1$ where dimension of identity matrix is $(\lambda \times \lambda)$. Here $\lambda = \min(N_A, N_B)$
- S is a diagonal matrix of dimension $(\lambda \times \lambda)$ with real non-negative entries. The diagonal entries are called singular values

2.4 Matrix Product States

The general idea of MPS involves taking the tensor of higher rank , *i.e.*, $c_{\sigma_1\sigma_2\ldots\sigma_N}$ and breaking it down into several tensors of smaller rank using SVD. These smaller tensors when contracted gives back the original tensor. MPS representation of coefficient $c_{\sigma_1\sigma_2\ldots\sigma_N}$ of any arbitrary pure state $|\psi\rangle$ of spin chain with N spins with open boundary condition is given by

$$c_{\sigma_1\sigma_2\ldots\sigma_N} = \sum_{\alpha} T^{\sigma_1}_{\alpha_1} T^{\sigma_2}_{\alpha_1,\alpha_2} \ldots T^{\sigma_{N-1}}_{\alpha_{N-2},\alpha_{N-1}} T^{\sigma_N}_{\alpha_{N-1}} \tag{2.5}$$

Here the summation over α means summation over all α_i indices where $i = 1, \dots, N$.

$$\begin{aligned} c_{\sigma_1,(\sigma_2\sigma_3)} &= U_{\sigma_1,\alpha_1} S_{\alpha_1,\alpha_1} V^\dagger_{\alpha_1,\sigma_2\sigma_3} = T^{\sigma_1}_{\alpha_1} Q_{\alpha_1,\sigma_2\sigma_3} \\ &= T^{\sigma_1}_{\alpha_1} Q_{\alpha_1\sigma_2,\sigma_3} = T^{\sigma_1}_{\alpha_1} U_{\alpha_1\sigma_2,\alpha_2} S_{\alpha_2,\alpha_2} V^\dagger_{\alpha_2,\sigma_3} \\ &= T^{\sigma_1}_{\alpha_1} T^{\sigma_2}_{\alpha_1,\alpha_2} Q_{\alpha_2,\sigma_3} = T^{\sigma_1}_{\alpha_1} T^{\sigma_2}_{\alpha_1,\alpha_2} T^{\sigma_3}_{\alpha_2} \end{aligned} \tag{2.6}$$

We will illustrate the decomposition of wavefunction $c_{\sigma_1\sigma_2\sigma_3}$ in Eq. 2.6 for chain of 3 spins. We start with rearrangement of indices of $c_{\sigma_1\sigma_2\sigma_3}$ to $c_{\sigma_1,(\sigma_2\sigma_3)}$ then we do the SVD. From SVD we get tensors U_{σ_1,α_1}, S_{α_1,α_1} and $V^\dagger_{\alpha_1,\sigma_2\sigma_3}$. We get $T^{\sigma_1}_{\alpha_1}$ from rearrangement of indices σ_1 and α_1 of tensor U_{σ_1,α_1}. Tensors S_{α_1,α_1} and $V^\dagger_{\alpha_1,\sigma_2\sigma_3}$ is assimilated into a new tensor $Q_{\alpha_1,\sigma_2\sigma_3}$. We repeat the rearrangement of indices and SVD for the new tensor $Q_{\alpha_1,\sigma_2\sigma_3}$ from which tensor T^{σ_i}'s are constructed. The last tensor $T^{\sigma_3}_{\alpha_2}$ is constructed somewhat differently from contracting S_{α_2,α_2} and $V^\dagger_{\alpha_2,\sigma_3}$ and rearrangement of resultant tensor.

For a pure state with closed boundary condition, MPS representation modifies to

$$c_{\sigma_1\sigma_2\dots\sigma_N} = \sum_\alpha T^{\sigma_0}_{\alpha_0,\alpha_1} T^{\sigma_2}_{\alpha_1,\alpha_2} \dots T^{\sigma_{N-1}}_{\alpha_{N-2},\alpha_{N-1}} T^{\sigma_N}_{\alpha_{N-1},\alpha_0} = \mathrm{Tr}\Big(T^{\sigma_1} T^{\sigma_2} \dots T^{\sigma_{N-1}} T^{\sigma_N}\Big) \tag{2.7}$$

Tensor diagrammatic notation of Eq. 2.5 and 2.7 are shown in Fig. 2.4(a) and (b) respectively. The difference between the MPS representation of the state in open and closed boundary conditions can be seen at the first and last tensor. In open boundary condition the first and last tensor *i.e* $T^{\sigma_1}_{\alpha_1}$ and $T^{\sigma_N}_{\alpha_N}$ are 2 rank tensor. In this thesis we only deal with system with open boundary condition. It is assumed that the contracted horizontal bonds have bond dimension D (internal dimension) for the approximate description of the low entanglement states. The vertical bands are physical degrees of freedom and have bond dimension d.

MPS representation reduces the number of variational parameters of the state $|\psi\rangle$ drastically if it is a low entanglement state. In Eq. 2.3 tensor $c_{\sigma_1\sigma_2\dots\sigma_N}$ has d^N number of variational parameters while we have $\mathcal{O}(NdD^2)$ parameters in the MPS representation in Eq. 2.5. The number of variational parameters for the MPS representation can be understood in the following way. We have roughly N number of tensors of rank three corresponding to each spin in the chain. For each tensor, there are three indices - one physical index with dimension d and two horizontal indices with dimension $\mathcal{O}(D)$ of each, which gives dD^2 parameter for each three-legged tensor. Since we have N such tensor, the number of variational parameters is $\mathcal{O}(NdD^2)$. For a fixed D, the number of variational parameters change from exponential in d to linear in d when we switch to MPS representation. The bond dimension D can be exponential in d for the highly

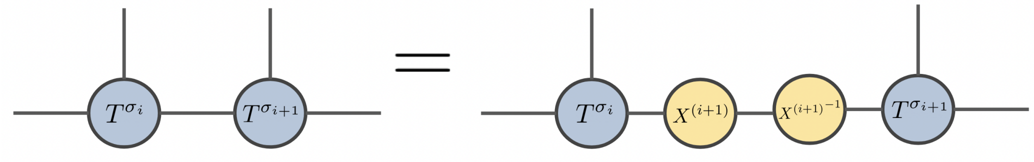

Fig. 2.5 Diagramatic notation for understanding the gauge degree of freedom in MPS representation arising from the invariance of state $|\psi\rangle$ after insertion of product of tensors $X_{i+1}X_{i+1}^{-1}$ in between the consecutive local tensor T

entangled statess such as volume law states, and hence MPS representation does not always reduce the complexity of state representation.

Gauge degrees of freedom and Canonical form

MPS representation of a pure state has a large gauge degrees of freedom, which can be seen as follows. Under the transformation

$$\tilde{T}^{\sigma_i}_{\beta_{i-1},\beta_i} = (X^{-1})^{(i)}_{\beta_{i-1},\alpha_{i-1}} T^{\sigma_i}_{\alpha_{i-1},\alpha_i} X^{(i+1)}_{\alpha_i,\beta_i} \tag{2.8}$$

for choice of $\{X^{(1)}, \dots, X^{(N-1)}\}$ invertible matrices with suitable dimensions, we have

$$\sum_{\alpha} T^{\sigma_1}_{\alpha_1} T^{\sigma_2}_{\alpha_1,\alpha_2} \dots T^{\sigma_{N-1}}_{\alpha_{N-2},\alpha_{N-1}} T^{\sigma_N}_{\alpha_{N-1}} = \sum_{\beta} \tilde{T}^{\sigma_1}_{\beta_1} \tilde{T}^{\sigma_2}_{\beta_1,\beta_2} \dots \tilde{T}^{\sigma_{N-1}}_{\beta_{N-2},\beta_{N-1}} \tilde{T}^{\sigma_N}_{\beta_{N-1}} \tag{2.9}$$

Equivalence in Eq. 2.9 shows the non-unique MPS representation of a state. Tensor diagram for Eq. 2.8 is shown in Fig. 2.5. For a given pure state $|\psi\rangle$ all the possible MPS representation of it forms a manifold. In this manifold of gauge equivalent MPS representation, we are interested in a particular MPS form called canonical form, which is very helpful in numerical implementation of MPS because of its useful properties. There are three types of canonical form - left, right and mixed. In the left canonical representation $c_{\sigma_1\sigma_2\dots\sigma_N}$ is given by

$$c_{\sigma_1\sigma_2\dots\sigma_N} = \sum_{\alpha} A^{\sigma_1}_{\alpha_1} A^{\sigma_2}_{\alpha_1,\alpha_2} \dots A^{\sigma_{N-1}}_{\alpha_{N-2},\alpha_{N-1}} A^{\sigma_N}_{\alpha_{N-1}} \tag{2.10}$$

The tensors A are “left-normalized” and satisfies the property

$$\sum_{\sigma_i} \sum_{\alpha_{i-1}} A^{\sigma_i\dagger}_{\alpha_{i-1},\alpha'_i} A^{\sigma_i}_{\alpha_{i-1},\alpha_i} = \delta_{\alpha_i,\alpha'_i} \tag{2.11}$$

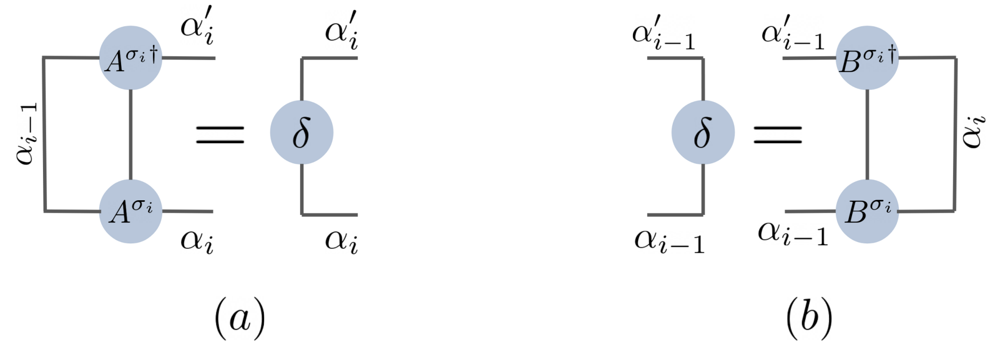

Fig. 2.6 Property of the left and right canonical form mentioned in Eq. 2.11 and 2.13 is shown in the tensor diagramatic notation in (a) and (b) respectively.

This is schematically shown in Fig. 2.6 (a). The right-canonical form represents the state in the form

$$c_{\sigma_1\sigma_2\ldots\sigma_N} = \sum_{\alpha} B^{\sigma_1}_{\alpha_1} B^{\sigma_2}_{\alpha_1,\alpha_2} \ldots B^{\sigma_{N-1}}_{\alpha_{N-2},\alpha_{N-1}} B^{\sigma_N}_{\alpha_{N-1}} \tag{2.12}$$

The tensors B are “right-normalized” and satisfies the property

$$\sum_{\sigma_i}\sum_{\alpha_i} B^{\sigma_i\dagger}_{\alpha'_{i-1},\alpha_i} B^{\sigma_i}_{\alpha_{i-1},\alpha_i} = \delta_{\alpha'_{i-1},\alpha_{i-1}} \tag{2.13}$$

Tensor diagramatic notation of the right normalization condition is shown in Fig. 2.6(b). Mixed canonical form is consturcted using both right and left normalized tensors and its has representation

$$c_{\sigma_1\sigma_2\ldots\sigma_N} = \sum_{\alpha} A^{\sigma_1}_{\alpha_1} \ldots A^{\sigma_l}_{\alpha_{l-1},\alpha_l} B^{\sigma_{l+1}}_{\alpha_l,\alpha_{l+1}} \ldots B^{\sigma_N}_{\alpha_{N-1}} \tag{2.14}$$

Using a suitable gauge any MPS representation can be converted to any of the three canonical form.

2.5 Matrix Product Operators

The idea of MPS can be straightforwardly generalized to the operators, and the analogous construction for operators is called Matrix Product Operators (MPO). Here we have two sets of physical indices *i.e* incoming indices $\sigma_i^{'}$ and outgoing indices σ_i. A

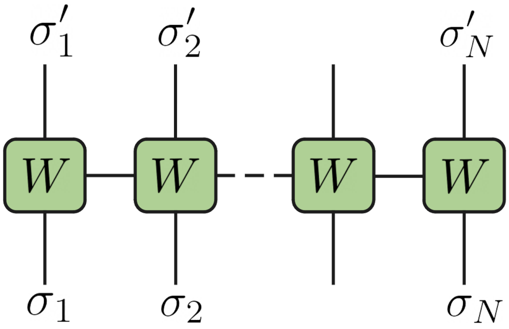

Fig. 2.7 Diagramatic notation for the MPO representation of opertor $\hat{O}$

general operator $\hat{O}$ can be written in MPO form as follows

$$\hat{O} = \sum_{\sigma,\sigma'} W^{\sigma_1\sigma'_1}_{[1]\beta_1} W^{\sigma_2\sigma'_2}_{[2]\beta_1,\beta_2} \dots W^{\sigma_N\sigma'_N}_{[L]\beta_N} |\sigma_1\sigma_2\dots\sigma_N\rangle\langle\sigma'_1\sigma'_2\dots\sigma'_N| \tag{2.15}$$

Diagrammatic representation of MPO is shown in Fig. 2.7. It is different from MPS in the sense that it has two vertical bonds corresponding to σ and σ'. Another way to think of MPO is that W's are rank 2 tensors with operator values entries (In this manner of thinking, local 2 rank tensors of MPS has vector as its entry). To clarify we will illustrate the MPO representation of the anisotropic Heisenberg model, which has Hamiltonian

$$H = J\sum_i(\sigma^x_i\sigma^x_{i+1} + \sigma^y_i\sigma^y_{i+1} + \Delta\sigma^z_i\sigma^z_{i+1}) - h\sum_i\sigma^z_i \tag{2.16}$$

σ' s are the Pauli spin operators, Δ is the anisotropy parameter, and h is the constant local field in the z direction. In the tensor product notation, it can be written as

$$\begin{aligned} H = J\Big(&\sigma^x_1 \otimes \sigma^x_2 \otimes \dots \otimes \mathbb{I} \otimes \mathbb{I} + \mathbb{I} \otimes \sigma^x_2 \otimes \sigma^x_3 \otimes \dots \otimes \mathbb{I} \otimes \mathbb{I} + \dots \\ &+ \sigma^y_1 \otimes \sigma^y_2 \otimes \dots \otimes \mathbb{I} \otimes \mathbb{I} + \mathbb{I} \otimes \sigma^y_2 \otimes \sigma^y_3 \otimes \dots \otimes \mathbb{I} \otimes \mathbb{I} \dots \\ &+ \Delta\sigma^z_1 \otimes \sigma^z_2 \otimes \dots \otimes \mathbb{I} \otimes \mathbb{I} + \dots\Big) \\ &- h\sigma^z_1 \otimes \mathbb{I} \otimes \dots \otimes \mathbb{I} \otimes \mathbb{I} - h\mathbb{I} \otimes \sigma^z_2 \otimes \mathbb{I} \otimes \dots \otimes \mathbb{I} \otimes \mathbb{I} \dots \end{aligned} \tag{2.17}$$

Corresponding MPO representation of the above Hamiltonian is

$$W_{[i]} = \begin{pmatrix} \mathbb{I} & 0 & 0 & 0 & 0 \\ \sigma^x & 0 & 0 & 0 & 0 \\ \sigma^y & 0 & 0 & 0 & 0 \\ \sigma^z & 0 & 0 & 0 & 0 \\ -h\sigma^z & J\sigma^x & J\sigma^y & \Delta\sigma^z & \mathbb{I} \end{pmatrix} \tag{2.18}$$

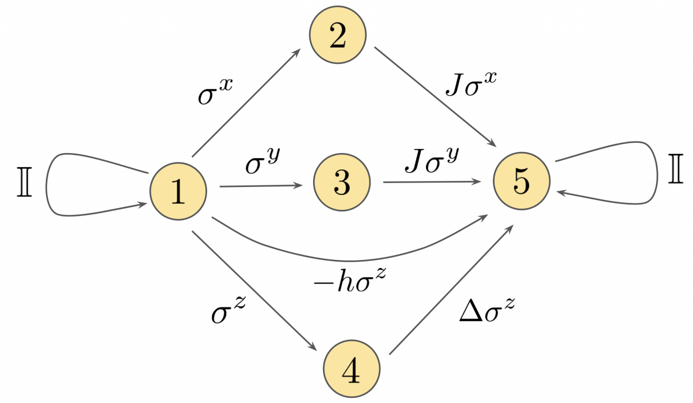

Fig. 2.8 Finite state automaton representation of MPO of Hamiltonian Eq. 2.16.

At left and right boundaries, the W's are given by

$$W_{[1]} = \begin{pmatrix} -h\sigma^z & J\sigma^x & J\sigma^y & \Delta\sigma^z & \mathbb{I} \end{pmatrix}, \quad W_{[L]} = \begin{pmatrix} \mathbb{I} \\ \sigma^x \\ \sigma^y \\ \sigma^z \\ -h\sigma^z \end{pmatrix} \tag{2.19}$$

Here MPO is of bond dimension 5. An elegant approach to constructing MPO is thinking it as finite-state machines [64]. We summarise the MPO construction as a finite state machine here. Lets start with the tensor product notation mentioned in Eq. 2.17 for Hamiltonian in Eq. 2.16.

Each individual term in this Eq. 2.17 will be treated as a string which is constructed using the four operators $\mathbb{I}, \sigma^x, \sigma^y, \sigma^z$. We will start from the right end of string. We can divide a string construction in three parts - no encounter of the interaction (string of $\mathbb{I}$ on the left), encountering a interaction and completion of interaction or local field. We introduce the concept of state for each bond in the string to incorporate the construction step mentioned before. For this particular example we need only five states.

State 1 corresponds to all operators being $\mathbb{I}$ to the left. When we encounter the interaction term in the string for which we need three states here 2, 3 and 4 corresponding to encountering operators σ^x, σ^y and σ^z. We need another state 5 to complete the interaction. For any arbitrary bond in the string the possible transitions and their corresponding weights are shown in the Fig. 2.8. The information encoded in the finite state machine shown in Fig. 2.8 is equivalent to MPO representation shown in Eq. 2.18.

MPO for chiral clock Hamiltonian

For convenience we will mention the chiral clock Hamiltonian again here

$$H = -J \sum_{i=1}^{N-1} (e^{\iota\theta}\sigma_i\sigma_{i+1}^\dagger + e^{-\iota\theta}\sigma_i^\dagger\sigma_{i+1}) - \sum_{i=1}^{N} (fe^{\iota\phi}\tau_i + fe^{-\iota\phi}\tau_i^\dagger) \tag{2.20}$$

MPO representation of the above Hamiltonian is

$$W_{[i]} = \begin{pmatrix} \mathbb{I} & 0 & 0 & 0 \\ \sigma^\dagger & 0 & 0 & 0 \\ \sigma & 0 & 0 & 0 \\ \Gamma & -Je^{\iota\theta}\sigma & -Je^{-\iota\theta}\sigma^\dagger & \mathbb{I} \end{pmatrix} \tag{2.21}$$

here $\Gamma = -fe^{\iota\phi}\tau - fe^{-\iota\phi}\tau^\dagger$. At left and right boundaries, the W's are given by

$$W_{[1]} = \begin{pmatrix} \Gamma & -Je^{\iota\theta}\sigma & -Je^{-\iota\theta}\sigma^\dagger & \mathbb{I} \end{pmatrix}, \quad W_{[L]} = \begin{pmatrix} \mathbb{I} \\ \sigma^\dagger \\ \sigma \\ \Gamma \end{pmatrix} \tag{2.22}$$

2.6 Computing Expectation values

For a local operator $\hat{O}^{[l]}$ local on site l, its expectation value with respect to state $|\psi\rangle$ is $\langle\psi|\hat{O}^{[l]}|\psi\rangle$. In the MPS representation, expression for the expectation value is

$$\langle\psi|\hat{O}^{[l]}|\psi\rangle = \sum_{\sigma,\sigma'} \sum_{\alpha,\alpha'} T^{\sigma_1}_{\alpha_1} T^{\sigma_1 \dagger}_{\alpha'_1} \dots T^{\sigma_l}_{\alpha_{l-1},\alpha_l} \hat{O}^{[l]\sigma_l,\sigma'_l} T^{\sigma'_l \dagger}_{\alpha'_{l-1},\alpha'_l} \dots T^{\sigma_N}_{\alpha_N} T^{\sigma'_N \dagger}_{\alpha_N} \tag{2.23}$$

The above complicated-looking expression can be easily evaluated using the canonical form. Among the right, left, and mixed canonical forms, mixed form simplifies Eq. 2.23 the most. We pick a particular site called the orthogonality center in mixed canonical form. Here we choose gauge transformation such that on the left (right) of the orthogonality center, all the local tensors are in the left (right) canonical form. In this canonical form, expression for $\langle\psi|\hat{O}^{[l]}|\psi\rangle$ is

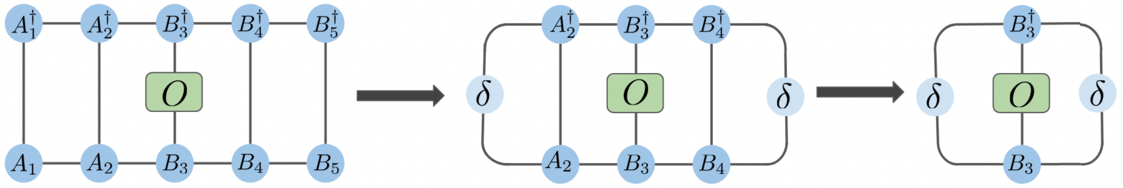

Fig. 2.9 Figure showing simplification of the calculation of the expectation value by using mixed canonical form.

$$\langle\psi|\hat{O}^{[l]}|\psi\rangle = \sum_{\sigma,\sigma'}\sum_{\alpha,\alpha'} A^{\sigma_1}_{\alpha_1} A^{\sigma_1\dagger}_{\alpha'_1} \dots B^{\sigma_l}_{\alpha_{l-1},\alpha_l} \hat{O}^{[l]\sigma_l,\sigma'_l} B^{\sigma'_l\dagger}_{\alpha'_{l-1},\alpha'_l} \dots B^{\sigma_N}_{\alpha_N} B^{\sigma_N\dagger}_{\alpha'_N} \tag{2.24}$$

$$= \sum_{\sigma_l,\sigma'_l}\sum_{\alpha,\alpha'} B^{\sigma_l}_{\alpha_{l-1},\alpha_l} \hat{O}^{[l]\sigma_l,\sigma'_l} B^{\sigma'_l\dagger}_{\alpha'_{l-1},\alpha'_l} \delta_{\alpha_{l-1},\alpha'_{l-1}} \delta_{\alpha_l,\alpha'_l} \tag{2.25}$$

In the simplification of the Eq. 2.25, we have used the property of the canonical form mentioned in Eq. 2.11 and 2.13. The minimum computational complexity of the evaluation of the tensor network is shown in Fig. 2.9 is $\mathcal{O}(NdD^3)$ while for the network shown in Fig. it is $\mathcal{O}(dD^2)$. This shows the significance of choosing the appropriate canonical form.

2.7 Ground state search

The ground state search problem looks for the state $|\psi\rangle$, which minimizes the

$$E = \frac{\langle\psi|\hat{H}|\psi\rangle}{\langle\psi|\psi\rangle} \tag{2.26}$$

This is done in the MPS language by introducing the Lagrange multiplier λ, which extremizes

$$\langle\psi|\hat{H}|\psi\rangle - \lambda\langle\psi|\psi\rangle \tag{2.27}$$

while preserving the norm $\langle\psi|\psi\rangle$. Search for the $|\psi\rangle$ that extremizes the Eq. 2.27 is a highly non-linear optimization problem. In the MPS representation, instead of optimizing all the local tensors A^{σ_i} simultaneously. The optimization retains the spirit of ground-state search using the Density Matrix Renormalization Group (DMRG) sweeping. The optimization procedure is being started with a random MPS state given

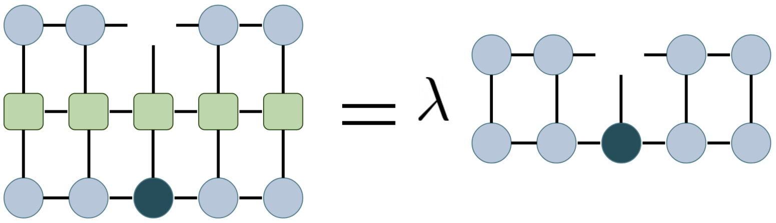

Fig. 2.10 Equation 2.30 can be visualized by the tensor network diagram shown. Darkened circle represents the local tensor $\vec{M}^{\sigma_i}$ and the H_{eff} is the rest of the tensor network after excluding $\vec{M}^{\sigma_i}$ in network shown in left hand side.

by

$$|\psi\rangle = \sum_{\alpha} A^{\sigma_1}_{\alpha_1} A^{\sigma_2}_{\alpha_1,\alpha_2} \dots A^{\sigma_{N-1}}_{\alpha_{N-1},\alpha_N} A^{\sigma_N}_{\alpha_N} |\sigma_1 \sigma_2 \dots \sigma_N\rangle \tag{2.28}$$

In the optimization, one of the local tensors is fixed denoted by M^{σ_i} and treated as a variational parameter. M^{σ_i} is treated as a vector, and the new minimization equation is

$$\vec{M^{\sigma_i}}^{\dagger} \mathcal{H}_{eff} \vec{M^{\sigma_i}} - \lambda \vec{M^{\sigma_i}}^{\dagger} \mathcal{N} \vec{M^{\sigma_i}} \tag{2.29}$$

Equation 2.29 is then minimized with respect to $\vec{M^{\sigma_i}}$ which leads to genralized eigenvalue problem

$$\mathcal{H}_{eff} \vec{M^{\sigma_i}} = \lambda \mathcal{N} \vec{M^{\sigma_i}} \tag{2.30}$$

The above equation is solved using standard eigenvalue packages. Tensor diagramatic notation for equation 2.30 is shown in Fig. 2.10. Index i in $\vec{M^{\sigma_i}}$ which corresponds to a physical site in the chain is varied from one end to another end of the chain in back and forth manner. In each iteration of the optimization, the rest of the local tensors are kept constant. This sweeping is continued till desirable convergence is achieved for energy.

2.8 Time evolution

Two main techniques are used to implement the time evolution (real or imaginary) in the MPS framework. The first one involves the approximating the matrix exponential , *i.e.*, $e^{-\iota Ht}$ using Suzuki-Trotter decomposition and then applying the approximated MPO to $|\psi\rangle$ which needs to be evolved. Another technique is called the time-dependent variational principle (tDVP), which relies on the variational manifold of uniform MPS. We will discuss the first technique as this is the method we have used in the works mentioned in this thesis.

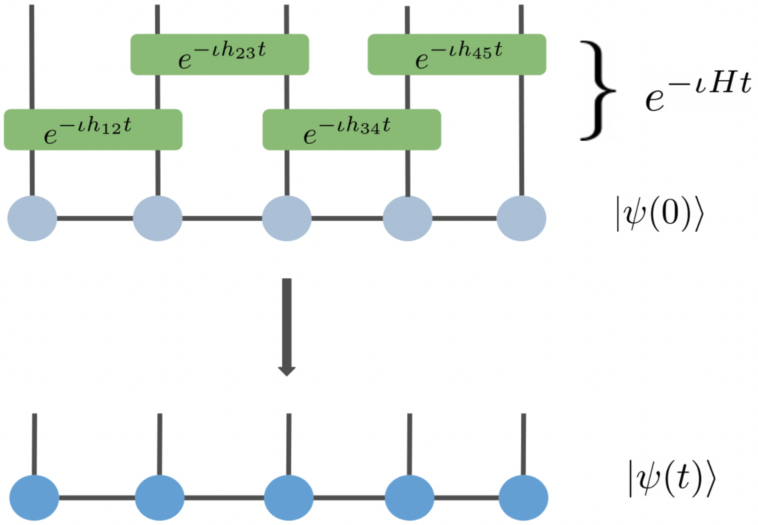

Fig. 2.11 Time evolution of an MPS $|\psi(0)\rangle$ using the MPO's estimated by first order Suzuki-Trotter decomposition mentioned in Eq. 2.32. After contracting MPO with MPS we get the time evolved state $|\psi(t)\rangle$.

We start with splitting the Hamiltonian H into two parts H_{odd} and H_{even} such that

$$H = H_{\text{odd}} + H_{\text{even}} \tag{2.31}$$

H_{odd} and H_{even} are the terms of the H which acts on the odd and even bonds of the chain. Both H_{odd} and H_{even} are of the form $\sum_i h_i$ which satisfies the condition that $[h_i, h_j] = 0$. Then the time evoution operator $e^{-\iota H\delta t}$ is approximated in terms of H_{odd} and H_{even} using Suzuki-Trotter decomposition which is explained below. A n^{th} order approximant of $e^{-\iota H\delta t}$ constructed using Suzuki-Trotter decomposition is acurate till $\mathcal{O}(\delta t^n)$. For example first order trotter decomposition is

$$e^{-\iota H\delta t} = e^{-\iota H_{\text{odd}}\delta t}e^{-\iota H_{\text{even}}\delta t} + \mathcal{O}(\delta t^2) \tag{2.32}$$

Individual matrix exponentials in Eq. 2.32 can be further written as following because of the commuting properties of the individual terms in the H_{odd} and H_{even}

$$U(\delta t) = e^{-\iota H_{\text{odd}}\delta t}e^{-\iota H_{\text{even}}\delta t} = \Pi_i e^{-\iota h_i^{\text{odd}}\delta t}\Pi_j e^{-\iota h_j^{\text{even}}\delta t} \tag{2.33}$$

Each term in Eq. 2.33 is then expressed as MPO and then applied on $|\psi\rangle$. After applying the MPO, the bond dimension of the resultant MPS increases, which is then

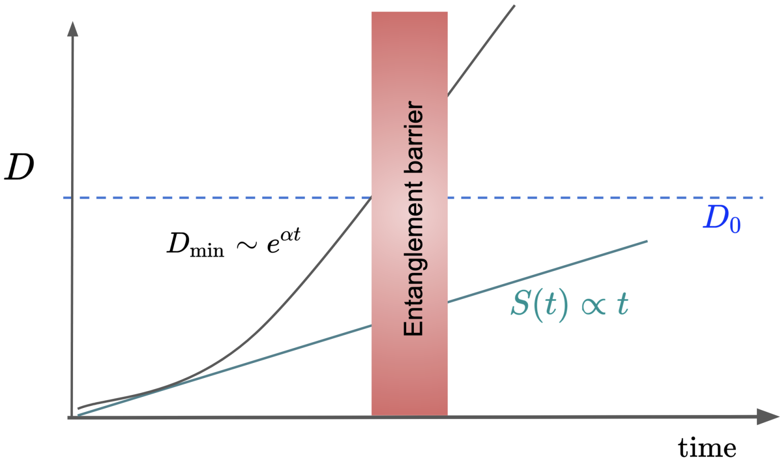

Fig. 2.12 Often in initially weakly entangled states, subsystem entanglement $S(t)$ grows linearly with time and the bond dimension D_{min} needed to accurately describe the state increases exponentially with time. Figure shows exponential growth of minimum bond dimension D_{min} with time results in entanglement barrier when D_{min} crosses the bond dimension D_0.

set to desirable dimension D by the compression procedure [37]. The diagrammatic notation is shown in Fig. 2.11.

We are primarily interested in the dynamics implemented by successive application of $U(\delta t)$. For the reliable study of dynamics, we need our time evolution operator to be as accurate as possible. There two ways to do this - using higher order approximants or using smaller δt. Using smaller δt involves more iterative steps to reach same time t. This leads to additional computational cost and the error acumulation associated with MPS truncation steps will be faster in the intermediate steps. The computational cost is smaller and error accumulation is slower if we use the higher order approximants with larger δt as there are less steps involved. We have used the fourth-order approximant of $U(\delta t)$ in our work. The time-dependent version of the fourth-order approximant of $U(\delta t)$ is constructed using the fractal decomposition, which is discussed in Sec. 3.5 of Chapter 3. The time-independent version is discussed in Sec. 5.5 of Chapter 5.

Time evolution using the MPS formalism becomes inaccurate and expensive due to exponentially increasing bond dimension [65–67]. There is a limit to the maximum bond dimension D_0 till we can go in our simulation which is decided by our computer's hardware. So the entanglement puts a barrier for the time until we can efficiently do the time evolution using MPS. This goes by the name of entanglement barrier and is schematically shown in Fig. 2.12.

2.9 Density matrices

Density matrices are the more generic representation of any quantum state as both pure and mixed states can be expressed using it. In Ref. [56] concept of Matrix Product Density Operator (MPDO) was introduced, which generalizes the MPS formalism from pure to mixed states. An MPDO for N spins with d local degrees of freedom is defined as

$$\rho = \sum_{\{s,s'\}=1}^{d} (M_1^{s_1,s_1'} \ldots M_N^{s_N,s_N'}) |s_1, \ldots, s_N\rangle\langle s_1', \ldots, s_N'| \tag{2.34}$$

where tensor M are related to local tensor A by

$$M_k^{s,s'} = \sum_{a=1}^{d_k} A_k^{s,a} \otimes (A_k^{s',a'})^* \tag{2.35}$$

A are local tensors of some pure state which lives in the extended local Hilbert space $\{s, a\}$ with a being the auxiliary physical degrees of freedom. This way of construction of MPDO is inspired by local purification and ensures the positivity of the resultant density matrix. Finite temperature states $\rho_\beta = e^{-\beta H}/Z$ can also be constructed [37] using the similar local purification technique by associating an auxiliary degree of freedom to each spin.

There is another way of representing the density matrices, which was introduced in [68]. This representation is based on the trick called Choi Isomorphism and represents the ρ in the form of MPS by clubbing the ket and bra indices of density matrix and treating it as a new ket index. We have used this MPS representation in our work which is discussed in detail in Sec. 5.4 of Chapter 5.

2.10 Conclusion

We have discussed the broad ideas involved in the MPS technique, which is used extensively to study non-equilibrium dynamics in this thesis. MPS ansatz effficiently and accurately represents the states with low entanglement. The dynamics can be studied in the MPS framework until the time scale set by entanglement barrier. We have discussed the implementation of time evolution using the Suzuki-Trotter decomposition of the time evolution operator $U(\delta t)$. Finer details of the fourth-order approximant used are discussed in Chapter 3 and 5.

Chapter 3

Boundary Driving a Critical $\mathbb{Z}_3$ Clock Chain

Low frequency perturbations at the boundary of critical quantum chains can be understood in terms of the sequence of boundary conditions imposed by them, as has been previously demonstrated in the Ising and related fermion models. Using extensive numerical simulations, we explore the scaling behavior of the Loschmidt echo under longitudinal field perturbations at the boundary of a critical $\mathbb{Z}_3$ Potts model. We show that at times much larger than the relaxation time after a boundary quench, the Loschmidt-echo has a power-law scaling with time as expected from interpreting the quench as insertion of boundary condition changing operators. Similar scaling is observed as a function of time-period under a low frequency square-wave pulse. We present numerical evidence which indicate that under a sinusoidal or triangular pulse, scaling with time period is modified by Kibble-Zurek mechanism, again similar to the case of the Ising model. Results confirm the validity, beyond the Ising model, of the treatment of the boundary perturbations in terms of the effect on boundary conditions.

3.1 Introduction

The search for robust phenomena in interacting many body quantum systems far out of equilibrium has seen a recent surge of activity motivated by the increasing ability to probe quantum dynamics in artificial many body systems [69, 70], and by the improvement in computational techniques that can reliably simulate dynamics in very large quantum many body systems[71, 72, 37, 73]. Attempts at developing general guiding principles like in equilibrium systems have prompted the investigation of tractable models and protocols for out of equilibrium systems.[74, 75]. Systems out of equilibrium due to time-periodic Hamiltonians are among the simplest of such tractable systems. The constant stroboscopic unitary time evolution operators in such systems allow natural extensions of equilibrium notions such as steady state ensembles and quasienergies [76, 77, 77], while at the same time demonstrating dynamical aspects that differ from equilibrium systems. Creative applications of Floquet physics[78, 79] have already lead to the demonstration or prediction of many out of equilibrium phenomena including Floquet localization[80, 80], freezing [81, 82], time crystals [83, 30, 84, 9, 85], topological phases [86–91], non adiabatic charge pumping[92], Floquet edge modes[93–95] etc. Periodic driving in generic interacting systems however leads to heating[96, 97], taking the system ultimately to a featureless time steady state. This fate can nevertheless be delayed in certain systems with long prethermalization times, strong disorder etc.[98–101]

A periodic drive wherein the time dependent part of the Hamiltonian is local could also lead to interesting physics in the long time limit, heating being avoided here due to dissipation into the surrounding medium. Lack of translational invariance as well as a need for large system sizes make analytical and numerical studies of such systems difficult. Local periodic drives at the boundary of critical 1D semi-infinite quantum system are nevertheless tractable in the long-time limit, owing to the possibility of mapping the problem to scenarios in 2D classical boundary critical phenomena[102]. From the point of view of numerical experiments, long chains can be used to mimic semi-infinite systems allowing simulations of the system sufficiently long before finite size corrections appear, allowing access to long time scaling properties.

In this spirit, critical quantum transverse field Ising model subjected to a periodic longitudinal field (of amplitude h_b) was explored in Ref-[5]. It was demonstrated that at low frequencies ($\omega = 2\pi/T$, where T much larger than the relevant relaxation times) the Loschmidt echo $|\langle\psi(0)|\psi(NT)\rangle|^2$ after N time steps has a frequency dependence of the form $(\omega h^{-\nu})^{N\gamma}$. When the time dependent boundary field has a square waveform, the exponent $\gamma = 4h_{\mathrm{BCC}}$ where h_{BCC} is the scaling dimension of the boundary condition changing operator corresponding to the change of boundary condition (for example from a up-spin to down-spin). This exponent γ is corrected by Kibble Zurek mechanism[103–105] to $\frac{4h_{\mathrm{BCC}}}{1+\nu}$ when the boundary field has a triangular or sinusoidal waveform. Numerical simulations of the Ising model with integrability breaking perturbations suggested that the scaling is robust in the presence of interactions. Similar scaling was also observed in fermionic models related to the Ising model[106].

In this work, we explore the quantum critical $\mathbb{Z}_3$ Potts model under similar boundary perturbations. The $\mathbb{Z}_3$ quantum Potts model generalizes the Ising model, and has a conformal critical point at the transverse field induced transition from the $\mathbb{Z}_3$ ordered phase to the paramagnetic phase. The Ising model following a Jordan Wigner transformation maps to a fermion problem[40] with a quadratic Hamiltonian and linear, exactly-solvable Heisenberg equations of motion allowing extensive analytical and numerical studies of its dynamics. The Potts model under a similar transformation, maps to a parafermion model with a quadratic Hamiltonian, which nevertheless does not yield linear equations of motion[107–109, 47]. We therefore rely on matrix product states(MPS) time evolution [73] to simulate the Potts chain and explore the scaling properties of Loschmidt echo.

The chapter is structured as follows. In section 3.3 we introduce the Potts model, describe the protocol for periodic drive and summarize the scaling relations expected. Details of the numerical simulations are presented in section 3.4. Results of the numerical simulation and their discussion are presented in section 3.6.

3.2 Boundary driven critical Ising chain

Hamiltonian of the Ising model with the boundary floquet drive studied in Reference [5] is given by

$$H(t) = -\sum_{i\geq 0}\left(J\sigma_i^z\sigma_{i+1}^z + h\sigma_i^x + \Gamma\sigma_i^x\sigma_{i+1}^x\right) - h_b(t)\sigma_0^z \tag{3.1}$$

Parameters J and h are set to 1 as Ising model is critical at this parameter value. Strength of the boundary field is $h_b(t)$ which is time dependent and periodic satisfies $h_b(t) = h_b(t+nT)$ for any integer n. Γ quantifies the strength of additional perturbation. Relaxation time t_b can be thought of as correlation length in the time direction along the boundary and is given by $t_b = |h_b^{-\nu_b}|$. Exponent ν_b is decided by the scaling dimension of the boundary field h_b. There are three relevant energy scales in the problem which are single particle bandwidth $\Lambda = 2J = 2$, relaxation time t_b and driving frequency $\omega = 2\pi/T$. Universality features in the low frequency drive was characterised by the scaling features of the Loschmidt echo $\mathcal{L} = \langle\psi_0|\psi(t)\rangle$, where $|\psi_0\rangle$ is the ground state of Hamiltonina at $t = 0$.

In the slow driving regime time scales are in the order $\omega \ll t_b^{-1} \ll \Lambda$. Universal features observed in this regime can be explained using the arguments borrowed from CFT and Kibble-Zurek mechanism. We are interested in the universality arising when boundary of system is perturbed around the critical point by varying the boundary field h_b. If boundary field is changed sharply then this change is equivalent to insertion of boundary condition changing (BCC) operators ϕ_{BCC}. Loscmidt echo at later time t when boundary field is quenched from $\pm h_b$ to $\mp h_b$ at $t=0$ is given by

$$\mathcal{L}(t) \sim \left|\left\langle \phi_{\mathrm{BCC}}(t=0)\right\rangle\right| = c_N\left(\frac{t}{t_b}\right)^{-\gamma} \tag{3.2}$$

For cases where boundary field is varied periodically with time period T, $\mathcal{L}$ after the N cycles of drive times is equivalent to calculating the expectation of $2N$ point function made up of BCC operators

$$\mathcal{L}(NT) \sim \left|\left\langle \prod_{n=0}^{2N-1} \phi_{\mathrm{BCC}}(nT/2)\right\rangle\right|^2 = c_N\left(\frac{T}{t_b}\right)^{-\gamma N} \tag{3.3}$$

Universal exponent γ depends on the scaling dimenson h_{+-} of ϕ_{BCC}. For step drive with boundary field changing between $\pm h_b$ and $\mp h_b$, exponent $\gamma = 4h_{+-}$. This was verified for both non-integrable ($\Gamma \neq 0$)and integrable case ($\Gamma = 0$).

Exponent γ is dependent on the driving protocol. For driving protocols where $h_b(t)$ crosses the criticial point *i.e* $h_b = 0$ slowly rather than suddenly like in the step drive, Kibble-Zurek time scale comes into the picture leading to modification of the exponent γ discussed in next subsection.

Kibble Zurek Scaling

According to adiabatic theorem when for any arbitrary Hamiltonian, if its parameter f is varied slowly enough system prepared in ground state will remain in the ground state manifold. But this theorem fails when we are close to the critical point f_c. Closer to the critical point relaxation time τ varies as $|f|^{-z\nu}$ for $f_c = 0$ and it diverges as we get closer to the critical point. Here z is dynamcial critical exponent and ν is correlation length critical exponent. Kibble-Zurek time t_{KZ} is the characterisitic time scale below which system is not adiabatic for a process where Hamitonian is parameter is varied smoothly with time.

For a linear ramp across the critical point f_c as shown in Fig. 3.1 where $|f(t)| = \lambda t$, t_{KZ} can be estimated using

$$t_{\mathrm{KZ}} = \tau(f(t)) \tag{3.4}$$

Using $\tau(f(t)) = |f(t)|^{-z\nu}$ we get

$$t_{\mathrm{KZ}} = \lambda^{\frac{-z\nu}{1+z\nu}} \tag{3.5}$$

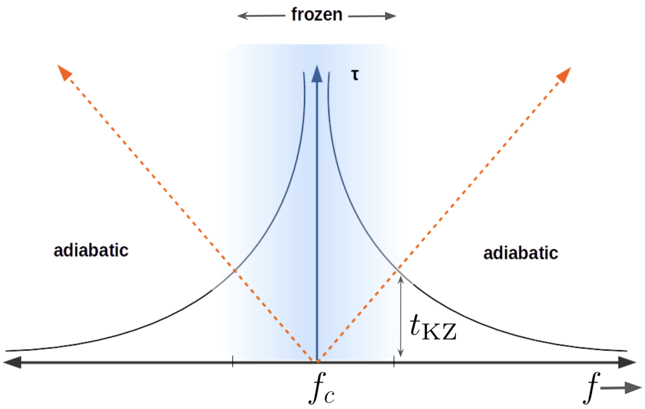

Fig. 3.1 Figure showing adibatic and frozen region resulting from divergence of relaxation time near the critical point f_c as Hamiltonian paramter f is varied. Kibble-Zurek time seperates the adiabatic and frozen region.

Kibble-Zurek mechanism expresses the non-equilibrium dynamics closer to the phase transition in terms of equilibrium critical exponents evident from Eq. 3.5. For a generic periodic drive with period T where the parameter varies as $f(t) = f\left|\frac{t}{T}\right|^{r}\text{sgn}(t)$ closer to the critical point $f_c = 0$, we have

$$t_{\rm KZ} \sim T^{\frac{rz\nu}{1+rz\nu}} f^{-\frac{z\nu}{1+rz\nu}} \tag{3.6}$$

For step drive we have $r = 0$ and for triangular or cosine drive $r = 1$. Drives where critical point is crossed smoothly the $t_{\rm KZ}$ is the relevant time scale and replaces t_b in Eq. 3.3 as we are in the frozen region. Replacing t_b by $t_{\rm KZ}$ gives

$$\mathcal{L}(NT) \sim c_N (Th_b)^{-\frac{\gamma N}{1+rz\nu}} \tag{3.7}$$

3.3 Model and description of scaling

In this section, we describe the Potts model and summarize the results that we borrow from boundary conformal field theory. The arguments, following Ref. [5] for the scaling behavior of the Loschmidt echo specialized to the scenarios considered in this paper are also presented. The $\mathbb{Z}_3$ Potts model is described by the Hamiltonian

$$H_0 = -f\sum_i \tau_i - J\sum_i \sigma_i\sigma_{i+1}^{\dagger} + h.c \tag{3.8}$$

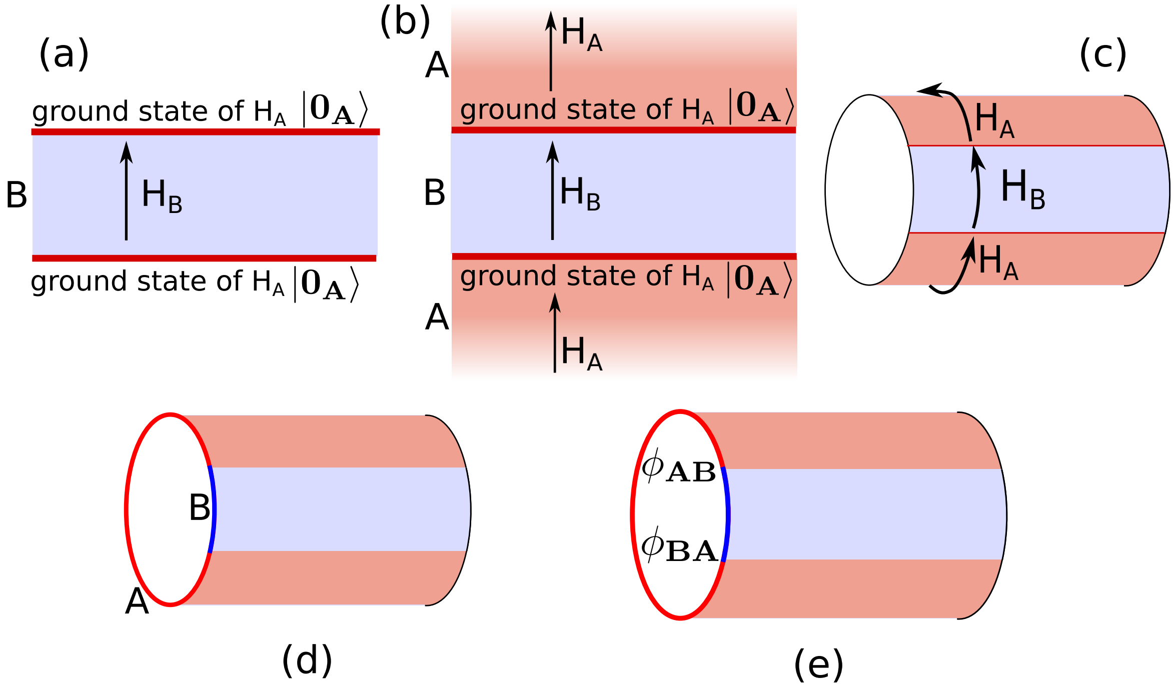
(a)
ground state of H_A |0_A⟩
B
H_B
ground state of H_A |0_A⟩
(b)
A
H_A
ground state of H_A |0_A⟩
B
H_B
ground state of H_A |0_A⟩
A
H_A
(c)
H_A
H_B
H_A
B
A
(d)
φ_AB
φ_BA
(e)

Fig. 3.2 (a) Overlap of the time evolved state $|\psi(t)\rangle = e^{-\imath H_B t}\,|0_A\rangle$ with the initial state $|0_A\rangle$ shown schematically. In complex time, this is the partition function on a strip with the fixed state $|0_A\rangle$ at the top and bottom ends of the strip. (b) Since $|0_A\rangle$ is the ground state of H_A, this can be interpreted as the state evolved after a long time from an arbitrary state under complex time evolution under H_A. (c) Identifying the arbitrary initial and final states maps the overlap to a partition function on a cylinder with Hamiltonians H_B and H_A in two regions. (d) Effect of the two Hamiltonians can be approximated as enforcing two boundary conditions in the corresponding regions. (e) The changing boundary conditions can be interpreted as insertion of suitable boundary condition changing operators. Figure reproduced with permission from Ref. [6].

σ and τ are $\mathbb{Z}_3$ generalizations of the Pauli matrices σ^z and σ^x given by

$$\sigma = \begin{pmatrix} 1 & 0 & 0 \\ 0 & \omega & 0 \\ 0 & 0 & \omega^2 \end{pmatrix}, \tau = \begin{pmatrix} 0 & 1 & 0 \\ 0 & 0 & 1 \\ 1 & 0 & 0 \end{pmatrix} \tag{3.9}$$

where ω is $\exp(\frac{2\pi}{3}\imath)$. σ and τ satisfies the algebra $\sigma^3 = \tau^3 = 1$ and $\tau\sigma = \omega\sigma\tau$ at each site, generalizing the algebra of Pauli matrices. The Hamiltonian Eq 3.8 is $\mathbb{Z}_3$ symmetric as it commutes with the generalized parity operator $P = \prod_{i=1}^{N} \tau_i$. There is a continuous phase transition at $f = J$ from a three fold symmetry broken ordered phase ($f < J$) to a paramagnetic phase $f > J$. The transition point is a conformal critical point, with the operators in the model related to the $\mathcal{M}(6,5)$ minimal model and a non-diagonal modular invariant as the partition function.[110, 111]

In this work, we study the Potts model with a boundary field. The Hamiltonian of the chain is time-dependent due to the boundary field and has the following form:

$$H = -h(t)m + H_0 \text{ where } m = \frac{\sigma_0 + \sigma_0^\dagger}{2} \tag{3.10}$$

For a positive $h(t)$, the ground state of the system has the boundary spin pointing in the $\langle\sigma_0\rangle \sim 1$ state (fixed boundary condition) and for negative $h(t)$, the boundary spin in the ground state is in a mixed state of $\langle\sigma_0\rangle = \omega$ and $\langle\sigma_0\rangle = \omega^2$ (mixed boundary condition). Two other fixed and mixed boundary conditions are obtained if the boundary term is replaced with $h\sigma_0 + h.c.$ and $\arg(h)$ is $\pm 2\pi/3$ and $\pi \pm 2\pi/3$ respectively. The fixed boundary conditions are RG fixed points in the parameter plane of the complex boundary field. Mixed boundary conditions under perturbation of h flow into nearby fixed boundary condition points.[112]

We consider a scenario where a time-periodic boundary field $h(t)$ toggles between positive and negative values. Initially, the chain is assumed to be in the ground state of the initial Hamiltonian. We will study the fate of the Loschmidt echo defined as the overlap of the time evolved state with the initial state $\mathcal{L} = |\langle\psi(0)|\psi(t)\rangle|^2$.

Consider the scenario where the boundary field is quenched from $+h_b$ to $-h_b$ ($h_b > 0$). The Loschmidt echo after this quench is given by $\mathcal{L}(t) = |\langle 0_A| \exp(-\imath t H_B)|0_A\rangle|^2$ where $|0_A\rangle$ is the ground state of the initial Hamiltonian $H_A = H_0 - h_b m$, and H_B is $H_0 + h_b m$. In order to map the problem to a 2D classical system, we can analytically continue to the complex time. The initial state upto proportionality constants can be identified with $\lim_{s\to\infty} \exp(-H_A s)|\alpha\rangle$ where α is a generic state with non-zero overlap with the ground state (schematically shown in Fig 3.2). Summing over all such states α maps the Loschmidt echo to

$$\mathcal{L}(-\imath\tau) \sim \lim_{s\to\infty} \mathrm{Tr}\left[e^{-sH_A}e^{-\tau H_B}e^{-sH_A}\right] \tag{3.11}$$

This can be identified with the partition function of a 2D classical system with periodic boundary conditions (Fig 3.2 c) and with a boundary field $-h_b$ along a tiny duration/distance along the imaginary time of τ, and $+h_b$ otherwise. Following the idea introduced in Ref. [5] we can approximate the effect of the boundary field to be to pin the boundary condition. Accordingly, the partition function can be replaced with that of a system with fixed boundary condition (labelled A in Fig 3.2d) whenever $h > 0$ and mixed boundary condition whenever $h < 0$ (labelled B in Fig 3.2d). A key result from boundary conformal field theory is that such a change in boundary condition can be interpreted as insertion (Fig 3.2e) of certain boundary condition changing operators.[113, 102, 110] The partition function in Fig 3.2d is interpreted as the correlation function of these operators separated by a distance τ. The dominant scaling dimension h_{BCC} of the operator that changes the boundary condition between the free and mixed boundary conditions can be inferred to be 2/5. The Loschmidt echo $\mathcal{L}(\imath\tau)$ scales in the same manner as the square of the correlation function at a distance along the boundary τ giving the result $\mathcal{L}(t) \sim |t|^{-4h_{\mathrm{BCC}}}$.

The above approximation is valid once the boundary spins have relaxed (over a time scale $h_b^{-\nu z}$ where $z = 1$ for the Potts model and ν is the boundary field correlation length exponent) in response to the boundary field quench. Treating this as the short time scale in the problem, the Loschmidt echo scales as $\mathcal{L}(t) \sim |th_b^{\nu}|^{-4h_{\mathrm{BCC}}}$. For the Potts model, it was argued in Ref-[114] that the spin-spin correlation function scales with distance as $1/r^{\eta_{||}}$ where $\eta_{||} = \frac{4}{3}$. Comparing this with $2d - 2/\nu$ (for $d = 1$ dimensional boundary), we infer the correlation length exponent along the boundary to be $\nu = 3$. Loschmidt echo under square-wave boundary field (amplitude h_b, period T) will now be an N point correlation function which scales with T as $\sim (Th^{\nu})^{-4Nh_{\mathrm{BCC}}}$. Note that the prefactors of the relation will have an N dependence in general which is not captured by these arguments, though this was absent in the Ising model.

For a periodic perturbation such as a sinusoidal or triangular wave that crosses $h = 0$ at a finite slope, unlike the square-wave, the short time scale is replaced by the Kibble Zurek time scale $\sim \lambda^{-\frac{z\nu}{1+z\nu}}$ ($z = 1$ for our system) where $\lambda \sim h_b/T$ is the rate at which the boundary field crosses the gapless system appearing at $h(t) = 0$. With this the Loschmidt echo scales with time as $\sim (Th_b^{\nu})^{-4N\frac{h_{\mathrm{BCC}}}{1+\nu}}$.

In summary, for the cases studied here, after a quench from $h = +h_b$ to $-h_b$ the Loschmidt echo should scale with time as $\mathcal{L}(t) \sim (th_b^3)^{-\gamma}$ where $\gamma = 8/5$. Loschmidt echo scales with the time period as $\mathcal{L}(t) \sim (Th_b^3)^{-\gamma N}$ where $\gamma = 8/5$ for square wave and $\gamma = 2/5$ for a triangular or sinusoidal wave.

3.4 Numerical methods

We use a matrix product representation of the states and Trotter decomposed time dependent unitary time evolution operators represented as matrix product operators to calculate the Loschmidt echo.[37] Ground state calculation was done using DMRG implementation in MPS language. The time evolution was performed in steps of $\Delta t = 10^{-3}$. The unitary time evolution was implemented as a sequence of two site gates using a time-dependent Suzuki-Trotter fourth order (per step) approximant [115] . The bond dimension of 300 was used for the calculations presented. Calculations were performed with bond-dimensions 150 and 100 in addition, to ensure that the Loschmidt echo curves (upto $t = 26/J$) have converged. In general the required bond dimensions were higher than 300 for simulations with $h_b < 0.2$ i.e. closer to the critical system, and therefore we have relied on data from $h_b \geq 0.4$. $J = h = 1$ was used for all the calculations presented. Chains of size $L = 180, 220, 260$ and 300 were studied and we have presented the data for the largest system size $L = 300$. Finite size effects sets in as the wavefronts from the change in boundary condition propogates into the chain. In order to avoid finite size effects, time evolution only for $N = 1$ could be reliably verified. In this work, we have restricted to the investigation of boundary fields that cause changes between fixed and mixed boundary conditions. Due to large bond dimensions, study of quenches into or from free boundary condition ($h = 0$) is unreliable. While the expected scaling dimenion $h_{\mathrm{BCC}} = 1/4$ was accurately obtained in those simulations, correlation length exponent ν which determines relaxation time scale showed significant system-size and bond-dimension dependence.

3.5 Fourth order approximant for time evolution

Calculation of the Loschmidt echo $\mathcal{L}(t)$ essentially breaks down to problem of estimating the matrix exponential of form $e^{(A+B)t}$. In Eq. 3.10 the time dependent Hamiltonian $H(t)$ we have time dependent boundary field $h(t)$ and the critical Hamiltonian H_0 which is time independent. We can see that $H(t)$ is of the form $A + B$. First we will discuss approximant for the matrix exponential of the case when the both matrices A and B are time independent as it will be needed for the time dependent case which is of relevance for our work.

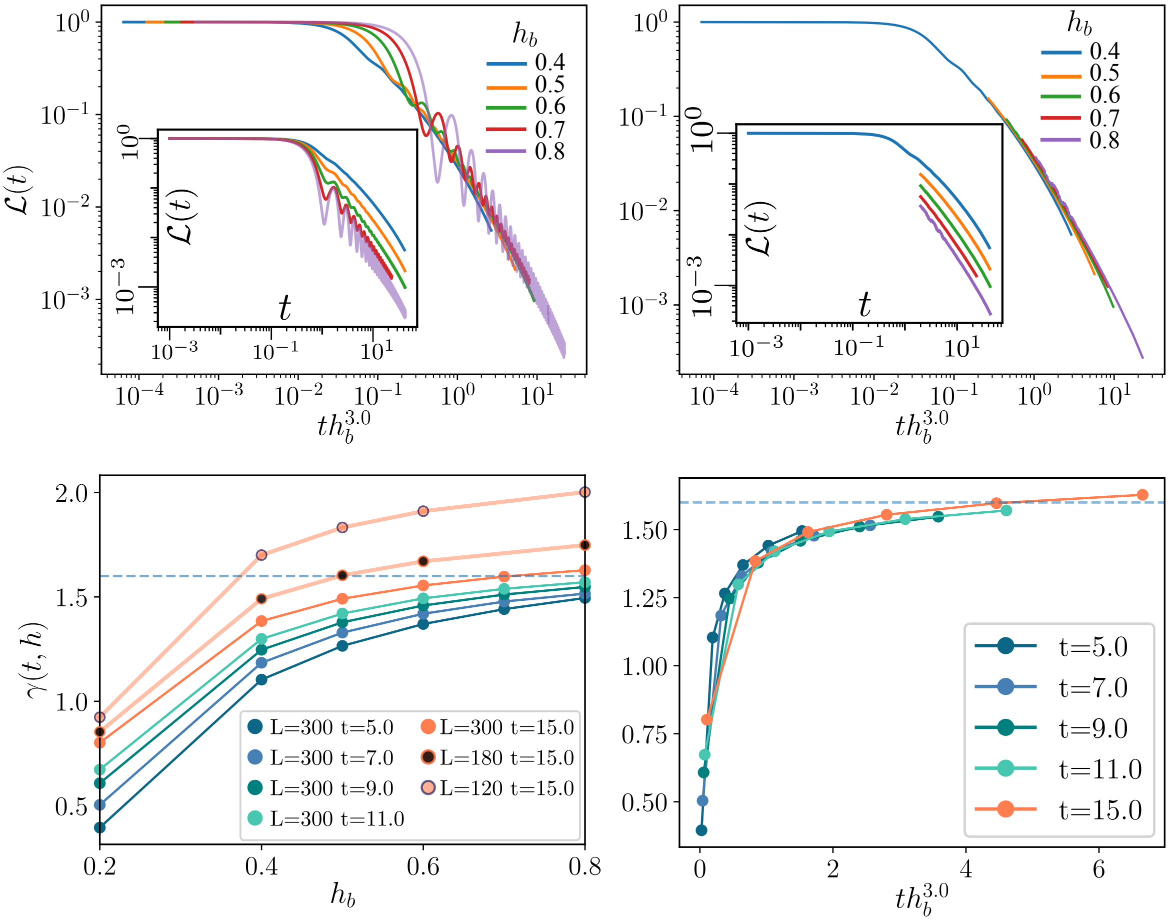

Fig. 3.3 (a) Loschmidt echo after a quench of the boundary field from h_b to $-h_b$ plotted as a function of the rescaled time $t/\tau = th_b^3$ for system size L=300. Inset shows the same data as a function of time. (b) Same as panel (a) but after filtering out the oscillatory components of the Loschmidt echo. (c) Exponent $\gamma(t, h_b)$ estimated near specific times t plotted as a function of h_b. $\gamma(t, h_b)$ is estimated from the slope of $\log \mathcal{L}(t)$ vs $\log t$ shown in panel (b). Comparison with data from $L = 120, 180$ indicate saturation to the expected exponent $8/5$ at large Th^3 in large systems. (d) Same as panel (c) but plotted as a function of rescaled time. Figure reproduced with permission from Ref. [6].

Using the Taylor expansion we can write $e^{(A+B)t}$ as

$$e^{(A+B)t} = 1 + (A+B)t + \frac{t^2}{2}(A^2 + AB + BA + B^2) + \mathcal{O}(t^3) \tag{3.12}$$

similarly we can get the expression for $e^{At}e^{Bt}$

$$e^{At}e^{Bt} = 1 + (A+B)t + \frac{t^2}{2}(A^2 + 2AB + B^2) + \mathcal{O}(t^3) \tag{3.13}$$

so from Eq. 3.13 it is clear that $e^{At}e^{Bt}$ is good first order approximant denoted by $S_1(t)$ (expression which is correct till first order in t) for $e^{(A+B)t}$ if $[A, B] \neq 0$ and it will also be the good second order approximant if $[A, B] = 0$. For $[A, B] \neq 0$, Equation 3.12 and 3.13 are related by

$$S_1(t) = e^{At}e^{Bt} = e^{(A+B)t+\mathcal{O}(t^2)} \tag{3.14}$$

Above decomposition is known as Suzuki-Trotter decomposition or exponential product formula. Our objective is to generalize the Eq. 3.14 to the following form which is correct till desirable order in t

$$S_m(t) = e^{Ap_1t}e^{Bp_2t}e^{Ap_3t}e^{Bp_4t}\dots e^{Bp_Mt} = e^{(A+B)t+\mathcal{O}(t^{m+1})} \tag{3.15}$$

To get the second order approximant we will use the following symmteric expression

$$S_2(t) = e^{\frac{t}{2}A}e^{tB}e^{\frac{t}{2}A} = e^{(A+B)t+t^3R_3+\dots} \tag{3.16}$$

This kind of symmetric approximants satisfies the following property that

$$S_2(t)S_2(-t) = \mathbb{I} \tag{3.17}$$

Due to property there will be no even order correction terms($e.g\ t^4R_4$) in eq 3.16. Using eq 3.16 we can construct the fourth order approximant in the following manner.

$$\begin{aligned}
S_4(t) &= S_2(s_2t)^2S_2((1-4s_2)t)S_2(s_2t)^2 \\
&= e^{\frac{s_2}{2}tA}e^{s_2tB}e^{s_2tA}e^{s_2tB}e^{\frac{1-3s_2}{2}tA}e^{(1-4s_2)tB}e^{\frac{1-3s_2}{2}tA}e^{s_2tB}e^{s_2tA}e^{s_2tB}e^{\frac{s_2}{2}tA} \\
&= \left[e^{s_2t(A+B)+s_2^3t^3R_3+\mathcal{O}(t^5)}\right]^2 e^{(1-4s_2)t(A+B)+(1-4s_2t)^3R_3+\mathcal{O}(t^5)}\left[e^{s_2t(A+B)+s_2^3t^3R_3+\mathcal{O}(t^5)}\right]^2 \\
&= e^{t(A+B)+[4s_2^3+(1-4s_2^3)]t^3R_3+\mathcal{O}(t^5)}
\end{aligned}$$

Since we want our expression to be correct till fourth order term $4s_2^3 + (1 - 4s_2^3)$ has to be zero. Otherwise it will contribute to t^3 terms. On solving $4s_2^3 + (1 - 4s_2^3) = 0$ we get the following solution

$$s_2 = \frac{1}{4 - \sqrt[3]{4}} = 0.414490771... \tag{3.18}$$

Whenever we have terms in the exponential which are time dependent we have to deal time ordered exponential

$$U(t_2; t_1) = T\left[\exp\left(-i\int_{t_1}^{t_2} H(s)ds\right)\right] \tag{3.19}$$

For the analysis we need the shift-time operator $\tau = i\frac{\overleftarrow{\partial}}{\partial t}$ which acts on the function on the left. It's action can be understood from the following equation

$$\begin{aligned} F(t)e^{-i\Delta t\mathcal{T}}G(t)e^{-i\Delta t\mathcal{T}}H(t) &= F(t+\Delta t)G(t)e^{-i\Delta t\mathcal{T}}H(t) \\ &= F(t+2\Delta t)G(t+\Delta t)H(t) \end{aligned}$$

We can express eq 3.19 in terms of $\mathcal{T}$ also which is finally going to be helpful for the trotter decomposition of $U(t+\Delta t; t)$

$$\begin{aligned} T\left[\exp\left(-i\int_{t}^{t+\Delta t} \mathcal{H}(s)ds\right)\right] &= \lim_{n\to\infty} e^{-i\frac{\Delta t}{n}\mathcal{H}(t+\Delta t)}e^{-i\frac{\Delta t}{n}\mathcal{H}(t+\frac{n-1}{n}\Delta t)}...e^{-i\frac{\Delta t}{n}\mathcal{H}(t+\frac{1}{n}\Delta t)} \\ &= \lim_{n\to\infty} e^{-i\frac{\Delta t}{n}\mathcal{H}(t)}e^{-i\frac{\Delta t}{n}\mathcal{T}}e^{-i\frac{\Delta t}{n}\mathcal{H}(t)}e^{-i\frac{\Delta t}{n}\mathcal{T}}...e^{-i\frac{\Delta t}{n}\mathcal{H}(t)}e^{-i\frac{\Delta t}{n}\mathcal{T}} \\ &= \lim_{n\to\infty}\left(e^{-i\frac{\Delta t}{n}\mathcal{H}(t)}e^{-i\frac{\Delta t}{n}\mathcal{T}}\right)^n \\ &= e^{-i\Delta t(\mathcal{H}(t)+\mathcal{T})} \end{aligned}$$

So we have the final expression

$$U(t+\Delta t; t) = e^{-i\Delta t(A(t)+B(t)+\mathcal{T})} \tag{3.20}$$

First order approximant denoted by $G_1(t+\Delta t; t)$for the RHS of the eq 3.20 is given by

$$\begin{aligned} G_1(t+\Delta t; t) &= e^{-\iota\Delta t A(t)}e^{-\iota\Delta t B(t)}e^{-\iota\Delta t\mathcal{T}} \\ &= e^{-\iota\Delta t A(t+\Delta t)}e^{-\iota\Delta t B(t+\Delta t)} \end{aligned} \tag{3.21}$$

Time dependent version for the second order approximant which is generalization of Eq. 3.16 is given by

$$\begin{aligned} G_2(t+\Delta t;t) &= e^{-\frac{\iota}{2}\Delta t\mathcal{T}} e^{-\frac{\iota}{2}\Delta t A(t)} e^{-\iota\Delta t B(t)} e^{-\frac{\iota}{2}\Delta t A(t)} e^{-\frac{\iota}{2}\Delta t\mathcal{T}} \\ &= e^{-\frac{\iota}{2}\Delta t A(t+\frac{\Delta t}{2})} e^{-\iota\Delta t B(t+\frac{\Delta t}{2})} e^{-\frac{\iota}{2}\Delta t A(t+\frac{\Delta t}{2})} \end{aligned} \tag{3.22}$$

Fourth order approximant can be constructed by the symmetrized arrangement of approximants G_2

$$\begin{aligned} G_4(t+\Delta t;t) &= (G_2(t+s_2\Delta t))^2 G_2(t+(1-4s_2)\Delta t)(G_2(t+s_2\Delta t))^2 \\ &= e^{-\frac{\iota s_2}{2}\Delta t A(t+\frac{(2-s_2)\Delta t}{2})} e^{-\iota s_2\Delta t B(t+\frac{(2-s_2)\Delta t}{2})} e^{-\frac{\iota s_2}{2}\Delta t A(t+\frac{(2-s_2)\Delta t}{2})} \\ &\times e^{-\frac{\iota s_2}{2}\Delta t A(t+\frac{(2-3s_2)\Delta t}{2})} e^{-\iota s_2\Delta t B(t+\frac{(2-3s_2)\Delta t}{2})} e^{-\frac{\iota s_2}{2}\Delta t A(t+\frac{(2-3s_2)\Delta t}{2})} \\ &\times e^{-\frac{\iota(1-4s_2)}{2}\Delta t A(t+\frac{\Delta t}{2})} e^{-\iota(1-4s_2)\Delta t B(t+\frac{\Delta t}{2})} e^{-\frac{\iota(1-4s_2)}{2}\Delta t A(t+\frac{\Delta t}{2})} \\ &\times e^{-\frac{\iota s_2}{2}\Delta t A(t+\frac{3s_2\Delta t}{2})} e^{-\iota s_2\Delta t B(t+\frac{3s_2\Delta t}{2})} e^{-\frac{\iota s_2}{2}\Delta t A(t+\frac{3s_2\Delta t}{2})} \\ &\times e^{-\frac{\iota s_2}{2}\Delta t A(t+\frac{s_2\Delta t}{2})} e^{-\iota s_2\Delta t B(t+\frac{s_2\Delta t}{2})} e^{-\frac{\iota s_2}{2}\Delta t A(t+\frac{s_2\Delta t}{2})} \end{aligned} \tag{3.23}$$

Above fourth order approximant was used for the time-evolution implementation.

3.6 Numerical results

In this section we present the numerical results for dynamics of Loschmidt echo under boundary perturbations. Figure 3.3 summarizes the results for Loschmidt echo as a function of time t after a quench from $H_+ = H_0 - h_b m$ to $H_- = H_0 + h_b m$, with the system starting from the ground state of the initial Hamiltonian. Results are presented for the largest system studied ($L = 300$). The Loschmidt echo (inset-a) approaches a power law scaling for t larger than the relaxation time scale $\tau = h_b^{-3}$, however for very large t, finite size effect sets in leading to deviation from power-law scaling behavior. For the small $h_b \leq 0.4$, the relaxation time is large and comparable to the time scale for onset of finite size effects, as a result a scaling region is not evident in this case. A power-law regime emerges for larger boundary fields where τ is smaller i.e. when h_b increases. However, as the boundary field approaches the local energy scale of $J = 1$, the power-law gets masked by an oscillatory component. Empirically we find that these oscillations decay with time and have a constant frequency. Figure 3.3(b-inset) shows the same data after filtering out a oscillatory component, and reveals a power-law scaling in the backdrop of the oscillations. The Loschmidt echo trace $\mathcal{L}(t)$ for different

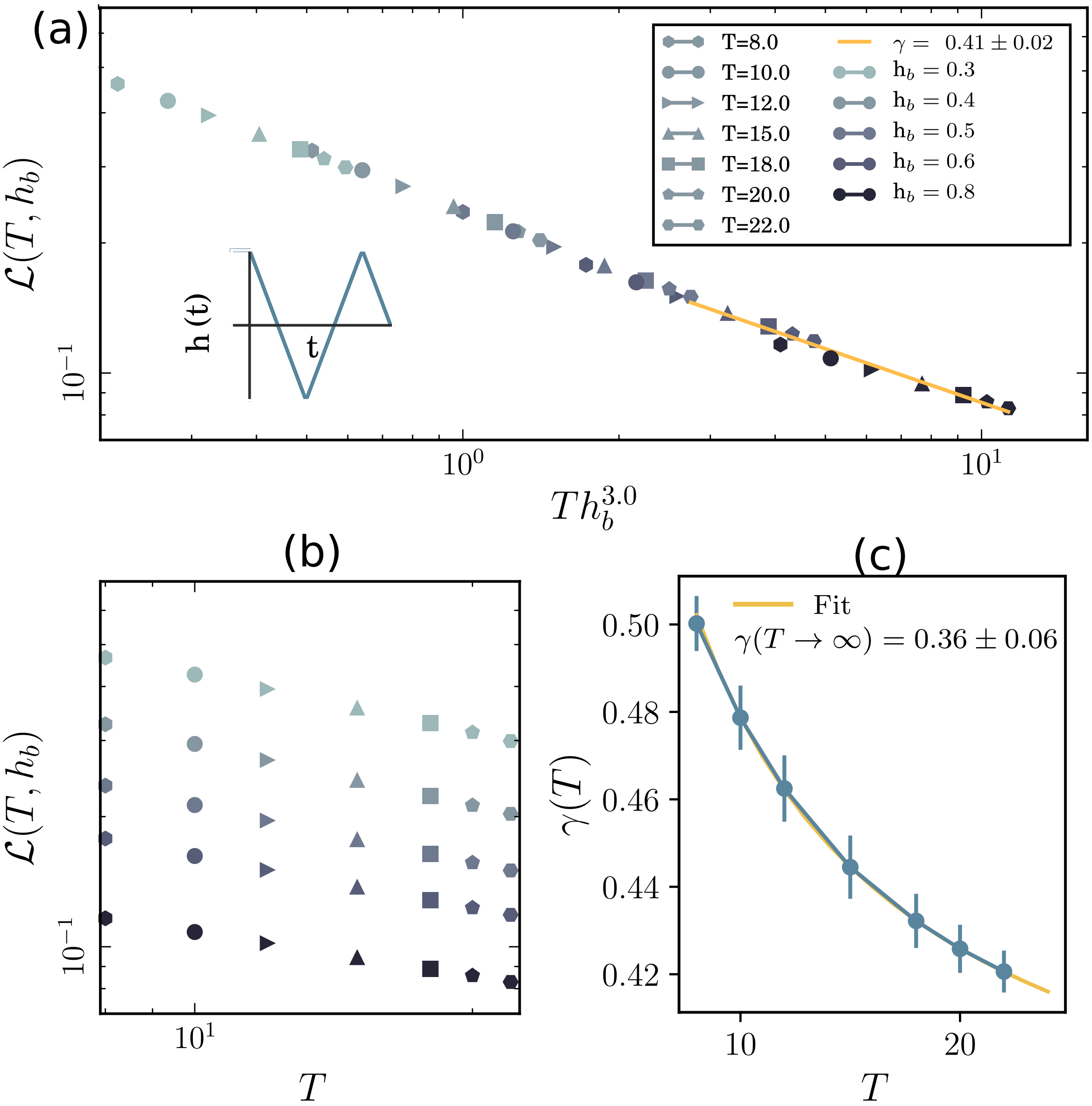

Fig. 3.4 (a) Loschmidt echo $\mathcal{L}(T)$ at the end of one drive cycle is plotted as a function of rescaled time period $T/\tau = Th_b^3$ for a triangular-wave boundary field for system size L=300 in the low frequency regime. (b) $\mathcal{L}(T)$ plotted as a function of the time period. (c) Scaling exponent $\gamma(T)$ estimated using data at fixed T by calculating the slope of $\ln \mathcal{L}$ vs $\ln Th_b^3$. Large T limit of γ is obtained by fitting the data to $\gamma(T) = \gamma(\infty) + \frac{axT^{-x}}{1+aT^{-x}}$. Figure reproduced with permission from Ref. [6].

h_b shows a scaling collapse when the time t is rescaled by the relaxation time scale (Fig 3.3(a)). Similar collapse is also seen in the Loschmidt echo after filtering out the oscillatory components.

Figure 3.3(c) shows the negative of the slope in the log-log plot of the filtered data as a function of h_b at different fixed times t. The slopes approach $\gamma = 8/5$ with increasing t as well as with increasing h_b (decreasing τ). Empirically, we find that the slopes approach the saturation values as a function of th_b^3 (Fig 3.3 (d)). For small systems, finite size effect sets in before the slope saturates. This can be seen from the slopes for $L = 120, 180, 300$ at $t = 15$ shown in Fig 3.3 (c). With increasing L, the time-scale when finite size effect sets in increases and saturation of the slope is evident.

Under a square-wave boundary perturbation oscillating between $H_\pm = H_0 + \mp h_b m$, when the initial state is the ground state of the initial Hamiltonian H_+, the Loschmidt echo after a single time period T namely $|\left\langle\psi(0)|e^{-\imath H_+ T/2}e^{-\imath H_- T/2}|\psi(0)\right\rangle|^2$ is the same as the Loschmidt echo after a time $T/2$ following a quench. Thus $\mathcal{L}(T, h_b) \sim (Th_b)^{-\gamma}$ where $\gamma = 8/5$.

Figure 3.4 summarizes the results for the Loschmidt-echo under a triangular wave like boundary perturbation after a single time-period. The initial state is the ground state of the Hamiltonian $H = H_0 - h_b m$. The Hamiltonian is linearly changed to $H = H_0 + h_b m$ and then linearly back to $H = H_0 - h_b m$ over a total time T. Figure 3.4(b) shows the Loschmidt echo for different values of T and h_b. The data at different values of T and h_b collapse when expressed as a function of Th_b^3 (Figure 3.4(a)). The slope estimated from the largest values of Th_b^3 was 0.41 ± 0.02. Exponent γ obtained by fitting the data to $\mathcal{L}(T, h_b) = A(Th_b^3)^{-\gamma}$ separately for each value of T is shown in Fig 3.4(c). $\gamma(T)$ approaches 0.4 as T increases. To get the estimate of the asymptotic value of the slope, we fitted the data to $\gamma(T) \approx \gamma(\infty) + cT^{-d}$ to get $\gamma(\infty) = 0.36 \pm 0.06$. These values are consistant with the expected value of $\gamma = \frac{4h_{\mathrm{BCC}}}{1+\nu} = \frac{2}{5}$.

Figure 3.5 shows the results for the Loschmidt-echo under a sinusoidal wave boundary perturbation after a single time-period T. The initial state is again the ground state of the Hamiltonian $H = H_0 - h_b m$. The Hamiltonian is changed to $H = H_0 - h_b m$ and then back to $H = H_0 + h_b m$ in a sinusoidal manner. The data at different values of T and h_b (Fig 3.5(b)) collapse when expressed as a function of Th_b^3 (Figure 3.5(a)). Slope estimated from the largest values of Th_b^3 was 0.46 ± 0.03. We believe the deviation is due to T not being large enough. Exponent γ obtained by fitting the data at each fixed T to $\mathcal{L}(T, h_b) = A(Th_b^3)^{-\gamma}$ again drifts towards 0.4 at large T. From fitting this data to $\gamma(T) \equiv -\frac{d\ln\mathcal{L}}{d\ln T} \approx \gamma(\infty) + cT^{-d}$, $\gamma(\infty)$ was found to be 0.39 ± 0.04, which is again consistant with the expected value of 2/5.

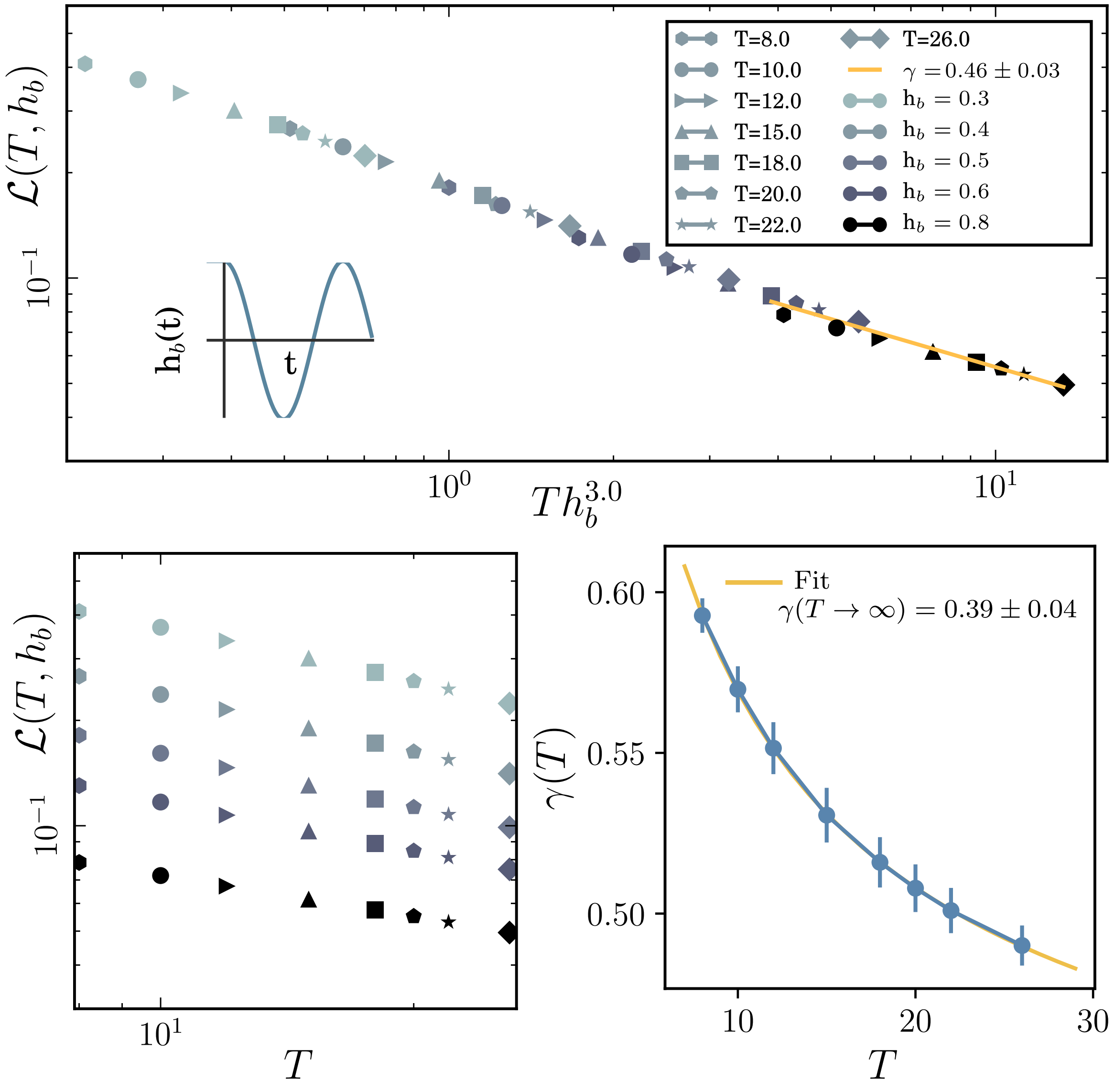

Fig. 3.5 Loschmidt echo for a sinusoidal wave perturbation for system size L=300 in the low frequency regime. Loschmidt echo at the end of one drive cycle (N=1) as a function of rescaled time period $T/\tau = Th_b^3$ is shown in panel (a). Panel (b) shows the same data as a function of T. Scaling exponent $\gamma(T)$ estimated from data at fixed time period T. Asymptotic value is estimated by fitting to $\gamma(\infty) + \frac{axT^{-x}}{1+aT^{-x}}$. Figure reproduced with permission from Ref. [6].

3.7 Conclusions

We have presented the results of dynamics of Loschmidt echo from numerical experiments on low frequency boundary fields on large, but finite, quantum critical $\mathbb{Z}_3$ Potts chains. The results obtained after single time period are in close agreement with what is expected from interpreting the fields as simply imposing a corresponding set of boundary conditions: Loschmidt echo scales with frequency as $(\omega h_b^{-\nu})^\gamma$ where γ is determined by (i) the boundary condition changing operators corresponding to the sequence of boundary condition changes imposed by the boundary field and (ii) the manner in which the boundary field crosses the $h = 0$ point. Unlike most results on Floquet systems that hold in the high-frequency regime derived from some variant of the Magnus expansion, the scaling results explored here hold in the lowest frequency regime. It will be useful to extend the result beyond Loschmidt echo and to physically measurable correlations of energy and magnetization.

Scaling of $\mathcal{L}$ in the model studied here was tractable due to the mapping to the classical 2D conformal critical system. The Potts model can be generalized to a broader class of chiral $\mathbb{Z}_3$ symmetric models[50, 116, 47] with $z \neq 1$, lacking a simple mapping to a 2D classical conformal critical point.[46, 117, 118, 52] It will be interesting to explore whether similar scaling properties apply to boundary field quenches within these models and if they do what dictates the scaling exponents? Our initial numerical experiments on boundary quenches in the chiral models indicated a steeper decay of the Loschmidt echo with time, therefore demanding a higher order of accuracy in the time evolution.

Chapter 4

Post quench entropy dynamics

We numerically study quenches from a fully ordered state to the ferromagnetic regime of the chiral $\mathbb{Z}_3$ clock model, where the physics can be understood in terms of sparse domain walls of six flavors. As in the previously studied models, the ballistic spread of entangled domain wall pairs generated by the quench lead to a linear growth of entropy with time, upto a time $\ell/2v_g$ in size-ℓ subsystems in the bulk where v_g is the maximal group velocity of domain walls. In small subsystems located in the bulk, the entropy continues to further grow, approaching $\ln 3$, as domain walls traverse the subsystem and increment the population of the two oppositely ordered states, restoring the $\mathbb{Z}_3$ symmetry. The latter growth in entropy is seen also in small subsystems near an open boundary in a non-chiral clock model. In contrast to this, in the case of the chiral model, the entropy of small subsystems near an open boundary saturates. We rationalize the difference in behavior in terms of qualitatively different scattering properties of domain walls at the open boundary in the chiral model. We also present empirical results for entropy growth, correlation spread, and energies of longitudinal-field-induced bound states of domain wall pairs in the chiral model.

4.1 Introduction

Quantum many-body dynamics in isolated systems has been an active area of contemporary research due in large part to realizations of tunable, almost isolated systems of long enough coherence times in cold atom experiments [27, 119–126] A key notion in this context is the entanglement between the subsystem and environment. Though not as easily measurable in experiments[127, 128] as local observables and correlation functions, entanglement in the eigenstates and its dynamics in general states give conceptual insights into broad questions of relaxation dynamics, dephasing, quantum measurements, thermalization, etc.[12, 13, 129–132]. Entanglement is also relevant to practical considerations in quantum engineering and in designs of algorithms for quantum many-body dynamics. [37]

A quench, in which an initial state with uncorrelated local observables undergoes a global change of the Hamiltonian, is a paradigmatic scenario that has been used to understand entanglement dynamics.[133] Under the new Hamiltonian, the initial state generically has a finite energy density above the ground state. The initial state, which in general is not an eigenstate of the new Hamiltonian, evolves with time. A large body of work on quenches in specific one dimensional systems has provided a semiclassical picture of the mechanism[134] for the entanglement growth during this time evolution.[135–145] Immediately after a quench, entangled quasiparticle pairs generated within short distances propagate away from each other. When these pairs are separated across the boundary between the subsystem and the environment, the subsystem effectively becomes entangled with its environment. The spreading of quasiparticles lead to decay of order parameters and induces correlations between initially uncorrelated local quantities in different parts of the system.[146–148] Thus the quasiparticle dynamics is closely connected to the growth of entanglement and correlations. The entanglement growth in a subsystem of length ℓ is encoded in the following expression[134]

$$S(t) \sim 2t \int_{v(k)<\frac{\ell}{2t}} dk v(k) f(k) + \ell \int_{v(k)>\frac{\ell}{2t}} dk f(k) \tag{4.1}$$

where $v(k)$ represents the velocity of the quasiparticle indexed by quantum number k, and $f(k)$ is a function that depends on the amount of such quasiparticles produced at the time of the quench. If the dominant contribution to the integrals comes from a narrow range of k(with a velocity v_m), the first term produces a linear-in-time growth in entanglement till a time $\ell/2v_m$. At large times the second term dominates, and as the slowest quasiparticles cross the subsystem boundary, this term saturates to a constant proportional to ℓ.

Studies on the 1D quantum transverse field Ising model (TFIM) and perturbations to this model have been crucial to guiding our intuition about post quench dynamics and relaxation in quantum chains.[147, 146, 148, 149]. Ref-[149] considered the non-equilibrium dynamics of a ferromagnetically ordered initial state, under a TFIM Hamiltonian with a longitudinal field perturbation aligned with the Ising order. Even a weak longitudinal field perturbation led to a strong suppression of the entanglement growth. The qualitative change in the entanglement dynamics could be attributed to the longitudinal field creating bound states of two different domain-wall-like quasiparticles of the Ising chain, preventing the original quasiparticles from spreading away from each other.

The TFIM is a $\mathbb{Z}_2$ symmetric member of a broad class of $\mathbb{Z}_n$ symmetric models with nearest neighbor interactions.[47] Simplest among these beyond the TFIM is the $\mathbb{Z}_3$ symmetric clock model. The $\mathbb{Z}_3$ model shares several features with the TFIM, such as a phase diagram with an ordered and paramagnetic phase and a continuous transition between them. The model can be transformed into a quadratic Hamiltonian of $\mathbb{Z}_3$ parafermions reminiscent of the quadratic Majorana Hamiltonian obtained following a Jordan Wigner transformation of the TFIM. The model generically has a chirality and has a richer set of domain wall flavors than the TFIM.

In this study, we numerically explore the dynamics after a weak quench in a $\mathbb{Z}_3$ symmetric chiral clock model with the goal of understanding the manner in which aspects of quench dynamics learned from TFIM extend to the $\mathbb{Z}_3$ chiral clock model, which has multiple domain wall flavors and chirality. Being non-integrable, we expect the clock model to thermalize [150, 14, 105]. However, we will not focus on questions of long-time behavior and thermalization and instead explore the effect of chirality on entanglement growth at short times that can be reliably studied using numerical tools. We will work with weak quenches of a fully ordered state to a final Hamiltonian that is in a ferromagnetic regime of the model, where the low energy quasiparticles are long-lived domain walls. We will also explore the effect of the longitudinal field perturbations motivated by observations made in Ref-[149]. This being a numerical study, we focus on attributes easily accessible in the computational basis. The generation of entangled quasiparticle pairs can be pictured in the expansions in computational basis as generation of finite amplitudes, after quench, for states with flipped spin domains of various sizes centered around all points of the system. Domain walls flank these flipped spin domains. Dispersion of these domain walls and their scattering properties at the boundary will be used to understand the dynamics of the subsystem entropy.

The clock model is parametrized by a parameter θ that determines the chirality of the model, with $\theta = 0$ representing the non-chiral model. After a quench, domain walls in the model, for any θ, are produced in opposite chirality pairs (such as $...AAABBB..$ and $...BBBAAA...$), therefore opposite chirality domain walls are equally abundant. As we show, the domain walls propagate with a velocity independent of θ or the chirality of the domain walls. As a result, we find that qualitative features of the entanglement growth in the bulk of the system are same for the non-chiral and the chiral model. Chirality however influences the scattering properties of domain walls at the open boundaries and hinders symmetry restoration in subsystems located close to the boundaries, preventing regions near the boundaries from thermalizing. The magnetization decays with time in the bulk of the system after a quench from the fully ordered state, indicating restoration of the $\mathbb{Z}_3$ symmetry in the final steady state. However, the magnetization at the boundary retains the initial value even in the steady-state. This can be related to a qualitatively different entanglement growth in small subsystems located in the bulk and at the boundary. Entanglement entropy of small subsystems in bulk continues to grow for times beyond the expected saturation time of $\ell/2v_g$ (v_g being the maximal group velocity of the domain walls), whereas at the boundary, the entanglement entropy saturates after a time scale ℓ/v_g. The robustness of magnetization near the boundary can also be interpreted in terms of long coherence times near the boundary in systems with strong zero modes.[151, 152] Our work gives a complementary microscopic perspective for the same physics.

We describe the $\mathbb{Z}_3$ chiral clock model in Sec. 4.3. For weak transverse fields, dynamics at low energies can be described in terms of far separated domain walls. Scattering properties of the domain walls at an open boundary are described in this limit. We will use this description to explain the contrasting behaviors of entropy growth in the small subsystems located near an open boundary of the system. Section 4.4 briefly describes the numerical time evolution calculations. Results of the numerical simulations in the non-chiral and the chiral models are presented following this in Sec. 4.5 and Sec. 4.6 respectively. We conclude with a summary of the results in Sec. 4.7.

4.2 Quench in TFIM

Effect of integrability on the thermalization was experimentally studied thorugh quantum Newton's cradle for quasi 1D bosonic gas clouds in Ref. [27]. It was shown that qunatum integrable systems can escape the fate of thermalization because of presence of extensive number of conserved charges in the system. Failure of thermalization for the integrable means that their steady state attained at long times can not be explained by the thermal density matrix instead it is satisfies another ensemble call Generalized Gibbs Ensemble (GGE) [17]. TFIM is one of the paradigmatic model to understand the features of quantum phase transition, dynamics, effect of integrability etc. because of its exact solvability.

Exact analytical results on the steady state properties after the generic quench were studied in [147, 148, 146]. For a generic quench it is analytically proved in Ref. [147] that steady state reduced density matrix at large times is described by appropriate

GGE. Using deteminant and form factor approach the steady state value of one and two point correlations for local and non-local spin operators (in equivalent fermionic representation) is calculated in [148]. Entanglement dynamics after the quench in TFIM is shown [135] to be perfectly in accordance with Calabrese-Cardy quasi-particle picture.

4.3 Model

This study explores the growth of entanglement after a fully ordered initial state (all spins in the same direction) undergoes a weak quench to a Hamiltonian with finite transverse field and small non-zero chirality (as described further below). Domain wall pairs are nucleated from every part of the chain after the quench. These domain walls propagate under the dynamics induced by the transverse field and lead to correlations between local properties of different parts of the chain. Introducing chirality in the model modifies the dynamics by creating a difference between energies of different domain wall flavors and modifies the scattering properties of domain walls at an open boundary. We aim to explore how chirality affects the entropy growth, correlation spread and magnetization.

Here we begin by describing the model. The $\mathbb{Z}_3$ chiral clock model in one dimension [50, 116, 109, 47] has the following Hamiltonian

$$H = -Je^{\imath\theta}\sum_i \sigma_i\sigma_{i+1}^{\dagger} - fe^{\imath\phi}\sum_i \tau_i + \text{h.c.} \tag{4.2}$$

where operators σ_i and τ_i located at the i^{th} site are

$$\sigma = \begin{pmatrix} 1 & 0 & 0 \\ 0 & \omega & 0 \\ 0 & 0 & \bar{\omega} \end{pmatrix} \quad \tau = \begin{pmatrix} 0 & 1 & 0 \\ 0 & 0 & 1 \\ 1 & 0 & 0 \end{pmatrix}. \tag{4.3}$$

Here $\omega = \exp(2\pi\imath/3)$ and $\bar{\omega} = \exp(-2\pi\imath/3)$. The algebra satisfied by the above operators: $\sigma_i^3 = \tau_i^3 = 1$ and $\sigma_i\tau_j = \delta_{ij}\bar{\omega}\tau_j\sigma_i$ presents a $\mathbb{Z}_3$ analogue of the algebra of Pauli matrices σ_z and σ_x; and the Hamiltonian forms a $\mathbb{Z}_3$ symmetric analogue of the $\mathbb{Z}_2$ symmetric spin-$\frac{1}{2}$ transverse field Ising model.[40] The Hamiltonian commutes with the $\mathbb{Z}_3$ generalization of the parity operator namely $P = \prod \tau_i$, which allows labeling of energy eigenstates with parity eigenvalues $1, \omega$, or $\bar{\omega}$. For simplicity we will work with systems with $\phi = 0$ and will use units where $\hbar = 1$. The chirality of the model is determined by θ and can be assumed to take values in the range $[0, 2\pi/3]$, as the physics at θ can be related to $\theta + 2\pi/3$ through a local unitary transformation by $\prod_i \tau_i^i$.

In the absence of a transverse field ($f = 0$), energy eigenstates are direct products of σ_i eigenstates at each site with energies $-2J\sum_i \cos(\theta + \alpha_{i,i+1})$ where $\alpha_{i,i+1} \in \{0, \pm 2\pi/3\}$ is $\arg(\langle\sigma_i\rangle/\langle\sigma_{i+1}\rangle)$. For θ in $[0, \pi/3]$, the ground state is described by $\alpha = 0$, corresponding to all spins pointing in the same direction (1, ω or $\bar{\omega}$). The simplest excitations are localized domain walls. In the non-chiral model the opposite chirality domain walls (...$AABB$... and ...$BBAA$...) as well as domain walls at different locations are degenerate. The ground state is ferromagnetic in the entire range $[0, \pi/3]$ but finite θ causes an energy difference $2J\sqrt{3}\sin\theta$ between domain walls of opposite chirality. The ground states in the regime $\theta > \pi/3$ have a twisted ordering with adjacent spins $\langle\sigma_i\rangle$ differing by a factor of ω. These domain walls disperse if the transverse field is non-zero, lifting the degeneracy of different domain wall states.

We will consider quenches to Hamiltonians with finite f, and a non-zero $\theta \in (0, \pi/6]$, *i.e.* in the regime where the classical ground state is still ferromagnetic but θ influences the dynamics by inducing a chirality to the domain walls. We find that quenches to larger θ result in more complex domain wall dynamics due to the possibility of a domain wall splitting into two as discussed later in this section.

The non-chiral model ($\theta = 0$) is ferromagnetic for $f < J$ and exhibits a continuous phase transition to a paramagnetic phase ($f > J$).[47, 49] The ground state in the ferromagnetic phase is three-fold degenerate (forming a parity multiplet) - with a splitting that decays exponentially with system size; but the excited states (for $f \neq 0$) have parity multiplets that show a power law decay of the splitting with system size.[47, 4] The chiral model with finite θ also shows a transition from a $\mathbb{Z}_3$ symmetry broken phase to the paramagnetic phase at some $f_c \lesssim J$.[3, 46, 52] Unlike the non-chiral case, the excited states in the broken $\mathbb{Z}_3$ symmetry phase have multiplets with a splitting that exponentially decays with system size. For weak transverse fields ($2f < J\sqrt{3}\sin\theta$), this degeneracy can be attributed to a weak zero-energy parafermion mode localized at the boundary in the Jordan Wigner transformed dual model.[47]

The power law decay with system size of the splitting in the non-chiral model can be understood as arising from the scattering properties at the boundary.[4] We present a simplified form of this model here and will use this as a basis to rationalize the entropy growth in subsystems near the boundary. In the limit of low energy densities, the states in the model can be understood in terms of a dilute set of domain walls, and interaction between domain walls may be neglected. For the discussions below, we will assume that transitions to the zero-domain-wall and two-domain-wall states are suppressed by an energy gap.

Now we focus on the dynamics of a single domain wall in the vicinity of a boundary. We denote by $|AB, i\rangle$ a direct product state representing a domain wall on the bond i separating regions of $\langle\sigma\rangle = A$ to the left and $\langle\sigma\rangle = B$ to the right. There are six possible domain wall types, but an incoming domain wall, say of type 1ω (with $\langle\sigma\rangle = 1$ to the left of i all the way to $-\infty$) that approaches a boundary on the right, can be reflected only as a 1ω or $1\bar{\omega}$ domain wall types at the boundary. Transition to any of the other domain walls such as $\omega 1$ will require global changes in the spin states.

The Hamiltonian projected into the space of these states can be written as

$$PHP = H_{1\omega} + H_{1\bar{\omega}} + H_{\text{boundary}}. \tag{4.4}$$

Here the Hamiltonian for each flavor of the domain wall is given by

$$\begin{aligned} H_{1\omega} &= \mu_+ \sum_i |1\omega, i\rangle\langle 1\omega, i| - f \sum_i |1\omega, i\rangle\langle 1\omega, i+1| + \text{h.c.} \\ H_{1\bar{\omega}} &= \mu_- \sum_i |1\bar{\omega}, i\rangle\langle 1\bar{\omega}, i| - f \sum_i |1\bar{\omega}, i\rangle\langle 1\bar{\omega}, i+1| + \text{h.c.} \end{aligned}$$

where

$$\mu_\pm = 2J[\cos\theta - \cos(\theta \mp 2\pi/3)] \tag{4.5}$$

Away from the boundaries, and away from each other, the Hamiltonian imparts a dispersion of $\epsilon_k^\pm = \mu_\pm - 2f\cos(k)$ to the domain walls. The boundary scatters between the two relevant domain wall types:

$$H_{\text{boundary}} = -f|1\omega, L-1\rangle\langle 1\bar{\omega}, L-1| + \text{h.c.}$$

The Hamiltonian is a tridiagonal matrix shown in Fig. 4.1(a). Relabeling the basis states as $\|x = i\rangle = |1\omega, i\rangle$ and $\|x = 2L - i - 1\rangle = |1\bar{\omega}, i\rangle$, this represents the Hamiltonian of a particle with kinetic energy $-2f\cos(k)$ traveling across a potential jump $\Delta = |\mu_+ - \mu_-| = 2\sqrt{3}J\sin\theta$ at the position L. In the relabeled form, states propagating away on the right of L represent, physically, a $1\bar{\omega}$ domain wall reflecting back towards the left from the boundary. For $\theta = 0$, gap Δ is zero and the particle tunnels across with unit probability; *i.e.* there is a complete reflection of the 1ω to a $1\bar{\omega}$ domain wall.[153] For larger θ such that the bandwidth is smaller than the gap, *i.e.* $2\sqrt{3}J\sin\theta > 4f$ the domain wall bounces back without any change in its flavor.

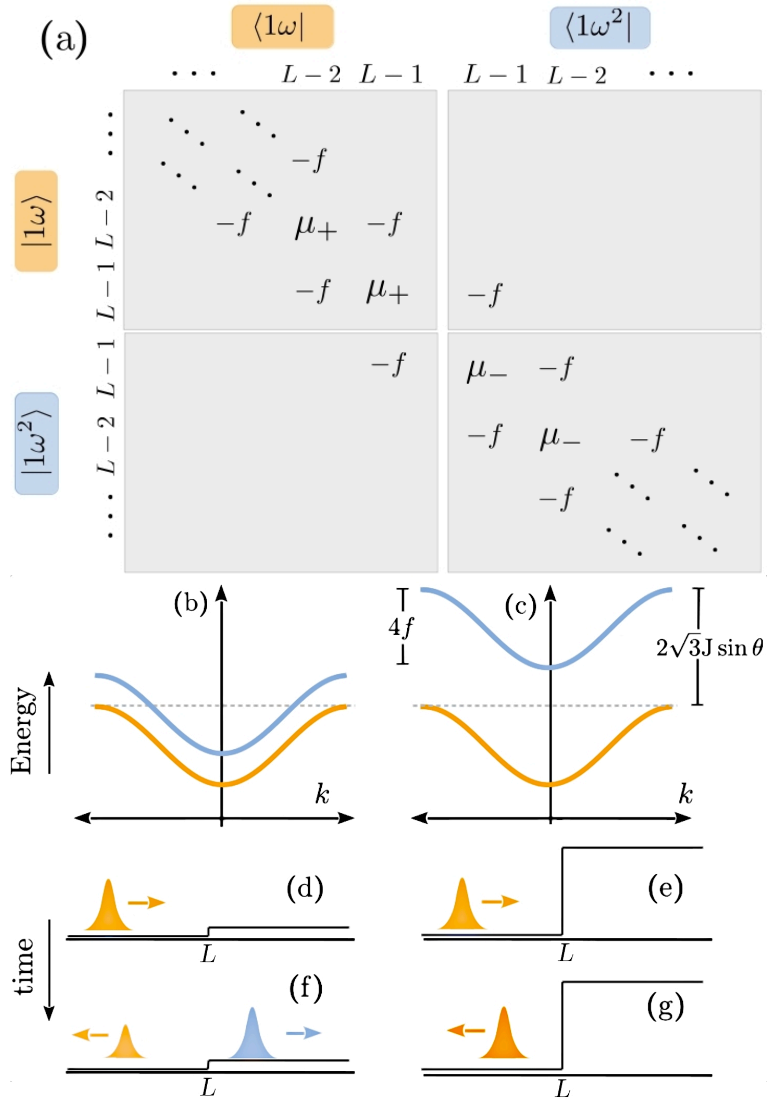

Fig. 4.1 Panel a shows the Hamiltonian matrix in the one-domain-wall space after relabeling $1\bar{\omega}$ domain wall at bond number $i < L$ as $x = 2L - i - 1$ and 1ω domain wall at bond number $i < L$ as $x = i$. Effective dispersions of opposite chirality (the two colors represent the bands for the two different chiralities) domain walls are shown schematically for the case of small θ(panel b) and large θ(panel c). Panels d and f schematically show the fate of a domain wall wave-packet that bounces off a boundary in a system with small θ. Panel d shows the incoming packet and panel f shows the fate after collision with the boundary. Incoming domain wall has one chirality (indicated in orange) whereas the reflected domain wall is primarily of opposite (blue) chirality. Panels e and g are similar but for a case where θ is larger. Here the domain wall bounces back without change in the flavor. Figure reproduced with permission from Ref. [7].

Boundary mediated tunneling from one domain wall flavor to another results in an increased energy splitting in excited states of the non-chiral model.[4] The nature of the zero mode and the analysis of the energy splitting are not directly related to the present work, but we will use the above effective model to make sense of the numerical results.

As θ approaches $\pi/6$, Eqn. 4.5 suggests that $\mu_+ \sim \mu_-/2$; so the energy of a domain wall of the form $1\bar{\omega}$ is same as that of a pair of domain walls of opposite chirality 1ω and $\omega\bar{\omega}$. Thus the $1\bar{\omega}$ can evolve into a domain wall pair of the form $1\omega\bar{\omega}$. We restrict to a discussion of the regime where the domain wall is stable. In the rest of this manuscript, we describe the results from numerical simulations of the quenches in the limit of small f, $\theta < \pi/6$, and $\phi = 0$ regime of the clock model.

4.4 Numerical simulation of the time evolution

States and operators are represented as matrix product states and matrix product operators [37] respectively, with a maximum bond dimension of 300. Time evolution of the states were implemented by using fourth order Suzuki-Trotter approximant [115] to represent $\exp(-\imath H\delta t)$ with time steps $\delta t = 10^{-3}$. This approximant decomposes the unitary operator as a sequence of two site gates acting on adjacent sites. Further details of the numerical implementation for the approximant is similar to that used in Ref [6] and has been summarized in the Appendix. We use J=1 in all numerical calculations.

4.5 Numerical results: Quench into the non-chiral model

In this section, we describe the dynamics after an initial state ψ_0, in which all sites are in the $\langle\sigma\rangle = 1$ direction, is quenched to the non-chiral Hamiltonian at finite transverse field. After the quench, the system evolves into a linear combination of the initial state and (with small amplitudes) domain wall pair states of the form $1\omega 1$ and $1\bar{\omega}1$. The flipped spin domains are nucleated from every part of the chain, and domain walls on the opposite sides of the flipped spin domain propagate in opposite directions with a characteristic velocity corresponding to the maximal group velocity $v_g = 2f$ (Sec. 4.3) of the domain walls; thereby expanding the flipped spin domains. This is schematically represented in Fig 4.2.

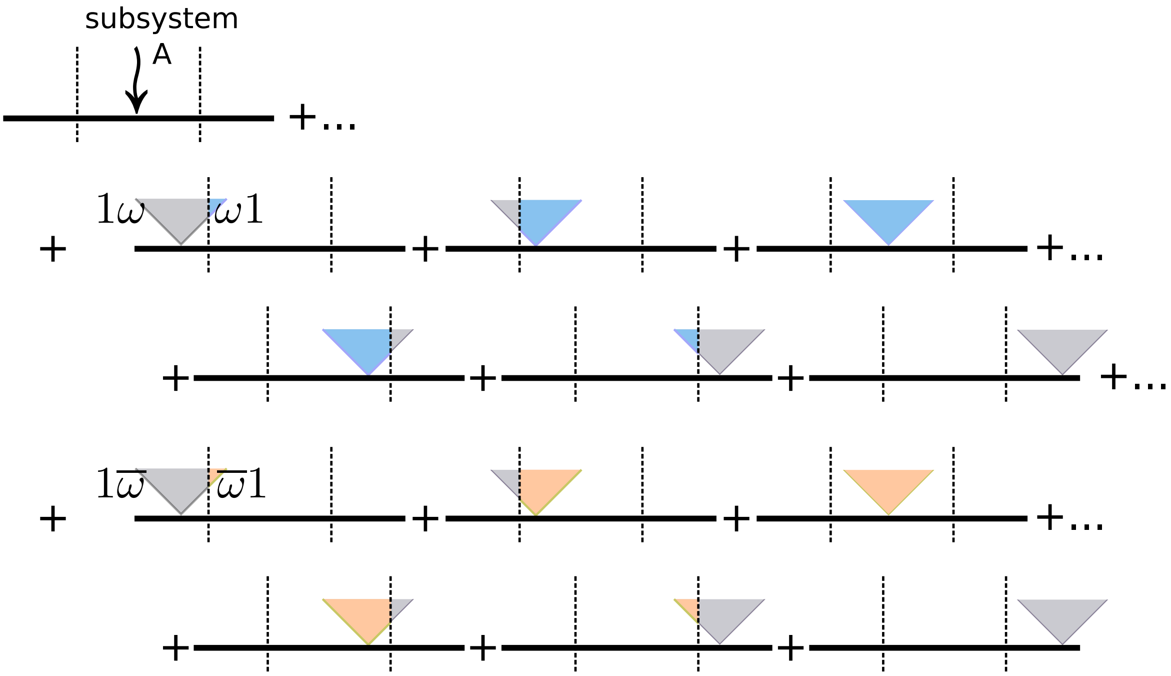

Fig. 4.2 Schematic representation of the state of the system after a weak quench. State after the quench is, to a good approximation, a linear combination of the ordered state and $1\omega 1$ and $1\bar{\omega}1$ type two domain wall states. The vertical direction represents the time evolution of domains in each term. Flipped spin domains are nucleated from all parts of the chain forming different terms of the linear combination in the computational basis. The domains expand as the domain walls propagate. In a system with non-linear dispersion, the domain walls of different momenta propagate at different group velocities. Dashed vertical lines demarcate a subsystem. For each cone, spins flipped to ω and $\bar{\omega}$ inside the subsystem are shown in blue and orange colors. The flipped spins outside the system are colored gray irrespective of direction of the spins inside them. Figure reproduced with permission from Ref. [7].

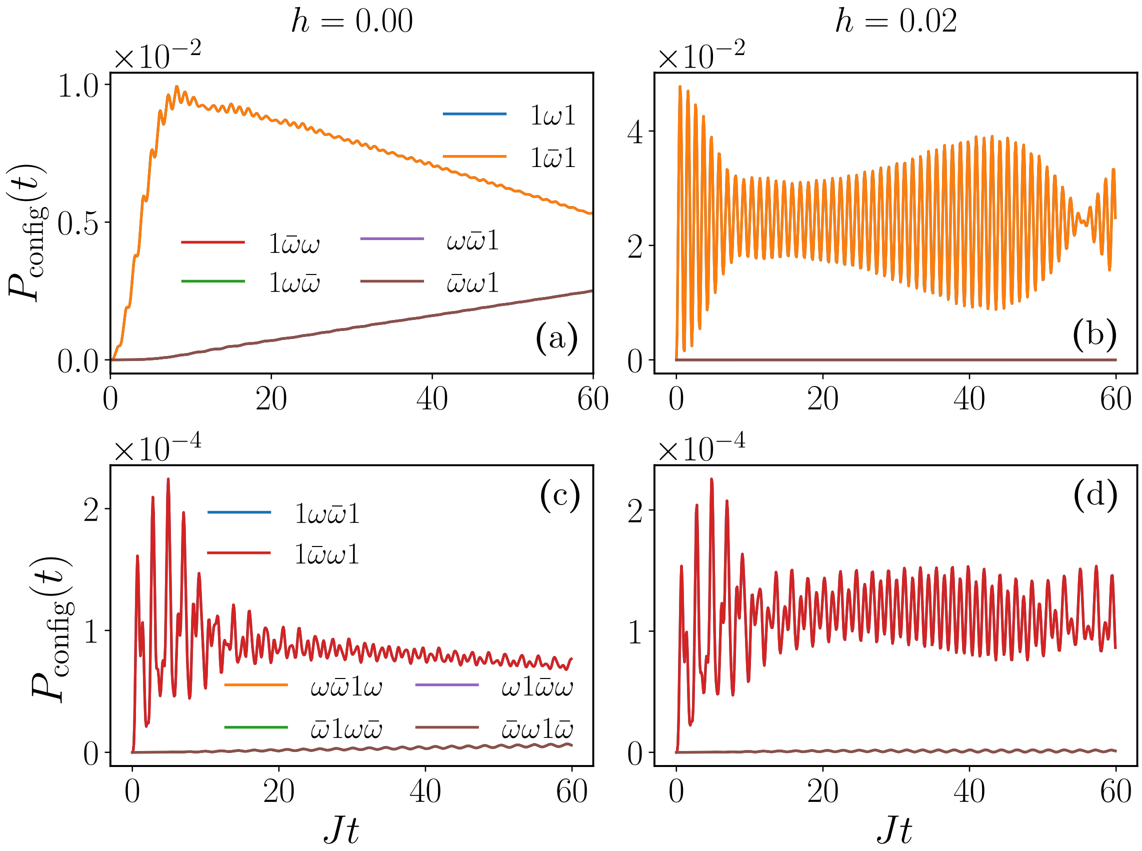

Fig. 4.3 Panel a shows the total probability of domain wall pair states that occur with non-zero probabilities after the quench from a fully ordered state to a final Hamiltonian with $f = 0.1$ and $\theta = 0$. System size is $L = 40$. Panel b shows the probabilities but in a system with an additional longitudinal field $h = 0.02$ in the final Hamiltonian. In Panel a and b, domain wall types $1\omega 1$ and $1\bar{\omega}1$ have equal probabilities and the corresponding lines (orange and blue) completely overlay over one another. Similarly, lines corresponding to domain wall configurations $1\omega\bar{\omega}$, $\bar{\omega}\omega 1$, $1\bar{\omega}\omega$ and $\omega\bar{\omega}1$ also overlay over each other. Panels (c,d) show the corresponding results for the three domain wall states of the form $ABCA$. Figure reproduced with permission from Ref. [7].

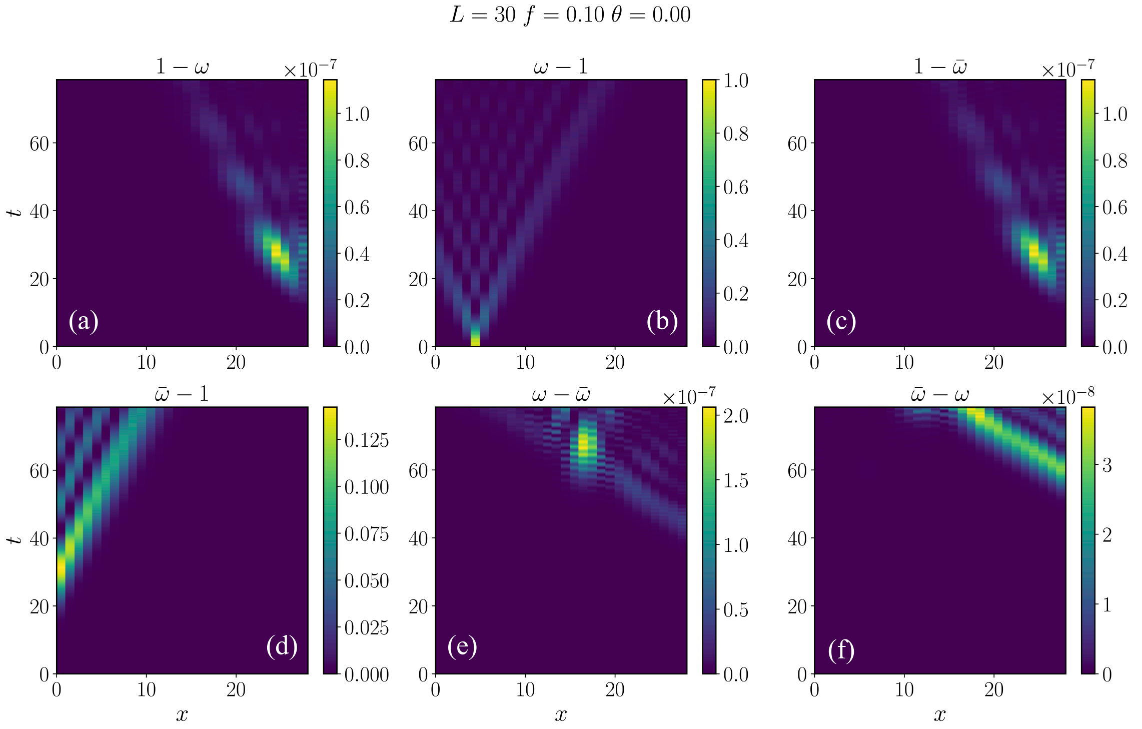

Fig. 4.4 Scattering dynamics of a domain wall of flavor $\ldots\omega\omega11\ldots$ localized at bond $x = 5$ is shown here for quench Hamiltonian parameters $f = 0.1$ and $\theta = 0.0$. From panel (a) to (f) in alphabetical order, probability of single domain wall flavors $1-\omega$, $\omega - 1$, $1-\bar{\omega}$, $\bar{\omega}-1$, $\omega-\bar{\omega}$ and $\bar{\omega}-\omega$ localized at bond x at time t is plotted with t and x on y and x axis respectively. In the panel (b) and (d) we can see that domain wall of flavor $\ldots\omega\omega11\ldots$ changes its flavor to $\ldots\bar{\omega}\bar{\omega}11\ldots$ after scattering from the boundary for the nonchiral quench.

Figure 4.3a presents the total probability weight (over all positions) of two domain wall states of different types, showing that among these, the $1\omega1$ and $1\bar{\omega}1$ are equally populated. Small domains of size 1 (where domain walls are separated by a distance of 1 lattice unit) show rapid oscillations and have been omitted. As time progresses, the domain wall pair states of the form $1\omega1$ ($1\bar{\omega}1$) formed in the vicinity of the left-hand-side boundary reflect off the boundary as a $\bar{\omega}\omega1$ ($\omega\bar{\omega}1$) domain wall pair states (as described in Sec 4.3). On the right hand side boundary, the domain walls scatter from the $1\omega1$ ($1\bar{\omega}1$) state into $1\omega\bar{\omega}$ ($1\bar{\omega}\omega$) state. Since the domain walls reach the boundary with a characteristic rate v_g, there is a linear rate of decrease of the population of the $1\omega1$ and $1\bar{\omega}1$ states as shown in Fig 4.3a. Correspondingly the population of the states of the types $1\omega\bar{\omega}$, $1\bar{\omega}\omega$, and $\omega\bar{\omega}1$, $\bar{\omega}\omega1$ linearly increase with time.

In the presence of an additional longitudinal field in the final Hamiltonian,

$$H_{\text{longitudinal}} = -h(\sigma + \sigma^\dagger) \tag{4.6}$$

the energy of the flipped spin domains have an (positive) energy contribution that grows linearly with the domain size. The domain wall pairs now appear to attract with an energy linear in the distance between them [149]. With this constrained domain wall dynamics, scattering processes at the boundary are suppressed as indicated by a constant probability on an average of the $1\omega1$ and $1\bar{\omega}1$ states in Fig 4.3b. (as opposed to a linear decay in the absence of h).

4.5.1 Magnetization

Here we present the results regarding local magnetization in the bulk of the system. Magnetization $\langle M\rangle = \langle \sigma + \sigma^\dagger\rangle/2$ is 1 in the initial state. After a time t from the quench, domain walls that originate within a neighborhood of radius $\sim v_g t$ around a site i cross this site at time t thereby reducing the local population of the state 1 at the site and increasing population of ω or $\bar{\omega}$; and decreasing the local magnetization at i linearly with time as shown in Fig 4.5a.

The instantaneous magnetization can be expressed in the eigenbasis of the Hamiltonian as

$$\langle M\rangle = \langle\psi(t)|M|\psi(t)\rangle = \sum_{i,j} \bar{c}_i c_j e^{\imath t(E_i - E_j)} M_{ij}. \tag{4.7}$$

Here c_i are the coefficients in the expansion of the initial state in the eigenbasis of the Hamiltonian and M_{ij} is the matrix element of a local magnetization in the eigenbasis of the Hamiltonian. This indicates that the power spectrum of the time dependent

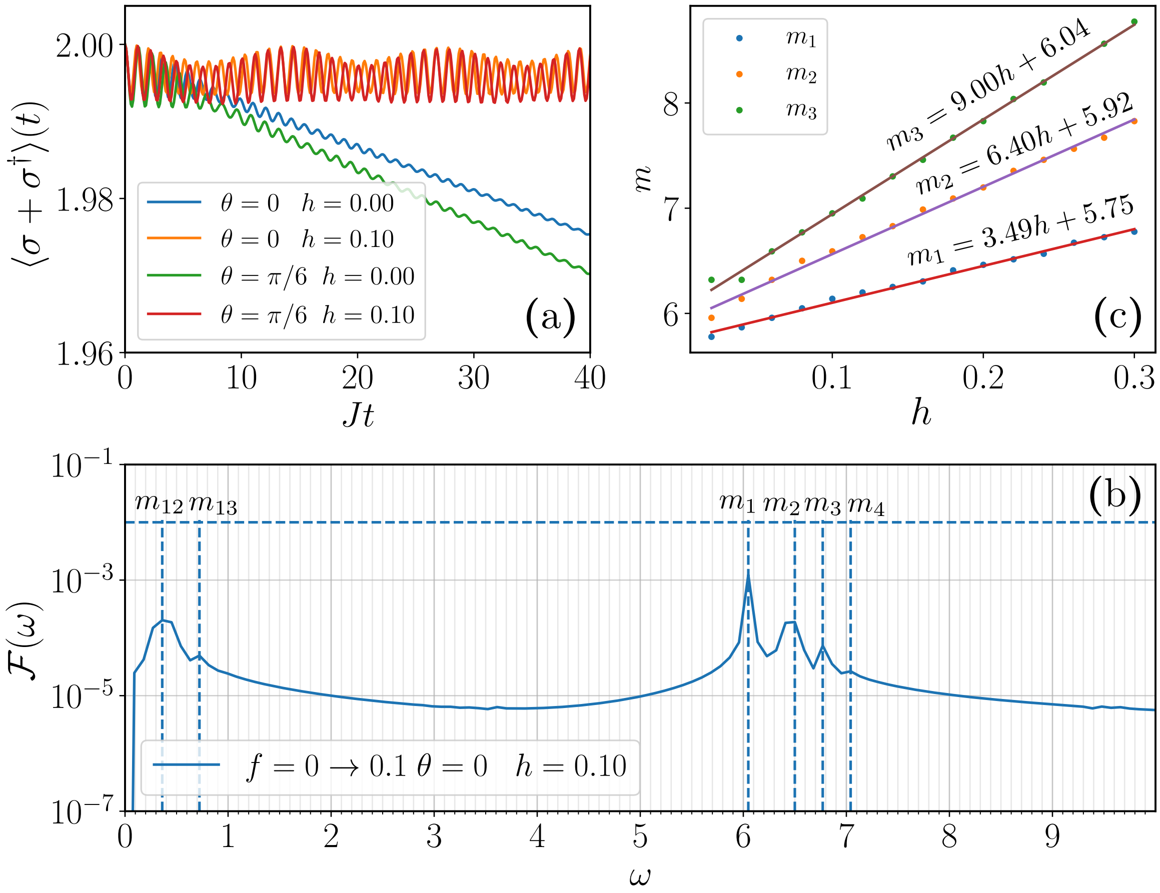

Fig. 4.5 Magnetization as a function of time for quenches to different final Hamiltonians is shown in panel a. Panel b shows the power spectrum of magnetization for a specific example where the final non-chiral Hamiltonian has $f = 0.1, h = 0.1$. The peaks correspond to the masses m_i of the domain wall bound states or the differences between the masses $m_{ij} = |m_i - m_j|$. Variation of first three masses with longitudinal field h is shown in panel c. System size used is $L = 40$. Figure reproduced with permission from Ref. [7].

oscillations of the magnetization carries the information of the gaps between finitely populated energy eigenstates. Peaks in this power spectrum occur at frequencies equal to the gaps between parts of the energy spectrum with a large energy-density-of-states (such as the bottom of the domain wall dispersion) or eigenstates with a large population (such as the ground state). Consistent with this, we find that the oscillatory part of the magnetization has a frequency peak equal to the gap between the ground state and the minimal kinetic energy of domain wall pairs:

$$m_2(\theta = 0) = \epsilon^{+}_{k=0} + \epsilon^{-}_{k=0} = 6J - 4f \tag{4.8}$$

In the presence of a longitudinal field, confinement of domain wall pairs prevents decrease in magnetization as shown in Fig 4.5a. The attractive interaction results in bound states of domain wall pairs. The energy minima of the dispersion of bound domain-wall-pairs (or equivalently the masses of bound domain wall pairs) can be extracted from the spectral peaks in the oscillatory part of the magnetization. The power spectrum of the magnetization oscillations at a finite longitudinal field is shown in Fig 4.5b. The peaks depend on h. A set of peaks split off from the one at $m_2(\theta = 0)$ as h is increased from 0 to finite values; these frequencies are labeled $m_1, m_2, m_3 \ldots$ and can be associated with the masses of different domain wall bound pairs. The frequencies of the peaks located at the lower end of the power spectrum match with the differences between these masses. Figure 4.5c shows the variation of the bound pair energies as a function of the longitudinal field h.

4.5.2 Two point correlations

We now consider the connected, equal time, correlations between local operators at spatially separated pair of points in the bulk. In particular we focus on $C(r,t) = \langle\psi(t)|\sigma_0\sigma_r^{\dagger}|\psi(t)\rangle_c$. We expect qualitative features of spread of correlations between other generic local operators to be the same; we focus on this as its imaginary component shows a non-zero (zero) value in a quench to the chiral (non-chiral) Hamiltonian.

The correlation C is zero everywhere in the initial state. The correlation C expanded in the computational basis shows that $C(r,t)$ is non zero if there are flipped spin domains that extend from 0 to r. The first among such domains appear when the domain wall pairs nucleated from $r/2$ at time 0 reach positions 0 and r at time $t = r/2v_g$. As a result the correlations $C(r,t)$ spread with a velocity $2v_g \sim 4f$. Correlation functions plotted in Fig 4.6a show the linearly expanding region with finite correlations. As expected from confinement of domain wall pairs, the presence of the longitudinal field

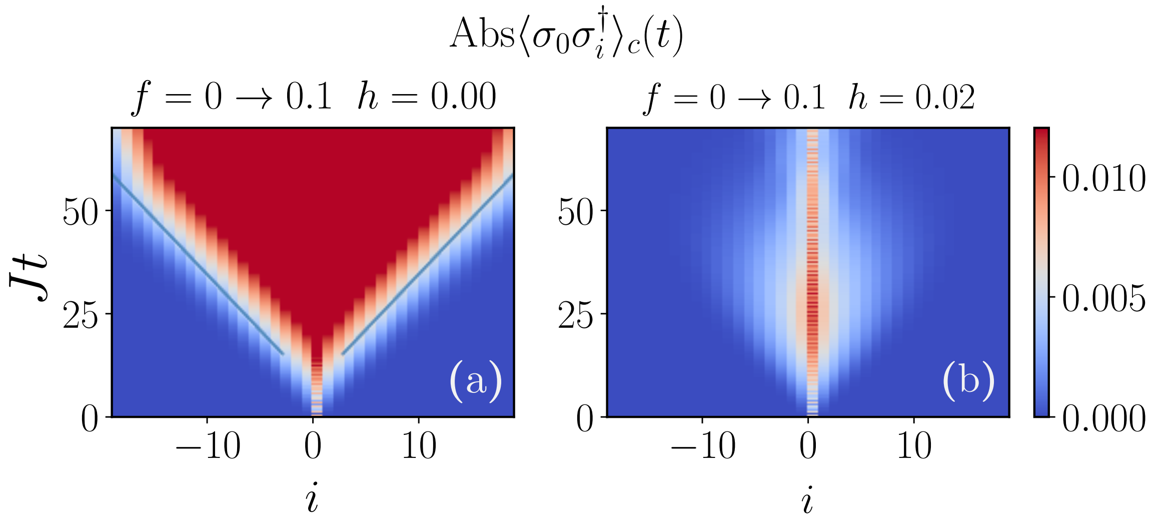

Fig. 4.6 Panel a shows the absolute value of the connected correlations as a function of position and time in the case of a quench to the non-chiral clock model. The lines show constant height contours and have a slope of 1.0/0.38 consistent with the expected correlation spread rate of $2v_g = 4f \sim 0.4$. Panel b shows same quantity in the case where the final Hamiltonian has an additional longitudinal field constraining the spread of domains. System size used is $L = 40$. Figure reproduced with permission from Ref. [7].

suppresses the spread of correlations (Fig 4.6b). In all cases we find that the imaginary part of the correlation is zero (this is guaranteed by translation symmetry of the initial state and final Hamiltonian in the bulk, and spatial parity symmetry).

4.5.3 Entanglement entropy

In this section, we present the numerical results for entanglement entropy growth in small subsystems after the system initially in the fully ordered state $|...1111...\rangle$ is quenched to a non-chiral Hamiltonian at finite f. The subsystems are initially unentangled. Shortly after the quench, the time evolved state is a linear combination of the fully ordered initial state and, with small amplitudes, states with flipped spin domains of typical size $\sim 2v_g t$ that were nucleated from every part of the chain at time $t = 0$ (Fig 4.2).

In order to evaluate the reduced density matrix of a contiguous segment A of size ℓ, the complementary region is traced out. Initially the subsystem is in a pure state with only the fully ordered state $|...111...\rangle_A$ populated. The entanglement entropy increases with time as progressively more flipped spin domains nucleated near the boundary of A (on either side of the boundary) cross the boundary. As time progresses more

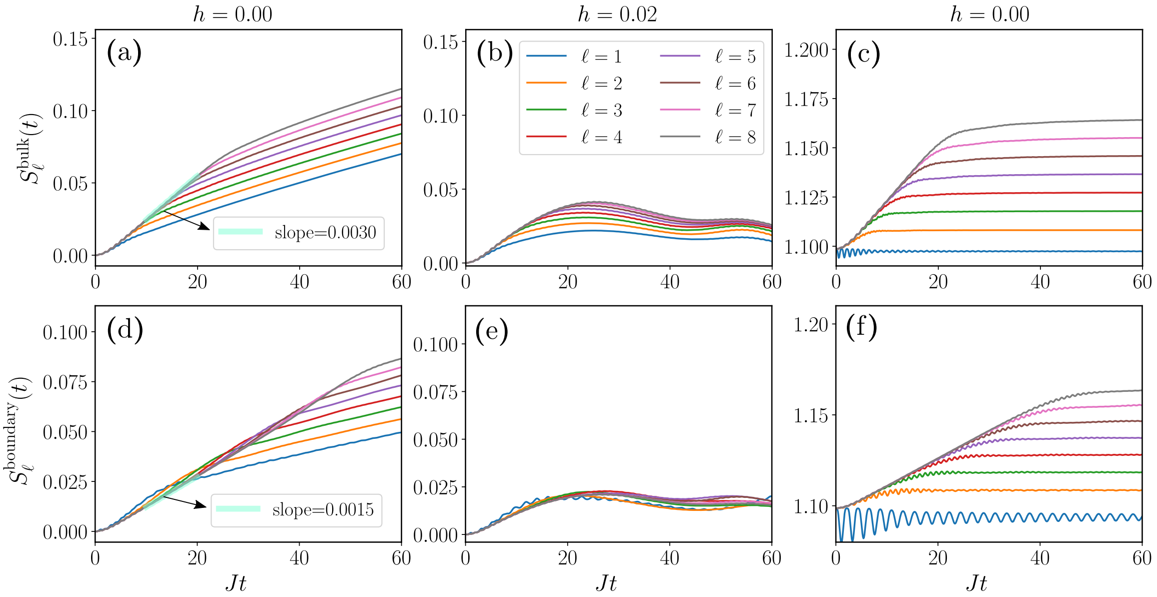

Fig. 4.7 Panel a shows entanglement growth in a subsystem in the bulk after a quench to the non-chiral Hamiltonian from a fully ordered initial state. The results for a subsystem at the boundary of the system is shown in panel d. Panels b and e show the corresponding results for the case of a quench to a Hamiltonian with an additional longitudinal field, demonstrating the suppression of entanglement growth. Panels c and f show the entropy growth in the bulk and near the boundary in a scenario where the initial state is the parity eigenstate $|11...1\rangle + |\omega\omega...\omega\rangle + |\bar{\omega}\bar{\omega}...\bar{\omega}\rangle$. System size simulated is $L = 40$. Figure reproduced with permission from Ref. [7].

states of the form $|\omega\omega...\omega 11...1\rangle_A$, $|\bar{\omega}\bar{\omega}..\bar{\omega}11...1\rangle_A$, $|1...11\omega\omega..\omega\rangle_A$, and $|1...11\bar{\omega}\bar{\omega}..\bar{\omega}\rangle_A$ are populated. Number of such states that are populated grow linearly with time initially. This results in a growth of entropy that is linear in time. Fig 4.7a shows entropy as a function of time in a small subsystem in the bulk. A rough estimate of the entanglement growth rate can be obtained from the data presented in Fig 4.3a. Probability p associated with domain walls nucleated from each point in space can be estimated to be $1/L$ times the total domain wall probabilities. As domain walls propagate into the subsystem previously unpopulated state of the subsystem is populated with a probability weight p. This adds an entropy of $s = -p \ln p$. Counting two kinds of domains ($1\omega 1$ and $1\bar{\omega}1$) crossing the two boundaries in either directions at a typical rate $\sim v_g$, the entropy growth rate is $\lambda = 8 v_g s$. From Fig 4.3, $p \approx 0.009/40$, resulting in $\lambda = 0.003$ which is close to the numerically obtained value in Fig 4.7a. This estimate ignores that the group velocity is not the same for all domain wall momenta and that there are off-diagonal entries in the density matrix.

At time $t = \ell/2v_g$, the domain wall pairs that originated in the vicinity of the center of A exit the subsystem. For $t > \ell/2v_g$, this equals the number of new domain walls that enter the system, resulting in a saturation of this mechanism of entanglement growth at an entropy value that is proportional to ℓ.

In a system that is initially prepared in the fully ordered ...1111... state, the exit of domain wall pairs that commence at $t = \ell/2v_g$ results in conversion of a fraction of the initial state $|..1111...\rangle_A$ into the oppositely ordered states $|...\omega\omega\omega...\rangle_A$ or $|...\bar{\omega}\bar{\omega}\bar{\omega}...\rangle_A$. Populations of these two oppositely ordered states increase with time as more and more domain walls exit the subsystem. This results in a further increase in the entropy after the expected saturation time of $\ell/2v_g$. We expect that the entropy of the small subsystem grows into that of a mixed state of all three ordered states with an entropy of $\sim \ln 3$. For large systems and for larger f, where the saturation entanglement is much larger than $\ln 3$, the latter growth will only provide a subleading contribution to total entanglement.

The saturation of the initial mechanism of entanglement growth at a time $\ell/2v_g$ (where the maximal group velocity v_g is $\sim 2f$) as well as further growth of entanglement can be seen in Fig 4.7a. Approach to $\ln 3$ is, unfortunately, not verifiable within the timescales of the simulations. As expected, entanglement growth is strongly suppressed even in the presence of a small longitudinal field (Fig 4.7b).

In contrast, entropy after a quench from an initial system prepared in one of the three fully ordered parity eigenstates starts from $\ln 3$ and increases with time linearly until the entropy saturates at the time $t = \ell/2v_g$. The above mentioned process

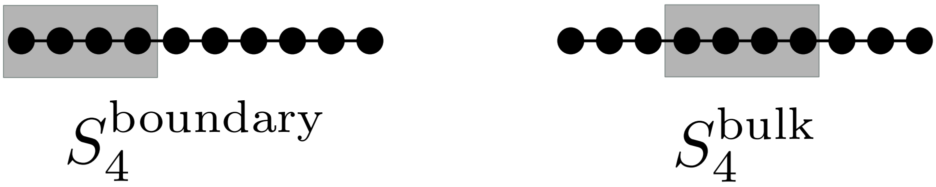

Fig. 4.8 Illustration of an $\ell = 4$ site subsystem located at the boundary (a) and one located in the bulk of the system (b). The entanglement entropy of these subsystems with the rest of the system are labeled as S_ℓ^{boundary} and S_ℓ^{bulk}. Figure reproduced with permission from Ref. [7].

which converts the population of $|...11111...\rangle_A$ into the oppositely ordered state in A is compensated by the reverse process resulting in no growth of entanglement after a time $t = \ell/2v_g$. This can be seen in simulations of the entropy growth after quench from the initial state $|...11...\rangle + |...\omega\omega...\rangle + |...\bar{\omega}\bar{\omega}\bar{\omega}...\rangle$, presented in Fig 4.7c.

For a subsystem located in the bulk, the entanglement growth occurs due to all domain walls that cross either one of the two boundaries of the subsystem. A subsystem located at the boundary of a system (Fig 4.8) on the other hand shows entanglement growth at half the rate as domain walls cross only one boundary. The saturation of this entropy growth occurs at a time when a domain wall pair nucleated at the boundary of the system exits the subsystem. This happens at the time $t = \ell/v_g$ when the domain wall pairs nucleated at the edge of the system at $t \sim 0$ reach the inner boundary of the subsystem. Fig 4.7d shows the entropy growth in a subsystem near the boundary for the same quench as in Fig. 4.7a. As expected, the entanglement growth rate at the boundary (Fig 4.7d) is half of that in the bulk (Fig 4.7a) and saturates in twice the time. Similar results hold in the case of parity eigenstate (Fig 4.7f).

4.6 Numerical results: Quench into the chiral Hamiltonian

Now we focus on dynamics in the system after a quench from the initial, fully ordered state, into the chiral Hamiltonian with finite f and θ. As mentioned in Sec 4.3, we focus on $\theta < \pi/6$, where the classical ground state (*i.e.* the Hamiltonian ignoring the transverse field) is ferromagnetic and the domain walls are well defined. The main effect of chirality then is to induce different energies to the domain walls of opposite chirality.

We will begin with a discussion of the probabilities of the domain wall flavors generated after the quench. Figure 4.9a presents the total probabilities of two domain

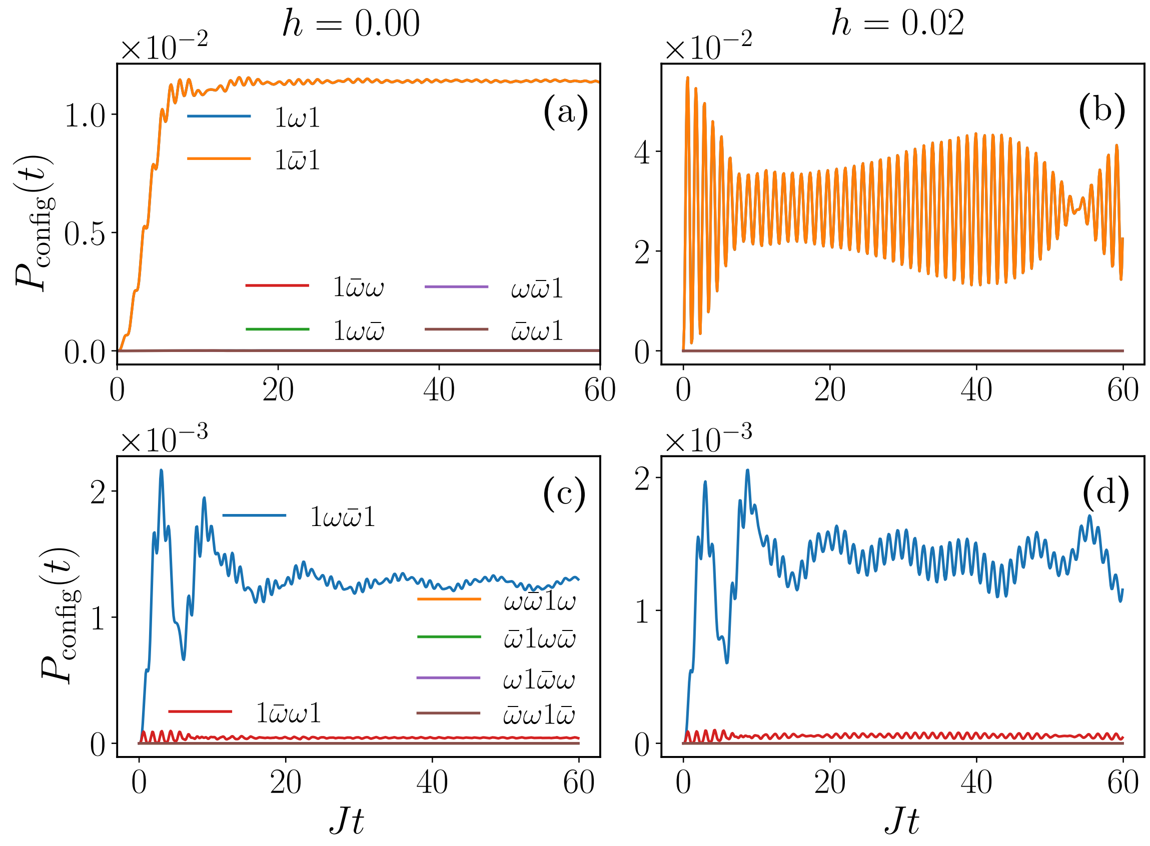

Fig. 4.9 Panel a shows the total probability (over all positions) of two domain wall states corresponding to the ones in Fig 4.3a after a quench to a Hamiltonian with $\theta = \pi/8$ and $f = 0.1$. Unlike the non-chiral case, the domain walls do not scatter into other forms at the boundary resulting in a steady probability. Panel b shows the same but with a final Hamiltonian that has an additional longitudinal field h. Panels c and d shows the probability weight of three domain wall states of type $ABCA$. Unlike the non-chiral case, the probabilities of $1\omega\bar{\omega}1$ and $1\bar{\omega}\omega 1$ states occur with different probabilities. Note that in Panels a and b lines corresponding to $1\bar{\omega}\omega$,$1\omega\bar{\omega}$, $\bar{\omega}\omega 1$ and $\omega\bar{\omega}1$ overlap on each other. Same is true of $1\omega 1$ and $1\bar{\omega}1$ lines. In panels c and d lines corresponding to $\omega\bar{\omega}1\omega$, $\bar{\omega}\omega 1\omega$, $\omega 1\bar{\omega}\omega$ and $\omega 1\omega\bar{\omega}$ overlap with each other. System size is $L = 50$. Figure reproduced with permission from Ref. [7].

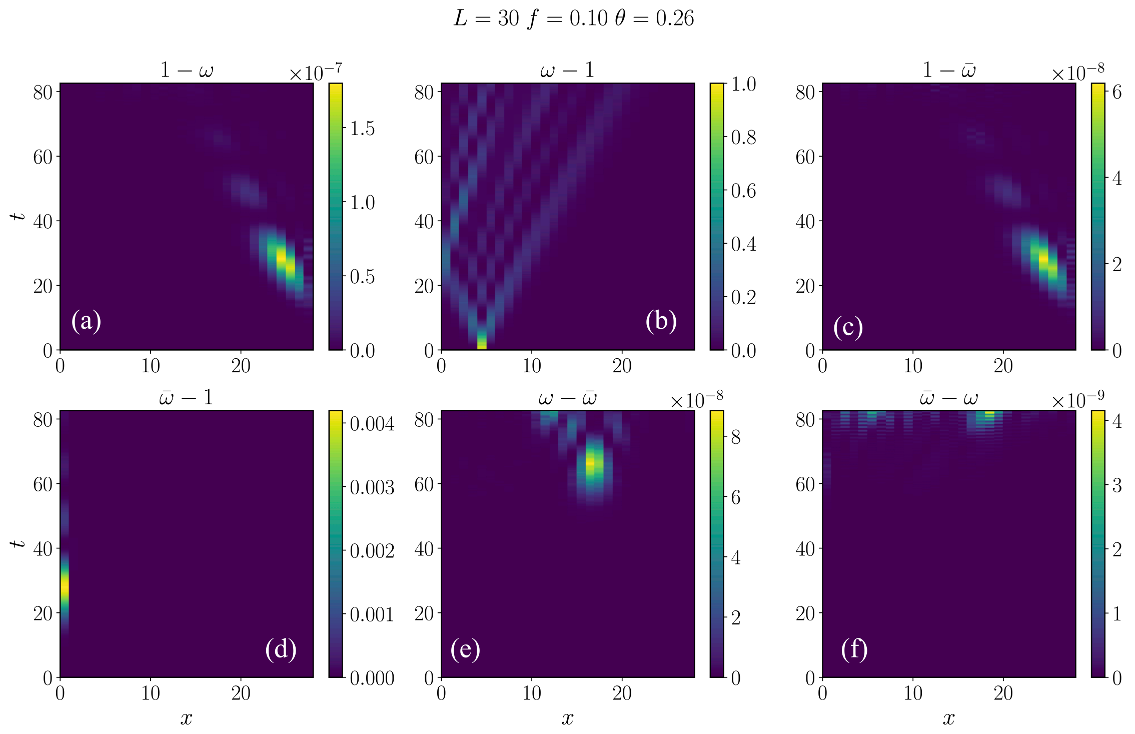

Fig. 4.10 Scattering dynamics of a domain wall of flavor $\ldots\omega\omega 11\ldots$ localized at bond $x = 5$ is shown here for quench Hamiltonian parameters $f = 0.1$ and $\theta = 0.26$. From panel (a) to (f) in alphabetical order, probability of single domain wall flavors $1-\omega$, $\omega-1$, $1-\bar{\omega}$, $\bar{\omega}-1$, $\omega-\bar{\omega}$ and $\bar{\omega}-\omega$ localized at bond x at time t is plotted with t and x on y and x axis respectively. In the panel (b) we can see that domain wall of flavor $\ldots\omega\omega 11\ldots$ retains its flavor after scattering from the boundary for the chiral quench.

wall states similar to the Fig 4.3a. Only the $1\omega 1$ and $1\bar{\omega}1$ domain walls are generated and these two occur with equal probabilities. The locality of the Hamiltonian does not allow for the formation of ABC domain wall pairs in the bulk. The post quench Hamiltonian considered here has $\theta = \pi/8$ and $f = 0.1$. Using the results at the end of Sec 4.3, we see that the gap between the domain wall bands (between the bottom of the upper domain wall band and the top of the lower domain wall band) is $2\sqrt{3}J\sin\theta - 4f > 0$ and therefore the domain walls bounce back from the boundary without change in its flavor. As a result the total probability of the $1\omega 1$ and $1\bar{\omega}1$ domain walls remain steady as seen in Fig 4.9a. This is unlike the non-chiral model discussed previously (Fig 4.3a).

Figure 4.9c shows the probabilities of $ABCA$ type three domain wall states. The $1\omega\bar{\omega}1$ states are generated with higher probability than the opposite chirality $1\bar{\omega}\omega 1$ type domain walls which has a higher energy. As discussed in Sec 4.3, as θ approaches

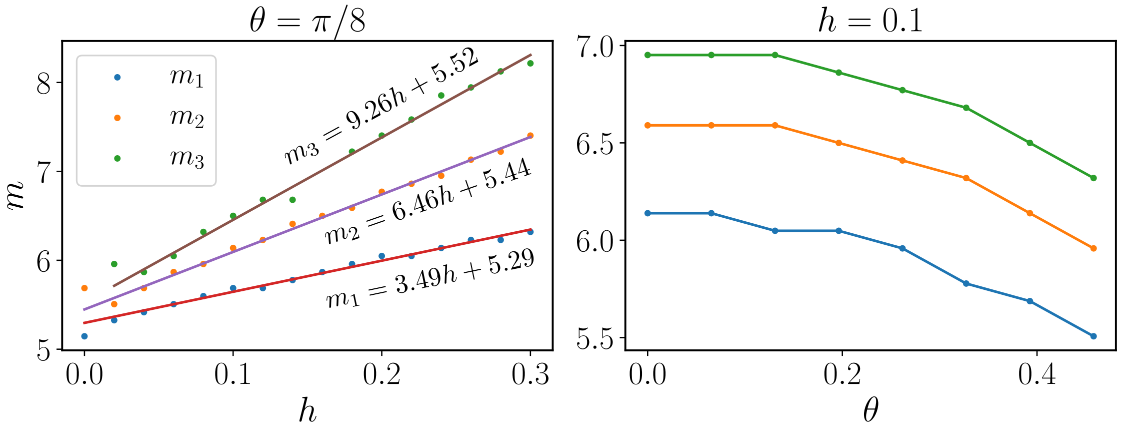

Fig. 4.11 Energy of bound domain wall pairs extracted from the power spectrum of magnetization in the same manner as in Fig 4.5. Panel a shows the masses as a function of the longitudinal field for a fixed θ. Panel b shows the dependence of the masses on θ for fixed h. Spectra are calculated from magnetization time series upto time $t = 90$ in a system of size $L = 40$. The scatter in the data is primarily caused by the finite frequency resolution in a Fourier transformation of data over a finite range of time. Figure reproduced with permission from Ref. [7].

$\pi/6$, the energy of the $1\bar{\omega}$ domain wall becomes close to that of a pair of domain walls $1\omega\bar{\omega}$. As a result two domain walls can evolve into three domain wall states. Numerics show that the three domain walls proliferate as $\theta \to \pi/6$. We will leave the analysis of this regime for later studies.

4.6.1 Magnetization

As in the case of the non-chiral model, magnetization decays linearly with time at short times (Fig 4.5a) with a small oscillatory component of (angular) frequency given by the total mass of a pair of opposite chirality domain walls, namely

$$m_2(\theta) = \epsilon^-_{k=0} + \epsilon^+_{k=0} = 6J\cos\theta - 4f. \tag{4.9}$$

Upon adding a longitudinal field, bound domain wall pairs are formed whose masses can be inferred from the magnetization oscillations as described in the Sec 4.4. Fig 4.11 summarizes the dependence of the masses on θ and h; masses appear to increase linearly with h and decrease monotonically with θ in the ranges considered.

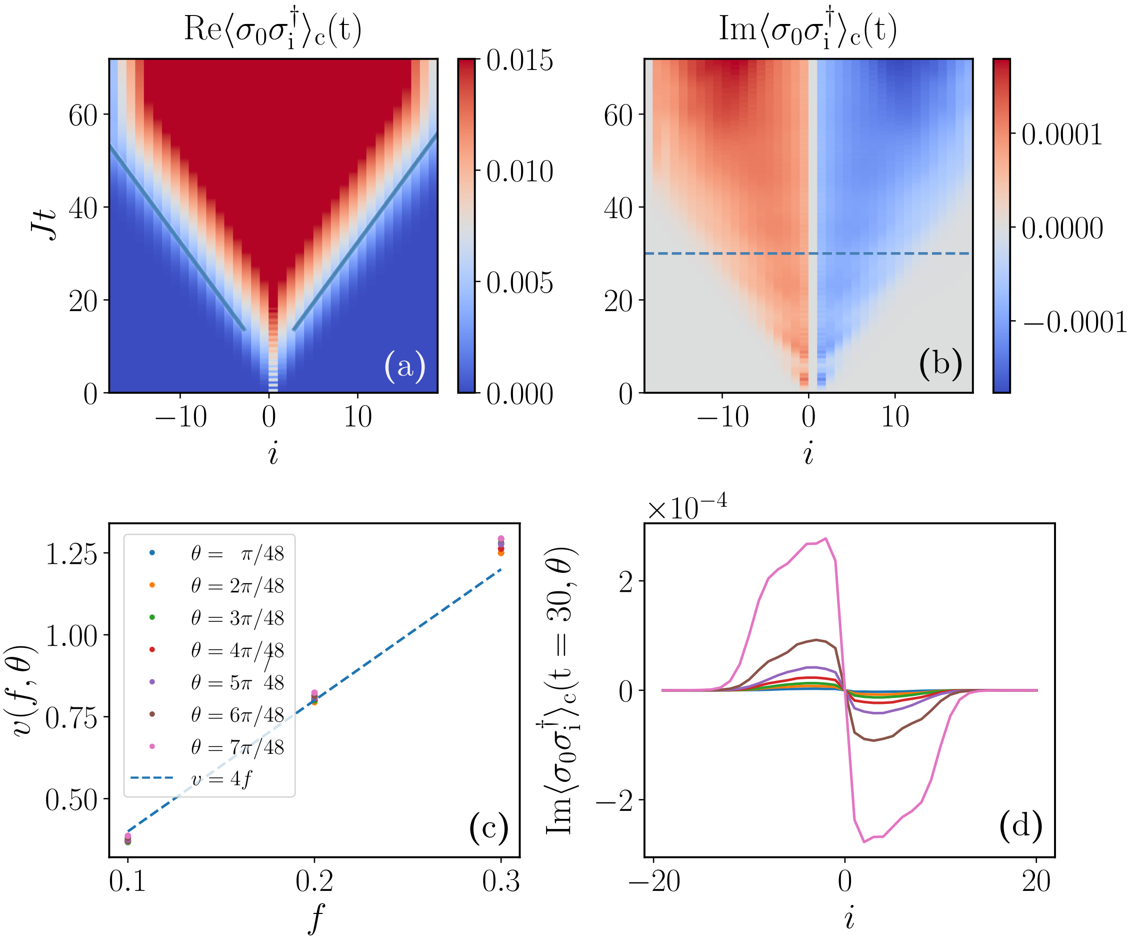

Fig. 4.12 Panels a and b show the real and imaginary parts of the correlator $C(i,t)$ after the fully ordered state is quenched to a final Hamiltonian with $f = 0.1, \theta = \pi/8$. Straight lines overlayed in the figure showing the rate of spread of correlations are obtained by fitting to constant C contours. The slope of the line is consistent with the expected rate of spread of correlations $2v_g = 4f$. Panel c shows the rate of spread as a function of f for different θ values. The dotted line shows the expected dependence $4f$. In Panel d, $\mathrm{Im}\langle\sigma_0\sigma_i^\dagger\rangle_c(t)$ as a function of position is shown for different θ values and a fixed time slice t (corresponding to the time slice indicated by the horizontal line in panel b). System size used for the calculation is $L = 40$. Figure reproduced with permission from Ref. [7].

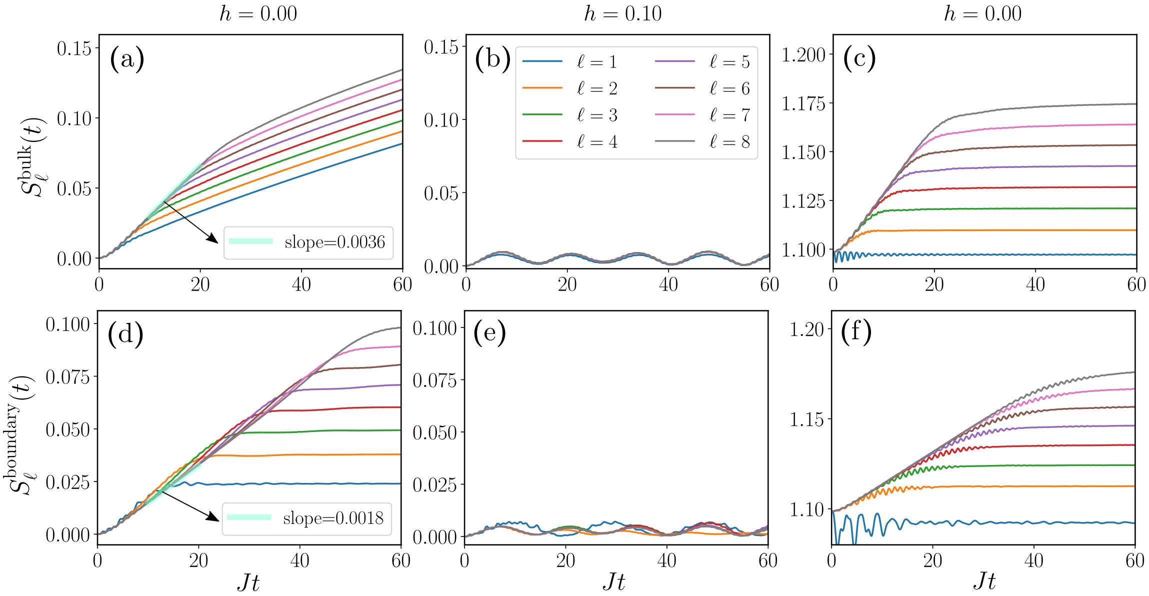

Fig. 4.13 Panels a and d show the entanglement entropy as a function of time for subsystems located in the bulk and at the edge of the system. Panels b and e show the same for the cases where the final Hamiltonian has an additional longitudinal field. Panels c and f show the results for the case where the initial state is a parity eigenstate of the form $|..1111...\rangle + |...\omega\omega\omega...\rangle + |...\bar{\omega}\bar{\omega}\bar{\omega}...\rangle$. Above results are obtained in a system of size $L = 40$ and for a final Hamiltonian with $f = 0.1$ and $\theta = \pi/8$. Figure reproduced with permission from Ref. [7].

4.6.2 Two point correlations

The connected two point correlations at equal times $C(r,t) = \langle\psi(t)|\sigma_0\sigma_r^\dagger|\psi(t)\rangle$ is shown in Fig 4.12. Since the domain wall velocities are independent of θ ($v_g \sim 2f$), the rate of spread of correlations ($2v_g$) remain the same as in the non-chiral model (Fig 4.12c).

Spatial parity is not a symmetry of the dynamics, therefore the imaginary part of the correlations is not necessarily zero. An expansion of the $\psi(t)$ in the computational basis (*i.e.* eigenbasis of σ) together with the results in Fig 4.9 indicates that the complex part of the correlations (Fig 4.12b) arise due to an excess occurrence of three domain wall states of one chirality over the other. Since the three domain wall states have low abundance, the imaginary part of the correlations is much smaller than the real part (Fig 4.12a,b). The difference between probabilities of opposite chirality three domain wall states increases with θ. This manifests in the increase with θ of the imaginary part of the correlations (Fig 4.12d).

4.6.3 Entanglement entropy

Now we describe the results for entanglement entropy growth after a quench into the chiral Hamiltonian. The entropy of small subsystems in the bulk (Fig 4.13a) grows linearly with time until $t \sim \ell/2v_g$ (where $v_g \sim 2f$). This regime is, as explained in Sec 4.6, described by population of new states with flipped spin domains. Following the saturation of this mechanism, the two oppositely ordered states are populated as the domain walls exit the system, resulting in further growth of the entropy. As in the case of the non-chiral model, when the initial state is a parity eigenstate, the entropy grows linearly from $\ln 3$ (entropy of subsystems of a parity eigenstate) and saturates at a time $t \sim \ell/2v_g$ (Fig 4.13f). The growth is strongly suppressed in the presence of a longitudinal field (Fig 4.13b).

Entanglement entropy of small subsystems located at the boundary of the system grows linearly with time till ℓ/v_g at a rate half that of the subsystems in the bulk. This is shown in Fig 4.13d. In the case of the quench to the non-chiral model, the entanglement entropy in the subsystem located at the boundary continues to grow after time ℓ/v_g. In contrast, here the entanglement entropy saturates to a constant (Fig 4.13d). This can be understood to arise from scattering properties at the boundary. In the chiral case, the domain walls of the form AB that reach the right hand side boundary are reflected back as a domain wall of the type AB. When the domain walls exit the subsystem, they leave the subsystem in the same state as the initial state

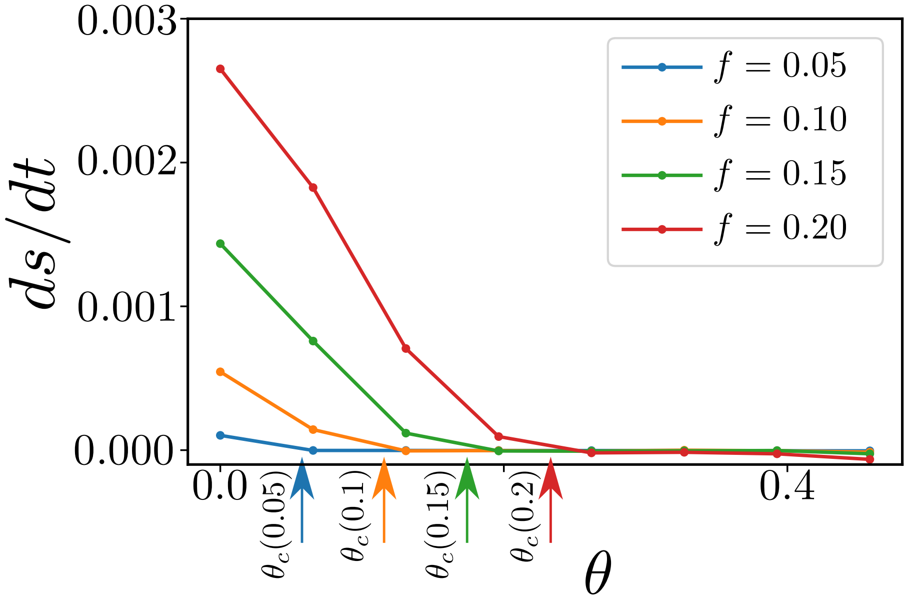

Fig. 4.14 Rate of change of entropy in a subsystem located at the edge at an instant ($Jt = 60$) after the saturation time ℓ/v_g is shown as a function of θ for different f in the final Hamiltonian. The arrows are crossover θ_c estimated for each f based on Eqn 4.10. Entropy saturates for $\theta > \theta_c$. Figure reproduced with permission from Ref. [7].

$|...1111...\rangle_A$. There is no increment in the population of the oppositely ordered states. This is unlike the non-chiral model.

In the non-chiral case, the incoming AB domain wall reflects at the open boundary as an AC domain wall. $AB \to AB$ type scattering (as opposed to $AB \to AC$) occurs if the opposite chirality domain walls have bands (Sec 4.3 and Fig 4.1b,c) that do not overlap *i.e.* if

$$2\sqrt{3}J\sin\theta > 4f. \tag{4.10}$$

This is verified in Fig. 4.14 which shows the rate of change of entropy after the expected saturation time ℓ/v_g in the subsystems located at the system edge, plotted as a function of θ. The rate of change is 0 for large θ and non-zero at small θ with an f-dependent crossover θ_c that is consistent with the above estimate ($\theta_c(f) \sim \sin^{-1}\frac{2f}{\sqrt{3}J}$, marked in the figure with arrows).

4.7 Summary and Conclusion

In this work, we have explored post quench domain wall dynamics in the ferromagnetic chiral clock model. Using finite size simulations, we have addressed the evolution of magnetization expectation values, equal time two point correlation functions, and entanglement growth, and a microscopic picture based on effective dynamics of single domain walls has been presented.

Entanglement growth and spread of correlation happen through evolution of domain-wall-pair states. Irrespective of θ, domain-wall-pair states of the type $1\omega 1$ and $1\bar{\omega}1$ form with equal probability from all points in the system immediately after the quench. Domain walls propagate with a maximal group velocity $v_g = 2f$ independent of the chirality parameter θ. As a consequence there is no qualitative difference between the non-chiral and chiral model in the entanglement and correlation spread in the bulk. In the non-chiral model, total probability of $1\omega 1$ and $1\bar{\omega}1$ states decay linearly with time as the domain walls scatter at the boundary and convert to $1\omega\bar{\omega}$, $1\bar{\omega}\omega$ due to collisions with the right boundary and to $\bar{\omega}\omega 1$ and $\omega\bar{\omega}1$ due to collisions on the left. In the chiral model, there is no such scattering to different domain wall types. Three-domain-wall states of the form $1\omega\bar{\omega}1$ and $1\bar{\omega}\omega 1$ are also generated with smaller probabilities compared to two-domain-wall states. In the chiral model the two types of three-domain-wall states are generated with unequal probabilities.

Magnetization decays linearly with time at short times accessible within our simulations. Oscillations around the linear decay have a frequency equal to the energy cost of two domain walls namely $6J\cos\theta - 4f$. In the presence of a longitudinal field that couples to $\sigma + \sigma^\dagger$, domain wall pairs form bound states of energies that appear to increase linearly with the field and decrease with the chirality.

Equal time two point correlations spread with the same speed $2v_g \sim 4f$ in both the chiral and non-chiral models. Imaginary part of the specific correlation $\langle \sigma_0(t)\sigma_r(t)^\dagger \rangle_c$ reflects the relative abundances of the opposite chirality three-domain-wall states. It is zero for the non-chiral model and increases in magnitude with θ.

Entanglement entropy in subsystems located in the bulk shows a linear growth, and saturates at a characteristic time scale $\tau_s \approx \ell/2v_g$. In small subsystems located in the bulk, a subleading growth of entanglement is seen after this time. In the non-chiral model, the similar behavior is seen even in the subsystems located at the boundary of the system (till a time $\tau_s \ \ell/v_g$). In the chiral models, with the chirality parameter $\theta > \sin^{-1}\frac{2f}{\sqrt{3}}$, the entanglement saturates to a constant.

We find that a linear-in-time entanglement growth is seen even outside the ferromagnetic regime of θ that we have studied. However, a simple isolated domain wall description is not sufficient to understand the behavior. At larger values of θ above $\pi/3$ where the ground state is not ferromagnetic, chirality in the ground state magnetization will have a more complex interplay with a longitudinal field than in the small θ cases we have studied. The second parameter in the model (ϕ) will act as an effective magnetic field to the domain wall particles, bringing in richer structures in the quenches in the model. We leave the exploration of the dynamics in the extended parameter space of the model for future studies.

The saturation of entanglement in the small subsystems at the edge of the system points to the inability of the spreading domains to thermalize the spins at the boundary of the system into an equally probable mixture of 1, ω and $\bar{\omega}$. As a consequence the initial magnetization survives at long times after quench. Careful accounting of the domain walls at the boundary after the saturation time indicates that the density of flipped spins near the boundary linearly changes with distance from the boundary. Consequently the post quench magnetization in the chiral model shows a linear decay of magnetization away from the boundary (Fig 4.15).

In contrast, the non-chiral model shows a magnetization that appears to decay to 0 at the boundary. Thus the θ dependent boundary scattering presents a peculiar scenario of a non thermal steady state near the boundary of this chain. Such a mechanism for failure of thermalization is related to the long coherence times of boundary spins in models carrying boundary zero modes in Jordan Wigner transformed dual description.[151, 152]

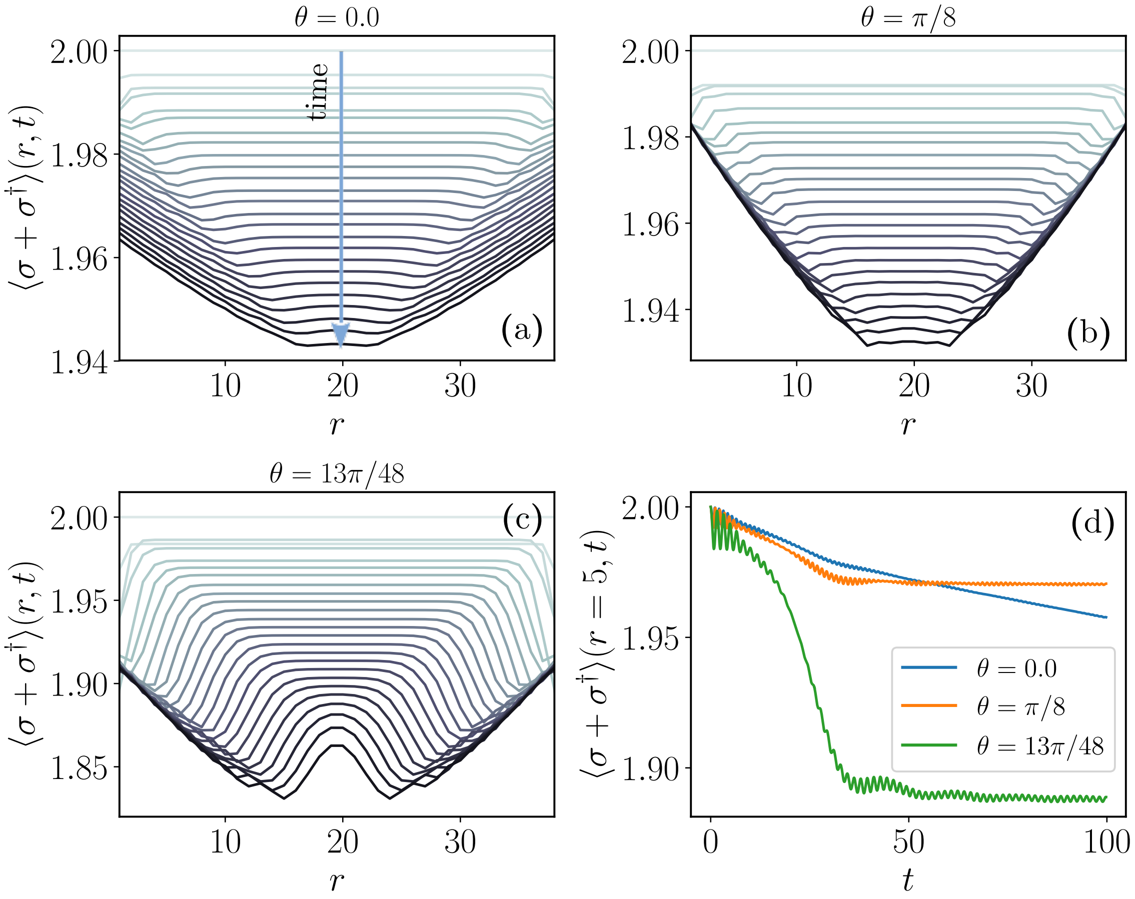

Fig. 4.15 Magnetization profile in the chain with open boundary conditions at the left and right ends. The magnetization at the boundary of the chain decays with time in the non-chiral model (panel a), whereas it saturates to constant in the chiral model (panels b,c). The saturation values vary linearly with distance from the boundary. Panel d shows the magnetization at a fixed position near the edge as a function of time for three different values of θ. Figure reproduced with permission from Ref. [7].

Chapter 5

Lindblad Master Equation implementation using MPS

5.1 Open Quantum System

An open quantum system S is a subsystem of a bigger closed quantum system represented by $S + B$ and the rest of the system dennoted by B is referred as environment or bath. In the rest of the chapter we refer S as system and $S + B$ as composite system. The Hamiltonian H_{tot} for $S + B$ is given by

$$H_{\text{tot}} = H \otimes \mathbb{I} + \mathbb{I} \otimes H_B + H_I \tag{5.1}$$

where H and H_B are the Hamiltonian of the system and environment, respectively. H_I is the system bath interaction Hamiltonian.

Since the composite system $S + B$ forms a closed quantum system, its dynamics is unitary, and the dynamics of the state ρ_{tot} of the composite system is given by the Liouville-von Neumann equation.

$$\frac{d\rho_{\text{tot}}(t)}{dt} = -\imath[H_{\text{tot}}, \rho_{\text{tot}}(t)] \tag{5.2}$$

with the assumption that H_{tot} is time-independent. We are interested in S part of the composite system. At any instant, everything that can be known about system from measurment within the system can be inferred from the density matrix. At any instant state of the system represented by ρ can be calculated from $\rho_{\text{tot}}(t)$ by tracing out the bath degrees of freedom *i.e*

$$\rho(t) = \mathrm{Tr_B}\rho_{\text{tot}}(\mathrm{t}) \tag{5.3}$$

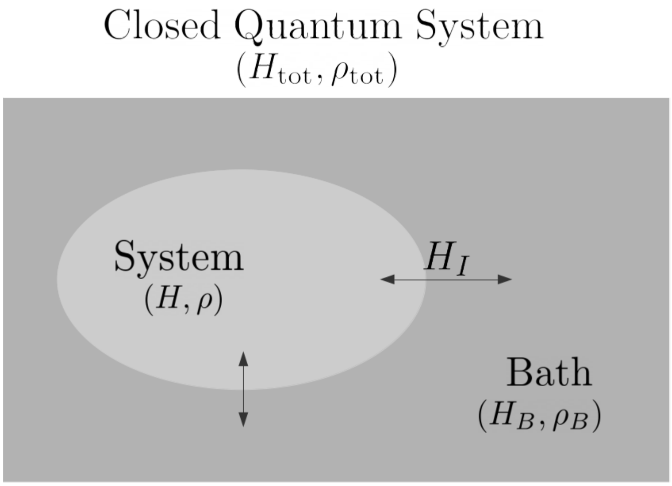

Fig. 5.1 Pictorial representation for a composite closed quantum system comprised of system and bath. Interaction between system and bath makes the system an open quantum system.

Equation of motion for $\rho(t)$ can be derived using the above Eq. 5.1, 5.2 and 5.3. This equation of motion for $\rho(t)$ is known as Quantum Master Equations (QME). Depending on the approximations involved like weak coupling, Markovianity, secular approximation, *etc.*, a different form of QME can be derived *e.g* Redfield Master equation, Born-Redfield Master equation, etc. Broad introduction of the Master equations can be found in Ref. [154]. We are mainly interested in the Lindblad form of the Master equation, which is discussed in the next section.

5.2 Lindblad Master Equation

For a composite quantum system comprised of system and bath, the most general form of Quantum Master Equation (QME) local in time is

$$\partial_t \rho(t) = -\imath[H, \rho(t)] + \mathcal{D}[\rho(t)] \tag{5.4}$$

Here H is the system Hamiltonian, and ρ is the system's density matrix. The first term is the Eq 5.4 refers to the usual unitary time evolution of the system in the absence of bath. The second term $\mathcal{D}[\rho]$ called a dissipator incorporates the dissipative effect induced by the bath because of system-bath interaction.

The hermiticity, trace preservation and positivity properties of ρ along with the requirement that the dynamics of composite system should be a unitary puts a strong restriction on the form of the dissipator in Eq 5.4. Aforementioned four conditions are also knows as Completely Positive and Trace Preserving (CPTP) condition. QME which is local in time and is CPTP is known as Lindblad Master Equation (LME)[155, 156] given by

$$\partial_t\rho(t) = -\iota[H, \rho(t)] + \sum_\alpha \gamma_\alpha\Big(L_\alpha\rho(t)L_\alpha^\dagger - \frac{1}{2}\{L_\alpha^\dagger L_\alpha, \rho(t)\}\Big) \tag{5.5}$$

L_α's are called jump operators and γ_α quantifies the system-bath coupling. Equation 5.5 also goes by the name of Gorini-Kossakowski-Sudarshan-Lindblad QME.

The jump operators L_α can be hermitian or non-hermitian. In terms of action over the real space, they can be local or non-local. The local form of jump operators is used in our later work to study the energy transport in the $\mathbb{Z}_3$ chiral clock model. The main disadvantage of LME over another form of QME is that given a thermal bath, it is tough to find the form of the jump operators L_α, which can imitate the actual bath effect.

5.3 Microscopic derivation of LME

The Lindblad form of the master equation can be derived from microscopic equations of motion. We will work on the interaction picture for this derivation. In the interaction picture, the Liouville-von Neumann equation is

$$\frac{d\tilde{\rho}_{\text{tot}}(t)}{dt} = -\iota[H_I(t), \tilde{\rho}_{\text{tot}}(t)] \tag{5.6}$$

The solution of the above differential equation is

$$\tilde{\rho}_{\text{tot}}(t) = \tilde{\rho}_{\text{tot}}(0) - \iota\int_0^t ds[\tilde{H}_I(s), \tilde{\rho}_{\text{tot}}(s)] \tag{5.7}$$

Inserting the above solution in Eq. 5.6 and tracing out the bath degrees of freedom gives the integro-differential equation for ρ

$$\frac{d\tilde{\rho}(t)}{dt} = -\int_0^t ds\text{tr}_B[\tilde{H}_I(t), [\tilde{H}_I(s), \tilde{\rho}(s)\otimes\tilde{\rho_B}]] \tag{5.8}$$

with the assumption that

$$\text{tr}_B[\tilde{H}_I(t), \tilde{\rho}_{\text{tot}}(0)] = 0 \tag{5.9}$$

Moreover, the coupling between the system and bath is assumed to be weak. This is called a Born approximation. The weak coupling approximation is given by the tensor product.

$$\tilde{\rho}_{\text{tot}}(t) \approx \tilde{\rho}(t) \otimes \rho_B \tag{5.10}$$

This approximation implies that at all times there is no entanglement between system and bath. Equation 5.8 is not local in time and rate of change of density matrix at time t depends on the state at time $s < t$ which makes solving it intractable both theoretically and numerically. We make it local by replacing $\tilde{\rho}(s)$ by $\tilde{\rho}(t)$, we assume that time evolution of $\tilde{\rho}(t)$ at time t depends only on $\tilde{\rho}(t)$ but not on previous instances which gives us the Redfield Master Equation.

$$\frac{d\tilde{\rho}(t)}{dt} = -\int_0^t ds \text{tr}_B[\tilde{H}_I(t), [\tilde{H}_I(s), \tilde{\rho}(t) \otimes \tilde{\rho_B}]] \tag{5.11}$$

The above Eq. 5.11 is not Markovian as the dynamics of $\tilde{\rho}$ depend on the choice of the initial state of the whole system. The issue of Markovianity can be resolved by replacing s with $t - s$ and changing the upper limit of the integral in Eq. 5.11 by ∞. The above last two substitution is allowed for the scenarios when the time scale of bath relaxation τ_B is much quicker than the time scale of variation in the system state , *i.e.*, $s \gg \tau_B$. The substitution mentioned gives the Markovian Master equation

$$\frac{d\tilde{\rho}(t)}{dt} = -\int_0^\infty ds \, \text{Tr}_B[\tilde{H}_I(t), [\tilde{H}_I(t-s), \tilde{\rho}(t) \otimes \tilde{\rho_B}]] \tag{5.12}$$

We are still not at the Lindblad form of the master equation, and a further approximation called secular approximation is needed. To explain the approximation, we consider that the interaction Hamiltonian H_I in the Schrodinger picture is of the form.

$$H_I = \sum_\alpha U_\alpha \otimes V_\alpha \tag{5.13}$$

Where U and V are hermitian operators acting on the system and bath, respectively. We can write the system operator U_α in the frequency space ω using the eigenstates of H_S

$$U_\alpha(\omega) = \sum_{\epsilon' - \epsilon = \omega} \Pi(\epsilon) U_\alpha \Pi(\epsilon') \tag{5.14}$$

where $\Pi(\epsilon)$ is the projector into the state $|\epsilon\rangle$. In the ω space, we can write the interaction Hamiltonian as

$$\tilde{H}_I = \sum_{\alpha,\omega} U_\alpha(\omega) \otimes V_\alpha = \sum_{\alpha,\omega} U_\alpha(\omega)^\dagger \otimes V_\alpha^\dagger \tag{5.15}$$

We assume that $\tilde{\rho_B}$ is the stationary state of the bath which means $[H_B, \tilde{\rho_B}] = 0$. Putting Eq. 5.15 in the Redfield Master equation and after some algebra, we have

$$\frac{d\tilde{\rho}(t)}{dt} = \sum_{\omega,\omega'}\sum_{\alpha,\beta} e^{\iota(\omega'-\omega)t}\Gamma_{\alpha,\beta}(\omega)\Big(U_\beta(\omega)\tilde{\rho}(t)U_\alpha^\dagger(\omega') - U_\alpha^\dagger(\omega')U_\beta(\omega)\tilde{\rho}(t)\Big) + \text{h.c} \tag{5.16}$$

where $\Gamma_{\alpha,\beta}(\omega)$ is the bath-bath correlation function defined as

$$\Gamma_{\alpha,\beta}(\omega) = \int_0^\infty ds e^{\iota\omega s}\langle V_\alpha^\dagger(t)V_\beta(t-s)\rangle_{\tilde{\rho}_B} \tag{5.17}$$

The system has two important time scales, which play an important role in the secular approximation. The first one is its intrinsic time scale τ_S defined by the typical frequency spacing ,*i.e.*, $|\omega-\omega'|$ involved in the eigen spectrum of H_S. Another important time scale is relaxation time τ_R of the open system. When $\tau_S \gg \tau_R$ then the terms in Eq. 5.16 with $\omega \neq \omega'$ may be neglected giving us the following equation

$$\frac{d\tilde{\rho}(t)}{dt} = \sum_{\omega}\sum_{\alpha,\beta} \Gamma_{\alpha,\beta}(\omega)\Big(U_\beta(\omega)\tilde{\rho}(t)U_\alpha^\dagger(\omega) - U_\alpha^\dagger(\omega)U_\beta(\omega)\tilde{\rho}(t)\Big) + \text{h.c} \tag{5.18}$$

Bath-bath correlation function $\Gamma_{\alpha\beta}(\omega)$ can be written as sum of hermitian and anti-hermitian function, $\gamma_{\alpha\beta}(\omega)$ and $\mathcal{S}_{\alpha\beta}(\omega)$ respectively as

$$\Gamma_{\alpha\beta}(\omega) = \frac{1}{2}\Big(\gamma_{\alpha\beta}(\omega) + \iota\mathcal{S}_{\alpha\beta}(\omega)\Big) \tag{5.19}$$

Function $\gamma_{\alpha\beta}(\omega)$ is given by

$$\begin{aligned}\gamma_{\alpha\beta}(\omega) &= \Gamma_{\alpha\beta}(\omega) + \Gamma_{\beta\alpha}^*(\omega)\\ &= \int_{-\infty}^\infty ds e^{\iota\omega s}\langle V_\alpha^\dagger(s)V_\beta(0)\rangle\end{aligned} \tag{5.20}$$

and $\mathcal{S}_{\alpha\beta}(\omega)$ is

$$\mathcal{S}_{\alpha\beta}(\omega)\frac{1}{2\iota}\Big(\gamma_{\alpha\beta}(\omega) - \gamma_{\beta\alpha}^*(\omega)\Big) \tag{5.21}$$

Using the above functions, Eq. 5.18 is finally recast into the Lindblad form

$$\frac{d\tilde{\rho}(t)}{dt} = -\iota[H_{\text{LS}}, \tilde{\rho}(t)] + \mathcal{D}[\tilde{\rho}(t)] \tag{5.22}$$

where H_{LS} is called the Lamb-shift Hamiltonian given by

$$H_{\mathrm{LS}} = \sum_{\omega} \sum_{\alpha,\beta} \mathcal{S}_{\alpha\beta}(\omega) U_{\alpha}^{\dagger}(\omega) U_{\beta}(\omega) \tag{5.23}$$

and the $\mathcal{D}[\tilde{\rho}(t)]$ is the dissipative part given by

$$\mathcal{D}[\tilde{\rho}] = \sum_{\omega} \sum_{\alpha\beta} \gamma_{\alpha\beta}(\omega) \Big(U_{\beta}(\omega) \tilde{\rho} U_{\alpha}^{\dagger}(\omega) - \frac{1}{2} \{ U_{\alpha}^{\dagger}(\omega) U_{\beta}(\omega), \tilde{\rho} \} \Big) \tag{5.24}$$

5.4 Choi Isomorphism

We saw in the section 5.2 that in the presence of both the dissipative dynamics of the system state represented by density matrix ρ is given by Eq. 5.5. For the concreteness of the state representation, we consider a spin chain with N spins, and its local Hilbert space dimension is d. Hence ρ acts on the Hilbert space of dimension d^N. In the tensor network formalism, Equation 5.5 can be simulated using MPO alone. The MPO representation for the density matrices is called Matrix Product Density Operators (MPDO). MPDO is different from the usual MPO because of the additional trace-preserving property that $\mathrm{tr}\rho = 1$.

LME can also be simulated using the MPS formalism. Choi Isomorphism is the mathematical tool that lets us represent the ρ in the form of MPS. It states that we can rewrite the coefficients of a matrix in the form of a vector by converting the bra index to ket index. The pictorial way to look at this vectorization process is shown in Fig. 5.2. The transformation can be thought of as reshaping the bra indices into ket indices and then merging with the original ket indices. We denote the new coupled indices by μ_i $(= \sigma_i \sigma_i')$. The vectorized version of the ρ is denoted by $|\rho\rangle$ and is given by

$$|\rho\rangle = \sum_{\sigma_1,\sigma'_1=1}^{d} \cdots \sum_{\sigma_N,\sigma'_N=1}^{d} A_1^{\sigma_1\sigma'_1} \ldots A_N^{\sigma_N\sigma'_N} |\sigma_1\sigma'_1 \ldots \sigma_N\sigma'_N\rangle \tag{5.25}$$

$$= \sum_{\mu_1=1}^{d^2} \cdots \sum_{\mu_N=1}^{d^2} A_1^{\mu_1} \ldots A_N^{\mu_N} |\mu_1 \ldots \mu_N\rangle \tag{5.26}$$

In the vectorized density matrix $|\rho\rangle$, it should be noted that after the vectorization now, the dimension of the physical indices has been bumped to d^2 from d because of the fusion of bra and ket indices. The trace preservation condition for the vectorized

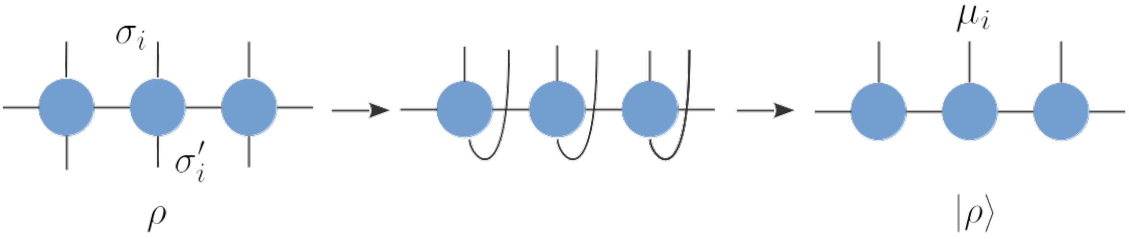

Fig. 5.2 Figure showing vectorization process of the density matrix ρ into vector $|\rho\rangle$ in the tensor network representation. The primed indices corresponds to the bra indices is transformed to ket indices and then both primed and non primed ket indices are fused into a single index μ_i.

density matrix $|\rho\rangle$ is given by

$$\sum_{\sigma_1,\sigma'_1=1}^{d} \cdots \sum_{\sigma_N,\sigma'_N=1}^{d} A_1^{\sigma_1\sigma'_1} \dots A_N^{\sigma_N\sigma'_N} \delta_{\sigma_1,\sigma'_1} \dots \delta_{\sigma_N,\sigma'_N} = 1 \tag{5.27}$$

LME after the vectorization is

$$\frac{d|\rho\rangle}{dt} = \mathcal{L}|\rho\rangle \tag{5.28}$$

where $\mathcal{L}$ is superoperator called Liouvillian, and In the LME, it has the form

$$\mathcal{L} = -\imath(H \otimes \mathbb{I} - \mathbb{I} \otimes H^T) + \sum_{\alpha} \left(L_\alpha \otimes L_\alpha^* - \frac{1}{2} L_\alpha^\dagger L_\alpha \otimes \mathbb{I} - \frac{1}{2} \mathbb{I} \otimes L_\alpha^* L_\alpha^T \right) \tag{5.29}$$

Here $\mathbb{I}$ is the Identity operator on the Hilbert space of dimension d^N. After the vectorization process, the operators acting on the $|\rho\rangle$ is of the form $A \otimes B$. Here, A acts on the ket indices, the non-primed ones, and B acts on the bra indices, which are primed in our notation. The operator acting on the $|\rho\rangle$ acts on the extended Hilbert space of dimension d^{2N} rather than the actual Hilbert space of our physical system.

For the time independent Liouvillian $|\rho(t)\rangle$ at any time t is given by

$$|\rho(t)\rangle = e^{\mathcal{L}t}|\rho(0)\rangle \tag{5.30}$$

Any system in a non-equilibrium setting, when modeled using an LME, at large $t$will lead to a steady-state. This steady-state is usually termed a Non-equilibrium

Steady-state (NESS). Mathematically NESS is given by the condition

$$\frac{d|\rho\rangle_{\text{NESS}}}{dt} = \mathcal{L}|\rho\rangle_{\text{NESS}} = 0 \tag{5.31}$$

Which means that NESS is the fixed point of the LME, or alternatively, NESS is the right eigenstate of the Liouvillian operator with zero eigenvalues. It is not always clear that state with zero eigenvalues are unique but we will assume that. This means that for a given non-equilibrium setting, NESS can be estimated in two ways. The first way is to evolve the $|\rho\rangle$ for very large t, which will give us the approximate NESS. The second way is to calculate the eigenstate with zero eigenvalue of the superoperator $\mathcal{L}$ which is computationally very costly when dealing with larger system sizes.

5.5 MPS implementation of time evolution

This section will discuss the MPS implementation of the LME after the vectorization. For the sake of concreteness, we will explain the construction in the context of $\mathbb{Z}_3$ chiral clock model, but the construction can be generalized to any other model.

For the $\mathbb{Z}_3$ chiral clock model the local hilbert dimension $d = 3$. After the vectorization of density matrix, state $|\rho\rangle$ which can be represented in the form of MPS has the dimension of the physical indices $d^2 = 9$. The states represented by the new index are 11, 1ω, $1\bar{\omega}$, $\omega 1$, $\omega\omega$, $\omega\bar{\omega}$, $\bar{\omega}1$, $\bar{\omega}\omega$ and $\bar{\omega}\bar{\omega}$. The basis states are of the form ij where i is the primed index of the density matrix ρ (not $|\rho\rangle$) and the j corresponds to the non primed index.

Now on the density matrix ρ, any arbitrary operator O can act on it from both right and left sides, as shown in the fig. 5.3 (c) and (d). If the operator O acts on ρ from the left, then the primed index gets contracted, and the action from the right leads to contraction of the non-primed index. So for every possible operator needed in our calculation, we constructed its two MPO form for the $|\rho\rangle$. The two different forms of the MPO constructed are shown in the figure 5.3. In the vectorized notation, the expectation value of operator O is estimated using the expression

$$\langle O\rangle = \langle\mathbb{I}|O|\rho\rangle \tag{5.32}$$

Here $\mathbb{I}$ is the Identity matrix. In the MPS language Eq. 5.32 the order of the contraction process plays a central role, heavily affecting the computational time. If the $O|\rho\rangle$ is estimated first and is then contracted with $\langle\mathbb{I}|$ then this way of calculating the expectation value is a prolonged process. It is slow because O and $|\rho\rangle$ are very dense

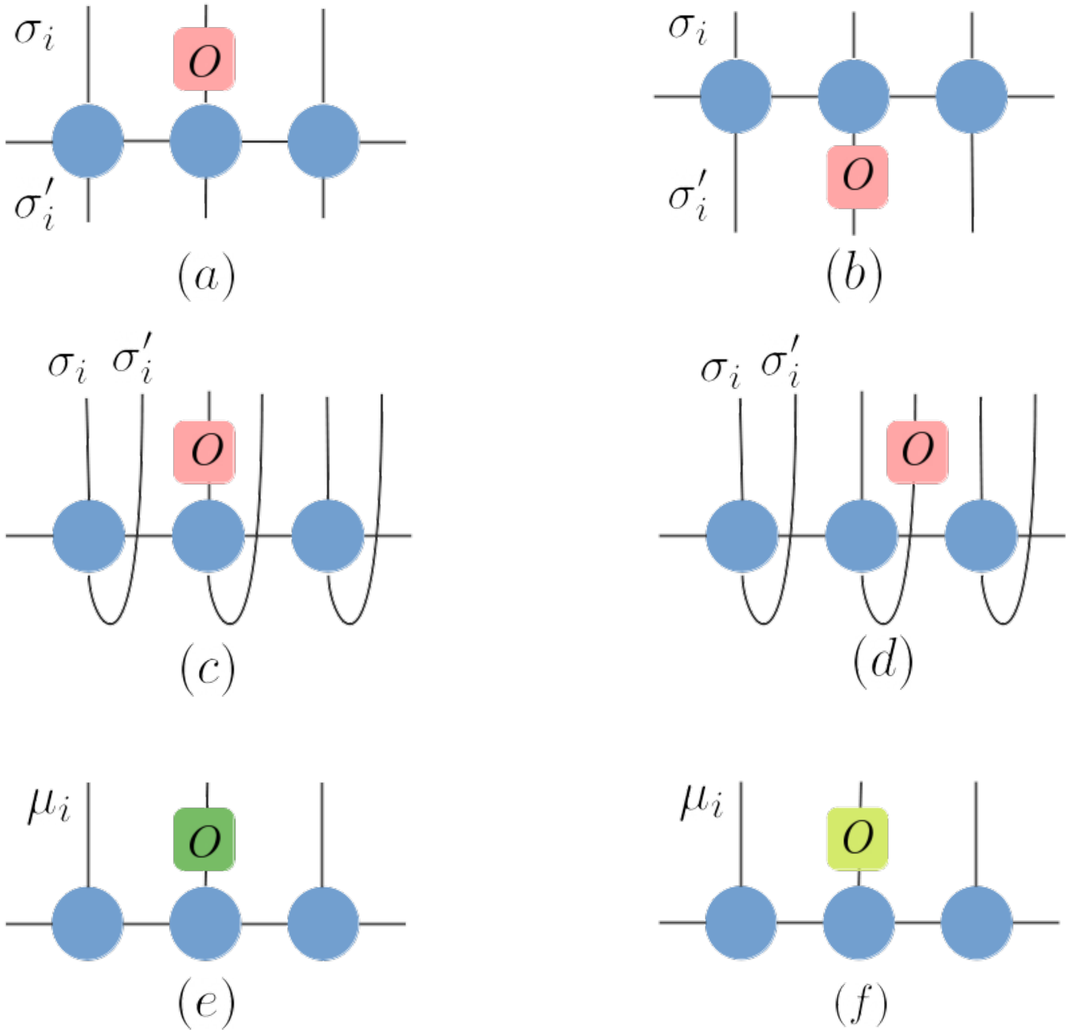
σ_i
O
σ'_i
(a)
σ_i
O
σ'_i
(b)
σ_i σ'_i
O
(c)
σ_i σ'_i
O
(d)
μ_i
O
(e)
μ_i
O
(f)

Fig. 5.3 Left and Right action of operator O on the ρ contracting with non primed and primed index is shown in Panel (a) and (b) respectively. Two different versions of the O are needed for its action on the $|\rho\rangle$ as shown in Panel (c) and (d). Version of O for the left and right action over the $|\rho\rangle$ are shown in green and yellow color in (e) and (f).

tensors resulting in a computationally costly contraction process. While if $\langle\mathbb{I}|O$ is evaluated first and is then contracted with $|\rho\rangle$, this is computationally very fast because contraction of $\langle\mathbb{I}|$ with O results in a very sparse tensor as $\langle\mathbb{I}|$ is highly sparse.

From Eq. 5.30 it is clear that $\mathcal{L}$ is the generator of the time translation for $|\rho\rangle$. Time evolution of the $|\rho\rangle$ is implemented using the fourth-order approximant for the $e^{\mathcal{L}t}$. The fourth-order approximant we used was first discussed in the following work [157, 158]. The central principle is still the same for deriving higher-order approximants, which is a higher-order approximant for matrix exponential is constructed using the product of lower-order approximants. Approximant of any desired order of a matrix exponential can be estimated using the following expression

$$W^{\mathrm{II}}(\tau_1)W^{\mathrm{II}}(\tau_2)\dots W^{\mathrm{II}}(\tau_n) = \exp(H\tau) + \mathcal{O}(\tau^p) \tag{5.33}$$

where W^{II}'s are the first order approximant and τ's are complex number. The form of $W^{\mathrm{II}}(\tau)$ is $1 - \mathrm{H}\tau$. For any given p in Eq. 5.33, the approximant constructed is correct till order $p-1$ in τ.

For a desired approximant of order $p-1$, the τ's on LHS of Eq. 5.33 is obtained by equating the coeffecients of τ till order $p-1$ on both sides of Eq. 5.33. For second order approximant we need only two W^{II}'s *i.e* n=2 and the τ's are

$$\tau_1 = \frac{1+\iota}{2}\tau$$
$$\tau_2 = \frac{1-\iota}{2}\tau$$

Third-order approximant needs $n = 4$ terms, and the τ's are

$$\begin{aligned}
\tau_1 &= \frac{1}{4}\Big(-\frac{1+\iota}{\sqrt{3}} + 1 + \iota\Big)\tau \\
\tau_2 &= \iota\tau_1 \\
\tau_3 &= -\iota\bar{\tau}_1 \\
\tau_4 &= \bar{\tau}_1
\end{aligned}$$

Fourth-order approximant can be obtained using 7 τ's, and they are

$$\begin{aligned}
\tau_1/\tau &= 0.2588533986109182 + 0.0447561340111419\iota \\
\tau_2/\tau &= -0.0315468581488038 + 0.2491190542755632\iota \\
\tau_3/\tau &= 0.1908290521106672 - 0.2318537492321061\iota \\
\tau_4/\tau &= 0.1637288148544367 \\
\tau_5 &= \bar{\tau}_3 \\
\tau_6 &= \bar{\tau}_2 \\
\tau_7 &= \bar{\tau}_1
\end{aligned}$$

5.6 Lindblad Dissipators

In this section, we will review the Lindblad dissipators typically used in the context of an open quantum system to study the transport properties. There are two types of LME, namely Global and Local Master Equations which are usually employed to study the transport properties. These master equations are named based on the features of the dissipators used in the Lindblad master equation.

In energy transport studies, the global master equation was firstly used in a numerical work [159] by Saito to study the normal heat transport in the quantum spin half chain. For the global master equation, we denote the corresponding dissipator by $\mathcal{D}_G[\rho]$. The general form of global dissipator $\mathcal{D}_G[\rho]$ is

$$\mathcal{D}_G[\rho] = [X_\alpha, R_\alpha \rho] + [X_\alpha, R_\alpha \rho]^\dagger \tag{5.34}$$

Here X_α is the system operator acting on the site which is directly attached to the reservoirs. Information about the effect of bath is contained in the operator R_α and is defined as

$$R_\alpha = \sum_{i,j} \frac{E_i - E_j}{e^{\beta_\alpha (E_i - E_j)} - 1} \langle i | X_\alpha | j \rangle \cdot |i\rangle\langle j| \tag{5.35}$$

E_i and $|i\rangle$ are the eigen energies and eigenstates of the system Hamiltonian H_{S}. The advantage of using a global dissipator is that the thermal temperature is set at the level of all system eigenstates. However, the downside in its numerical implementation is that all eigenstates are needed, which makes it very hard to use $\mathcal{D}_G[\rho]$ for the larger system sizes.

In Ref. [160], Prosen *et.al* came up with the interesting idea of using local Lindblad dissipators $\mathcal{D}_l$ to study the transport properties. Since in the global master equation is knowing all the eigenstates and eigenspectrum. They proposed the idea of local dissipators that act on a few degrees of freedom of the system. These dissipators set the temperature over these few degrees of freedom under some local Hamiltonian h_i. This local Hamiltonian h_i are dominant terms of H_S which has support at the site i of the chain.

Local Lindblad dissipators are of the following form so that LME satisfies the CPTP condition

$$\mathcal{D}_l = \sum_j [L_l^j, \rho L_l^{j\dagger}] + [L_l^j, \rho L_l^{j\dagger}]^\dagger \tag{5.36}$$

where L_l^j are the local Lindblad operators and sum $\sum_j$ is over all the local Lindblad dissipators indexed by j which act only on the eigenstates of h_l to set the temperature locally. If the system Hamiltonian H_S has conserved quantities like total magnetization etc. other than the usual total energy, then the $\mathcal{D}_l$ can be designed accordingly to study the transport properties of these other conserved quantities also.

Ref. [160] studied the spin transport in the XXZ spin half chain using single and two site-local Lindblad dissipators. Single site Lindblad operator L_i^l, α acting on the site i used to study the spin transport is as follows

$$L_{i,\alpha=1}^l = \frac{1}{2}\sqrt{\Gamma_+}\sigma^+, \quad L_{i,\alpha=2}^l = \frac{1}{2}\sqrt{\Gamma_-}\sigma^+$$

$$\Gamma_\pm = \sqrt{\frac{1 \mp \tanh \mu_i}{1 \pm \tanh \mu_i}}$$

Sites over which these Lindblad operators $L_{i,\alpha}^l$ are acting induces local magnetization $\langle \sigma_i^z \rangle \approx -\tanh \mu_i$. By carefully choosing the μ for each end of one-dimensional quantum spin chains, the desirable spin gradient is introduced in the system to study the spin transport.

This local spin bath setup has been used extensively to study the spin transport in one dimensional clean and a disordered spin-1/2 system like XXZ Hamiltonian, where total magnetization is a good quantum number for a closed system. Spin bath setup similar to used in [160] to study the spin and energy transport in XXZ chain in [161–164]. For the Heisenberg model, spin transport is studied in [162]. Transport regimes of the Aubry-André-Harper model are studied in [165] using a similar spin bath. The spin bath mentioned above is also used for fermionic Hamiltonian like the

Hubbard model. In [166] spin and charge transport are studied at the high-temperature regime of the Hubbard model.

We mentioned in the section 5.2 that LME does not represent the actual thermal baths but is the most used form of Master equation to study the transport properties. Generically the LME has been found to correctly describe the transport regimes, whether ballistic or diffusive etc. But in [167, 168] LME derived in the weak coupling regime along with secular approximation was found to be inaccurate for describing the Non-equilibrium steady states because of non-vanishing energy current resulting from violation from local conservation laws.

Chapter 6

Energy transport in $\mathbb{Z}_3$ chiral clock model

We characterize the energy transport in a one dimensional $\mathbb{Z}_3$ chiral clock model. The model generalizes the $\mathbb{Z}_2$ symmetric transverse field Ising model (TFIM). The model is parametrized by a chirality parameter θ, in addition to f and J which are analogous to the transverse field and the nearest neighbour spin coupling in the TFIM. Unlike the well studied TFIM and XYZ models, does not transform to a fermionic system. We use a matrix product states implementation of the Lindblad master equation to obtain the non-equilibrium steady state (NESS) in systems of sizes up to 48. We present the estimated NESS current and its scaling exponent γ as a function of θ at different f/J. The estimated $\gamma(f/J, \theta)$ point to a ballistic energy transport along a line of integrable points $f = J\cos 3\theta$ in the parameter space; all other points deviate from ballistic transport. Analysis of finite size effects within the available system sizes suggest a diffusive behavior away from the integrable points.

6.1 Introduction

Though energy transport has been studied for a long time, a microscopic description of energy transport in interacting quantum and classical systems is still under development, with many recent insights on connections between chaos and transport aided by the improved simulation methods. In classical systems, chaos is neither necessary nor a sufficient condition[169] for diffusive transport. Fermi-Pasta-Ulam problem has a positive Lyapounov exponent, but does not exhibit diffusive heat conduction in any parameter regime.

An extensive amount of work on high temperature transport focusing on spin-half models in one dimensional (1D) quantum systems [159, 170–178] have shown that breaking integrability generally leads to diffusive energy transport. It has been analytically argued that integrability in clean systems typically leads to ballistic energy transport [179, 174]. Interestingly, the relation does not extend to other conserved currents [160, 180, 162, 181, 164]. The XXZ chain in its zero-magnetization sector shows ballistic energy transport in all phases but spin transport is ballistic in the easy plane phase, diffusive in the easy axis phase, and super-diffusive at the isotropic point.[162, 175]. Both spin and energy transport are found to be ballistic in other magnetisation sectors.[174, 182, 163] On the other hand the same model, with a local longitudinal field, is non-integrable but shows ballistic spin transport[164]. Disorder further enriches transport physics in such systems [163].

In this work, we step away from the well-studied spin-1/2 model and explore a model with a three dimensional local Hilbert space, namely the $\mathbb{Z}_3$ symmetric chiral clock chain[50, 116, 109] which generalizes of the $\mathbb{Z}_2$ symmetric TFIM[40]. The latter which is mappable to free fermions is integrable and exhibits ballistic energy transport [183]. The $\mathbb{Z}_3$ clock model Hamiltonian is integrable in a fine tuned set of parameters but not in general. While the model shares several features with the TFIM, it is not mappable to a free fermionic Hamiltonian. We aim to address the question of how energy transport is affected by the model parameters, in particular how integrability affects transport in this model. Transport through the chain is simulated using the Lindblad master equation (LME) approach implemented using matrix product state (MPS) techniques [160, 184, 162, 178].

This chapter is structured as follows. In Sec. 6.3, we describe the chiral clock model and present the details of the Lindblad dissipators. We then describe the details for the MPS implementation of the LME in Sec. 6.5. We find that under a change of basis, the LME and transport properties in one part of the parameter space can be related to that in another part, reducing the parameter space to be studied. This is described in Sec. 6.4. Results for the simulations are presented in the Sec. 6.6 and conclude with Sec. 6.8.

6.2 Transport in spin-1/2 Models

Spin half chains are the simplest systems to study the energy transport in the context of quantum spin chains. Models like TFIM, XXZ and XYZ are the most studied cases as they are the integrable systems [185]. Extensive analytical as well as numerical studies have been done on these mentioned models. Several interesting transport features like rectification, negative differential conductivity, One-way street phenonmenon etc. has been already been observed in the different regimes of these models. We will mainly summarise the spin and energy transport behavior known in the different regimes of the models.

The energy transport behavior in TFIM is studied in the [177] for both clean and disordered case in the weak coupling regime. TFIM is an integrable model with no additional conserved quantities other than the global parity. In this analytical work complemented with numerics using the Monte carlo wavefunction approach. It is shown that the clean TFIM chain shows ballistic energy transport while the disordered chain exhibits the diffusive transport.

The most studied spin-1/2 integrable model is the XXZ model. This model is the archetypal model for studying the spin and energy transport because of its Bethe ansatz integrability. This model is also a testing ground for the principles of generalized hydrodynamics. Even though this model is integrable transport features are understood only in the high temperature regime. Total magnetization $M = \sum \sigma_i^z$ is a conserved quantity which allows studying the spin transport in this model. This total magnetization conservation arises from $U(1)$ rotational symmetry of the model about an axis. In high temperature regime, this model exhibits ballistic energy transport in all parameter regime and magnetization sector. In Ref. [162] spin transport was studied using the time dependent DMRG simulations in the zero magnetization sector. Spin transport was reported to be the ballistic in the easy plane ($\Delta < 1$), superdiffusive at the isotropic point ($\Delta = 1$) and diffusive along the easy axis ($\Delta > 1$). In the nonzero magenetization sector, spin transport is ballistic in all parameter regimes.

Ref. [176] studied the effect of disorder on the spin transport in the zero magnetization sector. The disorder in the model was incorporated in the additional field in the z-direction acting on all the sites. In the presence of disorder both diffusive and subdiffusive spin transport is seen depending on the disorder strength. Using the disorder scaling it was also reported that the characteristic length N_* in the disordered case is given by $1/h^{1.33}$, where h is disorder strength. For the correct estimation of the NESS it was pointed out that for $N < N_*$ system behave like a clean system, so larger system is needed to see the effect of disorder.

In the zero magentization sector, energy and spin transport have different behavior while in the nonzero magnetization sector both energy and spin have similar transport behavior. The effect of the disorder on the similar (dissimilar) behavior of spin and energy transport in the nonzero (zero) magnetization sector is studied in Ref. [163]

numerically using time dependent DMRG. Comparative qualitative behavior of spin and energy transport in different magnetization sector was found to be unscathed in the disordered limit. Note that in both above mentioned works, it was ensured that system is in the ergoidic phase.

Effect of breaking the $U(1)$ symmetry is studied in the Ref. [175]. It is broken using the parameter η in the Hamiltonian given by

$$H = \sum_i \left[(1+\eta)\sigma_i^x\sigma_{i+1}^x + (1-\eta)\sigma_i^y\sigma_{i+1}^y + \Delta\sigma_i^z\sigma_{i+1}^z\right] + \sum_i h_i\sigma_i^z \tag{6.1}$$

Within the ergodic phase it was shown that with increase in disorder strength, energy transport changes from diffusive to subdiffusive and the critical disorder strength for this transition increases with increase in parameter η.

6.3 Model

The $\mathbb{Z}_3$ chiral clock model for a chain of N spins in 1D, is described by the Hamiltonian[50, 116, 109, 47]

$$H(\theta,\phi) = -Je^{\iota\theta}\sum_{i=1}^{N-1}\sigma_i\sigma_{i+1}^\dagger - fe^{\iota\phi}\sum_{i=1}^{N}\tau_i + \text{H.c.} \tag{6.2}$$

Each spin has a three dimensional Hilbert space, and the local operators σ and τ have the following matrix representation

$$\sigma = \begin{pmatrix} 1 & 0 & 0 \\ 0 & \omega & 0 \\ 0 & 0 & \bar{\omega} \end{pmatrix} \quad \tau = \begin{pmatrix} 0 & 1 & 0 \\ 0 & 0 & 1 \\ 1 & 0 & 0 \end{pmatrix} \tag{6.3}$$

where $\omega = \exp(2\pi\iota/3)$. We will represent the single site eigenstates of the σ operator as $|1\rangle$, $|\omega\rangle$ and $|\bar{\omega}\rangle$. Operators σ and τ satisfy the algebra $\sigma_i^3 = \tau_i^3 = 1$, $\sigma_i\tau_i = \bar{\omega}\tau_i\sigma_i$, and $\sigma_i\tau_j = \tau_j\sigma_i$ for $i \neq j$. This algebra is a $\mathbb{Z}_3$ analog of the algebra of Pauli matrices σ_z and σ_x. Interplay between f, θ and ϕ results in a rich ground state phase diagram[3, 46, 117] hosting trivial, topological and incommensurate phases.

The model has a global $\mathbb{Z}_3$ parity symmetry associated with the operator $\mathcal{P} = \Pi_i\tau_i$. Apart from the global parity symmetry, the model can have other symmetries[186] namely time reversal $\mathcal{T}$, charge conjugation $\mathcal{C}$, and spatial inversion $\mathcal{S}$ depending on the values of parameters θ and ϕ. Under these symmetry transformations, σ and τ operators transform as $\mathcal{T}^\dagger\sigma\mathcal{T} = \sigma^\dagger$, $\mathcal{T}^\dagger\tau\mathcal{T} = \tau$, $\mathcal{C}^\dagger\sigma\mathcal{C} = \sigma^\dagger$, and $\mathcal{C}^\dagger\tau\mathcal{C} = \tau^\dagger$. Charge conjugation swaps the states $|\omega\rangle$ and $|\bar{\omega}\rangle$. Spatial inversion changes site index $i \to N - i + 1$. All three symmetries are present at $\theta = \phi = 0$ while the model has only spatial inversion symmetry when $\theta = 0$ and $\phi \neq 0$. None of the three symmetries are present when both θ and ϕ are non-zero. In this work we will focus on the models with $\phi = 0$ for simplicity. For $\phi = 0$ and $\theta \neq 0$, the individual symmetries $\mathcal{C}$ and $\mathcal{S}$ are broken but their products are preserved.

At $f = 0$, all the eigenstates of Hamiltonian can be chosen to be direct products of eigenstates of σ_i. Energy of each eigenstate is $-2J \sum_i \cos(\theta + \alpha_i)$, where $\alpha_i = \arg(\langle\sigma_i\rangle/\langle\sigma_{i+1}\rangle)$ which take values from $\{0, \pm 2\pi/3\}$. When $\theta \in (-\pi/3, \pi/3)$, all the spins in ground state are aligned in the same direction, either in 1, ω or $\bar{\omega}$. Ground state for $\theta \in (\pm\pi/3, \pm\pi)$ has consecutive spins oriented at relative angle of $\pm 2\pi/3$. Parameter f tunes quantum fluctuation in the model. At large f, the ordered phase is destroyed forming a paramagnetic phase. A second order phase transition separates the $\mathbb{Z}_3$ symmetry broken phase (small f) and $\mathbb{Z}_3$ symmetric phase(large f). The model was shown to be integrable along the line $f = J \cos 3\theta$ inside the ordered phase[187].

There has been limited studies of transport properties in the model. Non-equilibrium current in $\mathbb{Z}_3$ chiral clock chain with alternating sites are different temperatures have been studied in Ref [188]. At the critical integrable point described by $f = J$ and $\theta = 0$, energy transport between a ground state and high energy state was studied in a generalized hydrodynamics framework in Ref. [189]. We will study the energy transport in the ferromagnetic ($f < J$) regime and at varying values of θ.

A natural framework for investigation of transport properties is to attach baths with different characteristic temperatures at the opposite ends of the chain. This temperature difference creates an energy gradient and energy flow from high to low temperature end. In Ref.[160], Prosen *et al.* introduced the idea of using few-site jump operators to study transport properties under the dissipative dynamics of LME. This strategy provides computational simplicity and speedup leading to its extensive use for studying spin and fermionic chains[164, 162, 163, 165, 184, 178, 176, 190]. It has been argued that the local Lindblad approximations cannot faithfully reproduce the coherences produced by coupling to an actual quantum environment [168]. The local Lindblad operators we use are intended to maintain local energy densities at the ends of the chain rather than to mimic a realistic quantum bath. We assume that the transport properties are independent of the manner in which the local energy density is realized.

Dissipative dynamics of the system with bath attached at both ends is given by the LME[155]

$$\partial_t \rho(t) = \imath[\rho(t), H] + \mathcal{D}[\rho(t)] \tag{6.4}$$

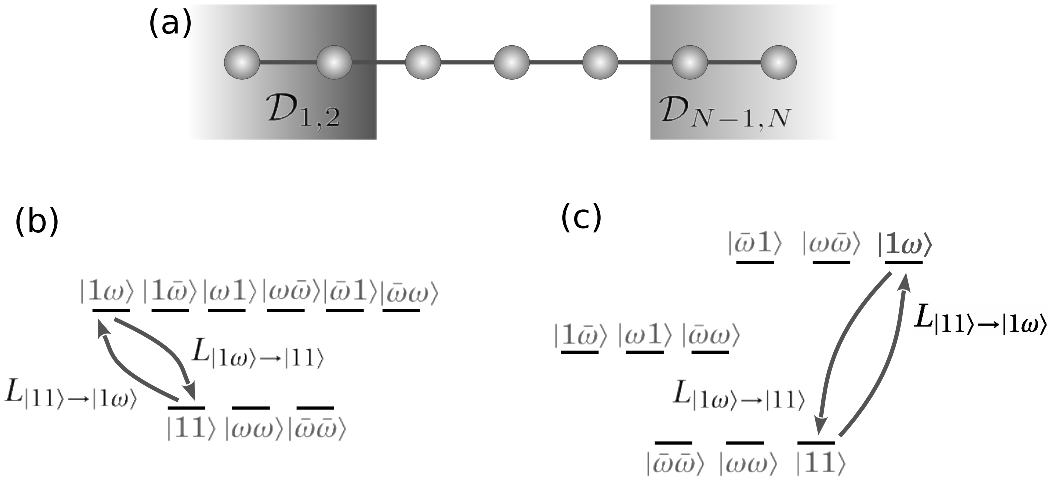
(a)
$\mathcal{D}_{1,2}$
$\mathcal{D}_{N-1,N}$
(b)
$|1\omega\rangle$ $|1\bar{\omega}\rangle$ $|\omega 1\rangle$ $|\omega\bar{\omega}\rangle$ $|\bar{\omega}1\rangle$ $|\bar{\omega}\omega\rangle$
$L_{|1\omega\rangle\to|11\rangle}$
$L_{|11\rangle\to|1\omega\rangle}$
$|11\rangle$ $|\omega\omega\rangle$ $|\bar{\omega}\bar{\omega}\rangle$
(c)
$|\bar{\omega}1\rangle$ $|\omega\bar{\omega}\rangle$ $|1\omega\rangle$
$L_{|11\rangle\to|1\omega\rangle}$
$|1\bar{\omega}\rangle$ $|\omega 1\rangle$ $|\bar{\omega}\omega\rangle$
$L_{|1\omega\rangle\to|11\rangle}$
$|\bar{\omega}\bar{\omega}\rangle$ $|\omega\omega\rangle$ $|11\rangle$

Fig. 6.1 Pictorial representation of the bath system setup is shown in panel (a). Action of the jump operators $L_{|11\rangle\to|1\omega\rangle}$ and $L_{|1\omega\rangle\to|11\rangle}$ are shown for the ferromagnetic regime for dissipators $\mathcal{D}^0$ and $\mathcal{D}^\theta$ is shown in (b) and (c). Figure reproduced with permission from Ref. [8].

where ρ is the density matrix of the system and $\mathcal{D}[\rho]$ is the Lindblad dissipator. The dissipator acts on the two sites at each end of the chain

$$\mathcal{D}[\rho] = \mathcal{D}_{1,2}(\beta_L)[\rho] + \mathcal{D}_{N-1,N}(\beta_R)[\rho] \tag{6.5}$$

where β_L and β_R parametrize the inverse temperature for left and right end of the chain respectively. We define two site boundary dissipative term $\mathcal{D}_{i,j}(\beta)[\rho]$ acting on the spin at site i and j using jump operators $L_{a\to b} = |b\rangle\langle a|$ as

$$\mathcal{D}_{i,j}(\beta)[\rho] = \lambda \sum_{ab} \Gamma_+(\beta)[L_{a\to b}, \rho L_{b\to a}] + \Gamma_-(\beta)[L_{a\to b}, \rho L_{b\to a}]^\dagger \tag{6.6}$$

Here λ quantifies the coupling strength between the system and the bath. The two-site states $|a\rangle$ and $|b\rangle$ are the eigenstates, with energy eigenvalues E_a and E_b, of a two-site Hamiltonian $h_{i,j}$ acting on sites i and j. The transition rates are given by $\Gamma_\pm = e^{\mp\beta(E_b-E_a)/2}$ as shown in Fig. 6.1(b). $h_{i,j}$ contains the dominant terms of the full Hamiltonian restricted to the ends of the chain.

In this manuscript, we have used two types of local boundary dissipators denoted by $\mathcal{D}^0_{i,j}$ and $\mathcal{D}^\theta_{i,j}$, constructed using two different choice of the two-site Hamiltonians $h^0_{i,j}$ and $h^\theta_{i,j}$.

1. $\mathcal{D}^0_{i,j}$ is defined using the two-site Hamiltonian $h^0_{i,j} = -J\sigma_i\sigma_j^\dagger + \text{H.c.}$ The ground state of h^0 is three fold degenerate ($|11\rangle$, $|\omega\omega\rangle$, and $|\bar{\omega}\bar{\omega}\rangle$) and its excited state is

six-fold degenerate with an energy gap of $3J$ between them. We have included Lindblad jump operators only between the non-degenerate eigenstates of h^0. We note that due to the ferromagnetic nature of h^0, use of $\mathcal{D}^0_{i,j}$ makes sense only when $\theta \in (-\pi/3, \pi/3)$ where the ferromagnetic states have a lower energy.

2. The dissipator $\mathcal{D}^\theta_{i,j}$ is constructed using $h^\theta_{i,j} = -Je^{\iota\theta}\sigma_i\sigma_j^\dagger + \text{H.c.}$ The ground state of h^θ is still three fold degenerate. These are the ferromagnetically aligned states when $\theta \in (-\pi/3, \pi/3)$ and When $\theta \in (\pi/3, \pi)$ the ground states are $|1\omega\rangle$, $|\omega\bar{\omega}\rangle$, and $|\bar{\omega}1\rangle$. Similarly, when $\theta \in (-\pi, -\pi/3)$, $|1\bar{\omega}\rangle$, $|\bar{\omega}\omega\rangle$, and $|\omega 1\rangle$ are the ground states. Introduction of the $e^{\iota\theta}$ prefactor in the local Hamiltonian breaks the six fold degeneracy of the excited states (except when θ is a multiple of $2\pi/3$). In defining the dissipator, we have included transitions between degenerate states of h^θ.

A schematic representation of the jump operators in $\mathcal{D}^0_{i,j}$ and $\mathcal{D}^\theta_{i,j}$ are shown in Fig. 6.1(b) and Fig. 6.1(c) respectively. The effective local temperatures generated by the two different dissipators as well as the length scales for thermalization near the boundary will be different for the two choice of dissipators. However we expect that qualitative features of transport will be similar in the two cases if the results are independent of the precise form of the bath. We indeed find this to be the case.

For finite dimensional systems, the LME has at least one fixed point (See Sec 4.2.2 of Ref. [191]). In small systems of upto 5 sites, we diagonalized the Liouvillian and found that it has a unique 0-eigenvalue state. Assuming the uniqueness to be true in larger systems, the time evolution under the above LME should approach a unique non-equilibrium steady state (NESS) defined as

$$\rho^\theta_{\text{NESS}} = \lim_{t\to\infty} \rho(t) \tag{6.7}$$

To obtain the NESS, we integrated the LME till large t and used saturation of local observables - energy current, energy density and magnetization on each site to check approach to steady state.

The local energy density E^θ_i at site i is chosen to be the three site operator

$$E^\theta_i = -\frac{J}{2}e^{\iota\theta}(\sigma_{i-1}\sigma_i^\dagger + \sigma_i\sigma_{i+1}^\dagger) - f\tau_i + \text{H.c} \tag{6.8}$$

The current operator on the bond between sites i and $i+1$ can be written as $I_i^\theta = \iota[E_{i+1}^\theta, E_i^\theta]$. We evaluate this to be

$$I_i^\theta = \iota \frac{fJe^{\iota\theta}}{2}(I_i^{(1)} + I_i^{(2)}) + \text{H.c} \tag{6.9}$$

where

$$\begin{aligned} I_i^{(1)} &= (\omega - 1)\sigma_i(\tau_i + \tau_{i+1})\sigma_{i+1}^\dagger \\ I_i^{(2)} &= (\bar{\omega} - 1)\sigma_i(\tau_i^\dagger + \tau_{i+1}^\dagger)\sigma_{i+1}^\dagger \end{aligned}$$

The energy and current operators satisfy the discrete continuity equation

$$\frac{dE_i^\theta}{dt} = \iota[H(\theta, 0), E_i^\theta] = I_i^\theta - I_{i-1}^\theta \tag{6.10}$$

The expectation value $\langle I_i \rangle_{\text{thermal}} = \text{Tr}(e^{-\beta H} I_i)/\mathcal{Z} = 0$ of the chosen form of the current operator is zero in the thermal state. This can be seen as follows. It can be checked that the unitary symmetry transformation operator $\mathcal{CS}$ introduced in Sec. 6.3 commutes with the Hamiltonian $H(\theta, 0)$ and anticommutes with I^θ. Now consider the expectation value of the symmetry transformed current:

$$\begin{aligned} \text{Tr}[e^{-\beta H}(\mathcal{CS})^\dagger I^\theta(\mathcal{CS})] &= \langle I^\theta \rangle_{\text{thermal}} \\ \text{Tr}[e^{-\beta H}(\mathcal{CS})^\dagger I^\theta(\mathcal{CS})] &= -\langle I^\theta \rangle_{\text{thermal}} \end{aligned} \tag{6.11}$$

suggesting that the current as defined is zero in the the thermal state. In the first equality we have used the cyclic property of the trace and the commutation of $\mathcal{CS}$ with H. In the second equality, we have used the anticommutation property with I.

Fick's law can be generalized to all transport regimes using an empirical exponent γ as

$$\langle I \rangle = \kappa \times (\langle E_N \rangle - \langle E_1 \rangle) \tag{6.12}$$

where κ is steady state energy conductance which scales as $1/N^\gamma$ with system size N. Ballistic and diffusive transport are characterized by $\gamma = 0$ and 1 respectively. Systems exhibiting a conduction with $0 < \gamma < 1$ and $\gamma > 1$ are said to have super-diffusive and sub-diffusive transport. We characterize the transport in the clock model from the scaling of $\langle I \rangle$ with N allowing us to estimate the exponent γ.

6.4 NESS currents at θ, $\theta + 2\pi/3$ and $-\theta$

In this section, we show that, under the time evolution (Eq 6.4) with the dissipator $\mathcal{D}^\theta$, the NESS current at θ is same as that at $-\theta$ and $\theta + 2\pi/3$. Using this equivalence of transport behavior at different θ, we can reduce the parameter region to be studied from $\theta \in [0, 2\pi)$ to $[0, \pi/3]$. To see the equivalence, we consider the unitary operators $\mathcal{U}_1 = \Pi_i \tau_i^i$ and $\mathcal{U}_2 = \Pi_i \mathcal{C}_i$. These transform the Hamiltonian as follows

$$\begin{aligned} \mathcal{U}_1^\dagger H(\theta, 0)\mathcal{U}_1 &= H(\theta + 2\pi/3, 0) \\ \mathcal{U}_2^\dagger H(\theta, 0)\mathcal{U}_2 &= H(-\theta, 0) \end{aligned} \tag{6.13}$$

Transformation of the dissipator $\mathcal{D}^\theta[\rho]$ under the unitaries $\mathcal{U}_1$ and $\mathcal{U}_2$ is given by

$$\begin{aligned} \mathcal{U}_1^\dagger \mathcal{D}^\theta[\rho]\mathcal{U}_1 &= \mathcal{D}^{\theta + 2\pi/3}[\mathcal{U}_1^\dagger \rho \mathcal{U}_1] \\ \mathcal{U}_2^\dagger \mathcal{D}^\theta[\rho]\mathcal{U}_2 &= \mathcal{D}^{-\theta}[\mathcal{U}_2^\dagger \rho \mathcal{U}_2] \end{aligned} \tag{6.14}$$

With these, it can be checked that the stationary solution ρ_{NESS} to the LME (Eq. 6.4) at $\theta + 2\pi/3$ and at $-\theta$ are related to the solution at θ by

$$\begin{aligned} \mathcal{U}_1^\dagger \rho_{\text{NESS}}^\theta \mathcal{U}_1 &= \rho_{\text{NESS}}^{\theta + 2\pi/3} \\ \mathcal{U}_2^\dagger \rho_{\text{NESS}}^\theta \mathcal{U}_2 &= \rho_{\text{NESS}}^{-\theta} \end{aligned} \tag{6.15}$$

Note that we have implicitly assumed that there is only one NESS at each θ. The energy density E_i^θ and current I_i^θ transform similarly to $H(\theta, 0)$ under $\mathcal{U}_1$ and $\mathcal{U}_2$.

The thermal expectation value of the current at $-\theta$ is given by

$$\langle I^{-\theta} \rangle = \text{Tr}[\rho^{-\theta} I^{-\theta}] = \text{Tr}[\mathcal{U}_2^\dagger \rho^\theta \mathcal{U}_2 \mathcal{U}_2^\dagger I^\theta \mathcal{U}_2] = \text{Tr}[\rho^\theta I^\theta] = \langle I^\theta \rangle \tag{6.16}$$

Similarly, we find that $\langle E_i^\theta \rangle = \langle E_i^{-\theta} \rangle = \langle E_i^{\theta + 2\pi/3} \rangle$ and $\langle I_i^\theta \rangle = \langle I_i^{-\theta} \rangle = \langle I_i^{\theta + 2\pi/3} \rangle$. These symmetries in the current and energy as a function of θ were verified in our numerical implementation of the LME. In Fig 6.2 symmetry in NESS current is shown for system size $N = 14$ and $f/J = 0.4$ using the dissipator $\mathcal{D}^\theta$. These results allow us to use the transport properties evaluated in $\theta \in [0, \pi/3]$ to infer the transport properties in the whole range $[0, 2\pi]$.

Similar arguments for the case of the dissipator $\mathcal{D}^0$ shows that the energy and currents at θ and $-\theta$ are equal to each other.

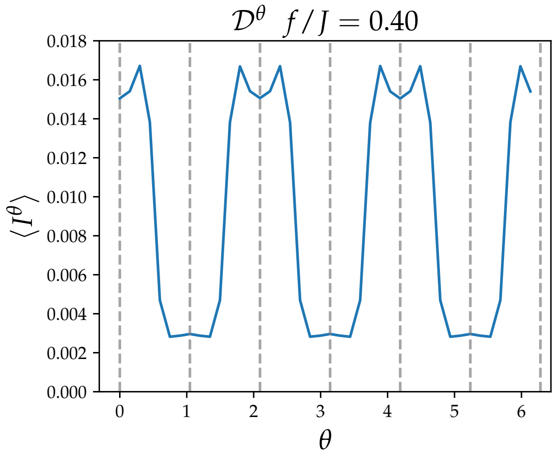

Fig. 6.2 Plot of the NESS current I^θ as a function of θ for its full range of values from 0 to 2π showing the equivalence of transport properties at θ, $-\theta$ and $\theta + 2\pi/3$. Data is shown for the system size $N = 14$, with the dissipator $\mathcal{D}^\theta$ at model parameters $f/J = 0.4$. Vertical lines show multiples of $\pi/3$. Inverse temperatures used for left and right baths are $\beta_L = 0.133$ and $\beta_R = 0.266$ respectively. Figure reproduced with permission from Ref. [8].

6.5 Numerical Implementation

Evolution under the LME (Eq. 6.4) was implemented using the Matrix Product State (MPS) formalism where we represent ρ as an MPS of the form

$$|\rho\rangle = \sum_{\sigma,\sigma'} A^{\sigma_1\sigma_1^{'}} A^{\sigma_2\sigma_2^{'}} \ldots A^{\sigma_N\sigma_N^{'}} |\sigma_1\sigma_2\ldots\sigma_N\rangle|\sigma_1^{'}\sigma_2^{'}\ldots\sigma_N^{'}\rangle \tag{6.17}$$

Each tensor A has physical indices of dimension 9. The MPS is normalized such that the density matrix satisfies the trace preserving condition:

$$\sum_{\sigma\sigma'} A^{\sigma_1\sigma_1^{'}} A^{\sigma_2\sigma_2^{'}} \ldots A^{\sigma_N\sigma_N^{'}} \delta_{\sigma_1\sigma_1^{'}} \delta_{\sigma_2\sigma_2^{'}} \ldots \delta_{\sigma_N\sigma_N^{'}} = 1 \tag{6.18}$$

In the LME (Eq. 6.4) operators can act on the density matrix ρ either from the left or right. Equivalent matrix product operator for the right and left action of operators on ρ contracts with non primed and primed indices respectively. We can write Eq. 6.4 in the super-operator form

$$\partial_t|\rho\rangle = \hat{\mathcal{L}}|\rho\rangle \tag{6.19}$$

where $\hat{\mathcal{L}}$ is a time independent super-operator called Liouvillian operator. The solution to Eq. 6.19 which can be formally written as $|\rho(t)\rangle = e^{\hat{\mathcal{L}}t}|\rho(0)\rangle$ can be evaluated using a fourth-order approximant to MPO similar to those used in Refs. [158, 157]. Matrix exponential approximant of any order can be expressed as product of several first order approximants $W^{\mathrm{II}}(\tau) = \mathbb{I} + \tau\mathcal{L}$ as

$$W^{\mathrm{II}}(\tau_1)W^{\mathrm{II}}(\tau_2)...W^{\mathrm{II}}(\tau_n) = \exp(\mathcal{L}t) + \mathcal{O}(t^{p+1}) \tag{6.20}$$

where τ's are complex numbers proportional to t. To obtain an approximant correct till order p, we match coefficients of t of each order up to p on both sides of Eq. 6.20. The τ_i are solutions of these p simultaneous nonlinear equations.

Assuming that the fixed point is unique, the choice of initial state should not affect the NESS. For completeness we describe the initial state preparation. We started with an infinite temperature state and time evolved it under the following Liouvillian $\mathcal{L}'[\rho]$

$$\mathcal{L}'[\rho] \equiv \imath[H,\rho] + \sum_{i=1}^{N-1} \mathcal{D}_{i,i+1}(\beta_i)[\rho] \tag{6.21}$$

with Lindblad dissipators $\mathcal{D}_{i,i+1}$ (Eq. 6.6) connected to all sites with inverse temperature at each site linearly varying with site number between β_L and β_R. The steady state of the time evolution under $\mathcal{L}'(t)$ is later used as an initial state for the actual time evolution. The initial state as well as the time evolved states are in equal mixtures of the three $\mathbb{Z}_3$ parity quantum numbers.

The inverse temperatures at the left and right ends are $\beta_L = 0.133$ and $\beta_R = 0.266$ respectively. The spin coupling is set to be $J = 1$ and the coupling to the Lindblad dissipators is set to $\lambda = 0.05$. Simulations were performed for systems with $f = 0.4$ and for a set of θ in the range $[0, \pi/3]$. Calculations were separately performed using the two different Lindblad dissipators $\mathcal{D}^0$ and $\mathcal{D}^\theta$. In all of our calculations, bond dimension χ being used is 200. For a select set of parameters we increased the bond dimension to 800, and no significant change was observed beyond 200 in the local observables.

6.6 Results

In this section we report the main results of the numerical simulations. The estimated current and energy density in the NESS, and the scaling exponent γ of the current as

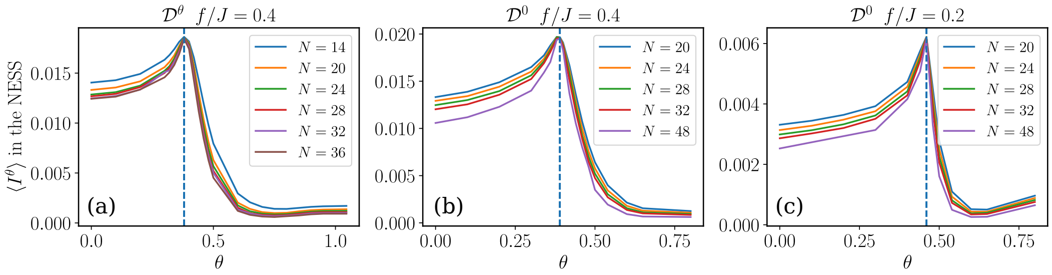

Fig. 6.3 NESS current $\langle I^\theta \rangle$ as a function of θ in the ferromagnetic regime. Panel (a) shows the current when the Liouvillian is defined using the dissipator $\mathcal{D}^\theta$ and $f/J = 0.4$. Panel (b) and (c) show the current for the case of the dissipator $\mathcal{D}^0$ with $f/J = 0.4$ and $f/J = 0.2$ respectively. Different lines indicate different system sizes. The peak current appears at the integrable point $\theta = \cos^{-1}(f/J)/3$ shown by vertical dashed lines in all cases. Inverse temperatures used for left and right bath are $\beta_L = 0.133$ and $\beta_R = 0.266$ respectively. Figure reproduced with permission from Ref. [8].

a function of system size are presented. In addition, we also present the level spacing statistics and the operator space entanglement entropy in the NESS.

6.6.1 NESS Current and Conductance

The mean NESS energy current $\langle I^\theta \rangle = \sum_i \langle I_i^\theta \rangle / N$ as a function of the chiral parameter θ is shown in Fig 6.3 (results do not change if the current at the center of the chain is used instead) Panel (a) shows the NESS current obtained using the dissipator $\mathcal{D}^\theta$ for parameter $f/J = 0.4$. Panels (b) and (c) show the same for the dissipator $\mathcal{D}^0$ for model parameter $f/J = 0.4$ and 0.2 respectively. In all cases we find a peak current at the θ where we expect the system to be integrable. When the model parameters are changed from $f/J = 0.4$ to $f/J = 0.2$, the θ at which the model is integrable changes. Accordingly the location of the peak current also changes. The NESS current is independent of the system size at the integrable point, consistent with it exhibiting a ballistic transport. The current decreases with the system size at other θ. These qualitative features are the same for both choice of dissipators.

At each value of θ, the system size dependence of the NESS current can be parametrized using γ obtained by fitting the NESS current measured in different system of sizes from $N = 14$ to $N = 48$ to the form $I^\theta(N_{\text{eff}}) = A N_{\text{eff}}^{-\gamma(\theta)}$. N_{eff} is the effective length of the chain which is $N - 4$ as two spins from each end is associated with the Lindblad dissipators. Figure 6.4(a) shows the current as a function of system

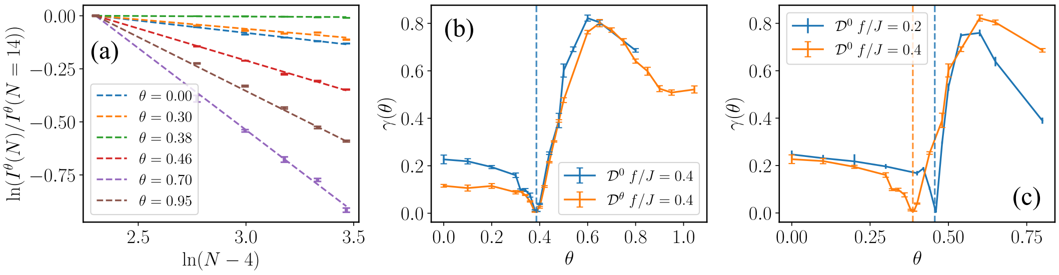

Fig. 6.4 Panel (a) presents $I^\theta(N)$ (rescaled by the current in the smallest system size) vs $N-4$ in log-scale for fixed values of θ for $f/J = 0.4$ and using the dissipator $\mathcal{D}^\theta$. Panels (b) and (c) show the scaling exponent γ estimated from the system size dependence of the NESS current $I^\theta(N)$. Estimated γ is plotted as function of θ in panels (b) and (c). In panel (b), we compare the exponent γ obtained from the two different choice of dissipators $\mathcal{D}^0$ and $\mathcal{D}^\theta$. In panel (c) we compare the estimated γ obtained using the same dissipator $\mathcal{D}^0$ but for $f/J = 0.2$ and $f/J = 0.4$. Inverse temperatures used for left and right bath are $\beta_L = 0.133$ and $\beta_R = 0.266$ respectively. Figure reproduced with permission from Ref. [8].

size for a representative set of values of θ. Within the range of system sizes accessible, we are able to fit the data to the power law form.

We present the estimated $\gamma(\theta)$ as a function of θ in panels (b) and (c) of Fig. 6.4. The estimates suggest a clear ballistic energy transport only at the integrable point where $\gamma \approx 0$. In Panel (b) of Fig. 6.4, scaling exponents computed using the two different dissipators show qualitatively the same behavior, and the two estimates quantitatively agree except in a region near small θ. We suspect that the difference at the small θ may be a consequence of different length scales associated with thermalization at the boundary, resulting in different effective lengths for the chain. In Fig. 6.4(c) γ is plotted for NESS obtained using the dissipator $\mathcal{D}^0$ for $f/J = 0.2$ and 0.4, showing ballistic transport at the expected value of $\theta = \frac{1}{3}\cos^{-1}(f/J)$.

Studies in disordered spin-1/2 systems have suggested large length scales at weak disorder leading to super-diffusive behavior being observed in finite size calculations [175, 176]. We cannot rule out a similar possibility - that a diffusive behavior emerges in larger systems - with the results from the currently accessible system sizes. Spatial profiles of the energy density and current in the NESS for the super-diffusive and ballistic cases are shown in Fig. 6.5. As expected the energy density is independent of the position in the bulk in the case of the ballistic system.

The analysis in this section relies on the scaling of the current with system size. This yields γ provided that the energy densities at the ends of the chain are independent of

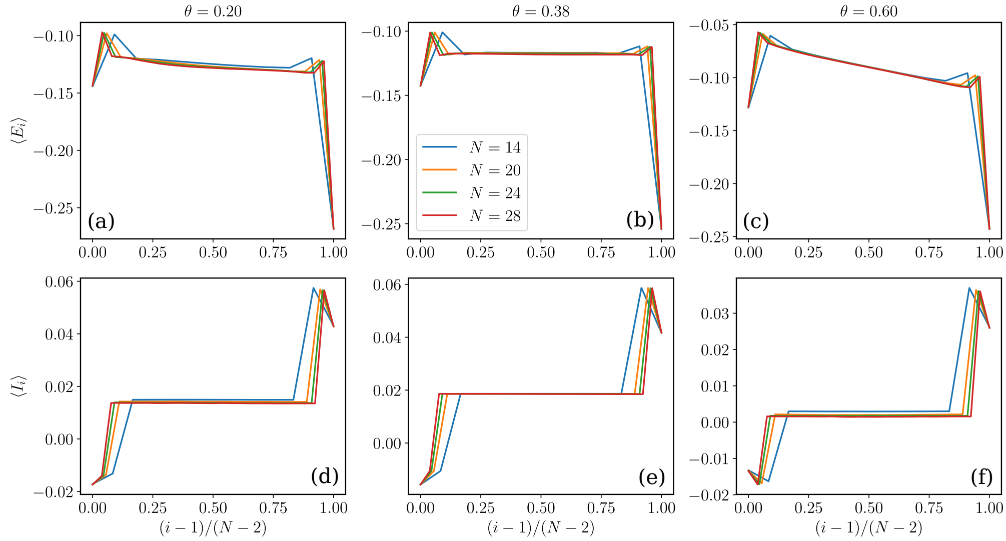

Fig. 6.5 Spatial profile of energy density and current for system sizes N=14, 20, 24, and 28 with position shown on the x-axis rescaled by a factor of $1/(N-2)$. Profiles for Hamiltonian parameters $\theta = 0.2$ in panel (a) and (d), $\theta = 0.38$ in panel (b) and (e), and $\theta = 0.2$ in panel (c) and (f). $\theta \sim 0.38$ is close to the integrable point. Inverse temperatures used for left and right bath are $\beta_L = 0.133$ and $\beta_R = 0.266$ respectively. Figure reproduced with permission from Ref. [8].

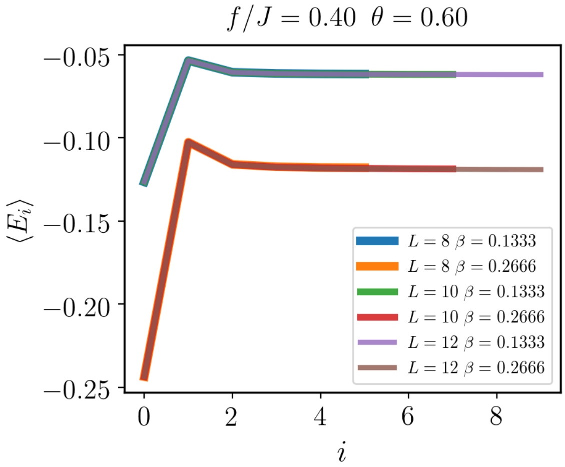

Fig. 6.6 Energy density as a function of the position in the NESS obtained after attaching only one bath to a chain. The two different lines indicate the energy densities realized upon attaching baths with parameters β_R and β_L. Different overlapping lines of different thicknesses show the data for different system sizes. Figure reproduced with permission from Ref. [8].

the system sizes (such that conductance is proportional to the current). In very large systems this can be true, but in small systems the energy densities can be affected by the bath at the other end, resulting in an energy difference that is system size dependent. An estimate of the local energy density that will be realized at the ends if there were local equilibration near the bath can be obtained by attaching only bath to the system. We performed this calculation for each of the two baths. Figure 6.6 presents the results one of these calculations. Figure 6.7 shows examples of energy densities as a function of position for different system sizes and parameter regimes (sites very close to the baths have been excluded). The estimates of the expected energy densities if the baths had locally equilibrated with the ends of the chain are shown in dotted lines.

At the θ very close to the integrable point (Fig. 6.7 panel (b)), the energy densities are midway between the bath energy densities (dotted lines). The energies are approximately independent of the position and system size. In the case of the θ larger than the integrable value (panel (d) of Fig 6.7), the energy densities realized in the chain are very close to the bath energy densities (indicated by the dotted lines). In the case of θ smaller than that of the integrable point, the energy densities are position dependent but are far from the estimated bath energy densities. The system size dependence of these energy density difference may then need to be taken into account to make a correct estimate of γ.

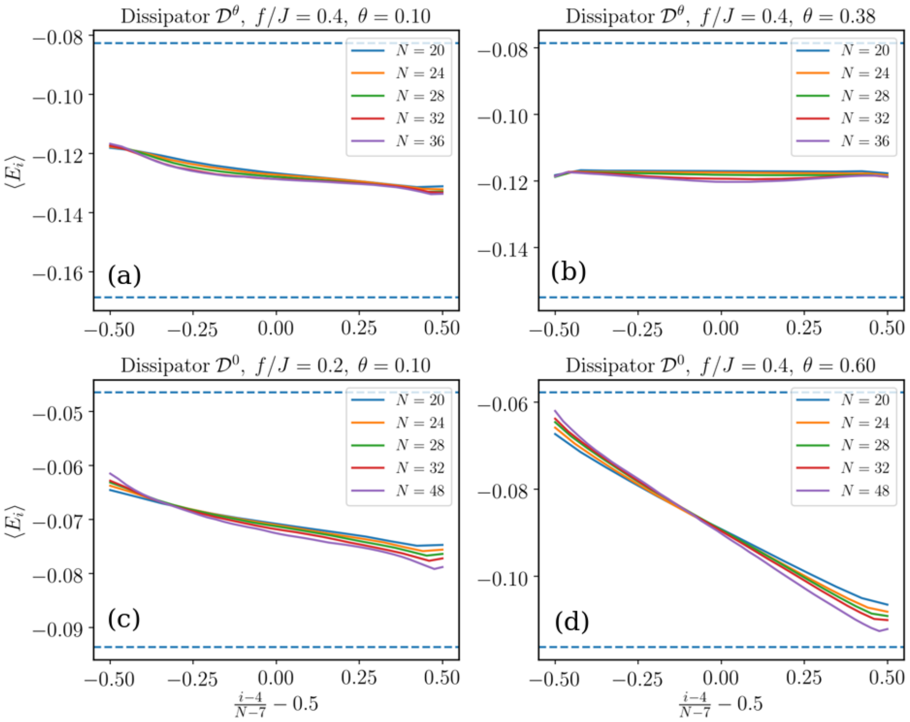

Fig. 6.7 Each panel shows the energy densities as a function of the position for different system sizes. Position on the x-axis has been rescaled and shifted that center of the chain is at 0 and the 4^{th} spin from the ends are at ±0.5. The two dotted lines show the expected energy densities had the each one of the baths fully equilibrated with the chain (See Fig 6.6). The four panels show the data for four different cases. Panels (a) and (c) show results for θ less than that of the integrable point. Panel (b) shows the data at a θ very close to the integrable point. Panel (d) shows the same at θ larger than that of the integrable point. Inverse temperatures used for left and right bath are $\beta_L = 0.133$ and $\beta_R = 0.266$ respectively. Figure reproduced with permission from Ref. [8].

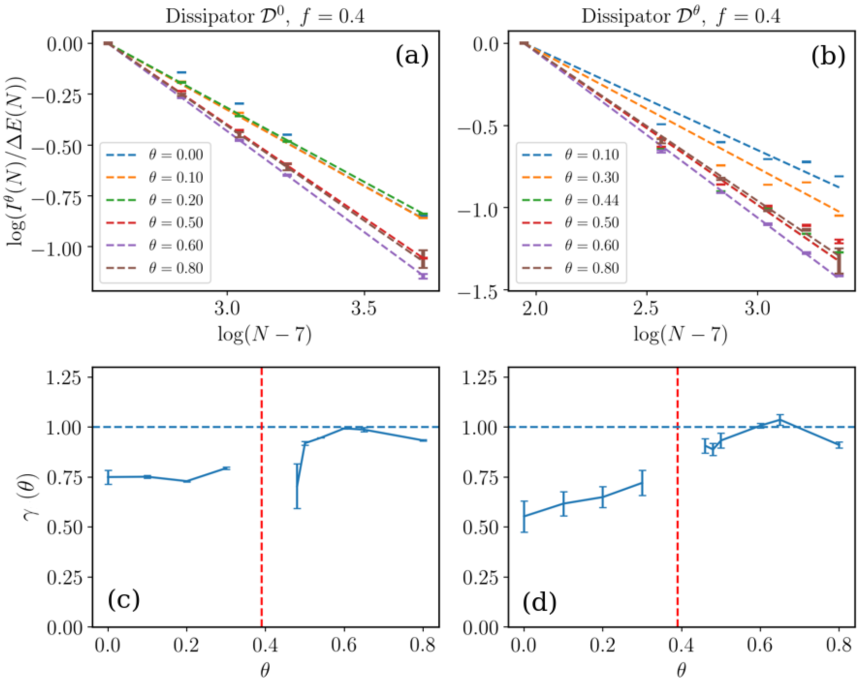

Fig. 6.8 In panel (a) and (b), $\log(I^\theta(N)/\Delta E)$ vs $\log(N-7)$ is shown for both dissipators $\mathcal{D}^0$ and $\mathcal{D}^\theta$. Scaling exponent γ is obtained by linearly fitting $\log(I^\theta(N)/\Delta E)$ vs $\log(N-7)$ data and is plotted as function of θ in panels (c) and (d). θ in the vicinity of integrable points (vertical dashed line) are not shown as the numerically obtained conductance κ show wild oscillations due to vanishing energy gradient. Figure reproduced with permission from Ref. [8].

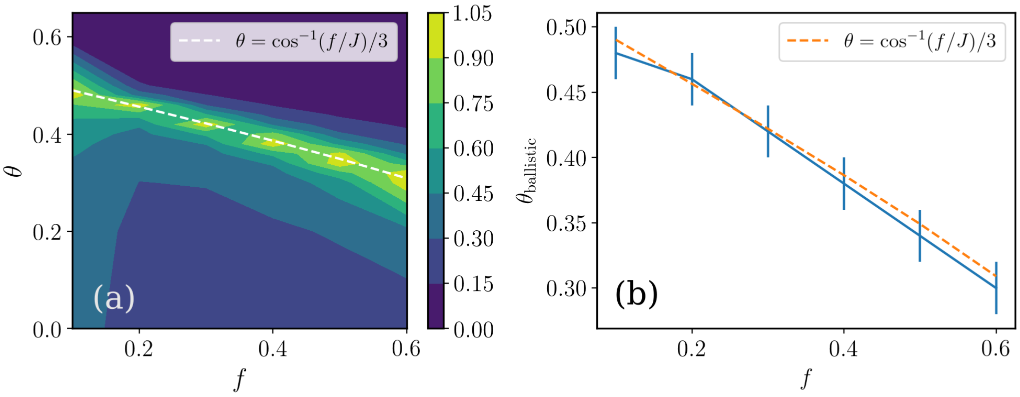

Fig. 6.9 (a) Rescaled current I_{rescaled} of NESS as a function of θ and f/J is plotted. Comparison of numerically estimated $\theta_{\text{ballistic}}$ and the integrable line $\theta = \cos^{-1}(f/J)/3$ is shown in (b). Figure reproduced with permission from Ref. [8].

In Fig. 6.8 we show the results of the γ estimated from the scaling with system size of the conductance. In order to define the conductance, we have assumed that the energy density differences are proportional to temperature differences, taking the ratio of the current to the energy density difference between the 4th site from either ends of the chain, distance between them being $N-7$. The scaling exponent obtained by fitting the conductance to $N^{-\gamma(\theta)}$ in the panels (c) and (d). The results indicate a larger value of γ than what was obtained from scaling of current.

For θ larger than that of the integrable point, the sites near the ends appear to have nearly equilibrated with the bath (Fig. 6.7(d)). In these cases we find the scaling γ to be very close to that of a diffusive system. For smaller θ, where the energy gradients are smaller and much larger system sizes may be needed in order to reliably estimate the true scaling properties. We have not shown the conductance scaling in the vicinity of the integrable points as the energy gradients are nearly zero and numerically estimated conductances show wild variations.

We now discuss a broader range of f values. For not too small system sizes, we expect the peak current and conductance κ to occur at the θ values exhibiting ballistic transport. We may therefore use the peak conductance at each f as a proxy to identify the values of θ at each f exhibiting ballistic transport. Figure 6.9 shows the estimated current re-scaled and shifted by f-dependent constants chosen such that for each f, the maximum value of I_{rescaled} is 1 and minimum is 0. Within the numerical uncertainties due to the finite resolution of θ values, we find that the peak current occurs along the expected line $f/J = \cos(3\theta)$ of integrable points [187, 47].

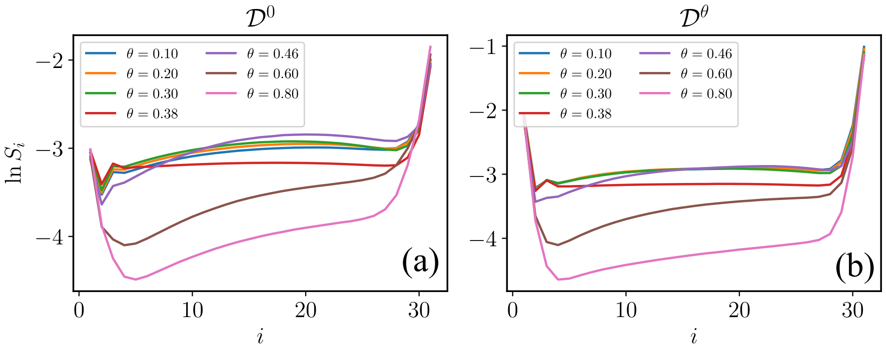

Fig. 6.10 Operator space entanglement entropy S_i plotted as a function of the bond location i. All data are for system size $N = 32$ and at $f/J = 0.4$. The two panels show the entropy for the NESS obtained under the dissipators $\mathcal{D}^0$ and $\mathcal{D}^\theta$. Figure reproduced with permission from Ref. [8].

6.6.2 Operator space entanglement

Analogous to the notion of entanglement between different bipartitions of many body states, one can define an operator space entanglement entropy (OSEE) [192, 193] from the MPS representation of the density operator. From the Schmidt decomposition of the state across a partition located at bond i, the entropy can be computed as $S_i = -\mathrm{Tr} R_i \log R_i$ where R_i is the reduced density matrix obtained as the partial trace $\mathrm{Tr}_{j>i} |\rho\rangle\langle\rho|$. OSEE of the NESS at different locations of the partition is shown for system size $N = 32$ and $f/J = 0.4$ is plotted in Fig.6.10. Empirically we find that at the integrable points, away from the edges, the OSEE is independent of the location of the partition, and for the non-integrable points, S_i shows weak position dependence.

The singular values from which the OSEE was constructed also is weakly position dependent in the case of the integrable points. Translation invariance of the entropy as well as of the expectation values of the local operators - energy density and current - at the integrable point suggest the possibility of a translation invariant MPS approximation for the NESS at the integrable points similar to Ref [194].

6.7 Level spacing statistics

To verify the connection between energy transport and quatnum chaos which has already been reported in the earlier works, we used the level spacing statistics and ratio[21]. Proper evaluation of the spacing statistics involves two major steps - Eigenspectrum of

Hamiltonian in a given symmetry sector and unfolding of the spectrum. Each of this steps are explained in subsequent subsections.

6.7.1 Spectrum through Exact Diagnoalization

Chiral clock Hamiltonian is invariant under the symmetries $\mathcal{P}$, $\mathcal{T}$ and $\mathcal{CS}$ for $\theta \neq 0$ and $\phi = 0$. For the correct numerical evaluation of the level spacing statistics we want the spectrum of the Hamiltonian which is from one of the symmetry sector of above mentioned symmetries. For spin chain of length N, when working in the eigenbasis of τ operator, we have 3^N many-body basis states in total. Under the global parity symmetry $\mathcal{P}$, eigenbasis can be split into three subsets of equal sizes *i.e* 3^{N-1}. Each of these subsets are indexed by the parity eigenvalue 1, ω or $\bar{\omega}$. We decided to work in the eigenbasis of τ operator because it provides major convenience in state representation of the parity eigenstates. The eigenstates of the τ operator are as follows

$$
\begin{aligned}
|O\rangle &= \frac{|1\rangle + |\omega\rangle + |\bar{\omega}\rangle}{\sqrt{3}} \\
|W\rangle &= \frac{|1\rangle + \omega|\omega\rangle + \bar{\omega}|\bar{\omega}\rangle}{\sqrt{3}} \\
|\bar{W}\rangle &= \frac{|1\rangle + \bar{\omega}|\omega\rangle + \omega|\bar{\omega}\rangle}{\sqrt{3}}
\end{aligned}
$$

with the eigenvalues 1, ω and $\bar{\omega}$ respectively. From the properties of operators $\mathcal{T}$ and $\mathcal{C}$, it is easy to see that eigenstates of τ operator transform as follows - $\mathcal{T}|O\rangle = |O\rangle$, $\mathcal{T}|W\rangle = |\bar{W}\rangle$, $\mathcal{T}|\bar{W}\rangle = |W\rangle$, $\mathcal{C}|O\rangle = |O\rangle$, $\mathcal{C}|W\rangle = |\bar{W}\rangle$ and $\mathcal{C}|\bar{W}\rangle = |W\rangle$.

When working in the τ eigenbasis of the form $|\psi\rangle = |\tau_1 \otimes \tau_2 \otimes \cdots \otimes \tau_N\rangle$, each basis state belongs to the one of the parity eigensector from the three possible parity sectors. The parity sector has the following properties under the operators $\mathcal{T}$ and $\mathcal{CS}$

- Parity sector with $\mathcal{P} = 1$ can be further divided into subsectors under the symmetries $\mathcal{T}$ and $\mathcal{CS}$
- Parity sector with $\mathcal{P} = \omega$ or $\bar{\omega}$ can not be further divided into subsectors under the symmetries $\mathcal{T}$ and $\mathcal{CS}$. As the action of $\mathcal{T}$ and $\mathcal{CS}$ on the parity basis states in these sectors changes the parity of the state from ω to $\bar{\omega}$ and vice-versa

Because of the above mentioned properties of the each parity sectors, It is sufficient to work in parity sectors with parity $\mathcal{P} = \omega$ or $\bar{\omega}$ as no further symmetries are presented in these sectors.

6.7.2 Unfolding Procedure

In the level spacing distribution of the spectrum of a Hamiltonian, we are interested in fluctuations in the energy levels of the spectrum. For the comparison of the level spacing of two different Hamiltonian, we can not compare them if they have different average spacings. Even for the different parts of a spectrum, comparison of level spacing can not be done if they have different average spacings. Unfolding is the procedure which enable us to make these comparisons by rescaling the eigenvalues through setting the local mean spacing to 1.

There is not a unique way to unfold a spectrum. We will describe the unfolding procedure that we have used in our work. We started with the ordered eigenvalues *i.e* $E_1 < E_2 \ldots E_n$ in increasing order of energy. Around 10 percent of the eigenvalues are thrown away from each end of the spectrum. Then we calculated the cumulative spectral function $\eta(E)$ which is

$$\eta(E) = \sum_{i=1}^{n} \Theta(E - E_i) \tag{6.22}$$

where n is the number of eigenvalues remained after throwing some off and Θ is Heaviside step function. Equation 6.22 essentially indexes the ordered eigenvalues. Cumulative spectral function $\eta(E)$ can be decomposed into the following form

$$\eta(E) = \xi(E) + \eta_{fl}(E) \tag{6.23}$$

where $\xi(E)$ is the smooth part and $\eta_{fl}(E)$ is the fluctuating part. The smooth part of the function is obtained by fitting the $\xi(E)$ to polynomial of degree 15.

Level spacing statistics (within a symmetry sector of $\mathbb{Z}_3$ parity) computed in a finite system of size $N = 11$ (Fig. 6.11) show Poisson statistics at the integrable point and a mixture of GOE and Poisson distributions at other values of θ. The distribution is closer to GOE away from the integrable points. Consistent with this, the estimates of γ increase away from the integrable points, however it does not indicate fully diffusive behavior in any region of θ.

6.8 Conclusion

A large body of studies on quantum transport in spin chains performed primarily on spin-half models have indicated that integrable systems show a ballistic energy transport

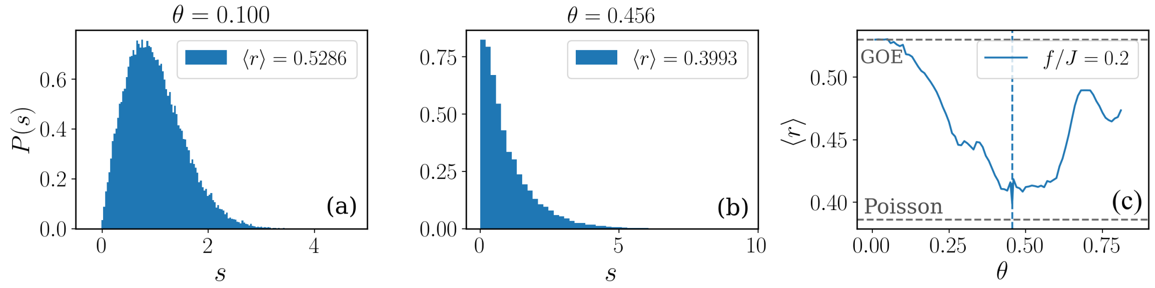

Fig. 6.11 Level spacing distributions for $\theta = 0.1$ and $\theta = 0.456$ (close to the ballistic point) are shown in panels (a) and (b) respectively. In (c), variation of mean level spacing ratio $\langle r \rangle$ is plotted versus θ showing change in level spacing statistics from GOE to Poissonian at the integrable point $\cos^{-1}(f/J)/3$. Figure reproduced with permission from Ref. [8].

and deviations from integrability generally lead to a diffusive behavior[173, 172, 170] with possible exceptions[164].

In this work we have studied the transport properties of the $\mathbb{Z}_3$ clock model that goes beyond the spin half chains. At the integrable points in the model parameter space, NESS shows a system size independent current, suggesting a ballistic energy transport. At all other values of the parameters the current decreases with the system size. The transport scaling exponent γ estimated from scaling of the current alone shows indicates a super-diffusive behavior. Careful analysis of the energy density profiles suggests that this is likely to be a consequence of finite size effects in the system. System size dependence of the energy gradient also needs to be taken into account. The scaling exponent inferred from the conductance instead shows the values closer to diffusive behavior. The results demonstrate the connection between integrability and ballistic transport in a larger class of models beyond the well-studied spin half chains.

We have used local Lindblad coupling to the edges of a finite chain of chiral $\mathbb{Z}_3$ clock to approximately model the coupling of the system to the bath. Within this approach, we obtained similar results when different dissipator models were used at the edge, suggesting a robustness of the results to the precise nature of the coupling of the system to the bath. Direct computation of the Drude weights can be an independent approach to verify the characterization of transport properties in the model [195–199].

Chapter 7

Temporal order in periodically driven spins in star-shaped clusters

We experimentally study the response of star-shaped clusters of initially unentangled $N = 4$, 10 and 37 nuclear spin-$\frac{1}{2}$ moments to an inexact π-pulse sequence, and show that an Ising coupling between the centre and the satellite spins results in robust period-two magnetization oscillations. The period is stable against bath-effects but the amplitude decays with a time scale that depends on the inexactness of the pulse. Simulations reveal a semiclassical picture where the rigidity of the period is due to a randomizing effect of the Larmor precession under the magnetization of surrounding spins. The time scales with stable periodicity increase with net initial magnetization even in the presence of perturbations, indicating a robust temporal ordered phase for large systems with finite magnetization per spin.

7.1 Introduction

Spontaneous symmetry-breaking is a central notion in many body physics, allowing us to explain several natural phenomena such as formation of a magnet or ice crystals. While there are many systems in which the underlying spatial symmetries are broken resulting in various crystalline phases, and a few classical systems that exhibit spontaneous temporal oscillations, it was only recently that the possibility of spontaneous breaking of time translation symmetry in quantum systems was considered. The initial proposals [200] for realizing a spontaneous breaking of continuous time translation symmetry were later shown to be forbidden in static equilibrium systems [201, 202]. However, in the attempt to understand quantum thermodynamics of driven systems, it was realized that an externally driven, disordered, interacting spin system can stabilize a phase which spontaneously break the discrete time translation ($\mathbb{Z}$) symmetry of the system to a subgroup $n\mathbb{Z}$ [99, 84, 203, 204]. The phenomenon was soon experimentally realized in trapped cold-atom systems that mimic a long range interacting disordered spin-half chain [30], and in dense collections of randomly interacting nitrogen vacancy spin impurities embedded in diamond [83, 205]. While this work was under review, similar observations were also realized in other solid NMR experiments[85].

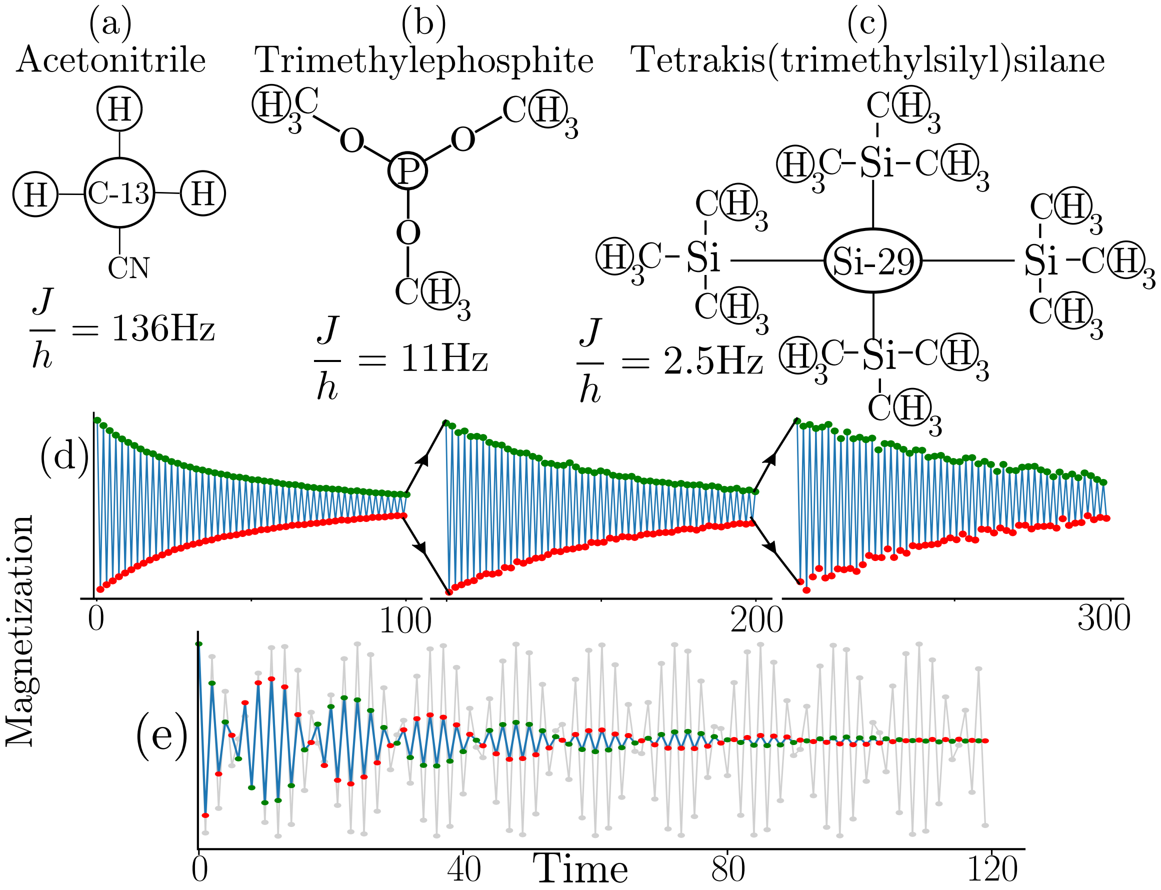

Fig. 7.1 Molecules used in the experiments - acetonitrile (a), trimethyl phosphite (TMP) (b) and tetrakis(trimethylsilyl)silane (c) with the 4, 10 and 37 NMR active nuclei encircled. (d) Experimentally measured magnetization $\langle S_i^z \rangle$ of satellite spins of TMP for the pulse sequence in Eq. 7.1 with $JT/\hbar = 6.5$ and $\theta = \pi - 0.1$. Red/green dots show the magnetization at odd/even time steps. For visibility in the plot, the y axis has been rescaled at every 100th time step. (e) Blue line shows experimentally measured magnetization oscillations of free/non-interacting spins of protons in acetonitrile which contain a spinless $\mathrm{C}-12$ central spin, at a pulse angle $\theta = \pi - 0.27$. Gray lines indicate the expected response in the absence of a bath. Figure reproduced with permission from Ref. [9].

In this work, we report on the observation of robust period two oscillations of magnetization in a cluster of nuclear spins in a simple star-shaped geometry with a central spin interacting with N surrounding satellite spins via Ising interactions mediated by the electron cloud in the molecule. The satellite spins do not interact with each other. Spins in each molecule show magnetization oscillations of period-two, as expected, when subjected to a sequence of transverse π-pulses (pulses that rotate every up/down spin by π radians). However the Ising interactions within the cluster result in the period rigidly locking on to two, even under a sequence of inexact π pulses (pulses that rotate by an amount $\pi - e$). Simulations of an isolated cluster show that the period is robust even in the presence of small perturbations and disorder that break the symmetries of the model. For the present work we perform nuclear magnetic resonance (NMR) experiments on acetonitrile, trimethyl phosphite (TMP) and tetrakis(trimethylsilyl) silane (TTSS) containing $4, 10$ and 37 spins [Fig 7.1 (a-c)] [206]. The experiments are performed on ensembles of $\sim 10^{15}$ molecules with a distribution of initial states, described by a direct product density matrix. High precision ensemble average magnetization measurements of central/satellite spins can be performed using free-induction decay signals. Period-two oscillation of individual spins result in corresponding oscillations of the ensemble average magnetization. Control experiments performed on molecules that contain a spinless isotope at the center show oscillations with frequencies that linearly vary with the deviation e, showing that the robustness of the period originates from interaction with the central spin. In the following, unless units are made explicit, frequencies are in units where the time period $T = 1$.

7.2 Model and numerical results

The unitary operator evolving the state of the cluster between successive steps is given by

$$U\left(J,\theta;t\right) = \exp\left[-\frac{\imath Jt}{\hbar} S_0^z \Sigma_{i=1}^{N-1} S_i^z\right] \text{ for } t \in [0,T) \tag{7.1}$$
$$U\left(J,\theta;T\right) = \exp\left[-\imath\theta \Sigma_{i=1}^{N-1} S_i^x\right] \exp\left[-\frac{\imath JT}{\hbar} S_0^z \Sigma_{i=1}^{N-1} S_i^z\right]$$

where J, T and θ are the Ising interaction strength, time period and the rotation angle characterizing the pulse. S_i^μ are spin operators. Site index $i = 0$ labels the central spin (See Ref [207, 208] for a description of liquid-state NMR which realizes the unitary)

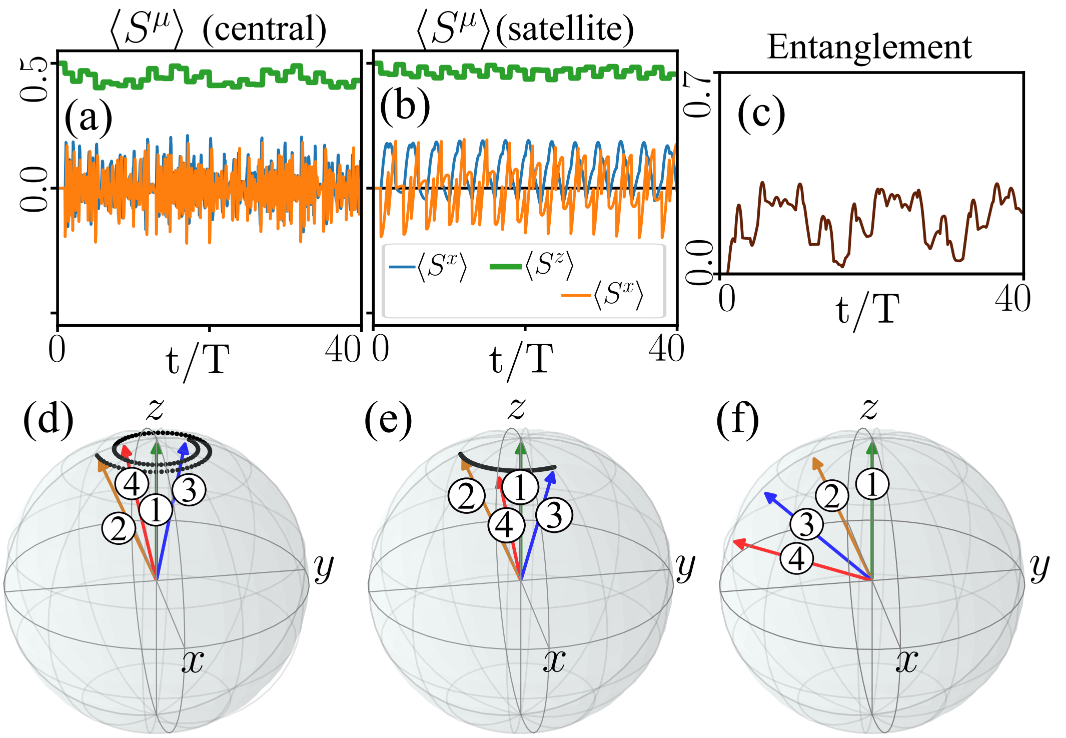

Fig. 7.2 Numerical simulations of spins in the rotating basis. (a-b) Time dependence of the expectation values of the three spin components of a satellite (a) and central (b) spin for a system with $N = 8$ spins, $\frac{JT}{\hbar} = 4$ and pulse angle $\theta = e = 0.4$. Initial state is the fully z-polarized state. (c) Entanglement entropy of the central spin. (d) Bloch sphere representing the spin components of a central spin (of a 6 spin cluster) at times $t = 0$, T^+, $2T^-$ and $2T^+$; $+/-$ labels the time just after/before the pulse. Sequence of intermediate dots track the evolution between time $t = T$ and $2T$. (e) Same as (d) but for a satellite spin. (f) Bloch vectors for a single isolated spin at successive time steps. Figure reproduced with permission from Ref. [9].

We will label the deviation from π pulse by $e = \pi - \theta$. To simplify the discussion below, it is useful to temporarily switch to a toggling frame of reference in which the basis of every spin rotates by an angle π about the x-axis after each pulse. On account of the $\mathbb{Z}_2$ symmetry of the model, the unitary operator in the rotating basis retains the same form as in Eq. 7.1 but with a reduced pulse angle $e = \pi - \theta$, *i.e.*, the spins in the rotating basis see a unitary operator $U(J, -e; t)$. A constant z-magnetization of all spins in the rotating basis picture corresponds to a period-two oscillation of all physical spins. Numerical simulations indeed show that a finite magnetization is maintained under a sequence of weak pulses (pulse angle $-e$). Presented below is a semiclassical picture inferred from numerical simulations (Fig 7.2).

For simplicity, we will consider the time evolution starting from a fully polarized initial state under a sequence of small pulses $\theta = -e$ (corresponding to $\theta = \pi - e$ experienced by the physical spins). During $0 < t < T$, the spins do not evolve as the state is an eigenstate of the unitary evolution (Eq. 7.1). At time $t = T$, the pulse rotates every spin by an angle e away from z-axis as shown on the Bloch sphere (see Fig. 7.2). During $T < t < 2T$, the central spin which is tilted away from the z-axis evolves under the Hamiltonian $H \approx -J \langle M_\mathrm{s} \rangle S_0^z$ where M_s is the net z magnetization of the satellite spins resulting in a Larmor-like precession as shown in Fig. 7.2(d). The orientation of the central spin at $t = 2T^-$ depends on the amount of precession $\frac{JT\langle M_\mathrm{s} \rangle}{\hbar}$. The e pulse at $t = 2T$ now brings the spin vector to a polar angle $0 < \theta < 2e$. Owing to the precession, the successive e pulses can now cancel each other. In contrast, in a set of non-interacting spins the angles always add constructively leading to a steady increase in the polar angle (ne after n pulses - Fig. 7.2(f)). Thus the randomizing effect of the interaction induced Larmor precession, causes the polarization of the central spin to survive longer than that of an isolated spin. We expect the same effect to be seen also on the surrounding spins except that they precess under the magnetization of the central spin alone resulting in a slower precession of the satellite spins compared to the central spin (Fig. 7.2(f)). Constant sign of the Bloch-vector component $\langle S^z \rangle$ in the rotating basis implies a period two oscillation of the physical spin orientation (Fig. 7.2(a,b)). Such a semiclassical picture assumes that the central spin is not maximally entangled with the surrounding spins, as otherwise the Bloch vector may vanish in length even when the polar angle is conserved. As shown in Fig. 7.2(c), the von Neumann entropy of the central spin stays below maximum ensuring finite Bloch vectors. Simulations of the small systems at much longer time scales using exact diagonalization indicate that entanglement of the system does not rise for time scales that increase exponentially with system size (Fig. 7.3(c,d)).

In the following, we will use the physical spin basis. To explore the stability of the period to perturbations other than e, we numerically simulated a pure spin system with a time independent perturbation to the Hamiltonian of the form $\sum_i h_i^x S_i^x + h_i^z S_i^z$. The quenched disorder h_i^x and h_i^z were picked uniformly from $[-\delta/2, \delta/2]$ and $[0, \delta]$ (in units where $T/\hbar = 1$). To compare the response of different system sizes, we fix the average magnetization per spin. We found that in all cases, the time scale in which there was a dominant period-two oscillation appeared to grow exponentially with system size (Fig. 7.3(b)). Similar increase in time scales were also observed in simulations with disorder free perturbations of the form $h_z \sum S_i^z$ and $J_x \sum S_i^x S_{i+1}^x$[208]. The time scales with stable period are higher when the initial state of the spin cluster had a larger

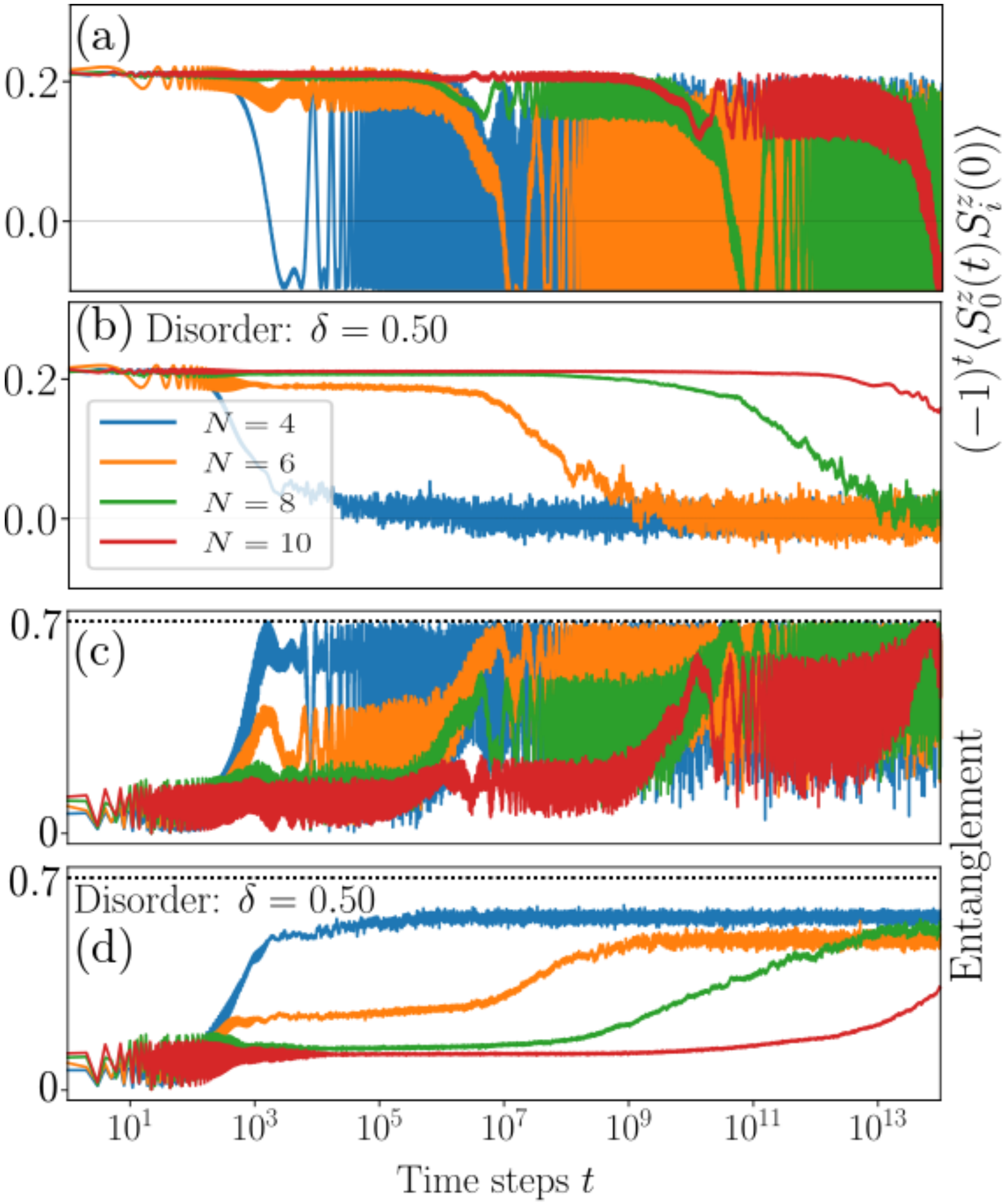

Fig. 7.3 (a,b) Time dependence of cross correlation (multiplied by $(-1)^t$) between the central spin S_0^z and a satellite spin S_i^z from simulations of systems of different sizes ($JT/\hbar = 4, e = 0.05$, $\psi = R_x(\pi/8)\,|\uparrow\uparrow\ldots\rangle$, $R_x(\pi/8)$ being the rotation of all spins by $\pi/8$ about x). Disorder strengths are 0 (a,c) and 0.5 (b,d). (c,d): Entanglement entropy of the central spin. Disorder averaging has been performed in (b,d). Figure reproduced with permission from Ref. [9].

total magnetization. Slow heating and stability in this disorder free system is likely to be associated with a prethermal regime similar to that in Ref [[100, 209]]. However, unlike the high frequency case discussed there, the experiments here are performed at low frequencies ($JT > 1$). Cross correlation between the central and satellite spins (Fig. 7.3(a,b)) show that different spins oscillate in synchrony suggesting that the robustness of the period is a collective behavior of all spins.

For small e and the $\mathbb{Z}_2$ symmetric unitary (Eq. 7.1), origin of the period-two oscillations at finite deviation e can be understood in a manner similar to that described in Ref [84]. The Floquet unitary describing the periodic drive commutes with the parity operator $P = \prod 2S_i^x$ and therefore the quasienergy eigenstates have a parity quantum number ± 1. The quasienergy states of the system at $\theta = 0$ occur in degenerate quasienergy pairs of opposite parity $\psi_\pm = |\sigma_0, m\rangle \pm |-\sigma_0, -m\rangle$, where $|\sigma_0, m\rangle$ is a state with central and satellite spins in an eigenstate of S_0^z and $\sum_{i=1}^{N-1} S_i^z$ with eigenvalues σ_0 and m. At small finite pulse angle $\theta = e$, the quasienergy-degeneracy is broken in a manner that depends on the magnetization $|m|$ as $\sim e^{2|m|+1}$. In the presence of a sequence of inexact π pulses $\theta = \pi - e$, the unitary is $U(J, \pi - e; T) = PU(J, -e; T)$ for which the states $\psi_\pm$ have quasienergies separated by $\pi + \mathcal{O}(e^{2|m|+1})$. A polarized direct product initial state $|\sigma_0, m\rangle$ is a symmetric or antisymmetric linear combination of the states $\psi_\pm$. As a result, the unitary for inexact π pulses acts on such a polarized state to flip the orientation of all the spins at each time step:

$$U\,|\sigma_0, m\rangle = U(\psi_+ \pm \psi_-) \sim \psi_+ \pm e^{-\imath\pi}\ \psi_- = |-\sigma_0, -m\rangle$$

resulting in a period-two magnetization oscillation. Better degeneracies of the higher magnetization initial states explains why initial states with larger magnetization shows stable periodicity for longer time scales. Subleading ocillations of other frequencies originate from mixing of $\psi_\pm$ with states of smaller magnetizations.

7.3 NMR setup:

The spin systems used for the experiments - Acetonitrile, TMP and TTSS are prepared in the solvents dimethyl sulfoxide/deuterated chloroform. The experiments are carried out at 300 K in a Bruker 400 MHz NMR-spectrometer equipped with an UltraShield superconducting magnet of strength 9.39 T. The unitary of Eq. 7.1 is realized in a doubly rotating frame [207, 208]. The θ pulses are realized by simultaneous resonant, short duration radio-frequency pulses on all spins. The pulse duration can be tuned to control θ. Interaction parameter $JT/\hbar$ can be set by tuning the time period T. After n pulses, any residual transverse magnetization is destroyed using a pulsed-field-gradient (PFG) and the final magnetization $\langle S^z \rangle$ is rotated into the transverse direction with the help of a $\pi/2$ detection pulse. The NMR signal is then detected as the oscillatory emf induced in a probe coil due to the precessing transverse magnetization about the Zeeman field [210, 208]. During each period, the measurement was performed immediately after the pulse.

Initial states in the experimental ensemble of $\sim 10^{15}$ molecules can be descibed by mixed state of the form $\rho = \prod_{i=0}^{N-1} \otimes \rho_i$, where $\rho_i = \frac{1}{2}(\mathbb{I} + \epsilon \sigma_i^z)$, and the purity $\epsilon \approx 10^{-5}$, σ^z being the Pauli matrix. The purity is inferred from the thermal equilibrium distribution at the magnetic field strength inside the spectrometer. Note that while the ensemble average magnetization is small, the ensemble contains subensembles of all possible initial magnetizations $-N/2 \leq M \leq N/2$, with a marginally higher fraction (parameterized by ϵ) with positive sign. Clusters with finite magnetization $|M|$ show stable periodic-two oscillations which collectively reflect in the ensemble average measurements.

7.4 Results and discussion

: Fig. 7.4 shows the measured satellite spin magnetizations in TMP and acetonitrile for an interaction parameter $\frac{JT}{\hbar} = 20.7$ ($J/h = 11$ Hz, $T = 0.3$ s). Magnetization oscillations on TMP (Fig. 7.4 (a,b,c)) show a clear peak at frequency half (subharmonic peak), whose height decreases with increase in the deviation e, vanishing at $e \approx 0.4\pi$ in agreement with the simulations. There are no discernible peaks in the spectrum at frequencies $\frac{\pi \pm e}{2\pi}$ expected from non-interacting spins. Fourier transforms were taken using standard FFT algorithms applied to the data from the chosen time window. For comparability, magnetization data was normalized such that initial magnetization was 1.

The RF pulses have ±5% distribution of θ values around the nominal value, due to the spatial inhomogeneity of the RF field over the volume of the sample. The experimental system suffers from decoherence due to coupling to an external thermal bath. This could explain the decay of the oscillation amplitudes with time [211]. Apart from this decay, the magnitude of the subharmonic peaks in each time window match the simulations. Interestingly the decay time decreases steadily with e (Fig 7.4 (c)).

Acetonitrile sample contains a mixture with 99% of the molecules carrying a spinless C-12 and 1% of the molecules containing spinful C-13 atom in the methyl

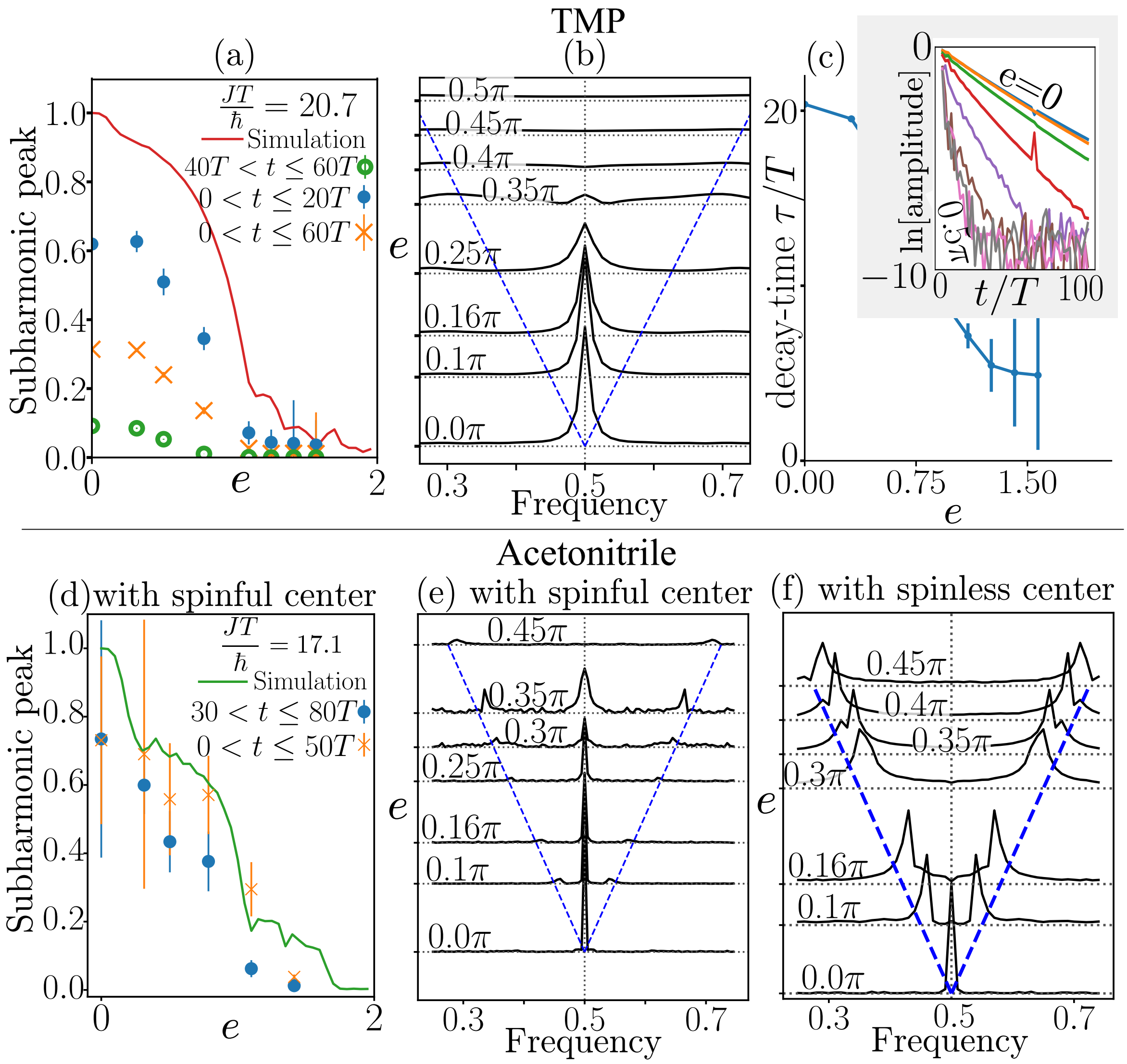

Fig. 7.4 Experimentally measured satellite spin magnetization $\sum_{i=1}^{N-1}\langle S_i^z\rangle$. (a,d): Magnitude of the subharmonic peak upon varying e in TMP and Acetonitrile. Solid continuous lines show results from simulations. Different markers indicate Fourier transforms of experimental measurements in different time windows. (b): Waterfall plot of the Fourier spectrum (time-window $0 < t < 80T$) of the experimentally observerd magnetization of TMP at different deviations e. Dashed blue lines indicate the location of peaks expected for a free spin. (c): Variation of the decay time of the experimentally observerd magnetization amplitude with e for TMP. (e,f): Same as (b) but for acetonitrile with a spinfull C-13 (e) and spinless C-12 (f) atom at the center. Figure reproduced with permission from Ref. [9].

group. Although NMR signal has contributions from the satellite spins of both isomers, their contributions can be separated in the frequency domain of the induced emf oscillations during the final measurement process thanks to the presence or absence of

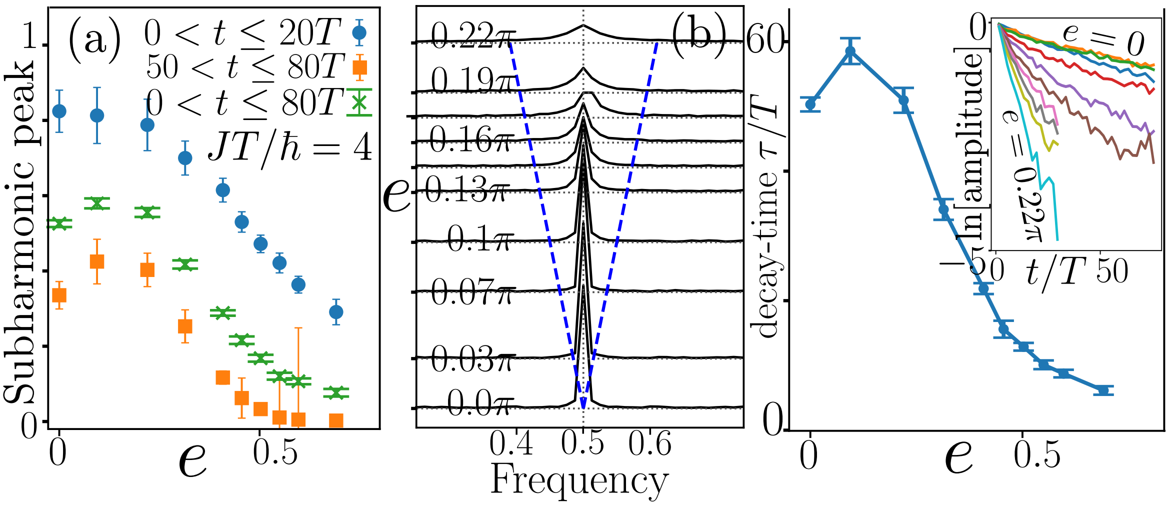

Fig. 7.5 Experimental values of central spin magnetization $\langle S_0^z \rangle$ in TTSS. (a): Subharmonic peak strength as a function of the deviation e. Different markers indicate Fourier transforms in different time windows. (b): Waterfall plot of the Fourier spectrum of the experimentally observed central spin magnetization at different e. Blue dashed line shows the location of the Fourier peaks expected for free spins. (c): Decay time scale as a function of e. Inset shows a semi log plot of the amplitude of magnetization as a function of time. Figure reproduced with permission from Ref. [9].

interaction with the central spin, and thus they can be analysed separately. Experiments on acetonitrile were performed at the parameter $\frac{JT}{\hbar} \approx 17.1$ ($J/h = 136$Hz, $T = .02$s). Figure 7.4(e) shows the Fourier transforms of magnetization of the satellite spins in acetonitrile that contain a spinfull C-13 central atom. Figure 7.4(f) shows the Fourier transform of the magnetization of the satellite spins in molecules containing a spinless C-12 central atom. In the absence of a central spin with which the satellites can interact, they oscillate like isolated spins with a frequency that varies linearly with e. Absence of stable period in this non interacting system clearly shows that the stability of period observed in other clusters arise from interactions. Fig. 7.5 shows the results for magnetization measurements of the central Si-29 spin of the TTSS molecule which has $N = 36$ satellite spins around the central atom. Experiments were performed at $JT/\hbar \approx 4$ ($J/h = 2.5$Hz, $T = 0.25$s).

7.5 Conclusion

We have experimentally demonstrated that stable temporal order can be realized in NMR spin-clusters. Absence of a stable period in the control experiment in C-12 acetonitrile shows that stability of the period requires interactions between the spins (as in C-13 acetonitrile). Though bath effects and other perturbations in the experiment lead to a magnetization decay with time, interestingly the period appears to be unaffected. Stability of the period in the spin cluster improves with increase in total initial magnetization. Therefore large systems with finite initial magnetization per spin, should show a stable temporal ordered phase. The stability of the oscillations in such systems can be interpreted as an error-correction on the pulse sequence and may find potential applications towards robust quantum information processing [212]. Eq.

Chapter 8

Conclusion

Interacting quantum many-body systems driven out-of-equilibrium exhibits a rich set of physical phenomena. Explorations in the field has helped us refine our description of the emergent macroscopic world, such as mechanisms for thermalization, equilibration, and decoherence. About a century of research into principles governing quantum and classical many-body systems in equilibrium have revealed a fascinating range of emergent structures in these systems. Spurred by the developments in quantum computing systems, precision experimental probes of quantum many-body dynamics, and a rapidly developing set of computational tools, there is increasing interest in understanding robust guiding principles applicable in the out-of-equilibrium settings.

The advent of DMRG and MPS formalisms for quantum many-body systems has led to the possibility of highly precise simulations of relatively long-time dynamics of large quantum many-body systems. In this work, we have analyzed aspects of dynamics in a specific interacting quantum system using MPS and related techniques. The works presented in this thesis are among the few which have attempted to explore out-of-equilibrium physics in models with local Hilbert space bigger than that of spin-1/2 particles. The larger Hilbert space, while resulting in richer structures such as more complex domain walls and richer phase diagram, also makes the calculations harder due to the faster growth of Hilbert space. Therefore, the power of the MPS formalism was crucial to the studies presented here. In addition to elucidation of the dynamical features in the chiral clock model, the effort put in this work has also resulted in developing local expertise in the broad range of techniques which can be applied to a strongly interacting quantum systems.

A quantum system can be driven out of equilibrium in various ways. Quenches, ramping, and periodic driving are the simplest methods employed to drive a closed system out of equilibrium. The system can also be connected to dissipative baths, making it an open quantum system. We have studied such out-of-equilibrium settings in context of a specific model namely chiral clock model.

Using insights from conformal field theory and Kibble-Zurek mechanism [103] it was shown that dynamics of Loschmidt echo follows the following universal scaling [5] for critical quantum Ising model under boundary Floquet drive in slow driving regime ($T >> h_b^{-\nu}$)

$$\mathcal{L}(NT) = c_N (T h_b^{-\nu})^{-N\gamma} \tag{8.1}$$

where N is an integer quantifying the number of Floquet drives, T is the time period and h_b is the magnitude of longitudinal field acting on the boundary spins. Scaling exponent γ depends on details of the drive sequence around the critical point. In chapter 3, we numerically studied the applicability of the arguments in the context of critical $\mathbb{Z}_3$ clock model [6] which is also described by CFT. We find that scaling Eq. 8.1 and the arguments derived from CFT and Kibble-Zurek mechanism indeed holds true for the non-trivial interacting model like $\mathbb{Z}_3$ clock model.

Effect of chirality specifically on entanglement dynamics after weak quenches is discussed in chapter 4. Chirality as well as multiple domain wall flavors in the makes physics richer than the Ising case. Relaxation in quantum quenches is understood in terms of the spread of domain walls as they are the carrier of energy. Unusual domain wall dynamics is seen at the boundary of the finite size chain because of the interplay between chiral parameter θ and f/J. At the boundary, the domain wall changes its flavor when parameter θ is less than critical value θ_c for the quench Hamiltonian. The domain wall flavor is preserved after scattering for θ larger than θ_c. This θ dependent scattering of domain walls from the boundary leads to different entanglement dynamics for the chiral and non-chiral quenches when the subsystem is considered at the boundary [7]. Long coherence time or slow relaxation observed for the boundary spins for chiral quenches is also related to θ dependent scattering [151].

In Chapter 6 we studied the energy transport in chiral clock model connected to dissipative baths modeled using local Lindblad dissipators. We have addressed the dependence of energy transport behavior on the Hamiltonian parameters θ and f/J. We found out that the chiral clock model shows ballistic energy transport on the integrable line $f/J = \cos(3\theta)$ and diffusive transport otherwise [8].

Through large scale numerical calculations we have explored range of questions pertaining to chiral clock model and parallelly developed numerical tools in the process. There are several aspects and parameter regimes of the chiral clock model which were unexplored in our studies. We have explored some aspects of it in the works discussed earlier. Summary of the partial results along with the open questions are addressed below.

Effect of the parameter ϕ, which acts as a uniform magnetic field for the domain walls and breaks time reversal symmetry makes physics richer, which needs to be explored. In the quenching problem, it will be interesting to see the effect of ϕ in the quench protocol from the ordered initial state on the dynamics of the domain wall, entanglement, local magnetization, *etc.* Characterizing the energy transport for the non-zero ϕ in the phase diagram is still an open question. Our analysis of energy transport in the chiral clock model can suffer from finite size effects. Our results can be verified by the numerical calculation of Drude weight.Transition between the gapped phases have dynamical critical exponent $z \neq 1$ for non-zero θ and ϕ, therefore it is unlikely to be described by conformal field theory. Boundary Floquet drive around such critical points with $z \neq 1$ makes an interesting problem to check the universal scaling of quantities like Loschmidt echo, entropy, *etc.*

Another way to look at thermalization is from the information perspective. Even though the dynamics of a closed quantum system is unitary, we know that quantum ergodic systems relax to a thermal state. In other words, by doing local measurements, we can not know from which state system started with *i.e* localized information is lost at large t because of information scrambling. Out-of-time order correlator (OTOC) is a useful quantifier to understand information scrambling in quantum and classical systems. OTOC essentially exploits the non-commutativity of local operators at different sites with time as Heisenberg operators are no more spatially local as time progresses. For a non-localized phase, OTOC has ballistic traveling wavefront at the late time with a rapid increase in front of the wavefront and saturation behind the wavefront. For the $\mathbb{Z}_3$ chiral clock model with some additional next nearest neighbour interaction, it was shown that there is an asymmetric flow of information using OTOC by tuning Hamiltonian parameters [213]. For the chiral clock model, the effect of parameters θ and ϕ on the behavior of OTOC and information propagation is still an open question. We have some preliminary results on the OTOC, which we will summarise. For a closed quantum system with Hamiltonian H, OTOC $\mathcal{F}_{ij}(t)$ is defined using the Heisenberg operator $\hat{O}(t) = e^{\iota Ht}\hat{O}e^{-\iota Ht}$ as

$$\mathcal{F}_{ij}(t) = \langle \hat{O}_i^\dagger(t)\hat{O}_j^\dagger(t)\hat{O}_i(0)\hat{O}_i(0)\rangle_\beta \tag{8.2}$$

where $\hat{O}_i = \sigma_i$ and $\hat{O}_j = \sigma_j$ are operators localized at site i and j. $\langle \dots \rangle_\beta$ is the thermal expectation value at inverse temperature β. It is more convenient to use relative OTOC

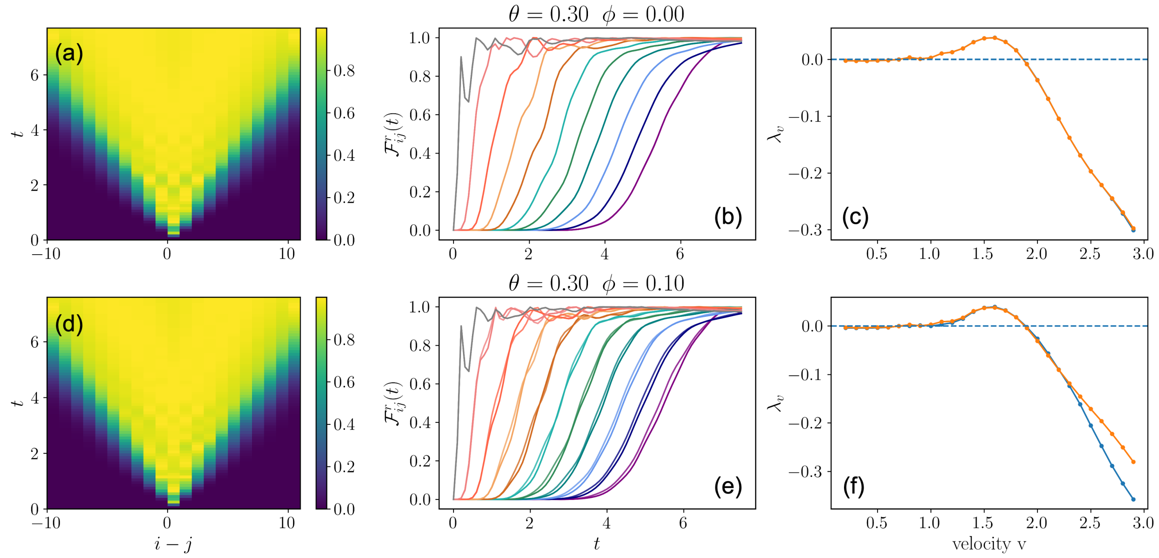

Fig. 8.1 Panels a and d show the heatmap for the relative OTOC $\mathcal{F}^r_{ij}$ versus operator separation distance $i - j$ for parameter $\phi = 0.0$ and 0.1 respectively. we have $\theta = 0.3$ for the all the plots presented here. Asymmtery inside the light cone between $+(i - j)$ and $-(i - j)$ is clearly visible when we use the lineplots with $\mathcal{F}^r_{ij}$ and t plotted in y and x axis respectively. Asymmtery inside the light cone can be seen for $(\theta, \phi) = (0.3, 0.1)$ which is plotted in panel (e) while inside of light cone is symmetric for $(\theta, \phi) = (0.3, 0.0)$ which is plotted in panel (b). Velocity dependent Lyapunov exponent λ_v [10] is ploted as a function of velocity v for cases $(\theta, \phi) = (0.3, 0.0)$ and $(\theta, \phi) = (0.3, 0.1)$ in panels (c) and (f). Data presented here is obtained using Krylov subspace technique.

defined as

$$\mathcal{F}^{r}_{ij}(t) = \frac{|\mathcal{F}_{ij}(t) - \mathcal{F}_{ij}(0)|}{\mathcal{F}_{ij}(0)} \tag{8.3}$$

For the chiral clock model, we studied the effect of parameters θ and ϕ at infinite temperature state using the Krylov subspace-based methods till $|i-j| = 10$. The results are also verified with MPS calculation.

Our empirical observation is that outside the light cone, there is no asymmetry in the operator spreading for every value of θ and ϕ. We observe that inside the light cone for $\theta \neq 0$ and $\phi \neq 0$, there is asymmetry in the operator spread which can be seen in the line plots for different $|i-j|$ in fig. 8.1 (b) and (e). This asymmetry is otherwise absent for $\phi = 0$ and $\theta \neq 0$.

References

[1] Paul Fendley, K. Sengupta, and Subir Sachdev. Competing density-wave orders in a one-dimensional hard-boson model. *Phys. Rev. B*, 69:075106, Feb 2004.

[2] Hannes Bernien, Sylvain Schwartz, Alexander Keesling, Harry Levine, Ahmed Omran, Hannes Pichler, Soonwon Choi, Alexander S. Zibrov, Manuel Endres, Markus Greiner, Vladan Vuletić, and Mikhail D. Lukin. Probing many-body dynamics on a 51-atom quantum simulator. *Nature*, 551(7682):579–584, November 2017.

[3] Ye Zhuang, Hitesh J. Changlani, Norm M. Tubman, and Taylor L. Hughes. Phase diagram of the z3 parafermionic chain with chiral interactions. *Phys. Rev. B*, 92:035154, Jul 2015.

[4] Adam S. Jermyn, Roger S. K. Mong, Jason Alicea, and Paul Fendley. Stability of zero modes in parafermion chains. *Phys. Rev. B*, 90:165106, Oct 2014.

[5] William Berdanier, Michael Kolodrubetz, Romain Vasseur, and Joel E. Moore. Floquet dynamics of boundary-driven systems at criticality. *Phys. Rev. Lett.*, 118:260602, Jun 2017.

[6] Naveen Nishad and G. J. Sreejith. Scaling of loschmidt echo in a boundary-driven critical $z3$ potts model. *Phys. Rev. B*, 101:144302, Apr 2020.

[7] Naveen Nishad, M. Santhosh, and G. J. Sreejith. Postquench entropy growth in a chiral clock model. *Phys. Rev. B*, 103:195141, May 2021.

[8] Naveen Nishad and G J Sreejith. Energy transport in z3 chiral clock model. *New Journal of Physics*, 24(1):013035, January 2022.

[9] Soham Pal, Naveen Nishad, T. S. Mahesh, and G. J. Sreejith. Temporal order in periodically driven spins in star-shaped clusters. *Phys. Rev. Lett.*, 120:180602, May 2018.

[10] Vedika Khemani, David A. Huse, and Adam Nahum. Velocity-dependent lyapunov exponents in many-body quantum, semiclassical, and classical chaos. *Phys. Rev. B*, 98:144304, Oct 2018.

[11] Takashi Mori, Tatsuhiko N Ikeda, Eriko Kaminishi, and Masahito Ueda. Thermalization and prethermalization in isolated quantum systems: a theoretical overview. *Journal of Physics B: Atomic, Molecular and Optical Physics*, 51(11):112001, may 2018.

[12] J. M. Deutsch. Quantum statistical mechanics in a closed system. *Phys. Rev. A*, 43:2046–2049, Feb 1991.

[13] Mark Srednicki. Chaos and quantum thermalization. *Phys. Rev. E*, 50:888–901, Aug 1994.

[14] Marcos Rigol, Vanja Dunjko, and Maxim Olshanii. Thermalization and its mechanism for generic isolated quantum systems. *Nature*, 452(7189):854–858, Apr 2008.

[15] Hyungwon Kim, Tatsuhiko N. Ikeda, and David A. Huse. Testing whether all eigenstates obey the eigenstate thermalization hypothesis. *Phys. Rev. E*, 90:052105, Nov 2014.

[16] Shoki Sugimoto, Ryusuke Hamazaki, and Masahito Ueda. Test of the eigenstate thermalization hypothesis based on local random matrix theory. *Phys. Rev. Lett.*, 126:120602, Mar 2021.

[17] Marcos Rigol, Vanja Dunjko, Vladimir Yurovsky, and Maxim Olshanii. Relaxation in a completely integrable many-body quantum system: An ab initio study of the dynamics of the highly excited states of 1d lattice hard-core bosons. *Phys. Rev. Lett.*, 98:050405, Feb 2007.

[18] Marcos Rigol, Alejandro Muramatsu, and Maxim Olshanii. Hard-core bosons on optical superlattices: Dynamics and relaxation in the superfluid and insulating regimes. *Phys. Rev. A*, 74:053616, Nov 2006.

[19] D.M. Basko, I.L. Aleiner, and B.L. Altshuler. Metal–insulator transition in a weakly interacting many-electron system with localized single-particle states. *Annals of Physics*, 321(5):1126–1205, May 2006.

[20] I. V. Gornyi, A. D. Mirlin, and D. G. Polyakov. Interacting electrons in disordered wires: Anderson localization and low-t transport. *Phys. Rev. Lett.*, 95:206603, Nov 2005.

[21] Vadim Oganesyan and David A. Huse. Localization of interacting fermions at high temperature. *Phys. Rev. B*, 75:155111, Apr 2007.

[22] Marko Žnidarič, Toma ž Prosen, and Peter Prelovšek. Many-body localization in the heisenberg xxz magnet in a random field. *Phys. Rev. B*, 77:064426, Feb 2008.

[23] Peter Reimann. Typical fast thermalization processes in closed many-body systems. *Nature Communications*, 7(1):10821, Mar 2016.

[24] Thiago R de Oliveira, Christos Charalambous, Daniel Jonathan, Maciej Lewenstein, and Arnau Riera. Equilibration time scales in closed many-body quantum systems. *New Journal of Physics*, 20(3):033032, March 2018.

[25] Sheldon Goldstein, Takashi Hara, and Hal Tasaki. Time scales in the approach to equilibrium of macroscopic quantum systems. *Phys. Rev. Lett.*, 111:140401, Oct 2013.

[26] Luis Pedro García-Pintos, Noah Linden, Artur S. L. Malabarba, Anthony J. Short, and Andreas Winter. Equilibration time scales of physically relevant observables. *Phys. Rev. X*, 7:031027, Aug 2017.

[27] Toshiya Kinoshita, Trevor Wenger, and David S. Weiss. A quantum newton's cradle. *Nature*, 440(7086):900–903, April 2006.

[28] R. Driben, B. A. Malomed, A. V. Yulin, and D. V. Skryabin. Newton's cradles in optics: From n-soliton fission to soliton chains. *Phys. Rev. A*, 87:063808, Jun 2013.

[29] C. J. Turner, A. A. Michailidis, D. A. Abanin, M. Serbyn, and Z. Papić. Quantum scarred eigenstates in a rydberg atom chain: Entanglement, breakdown of thermalization, and stability to perturbations. *Phys. Rev. B*, 98:155134, Oct 2018.

[30] J. Zhang, P. W. Hess, A. Kyprianidis, P. Becker, A. Lee, J. Smith, G. Pagano, I.-D. Potirniche, A. C. Potter, A. Vishwanath, N. Y. Yao, and C. Monroe. Observation of a discrete time crystal. *Nature*, 543(7644):217–220, mar 2017.

[31] J. Smits, L. Liao, H. T. C. Stoof, and P. van der Straten. Observation of a space-time crystal in a superfluid quantum gas. *Phys. Rev. Lett.*, 121:185301, Oct 2018.

[32] Xiao Mi, Matteo Ippoliti, Chris Quintana, Ami Greene, Zijun Chen, Jonathan Gross, Frank Arute, Kunal Arya, Juan Atalaya, Ryan Babbush, Joseph C. Bardin, Joao Basso, Andreas Bengtsson, Alexander Bilmes, Alexandre Bourassa, Leon Brill, Michael Broughton, Bob B. Buckley, David A. Buell, Brian Burkett, Nicholas Bushnell, Benjamin Chiaro, Roberto Collins, William Courtney, Dripto Debroy, Sean Demura, Alan R. Derk, Andrew Dunsworth, Daniel Eppens, Catherine Erickson, Edward Farhi, Austin G. Fowler, Brooks Foxen, Craig Gidney, Marissa Giustina, Matthew P. Harrigan, Sean D. Harrington, Jeremy Hilton, Alan Ho, Sabrina Hong, Trent Huang, Ashley Huff, William J. Huggins, L. B. Ioffe, Sergei V. Isakov, Justin Iveland, Evan Jeffrey, Zhang Jiang, Cody Jones, Dvir Kafri, Tanuj Khattar, Seon Kim, Alexei Kitaev, Paul V. Klimov, Alexander N. Korotkov, Fedor Kostritsa, David Landhuis, Pavel Laptev, Joonho Lee, Kenny Lee, Aditya Locharla, Erik Lucero, Orion Martin, Jarrod R. McClean, Trevor McCourt, Matt McEwen, Kevin C. Miao, Masoud Mohseni, Shirin Montazeri, Wojciech Mruczkiewicz, Ofer Naaman, Matthew Neeley, Charles Neill, Michael Newman, Murphy Yuezhen Niu, Thomas E. O'Brien, Alex Opremcak, Eric Ostby, Balint Pato, Andre Petukhov, Nicholas C. Rubin, Daniel Sank, Kevin J. Satzinger, Vladimir Shvarts, Yuan Su, Doug Strain, Marco Szalay, Matthew D. Trevithick, Benjamin Villalonga, Theodore White, Z. Jamie Yao, Ping Yeh, Juhwan Yoo, Adam Zalcman, Hartmut Neven, Sergio Boixo, Vadim Smelyanskiy, Anthony Megrant, Julian Kelly, Yu Chen, S. L. Sondhi, Roderich Moessner, Kostyantyn Kechedzhi, Vedika Khemani, and Pedram Roushan. Time-crystalline eigenstate order on a quantum processor. *Nature*, 601(7894):531–536, November 2021.

[33] Bruno Bertini, Pavel Kos, and Toma ž Prosen. Exact correlation functions for dual-unitary lattice models in $1 + 1$ dimensions. *Phys. Rev. Lett.*, 123:210601, Nov 2019.

[34] Adam Nahum, Sagar Vijay, and Jeongwan Haah. Operator spreading in random unitary circuits. *Phys. Rev. X*, 8:021014, Apr 2018.

[35] Brian Skinner, Jonathan Ruhman, and Adam Nahum. Measurement-induced phase transitions in the dynamics of entanglement. *Phys. Rev. X*, 9:031009, Jul 2019.

[36] Steven R. White. Density matrix formulation for quantum renormalization groups. *Phys. Rev. Lett.*, 69:2863–2866, Nov 1992.

[37] Ulrich Schollwöck. The density-matrix renormalization group in the age of matrix product states. *Annals of Physics*, 2011.

[38] J. Ignacio Cirac, David Pérez-García, Norbert Schuch, and Frank Verstraete. Matrix product states and projected entangled pair states: Concepts, symmetries, theorems, December 2021.

[39] Jutho Haegeman, J. Ignacio Cirac, Tobias J. Osborne, Iztok Pižorn, Henri Verschelde, and Frank Verstraete. Time-dependent variational principle for quantum lattices. *Phys. Rev. Lett.*, 107:070601, Aug 2011.

[40] Pierre Pfeuty. The one-dimensional ising model with a transverse field. *Annals of Physics*, 57(1):79–90, March 1970.

[41] Markus Greiner, Olaf Mandel, Tilman Esslinger, Theodor W. Hänsch, and Immanuel Bloch. Quantum phase transition from a superfluid to a mott insulator in a gas of ultracold atoms. *Nature*, 415(6867):39–44, Jan 2002.

[42] David A. Huse. Tricriticality of interacting hard squares: Some exact results. *Phys. Rev. Lett.*, 49:1121–1124, Oct 1982.

[43] Subir Sachdev, K. Sengupta, and S. M. Girvin. Mott insulators in strong electric fields. *Phys. Rev. B*, 66:075128, Aug 2002.

[44] C. J. Turner, A. A. Michailidis, D. A. Abanin, M. Serbyn, and Z. Papić. Weak ergodicity breaking from quantum many-body scars. *Nature Physics*, 14(7):745–749, Jul 2018.

[45] Natalia Chepiga and Frédéric Mila. Floating phase versus chiral transition in a 1d hard-boson model. *Phys. Rev. Lett.*, 122:017205, Jan 2019.

[46] Rhine Samajdar, Soonwon Choi, Hannes Pichler, Mikhail D. Lukin, and Subir Sachdev. Numerical study of the chiral z3 quantum phase transition in one spatial dimension. *Phys. Rev. A*, 98:023614, Aug 2018.

[47] Paul Fendley. Parafermionic edge zero modes inZn-invariant spin chains. *Journal of Statistical Mechanics: Theory and Experiment*, 2012(11):P11020, nov 2012.

[48] J. Sólyom and P. Pfeuty. Renormalization-group study of the hamiltonian version of the potts model. *Phys. Rev. B*, 24:218–229, Jul 1981.

[49] Johannes Motruk, Erez Berg, Ari M. Turner, and Frank Pollmann. Topological phases in gapped edges of fractionalized systems. *Phys. Rev. B*, 88:085115, Aug 2013.

[50] S. Ostlund. Incommensurate and commensurate phases in asymmetric clock models. *Phys. Rev. B*, 24:398–405, Jul 1981.

[51] V. L. Pokrovsky and A. L. Talapov. Ground state, spectrum, and phase diagram of two-dimensional incommensurate crystals. *Phys. Rev. Lett.*, 42:65–67, Jan 1979.

[52] Roopayan Ghosh, Arnab Sen, and K. Sengupta. Ramp and periodic dynamics across non-ising critical points. *Phys. Rev. B*, 97:014309, Jan 2018.

[53] P. Jordan and E. Wigner. Uber das paulische aquivalenzverbot. *Zeitschrift fur Physik*, 47(9-10):631–651, September 1928.

[54] Johannes Motruk, Erez Berg, Ari M. Turner, and Frank Pollmann. Topological phases in gapped edges of fractionalized systems. *Phys. Rev. B*, 88:085115, Aug 2013.

[55] M B Hastings. An area law for one-dimensional quantum systems. *Journal of Statistical Mechanics: Theory and Experiment*, 2007(08):P08024–P08024, aug 2007.

[56] F. Verstraete, J. J. García-Ripoll, and J. I. Cirac. Matrix product density operators: Simulation of finite-temperature and dissipative systems. *Phys. Rev. Lett.*, 93:207204, Nov 2004.

[57] G. Vidal, J. I. Latorre, E. Rico, and A. Kitaev. Entanglement in quantum critical phenomena. *Phys. Rev. Lett.*, 90:227902, Jun 2003.

[58] J. I. Latorre, E. Rico, and G. Vidal. Ground state entanglement in quantum spin chains. *Quant. Inf. Comput.*, 4:48–92, 2004.

[59] Michael M. Wolf. Violation of the entropic area law for fermions. *Phys. Rev. Lett.*, 96:010404, Jan 2006.

[60] Dimitri Gioev and Israel Klich. Entanglement entropy of fermions in any dimension and the widom conjecture. *Phys. Rev. Lett.*, 96:100503, Mar 2006.

[61] J. Eisert, M. Cramer, and M. B. Plenio. Colloquium: Area laws for the entanglement entropy. *Rev. Mod. Phys.*, 82:277–306, Feb 2010.

[62] Vincenzo Alba, Maurizio Fagotti, and Pasquale Calabrese. Entanglement entropy of excited states. *Journal of Statistical Mechanics: Theory and Experiment*, 2009(10):P10020, October 2009.

[63] F Ares, J G Esteve, F Falceto, and E Sánchez-Burillo. Excited state entanglement in homogeneous fermionic chains. *Journal of Physics A: Mathematical and Theoretical*, 47(24):245301, June 2014.

[64] Gregory M. Crosswhite, A. C. Doherty, and Guifré Vidal. Applying matrix product operators to model systems with long-range interactions. *Phys. Rev. B*, 78:035116, Jul 2008.

[65] Norbert Schuch, Michael M. Wolf, Frank Verstraete, and J. Ignacio Cirac. Entropy scaling and simulability by matrix product states. *Phys. Rev. Lett.*, 100:030504, Jan 2008.

[66] Jens Eisert and Tobias J. Osborne. General entanglement scaling laws from time evolution. *Phys. Rev. Lett.*, 97:150404, Oct 2006.

[67] N Schuch, M M Wolf, K G H Vollbrecht, and J I Cirac. On entropy growth and the hardness of simulating time evolution. *New Journal of Physics*, 10(3):033032, mar 2008.

[68] Michael Zwolak and Guifré Vidal. Mixed-state dynamics in one-dimensional quantum lattice systems: A time-dependent superoperator renormalization algorithm. *Phys. Rev. Lett.*, 93:207205, Nov 2004.

[69] I. M. Georgescu, S. Ashhab, and Franco Nori. Quantum simulation. *Rev. Mod. Phys.*, 86:153–185, Mar 2014.

[70] Immanuel Bloch, Jean Dalibard, and Sylvain Nascimbène. Quantum simulations with ultracold quantum gases. *Nature Physics*, 8(4):267–276, April 2012.

[71] Steven R. White and Adrian E. Feiguin. Real-time evolution using the density matrix renormalization group. *Phys. Rev. Lett.*, 93:076401, Aug 2004.

[72] Guifré Vidal. Efficient simulation of one-dimensional quantum many-body systems. *Phys. Rev. Lett.*, 93:040502, Jul 2004.

[73] Jutho Haegeman, Christian Lubich, Ivan Oseledets, Bart Vandereycken, and Frank Verstraete. Unifying time evolution and optimization with matrix product states. *Phys. Rev. B*, 94:165116, Oct 2016.

[74] R. Moessner and S. L. Sondhi. Equilibration and order in quantum floquet matter. *Nature Physics*, 13(5):424–428, 2017.

[75] Marin Bukov, Luca D'Alessio, and Anatoli Polkovnikov. Universal high-frequency behavior of periodically driven systems: from dynamical stabilization to floquet engineering. *Advances in Physics*, 64(2):139–226, 2015.

[76] Jon H. Shirley. Solution of the schrödinger equation with a hamiltonian periodic in time. *Phys. Rev.*, 138:B979–B987, May 1965.

[77] Hideo Sambe. Steady states and quasienergies of a quantum-mechanical system in an oscillating field. *Phys. Rev. A*, 7:2203–2213, Jun 1973.

[78] André Eckardt and Egidijus Anisimovas. High-frequency approximation for periodically driven quantum systems from a floquet-space perspective. *New Journal of Physics*, 17(9):093039, sep 2015.

[79] Naoto Tsuji, Takashi Oka, and Hideo Aoki. Correlated electron systems periodically driven out of equilibrium: Floquet + DMFT formalism. *Phys. Rev. B*, 78:235124, Dec 2008.

[80] Pedro Ponte, Z. Papić, Fran çois Huveneers, and Dmitry A. Abanin. Many-body localization in periodically driven systems. *Phys. Rev. Lett.*, 114:140401, Apr 2015.

[81] Arnab Das. Exotic freezing of response in a quantum many-body system. *Phys. Rev. B*, 82:172402, Nov 2010.

[82] Swathi S. Hegde, Hemant Katiyar, T. S. Mahesh, and Arnab Das. Freezing a quantum magnet by repeated quantum interference: An experimental realization. *Phys. Rev. B*, 90:174407, Nov 2014.

[83] Soonwon Choi, Joonhee Choi, Renate Landig, Georg Kucsko, Hengyun Zhou, Junichi Isoya, Fedor Jelezko, Shinobu Onoda, Hitoshi Sumiya, Vedika Khemani, Curt von Keyserlingk, Norman Y. Yao, Eugene Demler, and Mikhail D. Lukin. Observation of discrete time-crystalline order in a disordered dipolar many-body system. *Nature*, 543(7644):221–225, mar 2017.

[84] Dominic V. Else, Bela Bauer, and Chetan Nayak. Floquet time crystals. *Phys. Rev. Lett.*, 117:090402, Aug 2016.

[85] Jared Rovny, Robert L. Blum, and Sean E. Barrett. Observation of discrete-time-crystal signatures in an ordered dipolar many-body system. *Physical Review Letters*, 120(18), May 2018.

[86] Dominic V. Else and Chetan Nayak. Classification of topological phases in periodically driven interacting systems. *Phys. Rev. B*, 93:201103, May 2016.

[87] Rahul Roy and Fenner Harper. Abelian floquet symmetry-protected topological phases in one dimension. *Phys. Rev. B*, 94:125105, Sep 2016.

[88] Andrew C Potter, Takahiro Morimoto, and Ashvin Vishwanath. Classification of interacting topological floquet phases in one dimension. *Physical Review X*, 6(4):041001, 2016.

[89] C. W. von Keyserlingk and S. L. Sondhi. Phase structure of one-dimensional interacting floquet systems. i. abelian symmetry-protected topological phases. *Phys. Rev. B*, 93:245145, Jun 2016.

[90] Rahul Roy and Fenner Harper. Periodic table for floquet topological insulators. *Phys. Rev. B*, 96:155118, Oct 2017.

[91] I.-D. Potirniche, A. C. Potter, M. Schleier-Smith, A. Vishwanath, and N. Y. Yao. Floquet symmetry-protected topological phases in cold-atom systems. *Phys. Rev. Lett.*, 119:123601, Sep 2017.

[92] Paraj Titum, Erez Berg, Mark S. Rudner, Gil Refael, and Netanel H. Lindner. Anomalous floquet-anderson insulator as a nonadiabatic quantized charge pump. *Phys. Rev. X*, 6:021013, May 2016.

[93] Mark S. Rudner, Netanel H. Lindner, Erez Berg, and Michael Levin. Anomalous edge states and the bulk-edge correspondence for periodically driven two-dimensional systems. *Phys. Rev. X*, 3:031005, Jul 2013.

[94] Manisha Thakurathi, Aavishkar A. Patel, Diptiman Sen, and Amit Dutta. Floquet generation of majorana end modes and topological invariants. *Phys. Rev. B*, 88:155133, Oct 2013.

[95] G. J. Sreejith, Achilleas Lazarides, and Roderich Moessner. Parafermion chain with $2\pi/k$ floquet edge modes. *Phys. Rev. B*, 94:045127, Jul 2016.

[96] Luca D'Alessio and Marcos Rigol. Long-time behavior of isolated periodically driven interacting lattice systems. *Phys. Rev. X*, 4:041048, Dec 2014.

[97] Achilleas Lazarides, Arnab Das, and Roderich Moessner. Equilibrium states of generic quantum systems subject to periodic driving. *Phys. Rev. E*, 90:012110, Jul 2014.

[98] Pedro Ponte, Anushya Chandran, Z. Papić, and Dmitry A. Abanin. Periodically driven ergodic and many-body localized quantum systems. *Annals of Physics*, 353:196–204, February 2015.

[99] Vedika Khemani, Achilleas Lazarides, Roderich Moessner, and S. L. Sondhi. Phase structure of driven quantum systems. *Phys. Rev. Lett.*, 116:250401, Jun 2016.

[100] Dominic V. Else, Bela Bauer, and Chetan Nayak. Prethermal phases of matter protected by time-translation symmetry. *Phys. Rev. X*, 7:011026, Mar 2017.

[101] Wojciech De Roeck and Victor Verreet. Very slow heating for weakly driven quantum many-body systems, 2019.

[102] J. Cardy. Boundary conformal field theory. In *Encyclopedia of Mathematical Physics*, pages 333–340. Elsevier, 2006.

[103] Wojciech H. Zurek, Uwe Dorner, and Peter Zoller. Dynamics of a quantum phase transition. *Phys. Rev. Lett.*, 95:105701, Sep 2005.

[104] Diptiman Sen, K. Sengupta, and Shreyoshi Mondal. Defect production in nonlinear quench across a quantum critical point. *Phys. Rev. Lett.*, 101:016806, Jul 2008.

[105] Anatoli Polkovnikov, Krishnendu Sengupta, Alessandro Silva, and Mukund Vengalattore. Colloquium: Nonequilibrium dynamics of closed interacting quantum systems. *Reviews of Modern Physics*, 83(3):863–883, August 2011.

[106] R. Vasseur, J. P. Dahlhaus, and J. E. Moore. Universal nonequilibrium signatures of majorana zero modes in quench dynamics. *Phys. Rev. X*, 4:041007, Oct 2014.

[107] Eduardo Fradkin and Leo P. Kadanoff. Disorder variables and para-fermions in two-dimensional statistical mechanics. *Nuclear Physics B*, 170(1):1–15, August 1980.

[108] F. C. Alcaraz and R. Köberle. Hidden parafermions in $z(n)$ theories. *Phys. Rev. D*, 24:1562–1568, Sep 1981.

[109] Steven Howes, Leo P. Kadanoff, and Marcel Den Nijs. Quantum model for commensurate-incommensurate transitions. *Nuclear Physics B*, 215(2):169–208, January 1983.

[110] Philippe Di Francesco, Pierre Mathieu, and David Senechal. *Conformal field theory*. Graduate texts in contemporary physics. Springer, New York, NY, 1997.

[111] A. B. Zamolodchikov. Infinite Additional Symmetries in Two-Dimensional Conformal Quantum Field Theory. *Theor. Math. Phys.*, 65:1205–1213, 1985. [Teor. Mat. Fiz.65,347(1985)].

[112] Ian Affleck, Masaki Oshikawa, and Hubert Saleur. Boundary critical phenomena in the three-state potts model. *Journal of Physics A: Mathematical and General*, 31(28):5827–5842, jul 1998.

[113] John L Cardy. Boundary conditions, fusion rules and the verlinde formula. *Nuclear Physics B*, 324(3):581–596, 1989.

[114] John L. Cardy. Conformal invariance and surface critical behavior. *Nuclear Physics B*, 240(4):514–532, November 1984.

[115] Naomichi Hatano and Masuo Suzuki. *Finding Exponential Product Formulas of Higher Orders*, pages 37–68. Springer Berlin Heidelberg, November 2005.

[116] David A. Huse. Simple three-state model with infinitely many phases. *Phys. Rev. B*, 24:5180–5194, Nov 1981.

[117] Seth Whitsitt, Rhine Samajdar, and Subir Sachdev. Quantum field theory for the chiral clock transition in one spatial dimension. *Phys. Rev. B*, 98:205118, Nov 2018.

[118] Rui-Zhen Huang and Shuai Yin. Nonequilibrium critical dynamics in the quantum chiral clock model. *Phys. Rev. B*, 99:184104, May 2019.

[119] Lucia Hackermüller, Ulrich Schneider, Maria Moreno-Cardoner, Takuya Kitagawa, Thorsten Best, Sebastian Will, Eugene Demler, Ehud Altman, Immanuel Bloch, and Belén Paredes. Anomalous expansion of attractively interacting fermionic atoms in an optical lattice. *Science*, 327(5973):1621–1624, March 2010.

[120] S. Trotzky, Y-A. Chen, A. Flesch, I. P. McCulloch, U. Schollwöck, J. Eisert, and I. Bloch. Probing the relaxation towards equilibrium in an isolated strongly correlated one-dimensional bose gas. *Nature Physics*, 8(4):325–330, February 2012.

[121] M. Gring, M. Kuhnert, T. Langen, T. Kitagawa, B. Rauer, M. Schreitl, I. Mazets, D. Adu Smith, E. Demler, and J. Schmiedmayer. Relaxation and prethermalization in an isolated quantum system. *Science*, 337(6100):1318–1322, September 2012.

[122] Marc Cheneau, Peter Barmettler, Dario Poletti, Manuel Endres, Peter Schauß, Takeshi Fukuhara, Christian Gross, Immanuel Bloch, Corinna Kollath, and Stefan Kuhr. Light-cone-like spreading of correlations in a quantum many-body system. *Nature*, 481(7382):484–487, January 2012.

[123] Tim Langen, Remi Geiger, Maximilian Kuhnert, Bernhard Rauer, and Jörg Schmiedmayer. Local emergence of thermal correlations in an isolated quantum many-body system. *Nature Physics*, 9, 05 2013.

[124] Tim Langen, Sebastian Erne, Remi Geiger, Bernhard Rauer, Thomas Schweigler, Maximilian Kuhnert, Wolfgang Rohringer, Igor E Mazets, Thomas Gasenzer, and Jörg Schmiedmayer. Experimental observation of a generalized gibbs ensemble. *Science*, 348(6231):207–211, 2015.

[125] Takeshi Fukuhara, Peter Schauß, Manuel Endres, Sebastian Hild, Marc Cheneau, Immanuel Bloch, and Christian Gross. Microscopic observation of magnon bound states and their dynamics. *Nature*, 502, 09 2013.

[126] M. Schreiber, S. S. Hodgman, P. Bordia, H. P. Luschen, M. H. Fischer, R. Vosk, E. Altman, U. Schneider, and I. Bloch. Observation of many-body localization of interacting fermions in a quasirandom optical lattice. *Science*, 349(6250):842–845, July 2015.

[127] Rajibul Islam, Ruichao Ma, Philipp M. Preiss, M. Eric Tai, Alexander Lukin, Matthew Rispoli, and Markus Greiner. Measuring entanglement entropy in a quantum many-body system. *Nature*, 528(7580):77–83, December 2015.

[128] Adam Kaufman, M. Tai, Alexander Lukin, Matthew Rispoli, Robert Schittko, Philipp Preiss, and Markus Greiner. Quantum thermalization through entanglement in an isolated many-body system. *Science*, 353, 03 2016.

[129] Sandu Popescu, Anthony J Short, and Andreas Winter. Entanglement and the foundations of statistical mechanics. *Nature Physics*, 2(11):754–758, 2006.

[130] Jens H. Bardarson, Frank Pollmann, and Joel E. Moore. Unbounded growth of entanglement in models of many-body localization. *Phys. Rev. Lett.*, 109:017202, Jul 2012.

[131] Dmitry A. Abanin, Ehud Altman, Immanuel Bloch, and Maksym Serbyn. Colloquium: Many-body localization, thermalization, and entanglement. *Reviews of Modern Physics*, 91(2), May 2019.

[132] Christian Gogolin and Jens Eisert. Equilibration, thermalisation, and the emergence of statistical mechanics in closed quantum systems. *Reports on Progress in Physics*, 79(5):056001, April 2016.

[133] Fabian HL Essler and Maurizio Fagotti. Quench dynamics and relaxation in isolated integrable quantum spin chains. *Journal of Statistical Mechanics: Theory and Experiment*, 2016(6):064002, 2016.

[134] Pasquale Calabrese and John Cardy. Evolution of entanglement entropy in one-dimensional systems. *Journal of Statistical Mechanics: Theory and Experiment*, 2005(04):P04010, apr 2005.

[135] Maurizio Fagotti and Pasquale Calabrese. Evolution of entanglement entropy following a quantum quench: Analytic results for the xy chain in a transverse magnetic field. *Physical Review A*, 78, 04 2008.

[136] V. Eisler and I. Peschel. Entanglement in a periodic quench. *Annalen der Physik*, 17(6):410–423, June 2008.

[137] M. Ghasemi Nezhadhaghighi and M. A. Rajabpour. Entanglement dynamics in short- and long-range harmonic oscillators. *Phys. Rev. B*, 90:205438, Nov 2014.

[138] Jordan S. Cotler, Mark P. Hertzberg, Márk Mezei, and Mark T. Mueller. Entanglement growth after a global quench in free scalar field theory. *Journal of High Energy Physics*, 2016(11), November 2016.

[139] Andreas M Läuchli and Corinna Kollath. Spreading of correlations and entanglement after a quench in the one-dimensional bose–hubbard model. *Journal of Statistical Mechanics: Theory and Experiment*, 2008(05):P05018, May 2008.

[140] Vincenzo Alba and Pasquale Calabrese. Entanglement and thermodynamics after a quantum quench in integrable systems. *Proceedings of the National Academy of Sciences*, 114, 08 2016.

[141] Hyungwon Kim and David Huse. Ballistic spreading of entanglement in a diffusive nonintegrable system. *Physical review letters*, 111:127205, 09 2013.

[142] Gabriele De Chiara, Simone Montangero, Pasquale Calabrese, and Rosario Fazio. Entanglement entropy dynamics of heisenberg chains. *Journal of Statistical Mechanics: Theory and Experiment*, 2006(03):P03001–P03001, March 2006.

[143] Arnab Sen, Sourav Nandy, and K. Sengupta. Entanglement generation in periodically driven integrable systems: Dynamical phase transitions and steady state. *Phys. Rev. B*, 94:214301, Dec 2016.

[144] Bruno Bertini and Pasquale Calabrese. Prethermalization and thermalization in entanglement dynamics. *Phys. Rev. B*, 102:094303, Sep 2020.

[145] O Pomponio, L Pristyák, and G Takács. Quasi-particle spectrum and entanglement generation after a quench in the quantum potts spin chain. *Journal of Statistical Mechanics: Theory and Experiment*, 2019(1):013104, January 2019.

[146] Pasquale Calabrese, Fabian H. L. Essler, and Maurizio Fagotti. Quantum quench in the transverse-field ising chain. *Phys. Rev. Lett.*, 106:227203, Jun 2011.

[147] Pasquale Calabrese, Fabian H L Essler, and Maurizio Fagotti. Quantum quench in the transverse field ising chain: I. time evolution of order parameter correlators. *Journal of Statistical Mechanics: Theory and Experiment*, 2012(07):P07016, July 2012.

[148] Pasquale Calabrese, Fabian H L Essler, and Maurizio Fagotti. Quantum quenches in the transverse field ising chain: II. stationary state properties. *Journal of Statistical Mechanics: Theory and Experiment*, 2012(07):P07022, July 2012.

[149] Marton Kormos, Mario Collura, Gabor Takács, and Pasquale Calabrese. Real-time confinement following a quantum quench to a non-integrable model. *Nature Physics*, 13(3):246–249, Mar 2017.

[150] Peter E Finch, Michael Flohr, and Holger Frahm. Znclock models and chains ofso(n)2non-abelian anyons: symmetries, integrable points and low energy properties. *Journal of Statistical Mechanics: Theory and Experiment*, 2018(2):023103, February 2018.

[151] Jack Kemp, Norman Y Yao, Christopher R Laumann, and Paul Fendley. Long coherence times for edge spins. *Journal of Statistical Mechanics: Theory and Experiment*, 2017(6):063105, jun 2017.

[152] Dominic V. Else, Paul Fendley, Jack Kemp, and Chetan Nayak. Prethermal strong zero modes and topological qubits. *Phys. Rev. X*, 7:041062, Dec 2017.

[153] Leung Chim. Boundary s-matrix for the integrable q-potts model. *Journal of Physics A: Mathematical and General*, 28(24):7039–7050, dec 1995.

[154] Heinz-Peter Breuer and Francesco Petruccione. *The Theory of Open Quantum Systems*. Oxford University Press, January 2007.

[155] G. Lindblad. On the generators of quantum dynamical semigroups. *Communications in Mathematical Physics*, 48(2):119–130, Jun 1976.

[156] Vittorio Gorini, Andrzej Kossakowski, and E. C. G. Sudarshan. Completely positive dynamical semigroups of n-level systems. *Journal of Mathematical Physics*, 17(5):821–825, 1976.

[157] Michael P. Zaletel, Roger S. K. Mong, Christoph Karrasch, Joel E. Moore, and Frank Pollmann. Time-evolving a matrix product state with long-ranged interactions. *Phys. Rev. B*, 91:165112, Apr 2015.

[158] Kemal Bidzhiev and Grégoire Misguich. Out-of-equilibrium dynamics in a quantum impurity model: Numerics for particle transport and entanglement entropy. *Phys. Rev. B*, 96:195117, Nov 2017.

[159] K Saito. Strong evidence of normal heat conduction in a one-dimensional quantum system. *Europhysics Letters (EPL)*, 61(1):34–40, jan 2003.

[160] Tomaž Prosen and Marko Žnidarič. Matrix product simulations of non-equilibrium steady states of quantum spin chains. *Journal of Statistical Mechanics: Theory and Experiment*, 2009(02):P02035, feb 2009.

[161] Toma ž Prosen. Open xxz spin chain: Nonequilibrium steady state and a strict bound on ballistic transport. *Phys. Rev. Lett.*, 106:217206, May 2011.

[162] Marko Žnidarič. Spin transport in a one-dimensional anisotropic heisenberg model. *Phys. Rev. Lett.*, 106:220601, May 2011.

[163] J. J. Mendoza-Arenas, M. Žnidarič, V. K. Varma, J. Goold, S. R. Clark, and A. Scardicchio. Asymmetry in energy versus spin transport in certain interacting disordered systems. *Phys. Rev. B*, 99:094435, Mar 2019.

[164] Marlon Brenes, Eduardo Mascarenhas, Marcos Rigol, and John Goold. High-temperature coherent transport in the xxz chain in the presence of an impurity. *Phys. Rev. B*, 98:235128, Dec 2018.

[165] Yongchan Yoo, Junhyun Lee, and Brian Swingle. Nonequilibrium steady state phases of the interacting aubry-andré-harper model. *Phys. Rev. B*, 102:195142, Nov 2020.

[166] Toma ž Prosen and Marko Žnidarič. Diffusive high-temperature transport in the one-dimensional hubbard model. *Phys. Rev. B*, 86:125118, Sep 2012.

[167] Hannu Wichterich, Markus J. Henrich, Heinz-Peter Breuer, Jochen Gemmer, and Mathias Michel. Modeling heat transport through completely positive maps. *Phys. Rev. E*, 76:031115, Sep 2007.

[168] Devashish Tupkary, Abhishek Dhar, Manas Kulkarni, and Archak Purkayastha. Fundamental limitations in lindblad descriptions of systems weakly coupled to baths, 2021.

[169] Abhishek Dhar. Heat transport in low-dimensional systems. *Advances in Physics*, 57(5):457–537, 2008.

[170] C Mejía-Monasterio, T Prosen, and G Casati. Fourier's law in a quantum spin chain and the onset of quantum chaos. *Europhysics Letters (EPL)*, 72(4):520–526, nov 2005.

[171] F. Heidrich-Meisner, A. Honecker, and W. Brenig. Transport in quasi one-dimensional spin-1/2 systems. *The European Physical Journal Special Topics*, 151(1):135–145, Dec 2007.

[172] Keiji Saito. Study on energy diffusive phenomenon in quantum spin chains. *Journal of the Physical Society of Japan*, 72(Suppl.C):66–68, 2003.

[173] Saito, Takesue, and Miyashita. Thermal conduction in a quantum system. *Physical review. E, Statistical physics, plasmas, fluids, and related interdisciplinary topics*, 54 3:2404–2408, 1996.

[174] X. Zotos, F. Naef, and P. Prelovsek. Transport and conservation laws. *Phys. Rev. B*, 55:11029–11032, May 1997.

[175] M. Schulz, S. R. Taylor, C. A. Hooley, and A. Scardicchio. Energy transport in a disordered spin chain with broken u(1) symmetry: Diffusion, subdiffusion, and many-body localization. *Phys. Rev. B*, 98:180201, Nov 2018.

[176] Marko Žnidarič, Antonello Scardicchio, and Vipin Kerala Varma. Diffusive and subdiffusive spin transport in the ergodic phase of a many-body localizable system. *Phys. Rev. Lett.*, 117:040601, Jul 2016.

[177] Ke-Wei Sun, Chen Wang, and Qing-Hu Chen. Heat transport in an open transverse-field ising chain. *EPL (Europhysics Letters)*, 92(2):24002, oct 2010.

[178] João S. Ferreira and Michele Filippone. Ballistic-to-diffusive transition in spin chains with broken integrability. *Phys. Rev. B*, 102:184304, Nov 2020.

[179] H. Castella, X. Zotos, and P. Prelovsek. Integrability and ideal conductance at finite temperatures. *Phys. Rev. Lett.*, 74:972–975, Feb 1995.

[180] Sarang Gopalakrishnan and Romain Vasseur. Kinetic theory of spin diffusion and superdiffusion in xxz spin chains. *Phys. Rev. Lett.*, 122:127202, Mar 2019.

[181] Marko Ljubotina, Marko Žnidarič, and Tomaž Prosen. Spin diffusion from an inhomogeneous quench in an integrable system. *Nature Communications*, 8(1):16117, Jul 2017.

[182] J. J. Mendoza-Arenas, S. R. Clark, and D. Jaksch. Coexistence of energy diffusion and local thermalization in nonequilibrium xxz spin chains with integrability breaking. *Phys. Rev. E*, 91:042129, Apr 2015.

[183] Jinshan Wu and Mona Berciu. Heat transport in quantum spin chains: Relevance of integrability. *Phys. Rev. B*, 83:214416, Jun 2011.

[184] J J Mendoza-Arenas, S Al-Assam, S R Clark, and D Jaksch. Heat transport in theXXZspin chain: from ballistic to diffusive regimes and dephasing enhancement. *Journal of Statistical Mechanics: Theory and Experiment*, 2013(07):P07007, jul 2013.

[185] B. Bertini, F. Heidrich-Meisner, C. Karrasch, T. Prosen, R. Steinigeweg, and M. Žnidarič. Finite-temperature transport in one-dimensional quantum lattice models. *Rev. Mod. Phys.*, 93:025003, May 2021.

[186] Roger S K Mong, David J Clarke, Jason Alicea, Netanel H Lindner, and Paul Fendley. Parafermionic conformal field theory on the lattice. *Journal of Physics A: Mathematical and Theoretical*, 47(45):452001, oct 2014.

[187] Helen Au-Yang, Barry M. McCoy, Jacques H.H. Perk, Shuang Tang, and Mu-Lin Yan. Commuting transfer matrices in the chiral potts models: Solutions of star-triangle equations with genus >1. *Physics Letters A*, 123(5):219–223, August 1987.

[188] Ricardo Puebla, Alberto Imparato, Alessio Belenchia, and Mauro Paternostro. Open quantum rotors: Connecting correlations and physical currents, 2021.

[189] Leonardo Mazza, Jacopo Viti, Matteo Carrega, Davide Rossini, and Andrea De Luca. Energy transport in an integrable parafermionic chain via generalized hydrodynamics. *Phys. Rev. B*, 98:075421, Aug 2018.

[190] Shigeru Ajisaka, Felipe Barra, Carlos Mejía-Monasterio, and Toma ž Prosen. Nonequlibrium particle and energy currents in quantum chains connected to mesoscopic fermi reservoirs. *Phys. Rev. B*, 86:125111, Sep 2012.

[191] John Watrous. *The Theory of Quantum Information.* Cambridge University Press, April 2018.

[192] Toma ž Prosen and Iztok Pižorn. Operator space entanglement entropy in a transverse ising chain. *Phys. Rev. A*, 76:032316, Sep 2007.

[193] Iztok Pižorn and Toma ž Prosen. Operator space entanglement entropy in xy spin chains. *Phys. Rev. B*, 79:184416, May 2009.

[194] Marko Žnidarič. A matrix product solution for a nonequilibrium steady state of an XX chain. *Journal of Physics A: Mathematical and Theoretical*, 43(41):415004, September 2010.

[195] Ryogo Kubo. Statistical-mechanical theory of irreversible processes. i. general theory and simple applications to magnetic and conduction problems. *Journal of the Physical Society of Japan*, 12(6):570–586, 1957.

[196] Ryogo Kubo, Mario Yokota, and Sadao Nakajima. Statistical-mechanical theory of irreversible processes. ii. response to thermal disturbance. *Journal of the Physical Society of Japan*, 12(11):1203–1211, 1957.

[197] Subroto Mukerjee and B. Sriram Shastry. Signatures of diffusion and ballistic transport in the stiffness, dynamical correlation functions, and statistics of one-dimensional systems. *Phys. Rev. B*, 77:245131, Jun 2008.

[198] C. Karrasch, J. H. Bardarson, and J. E. Moore. Finite-temperature dynamical density matrix renormalization group and the drude weight of spin-1/2 chains. *Phys. Rev. Lett.*, 108:227206, May 2012.

[199] C. Karrasch, J. Hauschild, S. Langer, and F. Heidrich-Meisner. Drude weight of the spin-$\frac{1}{2}$ xxz chain: Density matrix renormalization group versus exact diagonalization. *Phys. Rev. B*, 87:245128, Jun 2013.

[200] Frank Wilczek. Quantum time crystals. *Phys. Rev. Lett.*, 109:160401, Oct 2012.

[201] Patrick Bruno. Comment on “quantum time crystals”. *Phys. Rev. Lett.*, 110:118901, Mar 2013.

[202] Haruki Watanabe and Masaki Oshikawa. Absence of quantum time crystals. *Phys. Rev. Lett.*, 114:251603, Jun 2015.

[203] C. W. von Keyserlingk, Vedika Khemani, and S. L. Sondhi. Absolute stability and spatiotemporal long-range order in floquet systems. *Phys. Rev. B*, 94:085112, Aug 2016.

[204] N. Y. Yao, A. C. Potter, I.-D. Potirniche, and A. Vishwanath. Discrete time crystals: Rigidity, criticality, and realizations. *Phys. Rev. Lett.*, 118:030401, Jan 2017.

[205] Wen Wei Ho, Soonwon Choi, Mikhail D. Lukin, and Dmitry A. Abanin. Critical time crystals in dipolar systems. *Phys. Rev. Lett.*, 119:010602, Jul 2017.

[206] Varad R. Pande, Gaurav Bhole, Deepak Khurana, and T. S. Mahesh. Strong algorithmic cooling in large star-topology quantum registers. *Phys. Rev. A*, 96:012330, Jul 2017.

[207] Malcolm H Levitt. *Spin dynamics: basics of nuclear magnetic resonance.* John Wiley & Sons, 2001.

[208] See supplementary material to this article.

[209] Dmitry A. Abanin, Wojciech De Roeck, and Fran çois Huveneers. Exponentially slow heating in periodically driven many-body systems. *Phys. Rev. Lett.*, 115:256803, Dec 2015.

[210] *Protein NMR Spectroscopy.* Elsevier, 2007.

[211] Achilleas Lazarides and Roderich Moessner. Fate of a discrete time crystal in an open system. *Phys. Rev. B*, 95:195135, May 2017.

[212] Soonwon Choi, Norman Y Yao, and Mikhail D Lukin. Quantum metrology based on strongly correlated matter. *arXiv preprint arXiv:1801.00042*, 2018.

[213] Shun-Yao Zhang and Dong-Ling Deng. Anomalous quantum information scrambling for F_3 parafermion chains. *Phys. Rev. B*, 103:195156, May 2021.